Processing of Oxide Dispersion Strengthened Alloys via Mechanical Alloying and Spark Plasma Sintering

A Dissertation

Presented in Partial Fulfillment of the Requirements for the

Degree of Doctor of Philosophy

with a

Major in Materials Science and Engineering

in the

College of Graduate Studies

University of Idaho

by

Somayeh Pasebani

July 2014

Major Professor: Indrajit Charit, Ph.D.

Authorization to Submit Dissertation

This dissertation of Somayeh Pasebani, submitted for the degree of Doctor of Philosophy in Materials Science and Engineering and titled "Processing of Oxide Dispersion Strengthened Alloys via Mechanical Alloying and Spark Plasma Sintering," has been reviewed in final form. Permission, as indicated by signatures and dates given below, is now granted to submit final copies to the College of Graduate Studies for approval.

Major Professor: _____ Date: _____
Indrajit Charit, Ph.D.

Committee Members: _____ Date: _____
Batric Pesic, Ph.D.

_____ Date: _____
Krishnan Raja, Ph.D.

_____ Date: _____
James I. Cole, Ph.D.

_____ Date: _____
Steven N. Bakhtiar, Ph.D.

Department Administrator: _____ Date: _____
Eric Aston, Ph.D.

Discipline's College Dean: _____ Date: _____
Larry A. Stauffer, Ph.D.

Final Approval and Acceptance

Dean of the College of Graduate Studies: _____ Date: _____
Jie Chen, Ph.D.

Abstract

Oxide dispersion strengthened (ODS) alloys are potential candidates to be used as high temperature structural materials in advanced nuclear and fossil energy systems because of highly stable microstructure and high creep strength. The high temperature properties of these alloys are caused by high density of dislocations and grain boundaries that are effectively pinned by ultrafine Y−Ti−O-enriched particles. The traditional processing method of ODS alloys is via mechanical alloying (MA) of high chromium content powder in combination with up to 0.5 wt.% Y_2O_3, followed by hot consolidation via hot extrusion or hot isostatic pressing. In current study, Fe-based ODS and nickel-based ODS alloys are developed by using spark plasma sintering (SPS). Furthermore, in Fe-based ODS alloys or so called "nanostructured ferritic steels", Y_2O_3 is replaced by equi-atomic percent of La_2O_3. Then, the effects of alloying composition, processing parameters including milling parameters and sintering parameters, on the microstructure characteristics and mechanical properties of the milled powder and consolidated alloys were investigated. Several Fe–14Cr based alloys with varying compositions were processed. Microstructural characteristics of the consolidated alloys were examined via transmission electron microscopy and atom probe tomography, and mechanical properties were evaluated using microhardness testing, shear punch testing and mini-compression testing. Lanthanum oxide (0.5 wt.%) was added to Fe–14Cr to improve microstructural stability and mechanical properties mainly due to formation of a high number density of La–Cr–O-enriched nanoclusters (NCs). The combined addition of La (0.5 wt.%), Ti (1 wt.%) and Mo (0.3 wt.%) to the Fe–14Cr base composition further enhanced the microstructural stability and mechanical properties. The NCs enriched in Cr–Ti–La–O with a number density of 1.4×10^{24} m^{-3} were found in this

alloy (sintered at 950 °C for 7 min) containing a bimodal grain size distribution. Formation mechanism of these NCs can be explained through the concentrations and diffusion rates of the initial oxide species formed during the milling process and initial stages of sintering as well as the thermodynamics nucleation barrier and their enthalpy of formation. Milling provided solid solution, high density of dislocations, vacancies in the powder and facilitated the nucleation of NCs and enhanced the densification behavior by initiating sintering at lower temperatures while lowering the activation energy for both grain boundary and volume diffusion. Significant densification occurred at temperatures greater than 950 ^{o}C with a relative density higher than 98%. High mechanical strength values were achieved in room and high temperature due to the combined strengthening mechanisms of work hardening, grain refinement, dispersion strengthening and solid solution strengthening. The microstructure of lanthana-bearing NFS was stable after self-ion irradiation at 500 °C up to 100 dpa. A notable irradiation hardening and enhanced dislocation activity occurred after irradiation.

On the other hand, nickel-based oxide dispersion strengthened (ODS) alloys were developed by adding 1.2 wt.% Y_2O_3 to Ni–20Cr matrix via MA and SPS. Additionally, 5 wt.% Al_2O_3 was added to Ni–20Cr–1.2Y_2O_3 to provide composite strengthening. Higher sintering temperature led to higher fraction of recrystallized grains, higher hardness, density, and higher volume fraction of annealing twins. Adding 1.2 wt.% Y_2O_3 to the Ni–20Cr matrix significantly reduced the grain size. Higher compression yield stress at 800 °C for Ni–20Cr–1.2Y_2O_3–5Al_2O_3 alloy was attributed to a combined effect of dispersion and composite strengthening.

Acknowledgements

I would like to thank my major professor Dr. Indrajit Charit for initiating this project, giving me a great opportunity to work with his group, teaching, guiding and supporting me through past four years. I am very much grateful for his trust, time, patience, dedication and encouragement. He gave me freedom and permission to bring in my own ideas. Without him this dissertation would not be in the format presented here. I truly appreciate him.

I would like to express my sincere gratitude and deepest respect to my committee members; Dr. Batric Pesic, Dr. Krishnan Raja, Dr. James I. Cole and Dr. Steven N. Bakhtiar for their valuable comments and taking time out of their tight schedule for improving the quality of my dissertation. I truly appreciate them.

I would like to acknowledge Dr. Eric Aston as the chair of the department of Chemical and Materials Engineering Department at University of Idaho and other faculty members. I truly appreciate the help of Chemical and Materials Engineering Department staff specially Mrs. Margaret Baker, Mrs. Gail Bergman, Dr. Dave MacPherson and Mr. Charles Cornwall for helping me a lot during past four years.

I greatly acknowledge the financial support of the Laboratory Directed Research and Development Program of Idaho National Laboratory (INL), Contract DE–AC07–05ID14517. Also, the financial support of the University Coal Research Program of the US Department of Energy (DOE) via a grant (DE–FE0008648) managed by the National Energy Technology Laboratory (NETL) is deeply acknowledged.

I also extend my sincere thanks to the Advanced Test Reactor National Scientific User Facility (ATRNSUF) organization and staff members for educational workshops, supporting

my research and offering me a great opportunity to use the state of the art characterization facilities. I acknowledge the staff of Microscopy and Characterization Suite (MaCS) facility at the Center for Advanced Energy Studies (CAES).

I am very much thankful to:

Dr. Darryl P. Butt for reviewing my papers, his valuable comments, and authorizing me to use the SPS machine.

Dr. Rajiv S. Mishra for giving me the opportunity to work in nickel-based ODS alloys project and his valuable inputs.

Mrs. Jatuporn Burns for her smile and for teaching me focused ion beam and nanoindentation procedure.

Dr. Sultan Alsagabi for being a loyal and supportive friend of mine, helping me in lab and giving me lots of positive energy.

Dr. Thomas J. Williams at UI electron microscopy center for being a great teacher and mentor for me.

Materials Science undergraduate students: Sweta Khanal, Brady McNall, Robert Meine, Mary O'Brien, Brandon Cisco for helping me in lab.

Dr. Jonathan A. Webb for his friendship, teaching me the spark plasma sintering procedure, and his useful comments and suggestions on sintering kinetics and hot deformation mechanisms.

Rhonda McConomy, O'Brien and Kovach Families for hosting me in Idaho Falls.

Dr. Yaqiao Wu, Dr. Kerry Allahar, Bryan Forsmann, Mrs. Joanna Taylor, Mrs. Kristi Moser, Mrs. Alice Allen, Mrs. Debbie McQueen, Mrs. Mary Catherine Thelen, Mrs. Kristi Hunter, Mrs. Kristi Martin, Mr. Nathan D. Jerred, Dr. Emmanuel Perez, Mrs. Donna Wuthrich, Dr. Ali Siahpush and Mrs. Motahareh Eftekhari for helping me a lot during my CAES visits.

Jon and Erin Harty, Molly Boers, Jonathan, Rachel and Holle Matteson, Moein Poudat, Destinie Davis, Caleb Murdock and his family and all of my good friends who made Moscow a much more pleasant town for me.

Above and beyond all, my supportive family and kind husband, Mazdak Shadkam, for always loving me and supporting my education.

دانش بود نیک فرجام تو

به مینو دهد چرخ آرام تو

فردوسی

درخت تو گر بار دانش بگیرد به

به زیر آوری چرخ نیلوفری را

پروین اعتصامی

Dedication

This is dedicated to my kind parents for their unconditional love and supports.

Table of Contents

List of Figures

List of Tables

CHAPTER 1: Introduction

1.1. Motivations and objectives

Developing advanced energy systems with higher efficiency and safety requires advanced high temperature materials. To achieve these advancements, materials with stable microstructure, high temperature mechanical strength and high creep resistance must be developed. Dispersion strengthening is the most common and effective way of improving strength of materials at high temperatures.

The high temperature strength of dispersion strengthened materials is directly related to the stability of the second phase particles. In the last two decades, mechanical alloying (MA) has emerged as a competitive route for processing high temperature alloys. Generally, the oxide dispersion strengthened (ODS) alloys are processed via MA and hot isostatic pressing (HIP) followed by a series of thermo-mechanical processing steps.

The purpose of this work is to assess the use of spark plasma sintering (SPS) to process advanced ODS alloys and eliminate the need for hot extrusion and hot pressing as intermediate processing steps. The SPS is a substantially more rapid process occurring at lower temperatures along with other advantages, such as reduced anisotropy.

Traditionally Y_2O_3 is the rare earth oxide used as dispersoids in ODS alloys. However, this work has utilized La_2O_3 in ODS steels in place of Y_2O_3 because of its abundance and lack of prior studies.

1.2. Background

1.2.1. Oxide dispersion strengthened alloys

The global obligation for reducing CO_2 emissions from the fossil power plants requires designing and constructing of higher efficiency plants. Increasing the maximum operating temperature of the power plants will lead to higher overall efficiency. Furthermore, nuclear power is considered as essentially emission-free and can become more reliable by improving further safety and efficiency. Such improvements can be achieved through development and use of high temperature structural materials. The ODS alloys have shown excellent potential for the use in high temperature applications where superior creep strength and oxidation resistance are required. Some example applications of ODS alloys are tubing for high temperature heat exchangers, sheet for burners and combustion chambers, fuel cladding materials for next generation nuclear reactors and gas turbine engines [1].

The ODS alloys can be distinguished from super-alloys by the dispersion of fine oxide particles and elongated grain shape that develop during recrystallization and heat treatment. The effect of adding minor elements or “dopants” to increase creep resistance was discovered by William Coolidge in 1910 when he was working at General Electric (GE) Company [2]. He could process thorium oxide dispersed tungsten and improve the creep resistance of tungsten. Then, the first dispersion strengthened material was designed as a structural load bearing system. It is a well known fact that the most effective dispersion hardening elements are oxides, and the strength of materials increases with higher volume fraction of the oxides as well as smaller interparticle spacing. In 1970, Benjamin [3] developed a new process called “mechanical alloying” to combine yttrium oxide and gamma prime hardening in a complex nickel-based super-alloy where age hardening and dispersion

strengthening were the dominant mechanisms at lower and higher temperatures, respectively.

Despite the promising response of the ODS alloys at high temperatures, some challenges are currently inhibiting the use of these alloys; these limitations are: (a) relatively high processing costs, (b) joints fabricated by conventional fusion welding techniques have low creep strength at high temperatures and (c) secondary recrystallization needs to be optimized [4].

1.2.2. Ferritic ODS steels

The structural material components for the advanced nuclear reactors will be exposed to higher temperatures (700 ^{o}C) and severe radiation exposure (200 dpa and beyond) [5]. The reduced-activation ferritic – martensitic (RAFM) steels have already been considered for core components of future nuclear reactors. In the RAFM steels, high activation elements such as Nb, Mo, Co, Ni, Cu, N, etc. have not been added. Although these steels show rapid radioactive decay after neutron irradiation and better mechanical properties and irradiation resistance compared to commercial steels, radiation embrittlement at lower temperatures (< 400 ^{o}C) and poor creep rupture behavior restrict them to be used in future reactors. Therefore, using ferritic – martensitic steels in next generation nuclear reactors will limit the operating temperatures to 550–600 °C. Similar limitations also have been observed in using other ferritic – martensitic steels such as those used in fossil fuel powder plants. One way to increase the operating temperature and maintain high thermal conductivity, low void swelling and low thermal expansion coefficient is to use ferritic ODS steels as an alternative to ferritic – martensitic steels [6]. High temperature mechanical strength of ODS steels is attributed to their microstructure that contains a high number density of nanometer-scale

Y_2O_3 / TiO_2 particles dispersed in a ferritic matrix [6]. During 1980s, Fisher [7] developed a 13–20 wt.% Cr ferritic steel via MA and hot extrusion. This steel later was marketed by the International Nickel Company (INCO) as MA956 and MA957 alloys.

The ODS steels have been developed and investigated for nuclear fission and fusion applications in Japan (Fe–12.8Cr–0.26Ti–1.54W–0.23 Y_2O_3) [8, 9], Europe (Eurofer97 alloy) [10], and the United States (12YWT, 14YWT) [11, 12]. Kimura *et al.* [13] suggested that the optimal Cr concentration to provide a good balance between corrosion resistance and aging embrittlement is approximately 16 wt.%. Additional Al up to 4 wt.% will improve corrosion resistance of 16 wt.% Cr ODS steel which is beneficial to high temperature strength.

Creep strength can be improved by adding small amount of zirconium (Zr) or hafnium (Hf). In the United States, some specific experimental model alloy compositions such as 12YWT [14] and 14YWT [15] were developed. These alloys contain 12–14% Cr, 3% W (a low activation replacement for Mo at mass ratio of ~2:1 to give approximately equal atomic fractions), 0.25% Y_2O_3 and 0.4% Ti (wt.%).

Odette *et al.* [5] emphasized on two key factors for ODS steels: (1) presence of high dislocation sink strengths and especially large numbers of stable nanometer-scale precipitates that could trap He in the form of fine-scale bubbles in order to restrict swelling and protect grain boundaries, and (2) high creep strength, allowing operation at temperatures above the displacement damage regime.

Commercial ODS products include MA956 and PM–2000 from Special Metals Corporation in the United States and Metallwerk Plansee GmbH in Germany, respectively.

Although there is continued interest in MA957alloy for potential nuclear applications, there is currently no commercial source for this alloy [6].

1.2.3. Nanostructured ferritic steels

Nanostructured ferritic steels (NFSs) are a sub-category of ODS steels that contain an ultrahigh number density of Y–Ti–O-enriched nanofeatures (NFs also termed as nanoclusters; NCs) along with fine grains and high density of dislocations [5]. A high density of NCs ($> 10^{24}$ m^{-3}) in the grain interior along with precipitates decorating grain boundaries are the intrinsic characteristics of NFSs. The major role of these NCs and precipitates is precipitation hardening and grain boundary pinning as well as providing high creep strength [8, 16]. Furthermore, they can create high surface area and preferential sites for capturing helium in fine bubbles [17].

The average size, size distribution, volume fraction and number density of NCs influence various properties of the NFSs [18]. The NCs are characterized by atom probe tomography (APT) and small angle neutron scattering (SANS). The NCs are identified to be Y–Ti–O-enriched, coherent GP zone-type of precipitates with complex crystal structure, non-stoichiometric composition and diameter of 1–3 nm [15, 19]. Unfortunately, the crystal structure and composition of NCs have not been precisely identified, and their characteristics would vary with composition and processing variables [15]. The stability of NCs have been examined in different studies [18, 20, 21], and they were reported to be stable up to 1200 °C; however, they underwent rapid instability at 1250 °C and experienced another phase transformation above 1350 °C [19]. The evolution of NCs is controlled by various mechanisms, such as solute diffusions and self diffusion in iron [18]. In a model suggested by Sakasegawa *et al.* [20], NCs in MA957 alloy were non-stoichiometric

nanometer-sized Y–Ti–O-enriched clusters (Y:Ti < 1) with much smaller size and higher number density than the stoichiometric $Y_2Ti_2O_7$ (Y:Ti = 1) particles. With annealing MA957 alloy at 1200 °C for 1 h, the non-stoichiometric NCs were stable but some of them were transformed to stoichiometric $Y_2Ti_2O_7$ particles with larger diameter. The model suggested by them is shown in Fig. 1.1. In this model, all of the titanium oxides were surrounded by Y-enriched shells. These titanium oxide particles with the Y-enriched shell grew during annealing and transformed to larger $Y_2Ti_2O_7$ particles. These $Y_2Ti_2O_7$ particles could contribute to the growth of $Y_2Ti_2O_7$ particles through "Ostwald ripening" mechanism. Therefore, diffusion of yttrium presumably plays the dominant role in the evolution of oxides because the growth of Y-enriched shell surrounding the titanium oxide particles was found to be the main reason for the growth of titanium oxide particles [20].

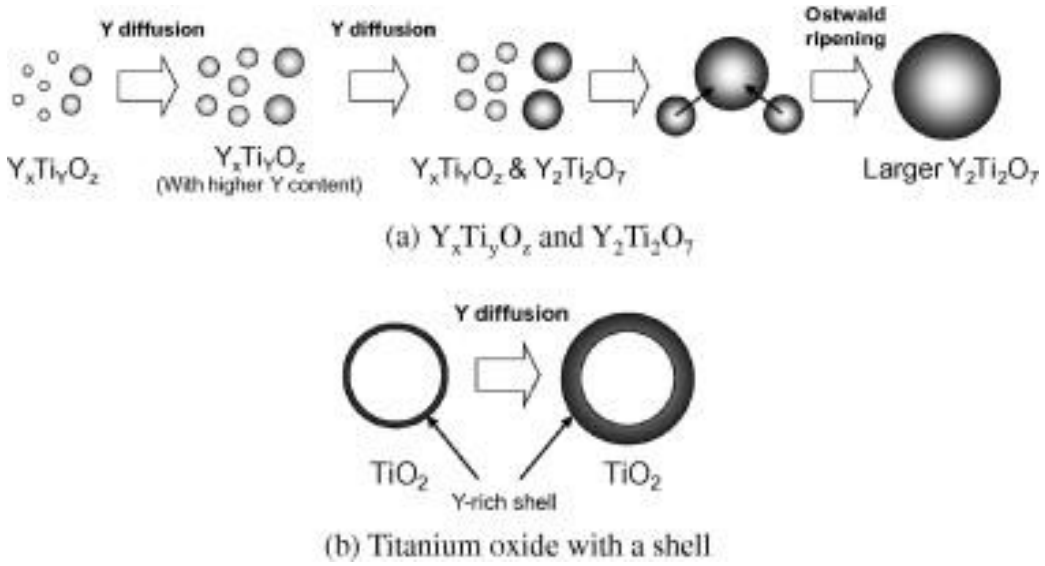

Figure 1.1. Schematic illustration for evolution mechanism of oxides [20] (Courtesy of Elsevier)

The chemical composition of some well known NFSs are presented in Table 1.1. It is clear that several alloying elements are required to produce the preferred combination of properties for NFSs.

Table 1.1. The composition of some commercial and experimental NFSs [6, 17]

Element (wt.%)	MA957	12YWT	14YWT	Eurofer97
Cr	14.0	12.58	13.1	9.0
W	0.01	2.44	0.54	1.1
Mo	0.29	0.02	0.01	–
Ti	0.92	0.35	0.19	–
Al	0.08	–	0.02	–
Y	0.26	0.16	0.22	0.19
O	0.02	0.16	0.11	0.13
C	0.01	0.05	0.05	0.07
N	0.03	0.014	0.04	–
Trace	Nb, Cu, Mn, Si	Co, Cu, V	Si, Ni, Mn, Cu	–
Fe	Bal.	Bal.	Bal.	Bal.

Chromium is added to provide oxidation resistance at high temperatures. The classic amount of Cr are in NFSs is in the range of 9–14 wt.% Cr. The Fe–Cr phase diagram is shown in Fig. 1.2. In this phase diagram, the austenite loop extends to 12.7 wt.% Cr, implying that the minimum level of Cr needed to have a fully ferritic alloy at all temperatures is 12.7 wt.% [22]. It is also well known that Fe–Cr ferritic alloys are susceptible to the so called “embrittlement at 475 °C” due to the phase separation within a low temperature miscibility gap into chromium-enriched α' and iron-rich α phases. This α–α' transformation occurs when the Cr level in iron exceeds the amount of 15 wt.% [23].

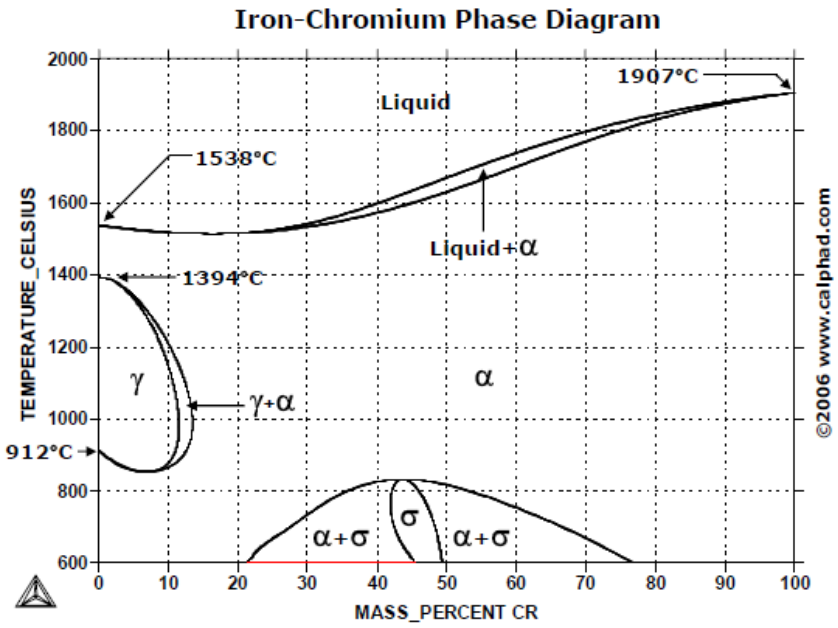

Figure 1.2. Fe–Cr phase diagram [26] (Courtesy of ASM)

Originally, the ODS alloys utilized addition of a very stable and insoluble oxide to a metallic system. These oxides can be alumina (Al_2O_3), yttria (Y_2O_3), thoria (ThO_2), titania (TiO_2), hafnium oxide (HfO_2), lanthana (La_2O_3) and other rare earth (RE) oxides. According to the Ellingham diagram [24], Y_2O_3 has the highest (negative) free energy of formation, and is, therefore, extremely stable at all temperatures. The phase diagram of Fe–Y is shown in Fig. 1.3 in which iron and yttrium are essentially immiscible leading to higher stability o f yttria in ODS alloys. There is no solid solution formation in Fe–Y phase diagram, rather an intermetallic compound with a composition of $Fe_{17}Y_2$ forms at the Fe-rich part of the diagram. Ukai *et al.* [25] suggested that Y_2O_3 content of about 0.4 wt.% is optimal to balance creep resistance and ductility in ODS steels. With higher amount of Y_2O_3 (> 0.4 wt.%), the creep rupture properties do not increase any further, and the elongation to fracture would decrease. The Fe–La phase diagram is shown in Fig. 1.4. There is no solubility of La in Fe and no intermetallic compound can form at all temperatures.

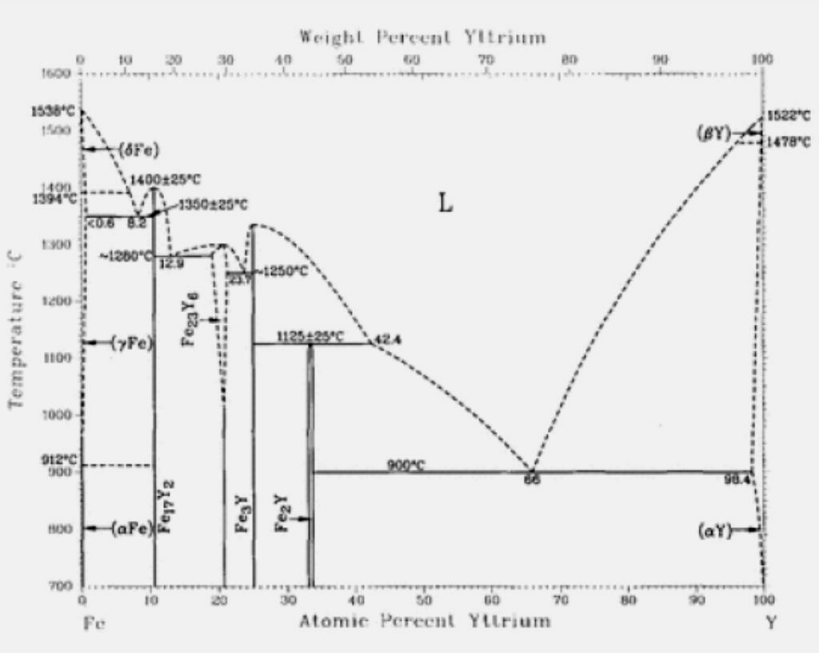

Figure 1.3. Fe–Y phase diagram [27] (Courtesy of Springer)

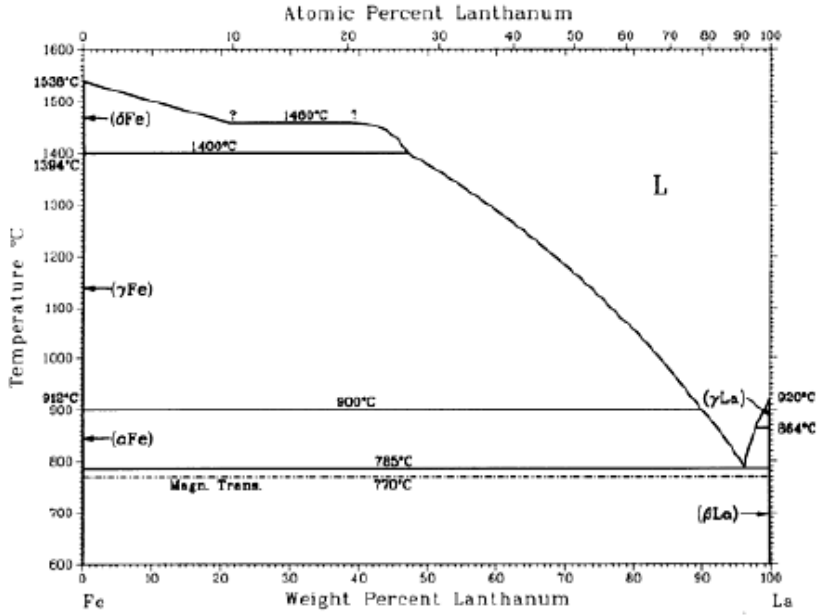

Figure 1.4. Fe–La phase diagram [26] (Courtesy of Springer)

Titanium is added to NFSs (i.e. MA957, 12YWT and 14YWT) to the level of less than 1 wt.% [17] and its role is to refine the oxide particle size by forming complex oxide such as Y_2TiO_5 and $Y_2Ti_2O_7$ [25]. Any excess titanium can act as an interstitial absorber for carbon,

oxygen and nitrogen as well as aiding in corrosion resistance. However, the formation of large TiN, TiO_2 and TiC particles should be minimized due to their detrimental effect on mechanical properties [25, 28]. In the presence of W (in 12YWT or 14YWT alloys), the addition of Ti up to 0.55 wt.% would increase the creep rupture strength [25]. The phase diagram of Fe–Ti is shown in Fig. 1.5.

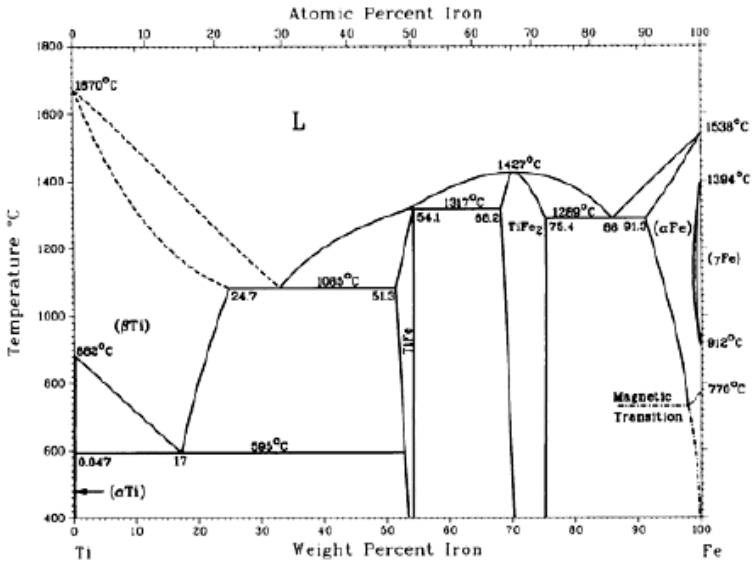

Figure 1.5. Fe–Ti phase diagram [26] (Courtesy of Springer)

Tungsten and / or molybdenum are added to the ferritic matrix for solid solution strengthening and stabilizing ferrite structure. Molybdenum is a strong solid solution strengthening (SSS) element for iron-based alloys. However, Mo is a high activation element (long-lived radioactive nuclides which does not decay in 100 years). The Fe–Mo phase diagram is shown in Fig. 1.6.

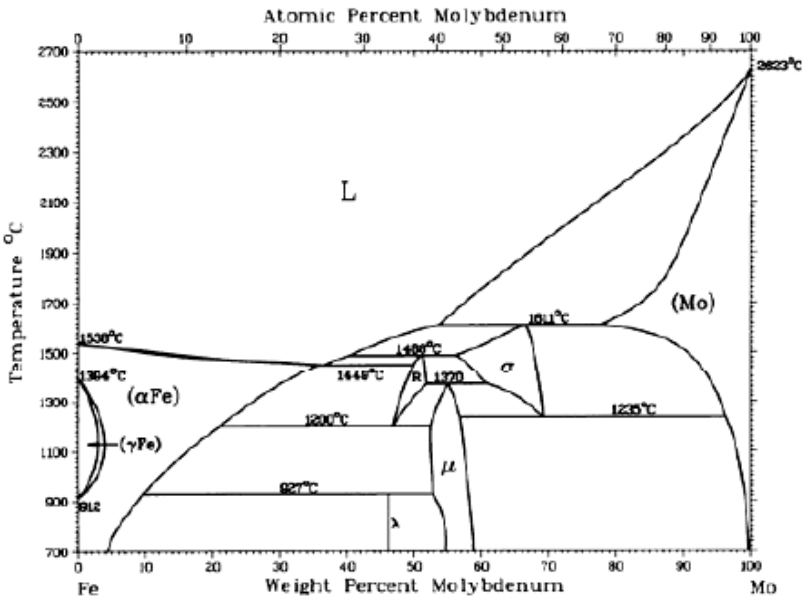

Figure 1.6. Fe–Mo phase diagram [26] (Courtesy of Springer)

It has been shown that tungsten is a viable alternative for SSS in radiation environments [29]. In solid solution design, 2 wt.% tungsten is roughly equivalent to 1 wt.% molybdenum, which is essentially equivalent in atomic fraction. However, milling of tungsten is very difficult and requires long time. Another drawback of tungsten is the formation of brittle Laves phase (Fe_2W) that would decrease the fracture toughness in ODS steels [29]. The Fe–W phase diagram is given in Fig. 1.7. The amount of tungsten in ODS steels has been suggested to be around 2–3 wt.% [15].

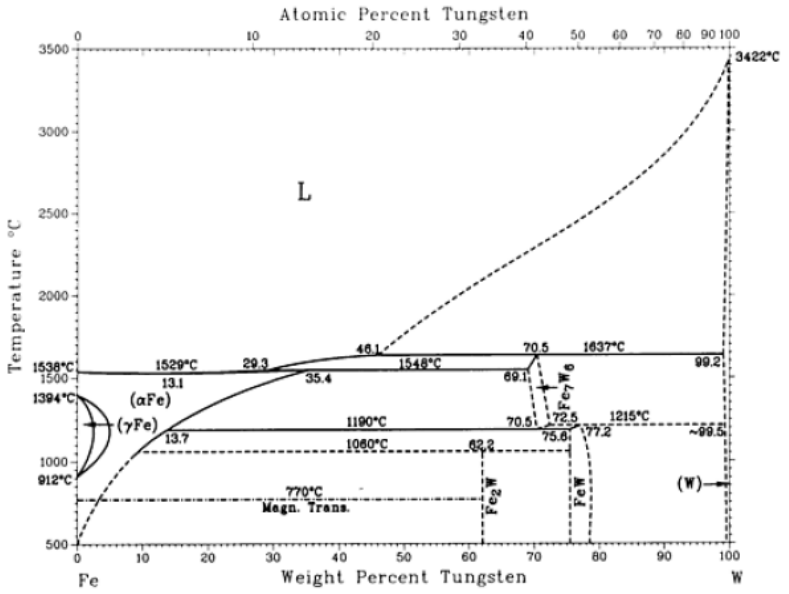

Figure 1.7. Fe–W phase diagram [26] (Courtesy of Springer)

1.2.4. Formation of nanoclusters in nanostructured ferritic steels

Nanograins and high dislocation densities are obtained after MA of the pre-alloyed or elemental powder. Following MA by consolidation, dislocations will partially recover and grains will recrystallize or grow. The final microstructure is strongly dependent on the processing temperature and the presence or absence of NCs [15, 30]. Another essential key in NFSs is the vacancies that are introduced during MA.

First principle studies by Fu *et al.* [31] have demonstrated that there is a strong vacancy–oxygen atom affinity that also improves with Ti and Y atom additions. As a result, higher levels of O and Y than equilibrium solubility limits could be achieved in the ferritic matrix, and diffusion of solutes would be slower. This would contribute to good high temperature and creep properties [32, 33].

During MA a non-equilibrium super-saturation of solute elements within the ferritic matrix can be obtained. Besides, a high density of defects such as vacancies, voids,

interstitials, dislocations, stacking faults, and grain boundaries are created in the milled powder [34]. One of main roles of the microstructural defects is to enhance kinetics of the alloy system by creating high diffusivity paths. In any super-saturated system two types of phase transformation are likely to occur: (1) classic precipitation reaction that occurs by nucleation (either homogeneous or mostly heterogeneous) and growth of precipitates controlled by thermodynamic and kinetics in the system [28, 35], (2) Spinodal decomposition type of transformation in which a non-equilibrium solid solution gets unstable and decomposes to regions enriched and lean in solutes. This type of transformation is independent of thermodynamics nucleation barrier and driven by kinetics. The product of such transformation is very stable precipitates on grain interior as well as grain boundaries and dislocations. Such meta-stable phases are known as GP–zones (discovered by Guinier and Preston) do not need high temperature for formation. These precipitates have a very low interfacial energy due to structural symmetry and similarity that make them thermodynamically stable. Formation mechanism of these phases would be enhanced by the presence of vacancies and dislocations created during MA [28, 35, 36].

Once the precipitate nuclei have been formed with no nucleation barrier, the growth stage will begin. The growth rate is totally diffusion controlled mechanism and dependent on the diffusion rate of solute atoms into / out across the interfaces. In a metallic system, precipitates whether coherent or incoherent will apply a degree of interfacial energy to the system. Minimization of the interfacial energy is achieved by the configuration geometry and formation of *spherical shape* of precipitates [35, 37]. The growth of precipitates is given by the following classic growth ($t^{0.5}$) relationship:

$$R=k\,(Dt)^{0.5} \qquad (1.1)\ [35]$$

where D is the volume diffusion coefficient in the matrix and k is dependent on concentration of solute in the matrix / precipitate interface (C_i^m), concentration of solute in the matrix far from the precipitate (C_∞^m) and the concentration at the precipitate (C^p) and is given by the following equation [35]:

$$k=\frac{-(C_i^m-C_\infty^m)}{2(C^p-C_i^m)} \quad (1.2)\ [35]$$

Growth of precipitates continuously occurs till the solutes concentration in the matrix reaches an equilibrium level. Coarsening can occur simultaneously as growth is happening; however, coarsening rate becomes much more significant after growth is accomplished. The coarsening mechanism is through "Ostwald Ripening" mechanism.

On the other hand, the solubility of these fine particles increases with reduction in their size which creates excess surface area to volume ratio and excess energy in the system. The driving force for growth of particles is reduction in surface interface area and interface energy. But as the particles grow and the surface energy decreases (which is thermodynamically favorable), the particle becomes incoherent and a region with high strain is formed around it (which is thermodynamically unfavorable). In a simpler explanation, during growth particle becomes incoherent but the level of surface energy decreases too. This process is based on changes in solubility of the solutes and a result of the increased chemical potential ($\Delta\mu$) due to interface energy (σ). The chemical potential is given by "Gibbs – Thomson" relationship:

$$\Delta\mu = \frac{2\sigma\times V_m}{r} \quad (1.3)\ [35]$$

where $2/r$ is the curvature of a *spherical* precipitate, V_m is the volume fraction of the precipitate and σ is a function of unit normal vector [35]. Coarsening of the precipitates is controlled by interface kinetics, lattice diffusion, grain boundary diffusion or dislocation

pipe diffusion [28, 38-41]. A comprehensive review on the formation of nanoclusters in ferritic alloys is presented by Alinger *et al*. [18]. As mentioned earlier, the formation of NCs is facilitated by milling, which creates high density of vacancies. Although the solubility of O in the bcc Fe lattice is extremely limited, O atoms bind strongly to vacancy, with a binding energy of −1.5 eV. This significantly increases the solubility of O in the presence of pre-existing vacancies. The presence of Y is also necessary for creating NCs, but the Y concentration must also be carefully controlled. Without Y, the stable alloying state is TiO_2 oxide phase, with a heat of formation of −4.3 eV per oxygen atom [31]. In the presence of Y, the cluster state becomes viable, and a small addition of Y actually enhances the formation of NCs instead of TiO_2. With too much Y, however, the $Y_2Ti_2O_7$ oxide phase, with a heat of formation of −5.6 eV, is likely to form. Thus, the condition for stable Y−Ti−O-enriched nanoclusters requires a well-dispersed Y concentration with more Ti than Y in the nanoclusters [42].

A kinetic Monte Carlo simulation study on the formation of NCs [43] has shown that smaller precipitates are Y–O-enriched and larger ones are Ti–O-enriched in two Fe–Y–O and Fe–Ti–O systems, respectively. This difference arises because of the disparity of diffusion coefficient between Ti and Y. The Ti diffusion coefficient is up to 10^5 times faster than the Y diffusion coefficient regardless of temperature. The diffusion coefficients of Fe, Y, Ti and O at 1150 °C are determined to be 1.1×10^{-20}, 1.5×10^{-23}, 1.7×10^{-20} and 1.0×10^{-14} (m^2s^{-1}), respectively [44]. This means by the time that nucleation of Y–O-enriched particles are over, the Ti–O-enriched particles would likely undergo coarsening. They concluded that smaller super-saturation in system will impact the influence of temperature on the kinetic

path; therefore, by choosing an appropriate chemical composition, formation of nanoparticles will be controlled better and higher mechanical strength will be achieved [43].

1.2.5. Mechanical alloying

Ball milling or MA is a powder processing method that has been used to synthesize a variety of phases. It involves cold welding, fracturing and re-welding of powder particles. MA has been utilized as a primary processing step toward manufacturing iron-based ODS and nickel-based ODS alloys. This technique was first developed by Benjamin in 1966−1970 [3, 45] to produce an ODS alloy with γ' precipitation hardening in a nickel-based super-alloy intended for gas turbine applications. Since the oxides cannot be dispersed in the liquid state, a solid state process was necessary [1].

The MA generally consists of loading the powder mixture into a stainless steel container sealed under a protective argon atmosphere (to avoid / minimize oxidation during milling) and adding a grinding medium (generally hardened steel or tungsten carbide balls). In case of milling ductile powders such as Ni, about 1–2 wt.% of a process control agent (PCA) (usually stearic acid) is normally added to prevent excessive cold welding of the particles. The types of mills generally used are SPEX mixer / mills (maximum 10 g of the powder per batch) and attritor mills (a few pounds of powder per batch). The times required for processing are short in the SPEX mills and are longer in the attritor mills. A comprehensive article about MA processing can be found in Ref. [46].

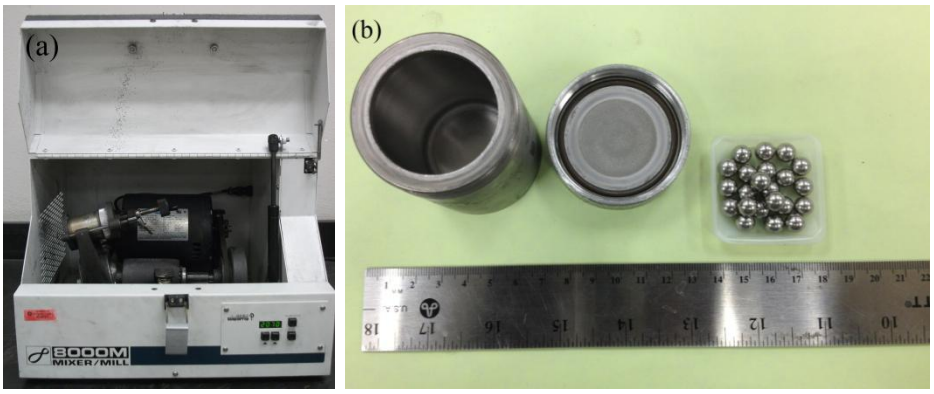

Figure 1.8. (a) SPEX mixer / mill high energy ball milling machine and (b) chromium hardened steel vial and balls

MA is a potential processing technique for producing nanocrystalline materials, amorphous and non-equilibrium phases. During MA, solid solubility significantly increases with increasing energy input. This increase in solid solubility is achieved only when both atomic size factor (< 15%) and similar crystal structure conditions are satisfied (known as Hume – Rothery rules). Solid solubility limit is determined by the ratio of intermixing (caused by shear forces) to the decomposition of the solid solution due to thermally activated jumps. If this ratio is very large, a fully random solid solution is achieved. Formation of nanostructures during milling has been established as the most effective mechanism to increase solid solubility due to higher volume fraction of atoms at the grain boundaries and enhanced (short circuit) diffusion paths [1].

The thermodynamics theory of solution during MA initiates with mixing of constituent particles each containing millions of identical atoms [47]. The average free energy of a mechanical mixture powder composed of pure (elemental) components of *A* and *B* with molar free energy of $\mu_A{}^\circ$ and $\mu_B{}^\circ$, respectively can be determined as below:

$$G(mixture) = (1-X)\mu_A^\circ + X\mu_B^\circ \qquad (1.4)\ [47]$$

where X is the molar fraction of B. On the contrary, the free energy of formation of a solution is different from that of mechanical mixture to the value of free energy of mixing, ΔG_M, that is essential term in thermodynamics of solutions. This is because there is an enthalpy change associated with change in near neighbor bonds along with significant contributions of the entropy of mixing. Figure 1.9 shows a progressive reduction of particles until an atomic solution is achieved [47].

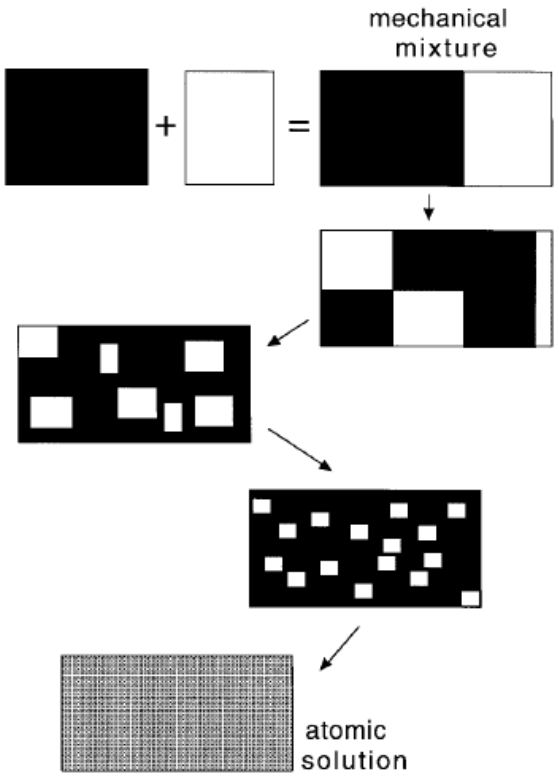

Figure 1.9. Schematic of atomic solution by progressive reduction in size during MA [47]
(Courtesy of Elsevier)

Assuming that there are m_A atoms per powder particle of A and m_B atoms per particle of B, the powders are mixed in a proportion that gives an average mole fraction X of B. The molar entropy of mixing when $m_A = m_B = 1$ can be calculated in the following equation:

$$\Delta S_M = -k\, N_a \times [(1-X)\ln(1-X) + X\ln(X)] \quad (1.5)\ [47]$$

when the particle sizes are reduced to atomic scale, the largest reduction in free energy occurs. The binding energy is the change in energy as the distance between a pair of atoms is reduced from ∞ distance to an equilibrium distance. For example, for a pair of *A* atoms it is written $-2\varepsilon_{AA}$. From the standard theory of atomic solutions, the molar enthalpy of mixing is given by:

$$\Delta H_M = ZN_a(1-X)X\omega \; where \; \omega = \varepsilon_{AA} + \varepsilon_{BB} - 2\varepsilon_{AB} \quad (1.6)\ [47]$$

where *Z* is the coordination number (CN). If we consider that particles are not mono-atomic, only the interface particles will be influenced by the unlike atoms and enthalpy of mixing can be written as:

$$\Delta H_M = ZN_a\, \omega 2\delta\, S_V X\,(1-X) \quad (1.7)\ [47]$$

where S_V is the amount of A/B interfacial area per unit volume and 2δ is the thickness of the interface and δ is a mono-layer of atoms. The interfacial energy per unit area, σ is given in the following equation:

$$\Delta H_1 = V_m S_v \times \sigma \quad (1.8)\ [47]$$

where V_m is the molar volume. During MA, the particle size gets reduced whereas S_v significantly increases.

The solution of particles during MA is only possible when the interfacial energy decreases as particles become smaller. This means particles must gain coherency with the matrix lattice as they become refined. This coherency can be obtained through fracture and welding of particles [47]. The particles dissolution is the inverse of precipitation mechanism and is shown in Fig. 1.10. As the particle size becomes smaller, higher coherency is achieved and reduces the interfacial energy of the system.

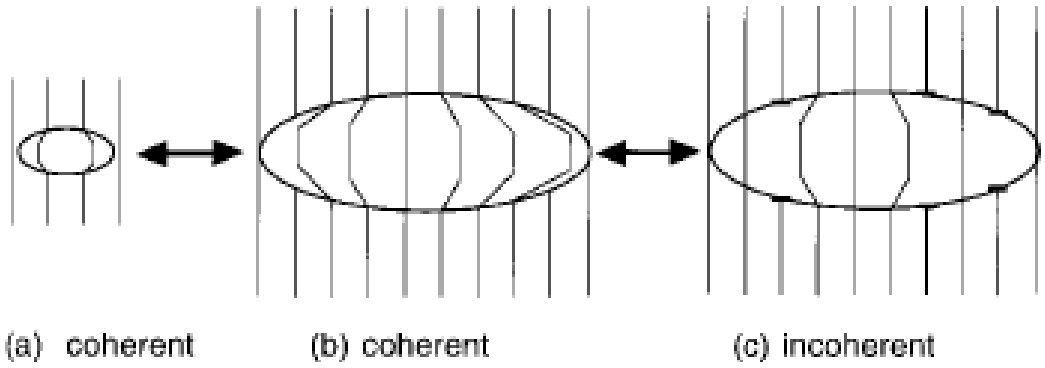

Figure 1.10. Changes in coherency as a function of particle size [47] (Courtesy of Elsevier)

In MA of ODS alloys, the brittle oxide particles are dispersed in a ductile matrix. Figures 1.11(a–c) illustrates a typical microstructural evolution during MA of the ODS alloys. At the initial stages of milling, aggressive ball – powder – ball collisions crush the ductile particles and make them flat. The brittle oxide particles get fragmented and become trapped in the ductile particles and along the inter-lamellar spacings (Fig. 1.11(a)). With further milling, the ductile powder particles acquire significant amount of plastic strain and become work hardened and the lamellae get refined as shown in Fig. 1.11(b). At this point, the composition of the individual particles moves toward the overall composition of the starting powder mixture. With further milling, lamellae refinement governs reducing the inter-lamellar spacing until the brittle oxide particles get consistently dispersed as shown in Fig. 1.11(c) [46].

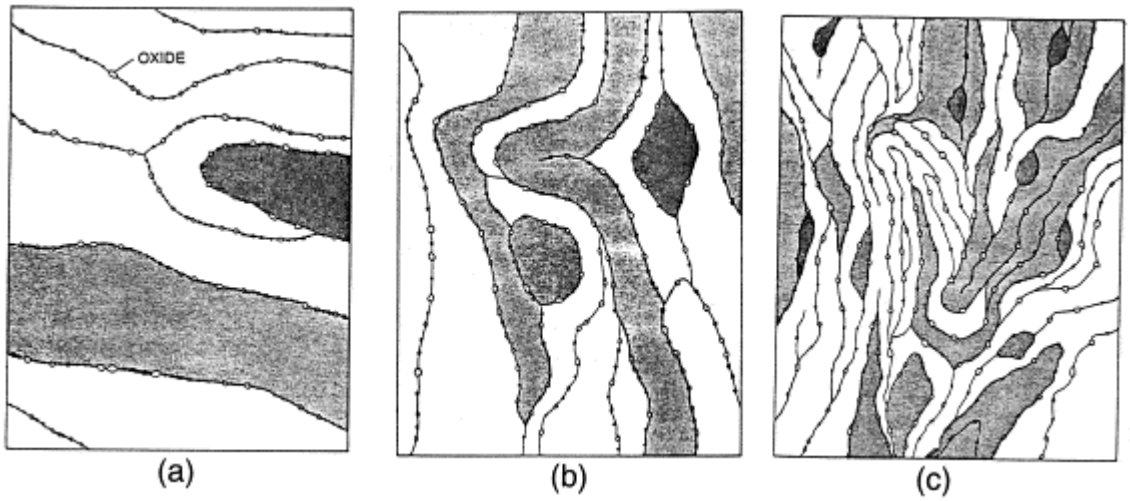

Figure 1.11. Schematics different stages of microstructural evolution during MA of ODS alloys (Courtesy of Elsevier) [46]

MA is a complex stochastic process with numerous variables such as milling container, milling speed, milling time, type, size, size distribution of the grinding medium, ball to powder ratio (BPR), extent of filling the vial, milling atmosphere, process control agent and temperature of milling [46]. Powder contamination is a major disadvantage of MA that can be minimized by using high purity metals, high purity atmosphere and using a milling media made from the same materials that is being milled and of course reducing the milling times as short as possible [1].

MA provides both solid solution strengthening and precipitation hardening in ODS alloys [1]. In processing ODS alloys, the role of ball milling appears complex. It could be summarized in two major phenomena occurring at the same time; dissolution of solutes within the matrix and nucleation of the first NCs [48, 49].

Vacancies incorporated during milling play a major role in nucleation of O-enriched clusters in Fe matrix. It has been determined that binding of O in Fe is weaker than binding of C and N in Fe. In other words, O–vacancy binding energy is much greater than that of

C–vacancy and N–vacancy [31, 50-52]. During MA, a high concentration of vacancies are created in the Fe lattice and bind with O. Elements such as Y and Ti also strongly bind with O–vacancy pair [34]. Fu *et al.* [31] studied the initial nucleation stage of the NCs during the milling. They discovered that with O atoms in O–vacancy pair located adjacent to interstitial octahedral sites, energy minimization forces that their neighbor sites ½[110] are energetically available for Ti solutes and the ½[112] sites potential sites for Y atoms. The binding of Ti–O–vacancy and Y–O–vacancy decrease the energy of the system even further. A review on role of O and vacancy in the formation of NCs can be found in Ref. [31].

Kimura *et al.* [53] suggested that dissolution of Y_2O_3 can be explained by formation of an amorphous layer around the grain boundary enriched in Y and O atoms. In this mechanism, the refining of Y_2O_3 particles during milling creates an extra amount of interface energy that is thermodynamically unfavorable. The increase in interfacial energy due to particle size reduction is a driving force for particle decomposition. At the same time, the nanograins formed due to heavy plastic deformation provide a high volume fraction of grain boundaries that can receive all the rejected atoms from the particle decomposition and reduce the chemical free energy of the system.

Whether the grain boundary layers can successfully dissolve all the rejected atoms from particle dissolution cannot be precisely identified since the solubility limit of atoms at the grain boundaries must be considered. When the particles decompose, formation of an amorphous grain boundary layer can increase the number of atoms and possibility of more particles dissolving in the alloy system [53].

1.2.6. Consolidation and sintering of the milled ODS powder

Conventional ingot metallurgy processing techniques are not applicable for ODS alloys due to significantly different melting points ($T_m^{Fe} = 1538\,°C, T_m^{Y_2O_3} = 2400\,°C$), buoyancy issues in the melt (ρ_{Fe}=7.87 g.cm^{-3}, $\rho_{Y_2O_3}$=5 g.cm^{-3}) and the thermodynamics insolubility. The most effective approach for ODS alloy fabrication is powder metallurgy route consisting of MA of the starting powders, followed by consolidation using either hot extrusion (HE) or hot isostatic pressing (HIP). Appropriate thermo-mechanical processing (TMP) is often performed to improve the microstructure and mechanical properties [54]. A conventional method of processing ODS alloys is schematically shown in Fig. 1.12.

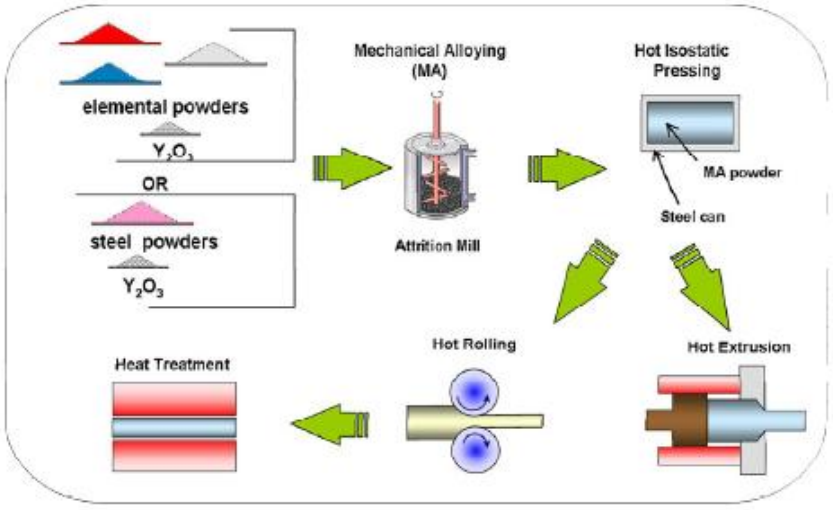

Figure 1.12. The conventional processing method of ODS alloys by powder metallurgy [54] (Courtesy of KIT Scientific Publishing)

The stored energy in the milled powder drive the recovery and recrystallization during consolidation step. Recrystallization which is nucleation and growth of strain-free grains with high angle boundaries can occur through different mechanisms: (1) nucleation and growth models of precipitation, (2) subgrain formation and growth until high angle

boundaries are formed and (3) strain induced boundary migrating (SIBM) in which a "bulge" develops on a high angle boundary as a result of strain gradients across the boundary [28, 55]. While recrystallization occurs in conventional alloys at about $0.5T_{m,}$ the recrystallization temperature of ODS alloys has been reported to be in the order of $0.9T_m$. This high recrystallization temperature has been attributed to boundary pinning by the nanoparticles [56, 57]. However, SIBM (bowing of grain boundaries) is a recrystallization in conventional alloys containing micron-sized grains. In the case of ODS alloys, the nanograins control the recrystallization phenomena. The reason is likely that nanograins are not topologically independent from each other to orient independently and freely, rather they are confined and in this way grain boundary junctions may act as pinning points to SIBM [28, 55].

During consolidation, hot deformation and dynamic recrystallization would occur. The deformation map for bcc iron is shown in Fig. 1.13. According to Ashby [58] there are at least 6 distinguishable and independent mechanisms involved when a polycrystalline material is plastically deformed; (1) a stress which exceeds the theoretical shear strength, (2) dislocation glide, (3) dislocation creep, (4) Nabarro – Herring creep, (5) Coble creep and (6) twinning mechanisms.

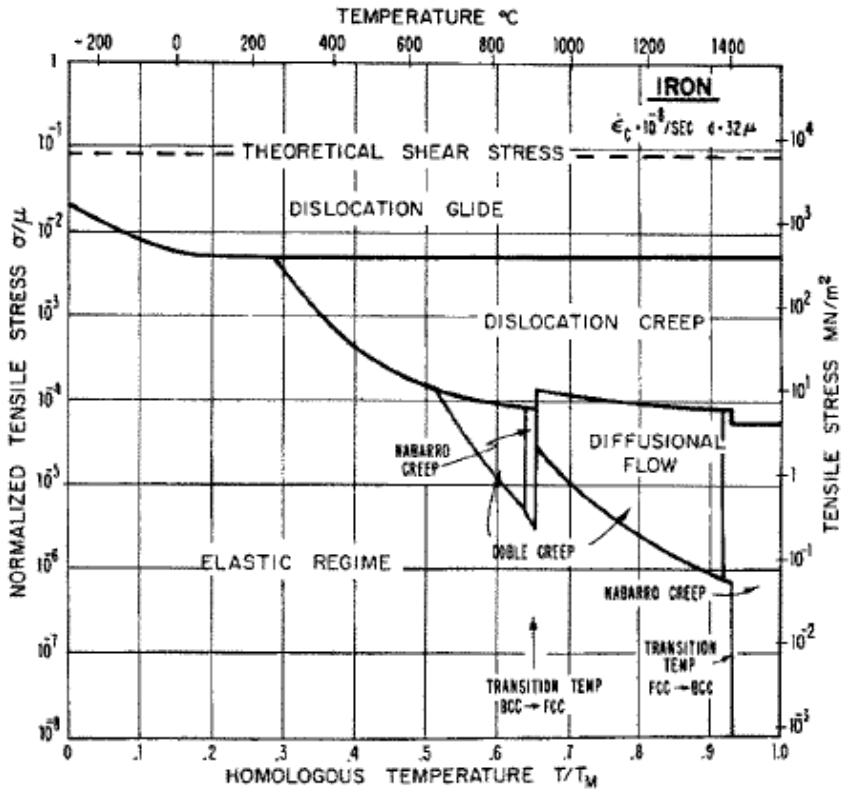

Figure 1.13. The deformation map for bcc iron [58] (Courtesy of Elsevier)

Dislocation glide is limited by the presence of obstacles such as impurities, solutes, other dislocations and precipitates. The strain rate is given by:

$$\dot{\varepsilon} = \dot{\varepsilon} \exp(-\frac{u}{kT}) \quad (1.9)\ [58]$$

where u_k is the energy the required activation energy to move a dislocation and can be calculated as below:

$$u = 2u_k\{1-\frac{\sigma_p}{\sigma}\}^2 \quad (1.10)\ [58]$$

where σ_p is the flow stress at 0 K and σ is the flow stress. At temperatures above $0.5T_m$ and relatively high stress, dislocations move toward the grain interiors to form dislocation cells. The dislocation creep is experimentally explained by the following equation:

$$\dot{\varepsilon} = A\ \frac{D_v \mu b}{kT}\ (\frac{\sigma}{\mu})^n \quad (1.11)\ [58]$$

where n and A are constant and D_v is the bulk self diffusion coefficient, μ is the shear modulus, b is the Burgers vector, $\dot{\varepsilon}$ is the strain rate, σ is the flow stress, T is the temperature and k is the *Boltzmann's* constant.

Diffusional flow of single atoms / ions (either by bulk or grain boundary transport) leads to the Newtonian – viscous creep of a polycrystal. The two alternative flow paths represent independent, additive contributions to the overall strain rate:

$$\dot{\varepsilon} = 14\frac{\sigma\Omega}{kT} \times \frac{1}{d^2}\, D_v \{1 + \frac{\delta\pi}{d}\, \frac{D_B}{D_v}\} \qquad (1.12)\ [58]$$

where Ω is the atomic volume, d is the grain size, D_v is the bulk self diffusion coefficient, D_B that for boundary diffusion and δ the effective cross section of a boundary for diffusional transport. When bulk diffusion dominates, the creep is often called Nabarro – Herring, or simply Nabarro creep; when boundary diffusion dominates, it is known as Coble creep. These two processes are independent and distinguishable [58].

1.2.6.1. Hot isostatic pressing of the ODS powder

HIP is a consolidation process that was invented in 1955 for diffusion bonding applications in nuclear industry and then was applied to the healing of castings and consolidating powders. It involves the simultaneous application of a high pressure and elevated temperature gas such as argon or nitrogen in a specifically assembled vessel [59]. In HIP, fully dense material can be achieved by removing both macro- and micro- porosity. Therefore, highly complex and near net shape components can be processed. The schematic of HIP process is shown in Fig. 1.14. The applied pressure as high as 2000 bar (200 MPa) and temperature up to 2000 °C are possible to achieve in HIP, making it applicable to sinter

a variety of materials including ceramics [60]. Traditionally HIP is being used to process ODS alloys and NFSs.

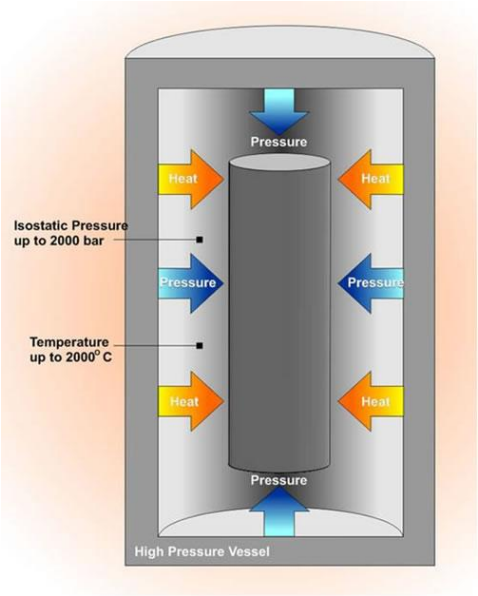

Figure 1.14. Schematic of HIP process [61]

A 3-stage mechanism of processing ODS steels based on high resolution transmission electron microscopy (HRTEM) studies have been proposed by Hsiung *et al.* [62, 63] and shown in Fig. 1.15. During ball milling, fragmentation of Y_2O_3 particles occur and a finely dispersed nanoparticles fragments will be obtained. Then agglomeration and amorphization of fragments mixed with the matrix would govern the formation of clusters in the form of MYO where M is the alloying element. In the last step, the amorphous oxide agglomerates to form oxide nanoparticles with a complex core and a shell enriched in solutes (M). This solute-enriched shell forms only when the rate of solute depletion form the core is higher than the rate of solute diffusion from the oxide / matrix interface during crystallization stage. Therefore, those solutes that are not involved with internal oxidation occurring in the core are depleted from the core and aggregate at the shell [62].

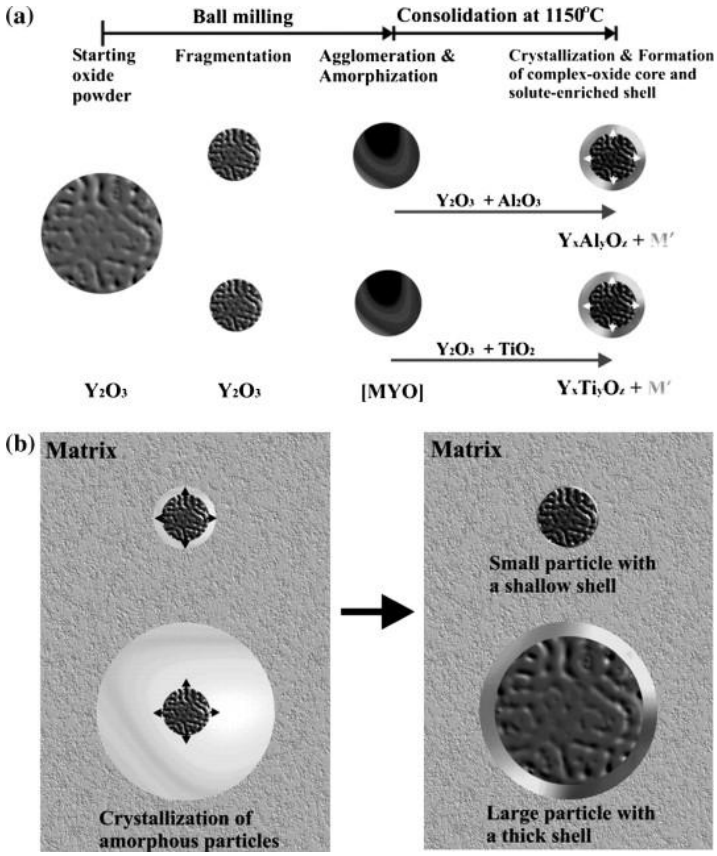

Figure 1.15. (a) Formation of oxide nanoparticles containing a core / shell structure during MA and HIP and (b) size effect on the formation of core / shell structures in oxide nanoparticles [62, 63] (Courtesy of Elsevier)

1.2.6.2. Spark plasma sintering of the ODS powder

SPS or pulsed electric current sintering (PECS) also known as field activated sintering technique (FAST) occurs under the influence of a uniaxial stress with the application of electrical power at a low voltage and moderate currents [64]. SPS is a relatively new sintering process that allows direct fabrication of bulk materials from powders using a fast heating rate (up to 1000 °C/min), short holding times (less than an hour) and low sintering temperatures (200–300 °C lower than most of the conventional sintering techniques) [65-69]. In SPS, heating power is not only distributed over the volume of the powder compact in a macroscopic scale, rather the pulsed electric current would disperse the heating power at

the locations at the microscopic scale (at the contact points of the powder particles), where energy is required for rapid sintering process [70]. Rapid densification by SPS cannot be correlated to the kinetically slow diffusion mechanisms such as grain boundary and volume diffusion, rather it should be correlated to mechanisms with faster kinetics, such as surface diffusion, diffusion through the melt, or time-independent processes such as plastic deformation [71]. A schematic of the SPS process is shown in Fig. 1.16. Example of some materials sintered by SPS are cutting tools (titanium nitrides [72], transition metal carbonitrides [73, 74]), ceramics (alumina [75], zirconia [76]), biomaterials [77], materials for nuclear energy applications ($W–UO_2$, W–UN) [78, 79], and many others.

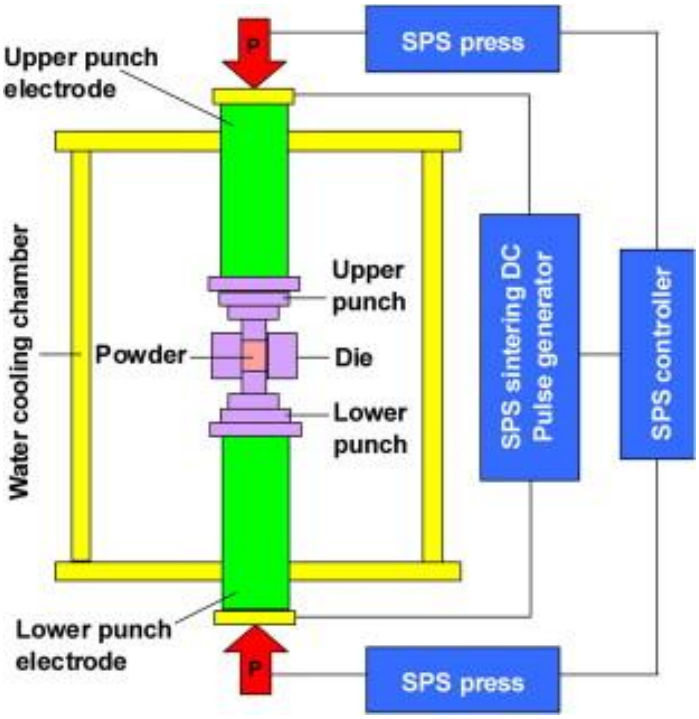

Figure 1. 16. Schematic of a SPS unit [65] (Courtesy of Elsevier)

The system consists of a SPS sintering machine with a uniaxial hydraulic unit and built-in water-cooled special energizing mechanism, a water-cooled vacuum chamber, atmosphere controls, vacuum exhaust unit, special sintering DC pulse generator and a SPS computer program controller.

The powder materials are stacked between the die and punch on the sintering stage in the chamber and held between the electrodes. Under pressure and pulsed current, the temperature quickly rises to 1000 – 2500 °C above the ambient temperature, resulting in the production of high quality sintered compacts [70]. A Dr. Sinter SPS-515S machine formerly manufactured by the SPS Syntex Inc. and currently being manufactured by the Fuji Electronic Industrial Co. Ltd. is shown in Fig. 1.17. This machine has the current capacity of 1500 A and hydraulic capacity of 50 kN operating in a 12:2 pulsed pattern mode (current is applied for 12 ms, followed by a 2 ms of no current). The interior of sintering chamber is shown in Fig. 1.18. The die and punches are placed inside the sintering chamber in direct contact with the electrode and hydraulic ram.

SPS was developed in the early 1960s by Inoue *et al.* [80, 81] based on the idea of using the plasma on electric discharge machine for sintering metals and ceramics. SPS has many advantages over conventional systems such as HIP; these advantages include but not limited to: (a) ease of operation and accurate control of sintering energy, (b) high sintering rate, (c) high reproducibility and (d) safety and reliability. The heating rate in SPS can be as high as 1000 °C/min allowing maintaining the intrinsic properties of nanopowders in their fully dense products [70].

Figure 1.17. A Dr. Sinter SPS-515S unit including sintering chamber, electrical unit and monitor / control unit from left to right

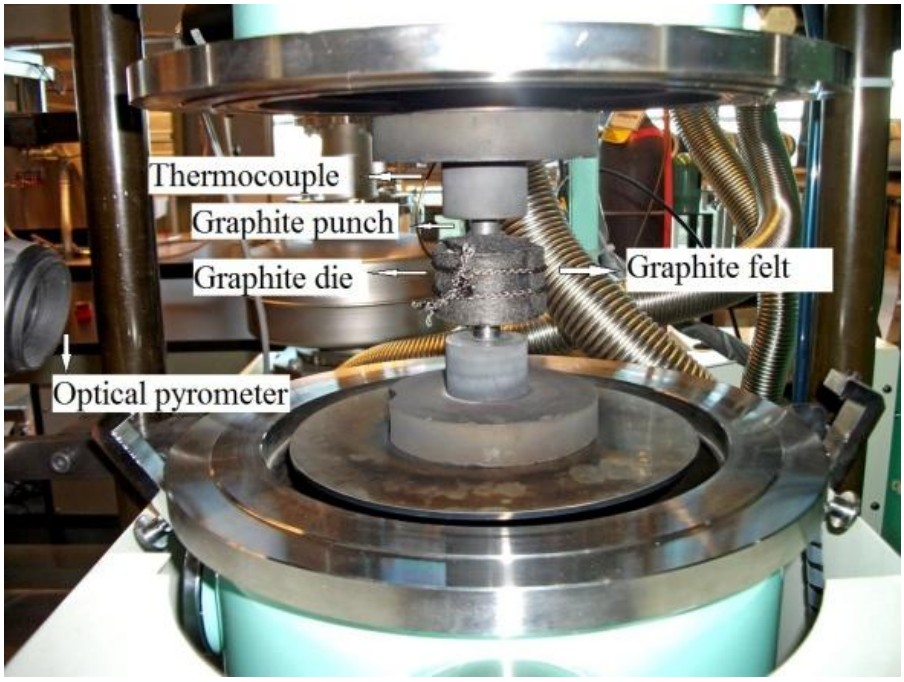

Figure 1.18. Interior of a sintering chamber showing die, punches, graphite spacers, thermocouple and optical pyrometer

Even though SPS has been developed as a promising technique for rapid densification of materials, its fundamental mechanism is still not well understood due to the complexity of the thermal, electrical and mechanical processes that are simultaneously evolving [65]. For example, the existence of spark plasma and occurrence of discharge in the sintering processes is still a controversial matter. The role of spark discharge is mentioned to eliminate the oxide films, adsorptive gas and any impurities present on the surface of the powder particles [82, 83], which leads to enhanced densification rate [84-87]. In addition to discharge effect, Joule heating and plastic deformation effects contribute to the densification of the powder [88-90]. Combination of these effects significantly improves the efficiency of SPS over the conventional sintering methods [91-94]. There is a debate going on the formation of plasma during SPS. While the absence of plasma has been suggested by some researchers [95], its presence has been shown by other researchers [65].

1.2.6.3. SPS mechanisms

Several mechanisms involved in SPS processing are proposed by researchers and some of them are summarized as below [70]:

I. Plasma generation

Ionization at the inter-particle contact due to spark discharges develops "impulsive pressures" facilitating diffusion of the atoms at powder particles contacts. The pulsed current has also a cleaning effect on the particle surfaces. The proof was based on the observation of a grain boundary formed between particles without any oxidation [96, 97]. This mechanism is still debated.

II. Electroplastic effect

Metal powders have been observed to exhibit lower yield strength under an electric field. Raichenko *et al.* [98] and Conrad [99] independently studied electro-plastic phenomena. The effects of high density electric current pulses (10^3–10^6 A.cm^{-2}) on the flow stress of metals at low homologous temperatures is mainly focused on the pre-exponential coefficient in "thermally-activated" motion of dislocations [99].

III. Joule heating

A flow of electric current through particles creates Joule heating which facilitates welding of the particles under mechanical pressure. Joule heating also contributes to a localized vaporization or cleaning of powder surfaces which provides more preferred paths for current flow [100]. Besides, Joule heating provides high heating rates which can provide a benefit by by-passing the grin coarsening [64]. The effect of a field on mass transport can be evaluated from the electro-migration theory:

$$J_i = \frac{D_i C_i}{RT}\left[\frac{RT\partial \ln C_i}{\partial x} + Fz^*E\right] \qquad (1.13)\ [64]$$

where j_i is the flux of diffusing groups of atoms, D_i is the diffusion coefficient of groups of atoms, C_i is the concentration of groups of atoms, F is Faraday's constant, z^* is the effective charge on the diffusing groups of atoms, E is the electric field, R is the gas constant and T is the temperature in Kelvin. It should be considered that temperature and current are not independent parameters and therefore Joule heating is a current-dependent property.

IV. Pulsed current

The pulsed DC current theoretically generates spark plasma, spark impact pressure, Joule heating and an electrical field diffusion effect. Due to generated high temperature

sputtering, adsorptive gas and impurities will be removed from the surface of the powder particles. The electrical field causes high-speed migration of ions leading to rapid mass diffusion [70].

V. Hydraulic pressure

Very high temperature localized at the gap between powder particles can clean the surface of the powder by eliminating the oxide or contamination layer forming "neck" [70]. Very high temperatures localized in the neck joints during the early phases of sintering may have two contributions: (a) the high localized temperature at the inter-particle contacts under the influence of a uniaxial pressure may allow the yield strength to be surpassed, allowing plastic flow to consolidate the particles, and (b) a high gradient in temperature leads to a higher dislocation density, which will aid in densification by increasing the rate of the power – law creep (a dislocation climb mechanism) [101-104].

The intrinsic effect of the pressure can be determined from the driving force for sintering:

$$\frac{d\rho}{(1-\rho)dt} = B\left(g\frac{\gamma}{x} + P\right) \qquad (1.14)\ [64]$$

where ρ is the fractional density, B is a term that includes diffusion coefficient and temperature involved, g is a geometric constant, γ is the surface energy, x is related to particle size, t is the time and P is the applied pressure.

1.2.6.4. Processing of ODS alloys via SPS

There have been only a limited number of studies on the application of SPS in consolidating the ODS steels and NFSs [105-110]. Srinivasarao *et al.* [108] processed a commercially pure nanocrystalline iron by milling and SPS. Its microstructure consisted of

nanograins (< 100 nm) as well as coarse grains (> 1μm) with uniform dispersion of nano-sized chromium oxide particles. Similar hetero-nanostructured ODS FeAl alloys were produced by Ji *et al.* [105]. Heintze *et al*. [106, 107] consolidated ODS Fe–9Cr model alloys including (Fe–9Cr, Fe–9Cr–0.3Y_2O_3 and Fe–9Cr–0.6Y_2O_3, wt.%) using SPS and studied mechanical properties as well as microstructural characteristics of these alloys. Allahar *et al.* [109] used SPS to consolidate Fe–16Cr–3Al (wt.%) powder by sequentially adding Y_2O_3 and Ti powders to produce Fe–16Cr–3Al–0.5Y_2O_3 (wt.%) and Fe–16Cr–3Al–0.5Y_2O_3-1Ti (wt.%) alloys.

1.2.7. Microstructural studies in ODS steels

Microstructure characteristics of different ODS steels and NFSs have been extensively studied by researchers [19, 62, 111-116]. Here only microstructure of some ODS steels are presented. The microstructure of MA957 alloy studied by Sakasegawa *et al.* [111] is shown in Fig. 1.19. The grains were elongated parallel to the extrusion direction and contain high dislocation density.

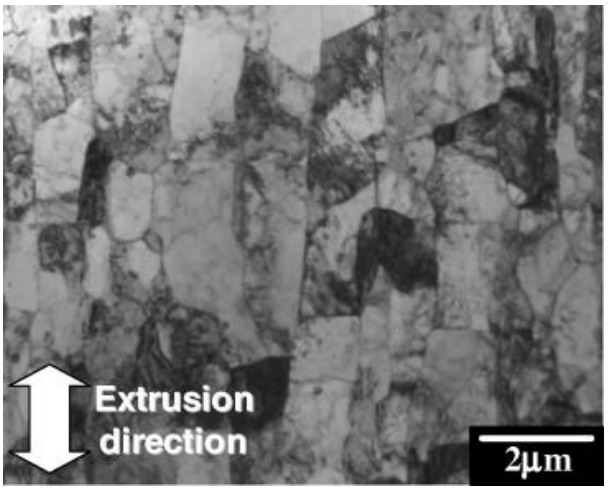

Figure 1.19. TEM micrograph of the as-extruded MA957 [111] (Courtesy of Elsevier)

The nanoparticles in MA957 have been identified by Wu *et al.* [112]. A HRTEM micrograph obtained from a particle ($d \approx 7$ nm) along with the corresponding fast Fourier transformation (FFT) pattern are shown in Fig. 1.20. These results were not consistent with either cubic $Y_2Ti_2O_7$ or hexagonal Y_2TiO_5 or YTi_2O_6. However, the diffraction data were much more consistent with orthorhombic Y_2TiO_5 〈1 $\bar{1}5$ 4〉 or $YTiO_3$ 〈2 1 $\bar{2}$〉 [112].

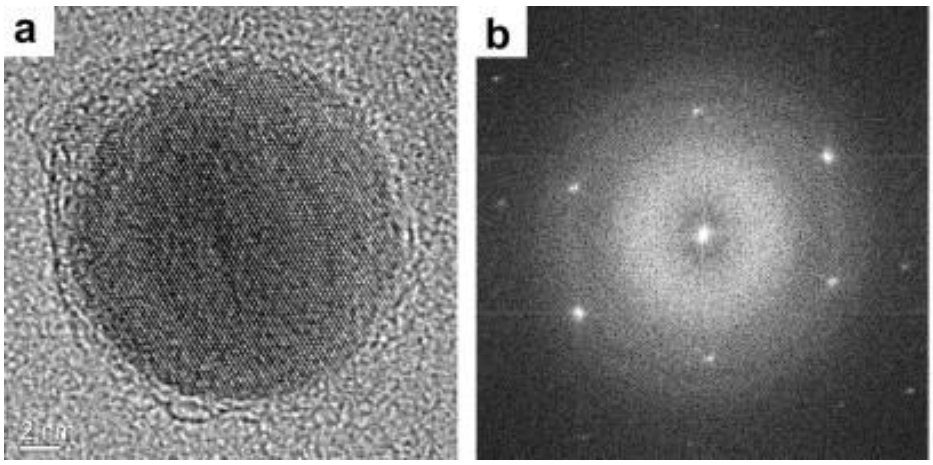

Figure 1.20. (a) A HRTEM micrograph from a feature and (b) the corresponding FFT pattern [112] (Courtesy of Elsevier)

A HTREM micrograph along a corresponding diffraction patterns for slightly smaller ~5–6 nm particle is shown in Fig. 1.21 in which the inter-planar spacing and angles are reasonably consistent with the $Y_2Ti_2O_7$ 〈011〉 [112]. The number density, chemical composition and average radius of NCs in ODS steels can be determined by APT studies. Studies on MA957 by Miller *et al.* [19] revealed a high number density ($\sim 2 \times 10^{24}$ m^{-3}) of ultrafine Ti–, Y– and O-enriched NCs in the ferrite matrix of the MA957, as shown in the atom maps in Fig. 1.22. The average Guinier radius of these NCs was determined to be

1.2 ± 0.4 nm. The average composition of them was estimated to be Fe–32.9±5.3Ti–15.4±7.3Y–39.9±6.9O–1.7±1.7Cr–0.02±0.2Mo (at.%) [19].

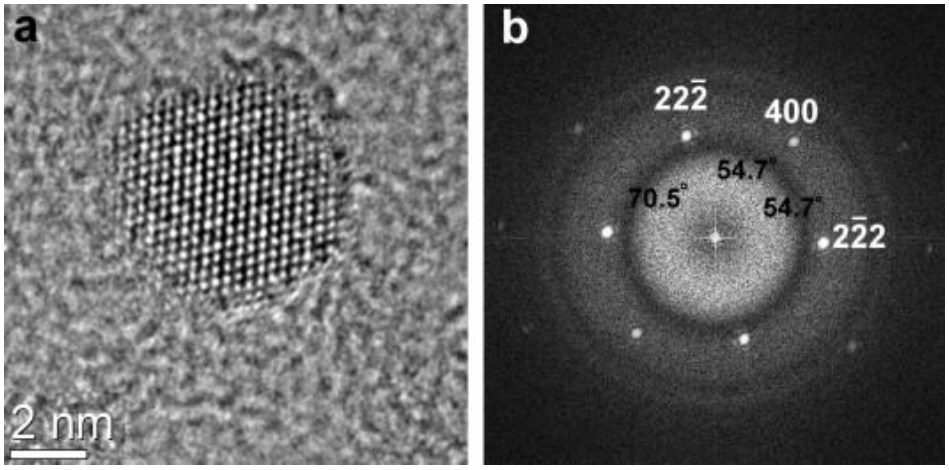

Figure 1.21. HRTEM lattice images of small NF in MA957 that is consistent with $Y_2Ti_2O_7$[112] (Courtesy of Elsevier)

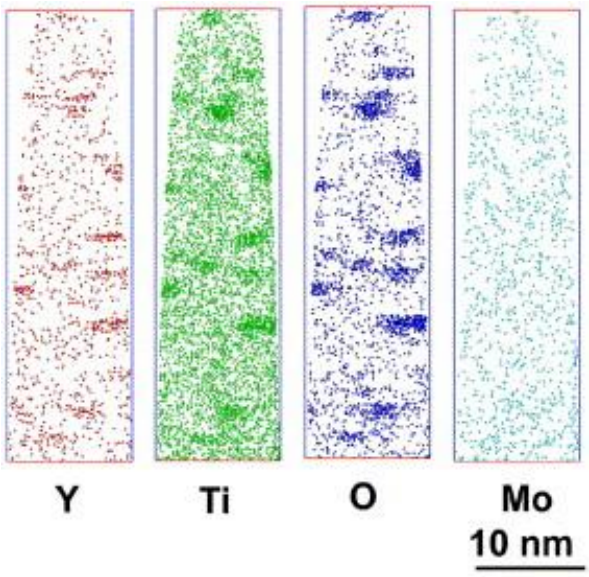

Figure 1.22. Atom maps in the MA957 alloy showing NCs enriched in Ti, Y and O [19] (Courtesy of Elsevier)

The general microstructure of the 14YWT–CR (pre-alloyed powder was made by Crucible Research) in the as-extruded (at 850 °C) condition and after thermal annealing for

1 h at 1000°C was studied by Miller *et al.* [117] and presented in Fig. 1.23. Transmission electron microscopy revealed uniformly distributed grains elongated parallel to extrusion with an average grain size of ~0.2–0.5 μm. Annealing for 1 h at 1000 °C did not have a significant effect on the grain size or on precipitate coarsening [117]. The nanoparticles in 14YWT alloy (HIPed) have been identified by Wen *et al.* [118] and shown in Fig. 1.24. The HRTEM image of Y–Ti–O-enriched nanoparticles revealed coherent interface particle / matrix with composition of pyrochlore $Y_2Ti_2O_7$ structure.

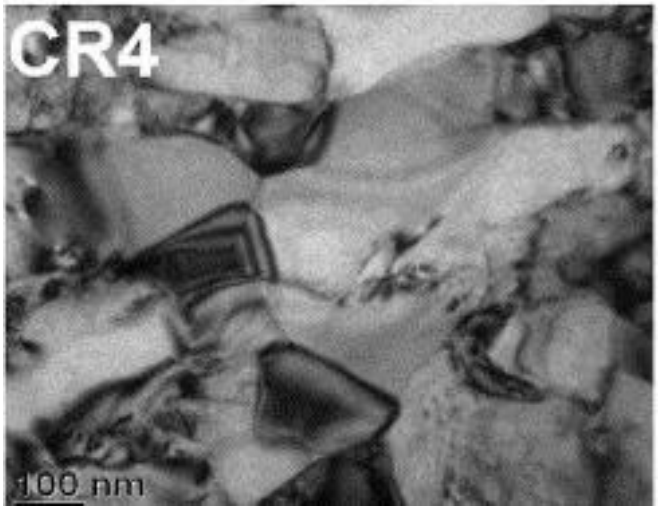

Figure 1.23. TEM micrograph showing general microstructure in extruded 14YWT [117]
(Courtesy of Elsevier)

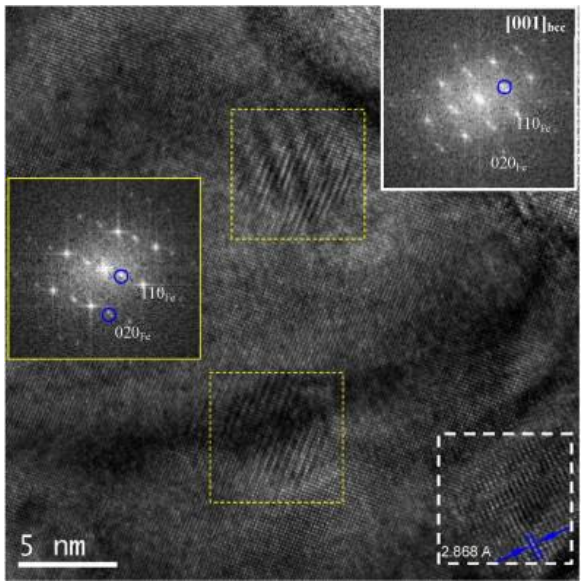

Figure 1.24. A HRTEM image along [0 0 1] of three Y–Ti–O nanoparticles in the 14YWT alloy, inset shows the FFT pattern of the pyrochlore $Y_2Ti_2O_7$ [118]

APT studies by Miller *et al.* [117] on the NCs in 14YWT extruded at 850 °C have shown a number density of 2×10^{23} m^{-3} of nanoclusters with average radius of 0.9±0.2 nm and average chemical composition of Fe–0.5±0.5Cr–5.4±4.5Y–43.8±2.3Ti–46.7±3.8O (at.%). An APT map of the nanoclusters from that study is shown in Fig. 1.25.

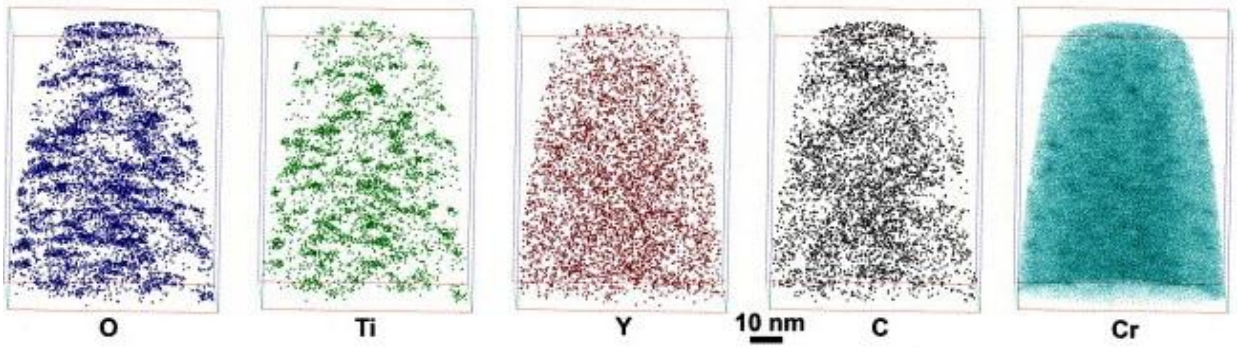

Figure 1.25. The APT maps of NCs in 14YWT [117] (Courtesy of Elsevier)

1.2.8. Mechanical properties of ODS steels

1.2.8.1. Tensile properties of ODS steels

Tensile properties of 14YWT alloy exhibited very high yield strength (YS) and ultimate tensile strength (UTS) at temperatures ranging from room temperature to 500 °C. For example, the YS and UTS values at room temperature were 1600 and 1749 MPa, respectively [119], which are significantly higher than those of 12YWT alloy (1300 MPa for YS and 1400 MPa for UTS) [120]. The tensile stress – strain curves for 14YWT alloy at different temperatures (room temperature to 1000 °C) are shown in Fig. 1.26. The corresponding tensile data are also presented in Table 1.2 [119]. The strength of 14YWT alloy decreases from about 400 °C at relatively high rate, and the rate of strength reduction decelerates at 800 °C and above. Although the decrease in the 400–800 °C regions is significant, the 14YWT alloy still offers high YS and UTS. This is a remarkably high strength at such high temperature for steels. Despite the 14YWT alloy displaying such high strengths over possible application temperature range (<800 °C), the measured total elongations are relatively low: 2.2–3.1% except for the temperature window of 600–700 °C [119].

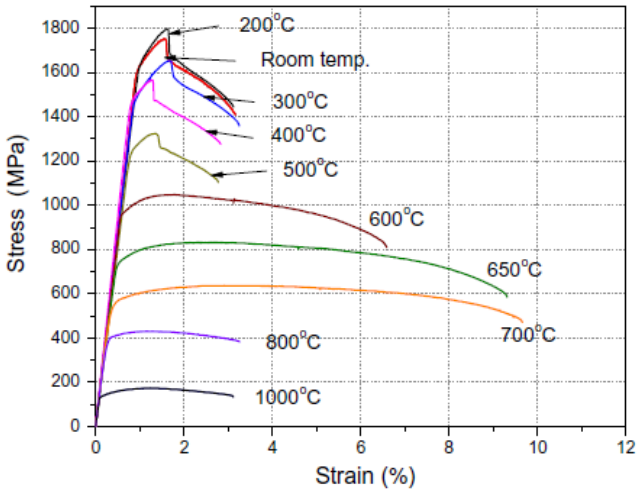

Figure 1.26. Stress–strain curves of 14YWT at various temperatures for a strain rate of 10^{-3} s^{-1}[119] (Courtesy of Elsevier)

Table 1.2. Tensile data for 14YWT for different temperatures [119] (Courtesy of Elsevier)

Temperature (°C)	YS (MPa)	UTS (MPa)	Total elongation (%)	Uniform elongation (%)	Reduction in area (%)
RT	1600	1749	2.4	0.7	31
200	1619	1792	2.4	0.7	25
300	1460	1651	2.5	0.8	–
400	1454	1558	2.2	0.5	–
500	1230	1322	2.2	0.7	19
550	1081	1181	3.0	0.9	–
600	952	1046	6.2	1.4	15
650	731	830	9.0	2.9	–
700	555	636	9.5	3.7	13
800	395	429	3.1	1.5	7
1000	133	172	3.1	1.5	7

A comparison study between YS and UTS data at different temperatures for some experimental and commercial ODS steels was done by Klueh *et al.* [6, 14]. The YS and UTS plots for different ODS steels as a function of test temperatures are shown in Fig. 1.27(a–b). In comparing the commercial steels to the experimental steels, the MA957 and 12YWT, the strongest of the commercial and experimental steels, respectively, have comparable

strengths. However, all steels approach a common low strength value as the temperature is increased to 900 °C and above [6, 14].

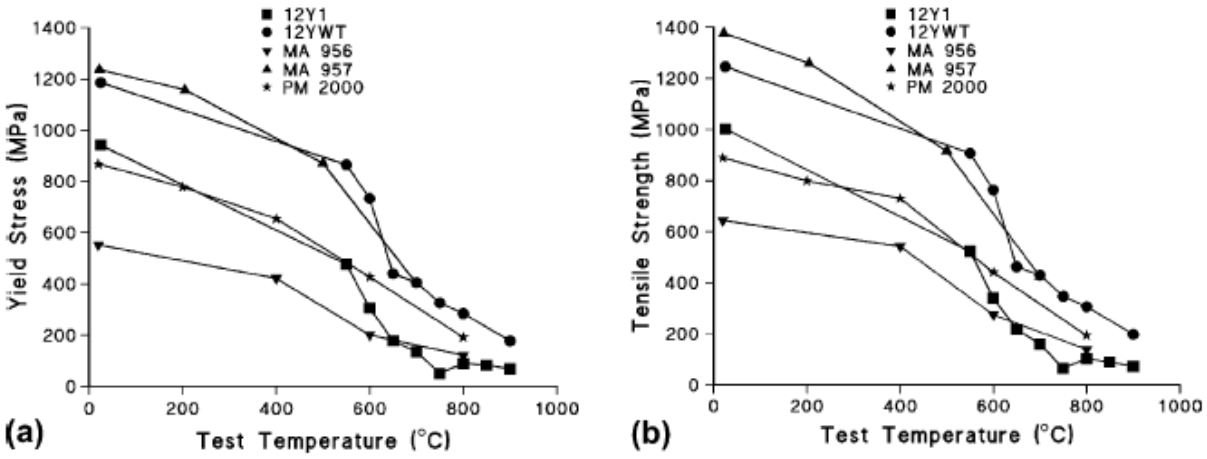

Figure 1.27. (a) yield stress and (b) ultimate tensile strength as a function of temperature for some experimental and commercial ODS steels [6] (Courtesy of Elsevier)

1.2.8.2. Creep behavior of ODS steels

The most important property for high temperature structural materials is thermal creep. The ODS steels such as MA957, 12YWT and 14YWT have excellent creep resistance [18, 19]. Analysis with the Larson – Miller parameter (which correlates creep rupture strength to operational time and is defined as LMP= T [25+log t] where T is temperature in K and t is rupture time in hours) has shown superior creep resistance for 12YWT compared to commercial ODS steel MA957 and ferritic – martensitic ODS steel. The creep-rupture strengths as a function of LMP for different ODS steels are shown in Fig. 1.28 [6, 14].

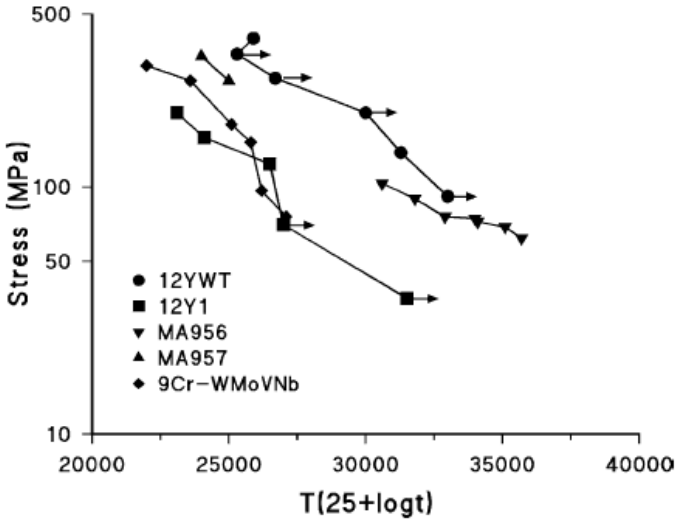

Figure 1.28. Creep-rupture strength as a function of Larson – Miller parameter for four ODS steels and a conventional ferritic – martensitic steel (The arrows indicate that the test is still in progress, or it was discontinued prior to rupture) [14] (Courtesy of Elsevier)

Creep behavior and deformation mechanism in 14YWT alloy has been studied by Brandes *et al.* [121] and Hayashi *et al*. [122]. The creep rates in 14YWT alloy are found to be six orders of magnitude slower than those predicted via conventional theory. This slower creep rate has been attributed to the presence of the NCs (2–5 nm in size) as well as numerous other small (5–50 nm) particles, both in the grain interiors and along grain boundaries. These NCs are thermally stable up to 1000 °C [19] and extremely effective at preventing grain boundary diffusion [121]. It might be anticipated that the grain boundary sliding is going to cause significantly larger creep rates due to the fine grain size in 14YWT alloy. However, the NCs on the grain boundaries would inhibit grain boundary sliding leading to a remarkable creep strength [33]. During creep in 14YWT alloy, the dislocations are often observed in roughly parallel configurations, moving on the glide planes. Dislocations, once nucleated, do not quickly traverse the small grains and become absorbed into the grain boundary. Rather, dislocation content remains within the grain volumes,

giving deformed alloys significant dislocation densities on the order of 10^{13} m^{-2}. Strong interactions between NCs and dislocations give rise to bowed dislocation; a small length of dislocation line gets trapped and unable to glide away from the NCs. Furthermore, strain field of the dislocation is accommodated by the NCs – matrix interface. Creep behavior in NFSs show near-Newtonian behavior at low stresses with small stress exponents and stable microstructure. The dominant deformation mechanism was proposed to be dislocation glide [33, 121, 122]. Observations of dislocation – NCs interactions demonstrate that gliding dislocations are readily trapped by the fine-scale particles adapting a new creep model for these alloys named "Kocks – Argon – Ashby" (KAA) model. In KAA model, NCs provide modest strengthening due to an attractive interaction with glissile dislocations and creep is controlled by stress-assisted thermal activation from such NCs traps [121].

A schematic of dislocation – NCs interaction during creep of 14YWT alloy is developed and suggested by Hayashi *et al.* [122]. In this model shown in Fig. 1.29, dislocations are initially trapped by the cluster cell (Fig. 1.29(a)), and locally bow out to the inner side of the cluster cell (Fig. 1.29(b)), and then fully bows out in the cell (Fig. 1.29(c)), and is finally released from the cluster cell. In locations such as those labeled "B", dislocations appear to be smoothly bowing between cluster cells [122].

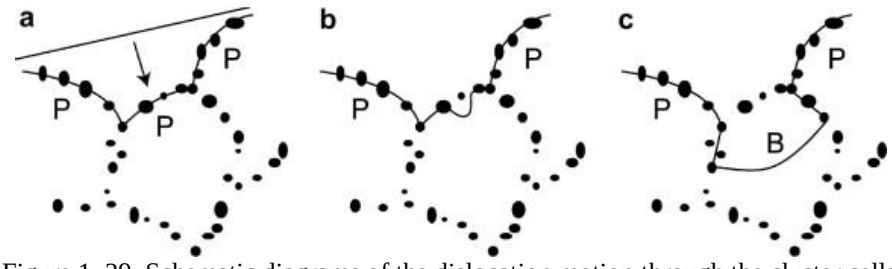

Figure 1. 29. Schematic diagrams of the dislocation motion through the cluster cells [122] (Courtesy of Elsevier)

1.2.8.3. Strengthening mechanisms of ODS steels

The strengthening mechanisms in ODS alloys include work hardening due to dislocation pile-up and dislocation – dislocation interactions, Hall – Petch strengthening due to grain refinement and grain boundary – dislocation interaction, solid solution due to lattice strain field and dispersion strengthening due to highly stable nanometric-sized particles that can stabilize the grain boundaries. At $0.5T_m$ and above only dispersion strengthening will remain effective and the efficiency of other mechanisms will be reduced [28]. Dispersion strengthening in ODS steels is caused only by high number density of Y–Ti–O-enriched nanoparticles that are highly stable at high temperatures and do not undergo any significant coarsening up to 1100 °C [19, 123].

In particles – dislocations interactions two major distinguishable phenomena would happen: (1) either dislocations would cut through (shear) the particles (as shown in Fig. 1.30) or (2) dislocation would bypass the particles. The latter mechanism is known as "Orowan mechanism".

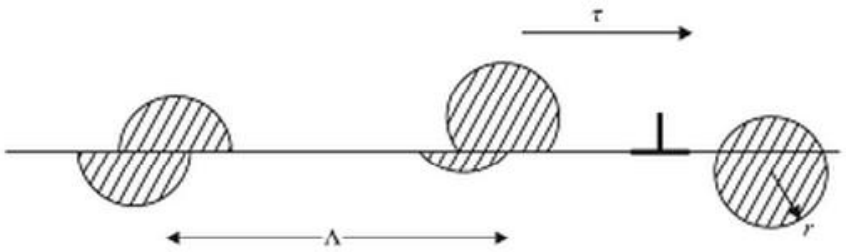

Figure 1.30. A dislocation cutting through a coherent deformable second phase particle [124]

As the dislocation shears the particle by one Burgers vector on the slip plane, produces a new interface on both sides of the particle. Then the specific particle – matrix interfacial

energy must be supplied for the cutting to occur. The maximum force to push the dislocation through the particle is

$$F_{max} = \pi r \gamma_{\alpha\beta} \quad (1.15)\ [124]$$

where r is the radius of the particle and $\gamma_{\alpha\beta}$ is the interfacial energy. The flow stress contribution to this force can be calculated from the following relationship:

$$\tau_{cut} = \frac{f_v \gamma_{\alpha\beta}}{b} \quad (1.16)\ [124]$$

where fv is the volume fraction of the precipitates and b is the Burgers vector. Several mechanisms have been proposed for the dislocations to bypass the precipitates: (a) Orowan mechanism, (b) Srolovitz mechanism, (3) general climb mechanism and (4) local climb mechanism. These mechanisms are shown in Fig. 1.31(a–d).

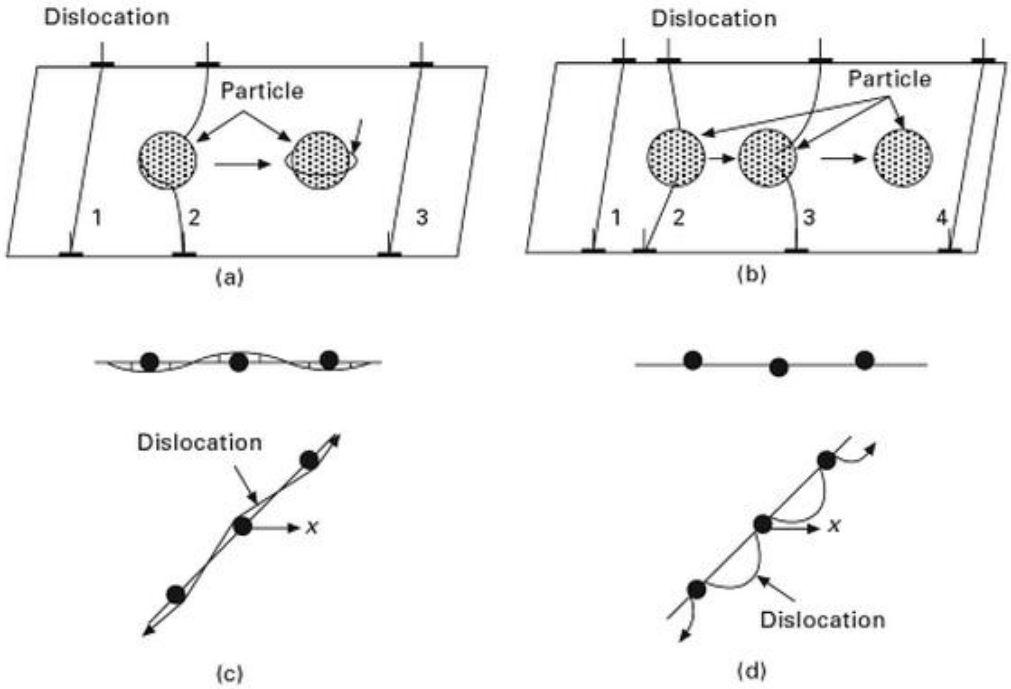

Figure 1.31. Schematic of dislocations passing through particles: (a) Orowan mechanism, (b) Srolovitz mechanism, (c) general climb mechanism and (d) local climb mechanism [125]

According to Orowan mechanism (shown in Fig. 1.31(a)), particle size and interparticle spacing are the key parameters for dispersion strengthening. The Orowan strengthening can be calculated from the following equation:

$$\Delta\tau_{CRSS} = \alpha \frac{0.81GB}{2\pi(1-\vartheta)^{0.5}} \times \frac{\ln\left(2\frac{r_{eff}}{r_o}\right)}{(\lambda - 2r_{eff})} \quad (1.17)\ [28, 126]$$

where $\Delta\tau_{CRSS}$ is the critical resolved shear stress for dislocation motion, α is the barrier strength coefficient, G is the shear modulus, b is the Burgers vector, υ is the Poisson's ratio, λ is inter-particle spacing, r_o is the dislocation inner cut-off radius, and r_{eff} is the effective particle radius and can be calculated using the following equation:

$$r_{eff} = \left(\frac{2}{3}\right)^{0.5} \times \mathrm{r} \quad (1.18)\ [127]$$

where r is the particle mean radii. The men particle spacing or λ can also be estimated using the following equation:

$$\lambda = \left(\frac{2\pi}{3}\right)^{0.5} \times \left(\frac{r_{eff}}{f^{0.5}}\right) = \frac{2\pi^{0.5}}{3} \times \frac{r}{f^{0.5}} \quad (1.19)\ [127]$$

where f is the volume fraction of the particles. In order to relate the $\Delta\tau_{CRSS}$ to yield stress the following relationship can be used:

$$\sigma_{Yield} = M\tau_{CRSS} \quad (1.20)\ [128]$$

where M is the *Taylor* factor and for bcc and fcc metals is approximately 3. According to Srolovitz mechanism, when the interface of matrix – particle is incoherent, dislocation strain field on the particle becomes relaxed by the interface sliding and volume diffusion as shown in Fig. 1.31(b) [125].

1.2.9. Thermal stability of ODS steels

The thermal stability of NFSs in the application temperature (800 °C) should be validated in order to use NFSs in the advanced cladding materials. In fact, the NFSs have shown outstanding thermal stability due to highly stable NCs [18, 19, 32, 42, 123, 129]. A series of aging experiments on MA957 alloy at 900–1000 °C up to 3000 h were conducted by Miao *et al.* [123] in which fine scale grain and dislocation structures were found to be stable up to 1000 °C. The NCs were also stable up to 900 °C, but did undergo some coarsening at temperatures above 900 °C. For example, the average diameter of NCs were reported to be 2.1±0.4, 2.1±0.4, 2.6±0.5 and 3.1±0.9 nm for the as-extruded, aged at 900 °C, 950 °C and 1000 °C, respectively. The coarsening regime in aged MA957 had the following relationship as a function of temperature and time:

$$d(T,t) = d_0 \times \left[t k_{co}^{*} \exp\left(\frac{-Q_{ec}}{RT}\right) + 1\right]^{p} \qquad (1.15)\ [123]$$

where, d_0 and $d(T,t)$ are the NCs size before and after aging, respectively, t is the aging time, T is the aging temperature in K, R is the gas constant, k'_{co} is the first yield coefficient and Q_{ec} is the effective activation energy for coarsening [123].

Similar to MA957 alloy, the experimental NFS developed by Alinger *et al.*[15] termed as 14YWT revealed a high thermal stability without evidence of any recrystallization or growth even up to 1400 °C [42].The Y–Ti–O-enriched NCs in 14YWT annealed at 1400 °C for 1 h were stable and did not undergo any coarsening as shown in Fig. 1.32.

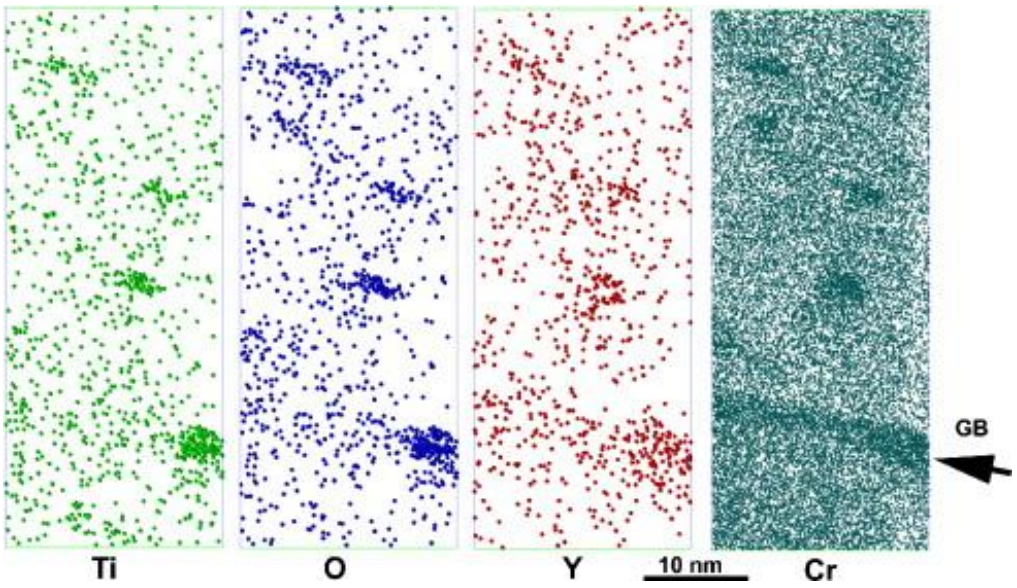

Figure 1.32. Atom maps showing NCs in 14YWT annealed at 1400 °C for 1 h [42] (Courtesy of Elsevier)

The remarkable thermal stability of Y–Ti–O-enriched NCs is due to strong chemical bonding between Y, Ti, and O atoms. The NCs in NFSs such as 14YWT or MA957 are found to be coherent with the matrix [44, 118], and therefore, the driving force for classic particle growth would be less. Rather, particle formation and growth is controlled by short-range (transfer of atoms across the particle boundary or interface) and long-range transport of atoms (diffusion in which atoms are transported over distances of several atomic spacing) [130]. The diffusion coefficients of Fe, Y, Ti and O at 1150 °C were determined to be 1.1×10^{-20}, 1.5×10^{-23}, 1.7×10^{-20} and 1.0×10^{-14} (m^2s^{-1}), respectively [44]. Since the Y, Ti and O atoms are strongly bonded together in NCs, further growth would force group migration of Y, Ti, and O–vacancy pairs. In order for an oxygen atom to migrate, a vacancy must be created first. The energy required to break an O–vacancy pair is 1.5 eV which is higher than the energy coming from just thermal fluctuations; for example the thermal fluctuation is only ~150 meV at 1400 °C. Recrystallization in 14YWT is significantly suppressed at

1400 °C because of O atoms acting as sinks for the vacancies (due to their strong binding energy) limiting the diffusion of Fe atoms. Furthermore, coherent NCs pin the grain boundaries and decelerate diffusion kinetics of Fe atoms [42]. Barnard *et al.* [44] studied the Ab-initio modeling of Ti–Y–O-enriched NCs and found that the NCs which are matched to the structure of pyrochlore ($Y_2Ti_2O_7$) are more stable than the coherent ones. In other words, the most energetically favorable nanocluster nuclei enriched in Ti–, Y–, O– are likely to resemble complex Ti–Y oxides that are at least partially incoherent with the Fe lattice. In the classical model or "on-lattice" method, Ti or Y atoms are located in Fe substitutional lattice sites; O atoms are located in Fe octahedral interstitial sites and NCs that are perfectly coherent with Fe host lattice. In a modified model presented by Barnard *et al.* [44] and referred to as "structure-matching" model, Ti–O and Y–O structures are embedded in Fe lattice with as little distortion as possible (to both Fe and oxide structure). In this model which is shown in Fig. 1.33, Ti and Y atoms do not have to occupy the Fe lattice sites and strained NCs are volume matched with a strained Fe host lattice.

The contribution of interfacial energy, local strain and bulk formation energy should be considered to calculate the formation energies. The interfacial energies were calculated to be lower for "on-lattice" NCs but bulk-like configuration of the M and O atoms will be more stable in "structure-matched" model. The presence of Cr, suppresses the nucleation of Ti–O nanoprecipitates and formation of stable nanoprecipitates is dependent on Y atoms. The strain energy of Y–O clusters is larger in the "on-lattice" model than "structure-matched" model stabilizing the Y–O clusters even further [44]. A fully relaxed "structure-matched" Ti–Y–O-enriched cluster and the corresponding structure in bulk pyrochlore structure $Y_2Ti_2O_7$ are depicted in Fig. 1.34.

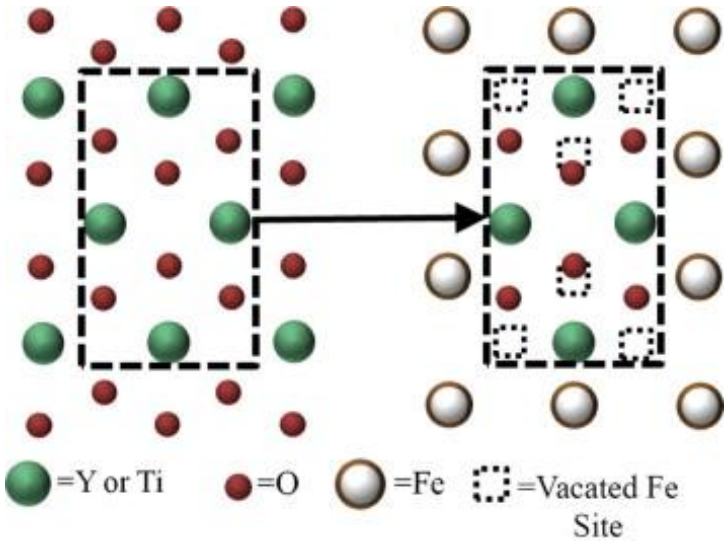

Figure 1.33. "Structure-matching" model for partially incoherent NCs [44] (Courtesy of Elsevier)

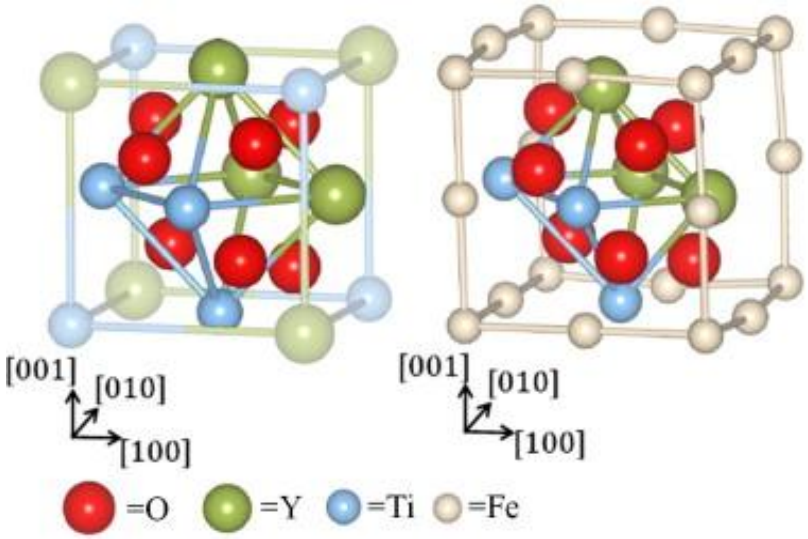

Figure 1.34. A "structure-matched" cluster: pyrochlore $Y_2Ti_2O_7$ (left) and embedded in Fe after full ionic relaxation (right) [44] (Courtesy of Elsevier)

1.2.10. Irradiation stability of ODS steels

The targeted temperatures and damage levels for future reactor concepts are considered to be as high as 700 °C and 200 dpa, respectively [5, 131-133]. The NCs in NFSs provide creep resistance and radiation damage resistance by increasing the amount of interfaces that

can act as effective sinks enhancing the self interstitial atoms (SI) – vacancy recombination [6, 134]. The irradiation stability of 14YWT alloy under 5 MeV Ni^{2+} ions at 300 °C, 450 °C, 600 °C, with an ion fluence of 1.49×10^{21} m^{-2}, Ni ion flux of 1.04×10^{17} $m^{-2}.s^{-1}$, corresponding to a dose damage rate 1.39×10^{-2} dpa/s at the damage peak (~1600 nm), up to a total dose of 200 dpa was studied by He *et al.* [131]. With irradiation at 300 °C, size and number density of NCs decreased but the changes were not as pronounced for samples irradiated at 450 and 600 °C indicating NCS are more stable at high temperatures.

In irradiation of 14YWT alloy at 300 °C significant radiation hardening (~250 MPa) has been reported by McClintock *et al.* [135], and almost no hardening was detected for the samples irradiated at 580 and 670 °C. The irradiation dose was 1.5 dpa in the High Flux Isotope Reactor (HFIR) at Oak Ridge National Laboratory (ORNL). Small "rabbit" capsules designed to maintain irradiation temperatures of 300, 600, and 750 °C were used [135]. Certain *et al.* [136] discovered a "dynamic stability" in NCs in 14YWT alloy (irradiation condition: 5 MeV Ni^{+2} ions, dose: 5, 50 and 100 dpa, Temp: –75, 300, 450 and 600 °C) in which solute atoms continually get ejected from clusters by collision cascades and then diffuse back to rejoin clusters leading to overall stability. This stability is due to diffusion of solutes under high temperature irradiation, and NCs did not exhibit stability under low temperature irradiation (no diffusion) [136]. The nanoparticles in MA957 alloy with diameter higher than 5 nm (pyrochlore) were stable after irradiation at 412 °C up to 50 dpa and 430 °C up to 75 dpa in the French small-scale prototype fast breeder reactor named "Phenix". The radiation-induced change in lattice parameter of the nanoparticles was found to be due to disordering by cascade effects [137].

Miller *et al.* [138] conducted APT studies of the neutron irradiated MA957 alloy and found that the microstructure is remarkably tolerant to neutron irradiation, and NCs size, size distribution and number density did not significantly change after irradiation (irradiation condition: High Flux Isotope Reactor to a dose of 3 dpa at a controlled temperature of 600 °C, fluence of 5.8×10^{21} cm^{-2} ($E > 1$ MeV), a fast flux of $2–5 \times 10^{14}$ cm^{-2} s^{-1} ($E > 0.1$ MeV), displacement damage rate of 3.7×10^{-7} dpa/s [138]. Yamashita *et al.* [139] observed the microstructural evolution of heavily neutron-irradiated MA957 at ~700 °C and reported that the size of NCs between unirradiated and irradiated specimens (at 500 and 700 °C) did not change, though the number densities decreased by about one-half after irradiation because recoil re-solution of oxide particles was induced by ballistic bombardment of high energy neutron. Furthermore, they found that oxide particles were effective in pinning dislocations even under neutron irradiation to a dose of ~100 dpa at 700 °C.

References

[1] C. Suryanarayana, E. Ivanov, V.V. Boldyrev, Mater. Sci. Eng. A, 304–306 (2001) 151–158.

[2] W.D. Coolidge, Patent, U.S.A. (1913).

[3] J.S. Benjamin, Metal. Trans., 1 (1970) 2943–2951.

[4] UK-US Collaboration on Fossil Energy R&D Advanced Materials, http://us–uk.fossil.energy.gov/.

[5] G.R. Odette, M.J. Alinger, B.D. Wirth BD, Annu. Rev. Mater. Res., 38 (2008) 471–503.

[6] R.L. Klueh, J.P. Shingledecker, R.W. Sweindeman, D.T. Hoelzer, J. Nucl. Mater., 341 (2005) 103–114.

[7] J.J. Fisher, Patent, U.S.A. (1978).

[8] S. Ukai, T. Nishida, H. Okada, T. Okuda, M. Fujiwara, K. Asabe, J. Nucl. Sci. Technol., 34 (1997) 256–263.

[9] S. Ukai, T. Yoshitake, S. Mizuta, Y. Matsudaira, S. Hagi, T. Kobayashi, J. Nucl. Sci. Technol., 36 (1999) 710–712.

[10] A. Alamo, H. Regle, G. Pons, L.L. Bechade, Mater. Sci. Forum, 88–90 (1992) 183–190.

[11] D.K. Mukhopadhyay, F.H. Froes, D.S. Gelles, J. Nucl. Mater., 258-263 (1998) 1209–1215.

[12] M.K. Miller, E.A. Kenik, K.F. Russell, L. Heatherly, D.T. Hoelzer, P.J. Maziasz, Mater. Sci. Eng. A, 353 (2003) 140–145.

[13] A. Kimura, R. Kasada, N. Iwata, H. Kishimoto, C.H. Zhang, J. Isselin, P.Dou, J.H. Lee, N. Muthukumar, T. Okuda, M. Inoue, S. Ukai, S. Ohnuki, T. Fujisawa, T.F. Abe, J. Nucl. Mater., 417 (2011) 176–179.

[14] R.L. Klueh, P.J. Maziasz, I.S. Kim, L. Heatherly, D.T. Hoelzer, N. Hashimoto, E.A. Kenik, K. Miyahara, J. Nucl. Mater., 307 (2002) 773–777.

[15] M.J. Alinger, G.R. Odette, D.T. Hoezler, Acta Mater., 57 (2009) 392–406.

[16] M.L. Hamilton, D.S. Gelles, R.J. Lobsinger, G.D. Johnson GD, W.F. Brown, M. Paxton, PNNL report, Richland, WA (2000)

[17] M.K. Miller, C.M. Parish, Mater. Sci. Technol., 27 (2011) 729–734.

[18] M.J. Alinger, G.R. Odette, D.T. Hoezler, J. Nucl. Mater., 329–333 (2004) 382–386.

[19] M.K. Miller, D.T. Hoelzer, E.A. Kenik, K.F. Russell, J. Nucl. Mater., 329–333, Part A (2004) 338–341.

[20] H. Sakasegawa, F. Legendre, L. Boulanger, M. Brocq, L. Chaffron, T. Cozzika, J. Malaplate, J. Henry, Y. de Carlan, J. Nucl. Mater., 417 (2011) 229–232.

[21] J.H. Kim, K.M. Kim, T.S. Byun, D.W. Lee, C.H. Park, Therm. Acta, 579 (2014) 1–8.

[22] H.B. I. Bogomol, T. Zhao, T. Nishimura, Y. Sakka, P. Loboda, O. Vasylkiv, Scripta Mater., 71 (2014) 17–20.

[23] S. S. Brenner, M. K. Miller, W. A. Soffa, Scripta. Metall., 16 (1982) 831–836.

[24] H.J.T. Ellingham, J. Soc. Chem. Ind., 63 (1944) 125–133.

[25] S. Ukai, M. Harada, H. Okada, M. Inoue, S. Nomura, S. Shikakura, J. Nucl. Mater., 204 (1993) 65–73.

[26] ASM International Committees, ASM Handbook,Volume 3: Alloy Phase Diagrams, ASM International, Materials Park, Ohio, 1992.

[27] B.W. Zhang, G. Liu, K. Han, J. Phase. Equilib., 13 (1992) 304–308.

[28] M.J. Alinger, On the formation and stability of nanometer scale precipitates in ferritic alloys during processing and high temperature service, Materials Engineering, Ph.D. Dissertation (2004) University of California Santa Barbara, USA.

[29] S.B. Kim, K.W. Paik, Y.G. Kim, Mater. Sci. Eng. A, 247 (1998) 67–75.

[30] S. Ohtsuka, S. Ukai, M. Fujiwara, T. Kaito, T. Narita, J. Phys. Chem., 66 (2005) 571–575.

[31] C. L. Fu, M. Krcmar, G. S. Painter, X.Q. Chen, Phys. Rev. Lett., 99 (2007) 225502–225505.

[32] M. K. Miller, D. T. Hoelzer, E. A. Kenik, K. F. Russell, Intermetallics, 13 (2005) 387–392.

[33] J.H. Schneibel, C.T. Liu, M.K. Miller, M.J. Mills, P. Sarosi, M. Heilmaierc, D. Sturmc, Scipta Mater., 61 (2009) 793–796.

[34] P. Pochet, P. Bellon, L. Boulanger, L. Chaffron, G. Martin, Mater. Sci. Forum, 269–272 (1998) 655-664.

[35] J.W. Martin, R.D. Doherty, B. Cantor, Stability of microstructure in metallic systems, Cambridge University Press, New York, NY, 1997.

[36] C. Suryanarayana, N. Al-Aqeeli, Prog. Mater. Sci., 58 (2013) 383–502.

[37] D.A. Porter, K.E. Easterling, Phase Transformations in Metals and Alloys, Third Edition (Revised Reprint), CRC Press, 1992.

[38] A.J. Ardell, Acta Metall., 20 (1972) 601–609.

[39] A.J. Ardell, Euro. Cer. Soc., 19 (1999) 2217–2231.

[40] A.J. Ardell, Mater. Sci. Eng. A, 238 (1997) 108–120.

[41] P.K. Footner, C.B. Alcock, Metal. Trans., 3 (1972) 2633–2637.

[42] X.L. Wang, C.T. Liu, U. Keiderling, A.D. Stoica, L. Yang, M.K. Miller, C.L. Fu, D. Ma, K. An, J. Alloy. Compd., 529 (2012) 96–101.

[43] C. Hin, B.D. Wirth, Mater. Sci. Eng. A, 528 (2011) 2056–2061.

[44] L. Barnard, G.R. Odette, I. Szlufarska, D. Morgan, Acta Mater., 60 (2012) 935–947.

[45] J.S. Benjamin, Sci. Am., 234 (1976) 40–48.

[46] C. Suryanarayana, Prog. Mater. Sci., 46 (2001) 1–184.

[47] H.K.D.H. Bhadeshia, Mater. Sci. Technol., 16 (2000) 1404–1411.

[48] M. Brocq, B. Radiguet, S. Poissonnet, F. Cuvilly, P. Pareige, F. Legendre, J. Nucl. Mater., 409 (2011) 80–85.

[49] S. Pasebani, I. Charit, Y.Q. Wu, D.P. Butt, J.I. Cole, Acta Mater., 61 (2013) 5605–5617.

[50] C. Domain, C.S. Becquart, Phys. Rev. B, 65 (2001) 024103–024116.

[51] C. Domain, C.S. Becquart, J. Foct, Phys. Rev. B, 69 (2004) 144112–144125.

[52] D.E. Jiang, E.A. Carter, Phys. Rev. B, 67 (2003) 214103–214111.

[53] Y. Kimura, S. Takaki, S. Suejima, R. Uemori, H. Tamehiro, ISIJ Inter., 39 (1999) 176–182.

[54] P. He, On the structure–property correlation and the evolution of nanofeatures in 12–13.5% Cr oxide dispersion strengthened ferritic steels, Materials Engineering, Ph.D. Dissertation (2013) Karlsruher Institut für Technologie (KIT), Germany.

[55] W. Sha, H.K.D.H. Bhadeshia, Mater. Sci. Eng. A, A223 (1997) 91–98.

[56] R.C. Klug, G. Krauss, D.K. Matlock, Metal. Mater. Trans. A, 27A (1996) 1945–1960.

[57] T.S. Chou, Mater. Sci. Eng. A, A223 (1997) 78–90.

[58] M.F. Ashby, Acta Metall., 20 (1972) 887–897.

[59] N.L. Loh, K.Y. Sia, J. Mater. Process. Technol., 30 (1992) 45–65.

[60] M.H. Bocanegra-Bernal, J. Mater. Sci., 39 (2004) 6399–6420.

[61] http://www.azom.com/article.aspx?ArticleID=5769.

[62] L. Hsiung, M. Fluss, S. Tumey, J. Kuntz, B. El-Dasher, M. Wall, B. Choi, A. Kimura, F. Willaime, Y. Serruys, J. Nucl. Mater., 409 (2011) 72–79.

[63] L.L. Hsiung, M.J. Fluss, S.J. Tumey, B.W. Choi, Y. Serruys, F. Willaime, A. Kimura, Phys. Rev. B, 82 (2010) 184103–184113.

[64] Z.A. Munir, U. Anselmi-Tamburini, M. Ohyanagi, J. Mater. Sci., 41 (2006) 763–777.

[65] Z.H. Zhang, Z.F. Liu, J.F. Lu, X.B. Shen, F.C. Wang, Y.D. Wang, Scripta. Mater., 81 (2014) 56–59.

[66] R. Orru, R. Licheri, A.M. Locci, A. Cincotti, G. Cao, Mater. Sci. Eng. R, 63 (2009) 127–287.

[67] I. Bogomol, H. Borodianska, T. Zhao, T. Nishimura, Y. Sakka, P. Loboda, O. Vasylkiv, Scripta Mater., 71 (2014) 17–20.

[68] J.G. Santanach, A. Weibel, C. Estournès, Q. Yang, C. Laurent, A. Peigney, Acta Mater., 59 (2011) 1400–1408.

[69] S.H. Lee, H.C. Oh, B.H. An, H.D. Kim, Scripta Mater., 69 (2013) 135–138.

[70] M. Suárez, A. Fernández, J.L. Menéndez, R. Torrecillas, H. U. Kessel, J. Hennicke, R. Kirchner, T. Kessel, Challenges and Opportunities for Spark Plasma Sintering: A Key Technology for a New Generation of Materials, In TechOpen 2013.

[71] R. Chaim, Mater. Sci. Eng. A, 443 (2007) 25–32.

[72] T. Graziani, A. Bellosi, J. Mater. Sci. Lett., 14 (1995) 1078–1081.

[73] F. Monteverde, V. Medri, A. Bellosi, J. Eur. Cer. Soc., 22 (2002) 2587–2593.

[74] A. Borrell, M.D. Salvador, V. García-Rocha, A. Fernández, E. Chicardi, F.J. Gotor, Mater. Sci. Eng. A, 543 (2012) 173–179.

[75] R. Apetz, M.P.B. Van Bruggen, J. Am. Ceram. Soc., 86 (2003) 480–486.

[76] S.R. Casolco, J. Xu, J.E. Garay, Scipta Mater., 58 (2008) 516–519.

[77] W. Que, K.A. Khor, J.L. Xu, L.G. Yu, J. Eur. Cer. Soc., 28 (2008) 3083–3090.

[78] R.C. O'Brien, R. M. Ambrosi, N.P. Bannister, S.D. Howe, H.V. Atkinson, J. Nucl. Mater., 393 (2009) 108–113.

[79] R.C. O'Brien, R.M. Ambrosi, N.P. Bannister, S.D. Howe, H.V. Atkinson, J. Nucl. Mater., 377 (2008) 506–521.

[80] K. Inoue, Patent, No. 3 241 956, U.S.A. (1966).

[81] K. Inoue, Patent, No. 3 250 892, U.S.A. (1966).

[82] W. Liu, M. Naka, Scripta Mater., 48 (2003) 1225–1230.

[83] I.W. Chen, X.H. Wang, Nature, 404 (2000) 168–171.

[84] L. Gao, H.Z. Wang, J.S. Hong, H. Miyamoto, K. Miyamoto, Y. Nishikawa, S.D. Torre, Nanostruct. Mater., 11 (1999) 43–49.

[85] D.S. Perera, M. Tokita, S. Moricca, J. Eur. Ceram. Soc., 18 (1998) 401–404.

[86] X.P. Li, M. Yan, H. Imai, K. Kondoh, G.B. Schaffer, M. Qian, J. Non-Cryst. Solid., 375 (2013) 95–98.

[87] G.D. Dutel, P. Langlois, D. Tingaud, G. Dirras, Mater. Charact., 79 (2013) 76–83.

[88] S. Wei, Z.H. Zhang, F.C. Wang, X.B. Shen, H.N. Cai, S.K. Lee, L. Wang, Mater. Sci. Eng. A, 560 (2013) 249–255.

[89] H. Jabbar, J.P. Monchoux, M. Thomas, A. Couret, Acta Mater., 59 (2011) 7574–7585.

[90] F. Zhang, C. Mihoc, F. Ahmed, C. Lathe, E. Burkel, Chem. Phys. Lett., 510 (2011) 109–114.

[91] A.L. Ortiz, E. Ciudad, T.N. Baymukhametov, O. Borrero-López, A.L. Vasiliev, M. Nygren, Scripta Mater., 77 (2014) 9–12.

[92] E. Olevsky, I. Bogachev, A. Maximenko, Scripta Mater., 69 (2013) 112–116.

[93] X. Li, D. Jiang, J. Zhang, Q. Lin, Z. Chen, Z. Huang, Ceram. Int., 40 (2014) 4359–4366.

[94] T. Hungría, H. Amorín, M. Algueró, A. Castro, Scripta Mater., 64 (2011) 97–100.

[95] D.M. Hulbert, A. Anders, J. Andersson, E.J. Lavernia, A.K. Mukherjee, Scripta Mater., 60 (2009) 835–838.

[96] J. Groza, A. Zavaliangos, Mater. Sci. Eng. A, 287 (2000) 171–177.

[97] J. Groza, K.R. Anderson, M. Fendorf, C.J. Echer, Mater. Sci. Eng. A, 270 (1999) 278–282.

[98] A.I. Raichenko, G.L. Burenkov, V.I. Leshchinsky, Phys. Sinter., 5 (1976) 215–225.

[99] H. Conrad, Mater. Sci. Eng. A, 322 (2002) 100–107.

[100] D. Tiwari, B. Basu, K. Biswas, Ceram. Int., 35 (2009) 699–708.

[101] E.A. Olevsky, L. Froyen, J. Am. Ceram. Soc. , 92 (2009) 122–132.

[102] E.A. Olevsky, L. Froyen, Scripta Mater., 55 (2006) 1175–1178.

[103] E.A. Olevsky, S. Kandukuri, L. Froyen, J. App. Phys., 102 (2007) 114913–114924.

[104] J.A. Webb, Analysis and fabrication of tungtesn cermet materials for ultra-high temperature reactor appications via pulsed electric current sintering (PECS), Nuclear Engineering, Ph.D. Dissertation (2012) University of Idaho, USA.

[105] G. Ji, F. Bernard, S. Launois, T. Grosdidier, Mater. Sci. Eng. A, 559 (2013) 566–573.

[106] C. Heintze, A.H. Mayoral, A. Ulbricht, F. Bergner, A. Shariq, T. Weissgarber, H. Frielinghaus, J. Nucl. Mater., 428 (2012) 139–146.

[107] C. Heintze, F. Bergner, A. Ulbricht, M. Hernandez, U. Keiderling, R. Lindau, T. Weissgarber, J. Nucl. Mater., 416 (2011) 35–39.

[108] B. Srinivasarao, K. Ohishi, T. Ohkubo, K. Hono, Acta Mater., 57 (2009) 3277–3286.

[109] K.N. Allahar, J. Burns, B. Jaques, Y.Q. Wu, I. Charit, J. Cole, D.P. Butt, J. Nucl. Mater., 443 (2013) 256–265.

[110] S. Pasebani, I. Charit, J. Alloy. Compd., 599 (2014) 206–211.

[111] H. Sakasegawa, L. Chaffron, F. Legendre, M. Brocq, L. Boulanger, S. Poissonnet, Y. de Carlan, J. Bechade, T. Cozzika, J. Malaplate, J. Nucl. Mater., 386–388 (2009) 511–514.

[112] Y. Wu, E.M. Haney, N.J. Cunningham, G.R. Odette, Acta Mater., 60 (2012) 3456–3468.

[113] P. Miao, G.R. Odette, J. Gould, J. Bernath, R. Miller, M. Alinger, C. Zanis, J. Nucl. Mater., 367–370, Part B (2007) 1197–1202.

[114] T. Yamamoto, G.R. Odette, P.Miao, D.T. Hoelzer, J. Bentley, N. Hashimoto, H. Tanigawa, R.J. Kurtz, J. Nucl. Mater., 367–370 (2007) 399–410.

[115] Z. Oksiuta, P. Hosemann, S.C. Vogel, N. Baluc, J. Nucl. Mater., 451 (2014) 320–327.

[116] M.A. Auger, V. de Castro, T. Leguey, A. Muñoz, R. Pareja, J. Nucl. Mater., 436 (2013) 68–75.

[117] M.K. Miller, K.F. Russell, D.T. Hoelzer, J. Nucl. Mater., 351 (2006) 261–268.

[118] Y. Wen, Y. Liu, A. Hirata, F. Liu, T. Fujita, Y. Dou, D. Liu, B. Liu, Z. Liu, C.T. Liu, Mater. Sci. Eng. A, 544 (2012) 59–69.

[119] J.H. Kim, T.S. Byun, D.T. Hoelzer, J. Nucl. Mater., 407 (2010) 143–150.

[120] M.A. Sokolov, D.T. Hoelzer, R.E. Stoller, D.A. McClintock, J. Nucl. Mater., 370 (2007) 213–216.

[121] M.C. Brandes, L. Kovarik, M.K. Miller, G.S. Daehn, M.J. Mills, Acta Mater., 60 (2012) 1827–1839.

[122] T. Hayashi, P.M. Sarosi, J.H. Schneibel, M.J. Mills, Acta Mater., 56 (2008) 1407–1416.

[123] P. Miao, G.R. Odette, T. Yamamoto, M. Alinger, D. Klingensmith, J. Nucl. Mater., 377 (2008) 59–64.

[124] M.N. Shetty, Dislocations and mechanical behaviour of materials, PHI Learning, New Delhi, 2013.

[125] F. Abe, T.U. Kern, R. Viswanathan, Creep-resistant steels, Woodhead Publishing, Cambridge, 2008.

[126] J.W. Martin, Cambridge University Press, New York, 1980.

[127] A.J. Ardell, Metall.Trans. A, 16A (1985) 2131–2165.

[128] U.F. Kocks, Metall. Mater. Trans. A, 1 (1970) 1121–1143.

[129] Z. Oksiuta, M. Lewandowska, K.J. Kurzydłowski, Mech. Mater., 67 (2013) 15–24.

[130] R.D. Doherty, R.W. Cahn, P. Hason, Physical Metallurgy, Elsevier Science B.V., The Netherlands 1998.

[131] J. He, F. Wan, K. Sridharan, T.R. Allen, A. Certain, V. Shutthanandan, Y.Q. Wu, J. Nucl. Mater., 455 (2014) 41–45.

[132] T.R. Allen, J. Gan, J.I. Cole, M.K. Miller, J.T. Busby, S. Shutthanand, S. Thevuthasan, J. Nucl. Mater., 375 (2008) 26–37.

[133] S.J. Zinkle, P. J. Maziasz, R. E. Stoller, J. Nucl. Mater., 206 (1993) 266–286.

[134] S. Ukai, M. Fujiwara, J. Nucl. Mater., 307–311, Part 1 (2002) 749–757.

[135] D.A. McClintock, D.T. Hoelzer, M.A. Sokolov, R.K. Nanstad, J. Nucl. Mater., 386–388 (2009) 307–311.

[136] A. Certain, S. Kuchibhatla, V. Shutthanandan, D.T. Hoelzer, T.R. Allen, J. Nucl. Mater., 434 (2013) 311–321.

[137] J. Ribis, M.L. Lescoat, Y. de Carlan, J.M. Costantini, I. Monnet, T. Cozzika, F. Delabrouille, J. Malaplate, J. Nucl. Mater., 417 (2011) 262–265.

[138] M.K. Miller, D.T. Hoelzer, J. Nucl. Mater., 418 (2011) 307–310.

[139] S. Yamashita, N. Akasaka, S. Ukai, S. Ohnuki, J. Nucl. Mater., 367–370 Part A (2007) 202–207.

CHAPTER 2: A Preliminary Study on the Development of La_2O_3-Bearing Nanostructured Ferritic Steels via High Energy Ball Milling

Somayeh Pasebani[1,4], Indrajit Charit[1,4], Darryl P. Butt[2,4] and James I. Cole[3,4]

[1] Department of Chemical and Materials Engineering, University of Idaho, Moscow, ID 83844, USA

[2] Department of Materials Science and Engineering, Boise State University, Boise, ID 83725, USA

[3] Idaho National Laboratory, Idaho Falls, ID 83401, USA

[4] Center for Advanced Energy Studies (CAES), Idaho Falls, ID 83401, USA

(*Published in the Journal of Nuclear Materials, Volume 434 (2013) pages 282–286*)

Abstract

Elemental powder mixture of Fe–Cr–Ti–Mo and La_2O_3 were ball milled for different milling times in a high energy shaker mill. Effects of ball milling time on crystallite size, particle size and hardness were investigated using X-ray diffraction (XRD), scanning electron microscopy (SEM) and microhardness tester. After 10 h of ball milling, the smallest crystallite size and highest hardness were ~ 24 nm and ~ 970 HV, respectively. Transmission electron microscopy (TEM) studies have revealed nanoscale features 2–5 nm in diameter present in the milled powder. Local atom probe tomography studies have shown that these nanoscale features were possibly nanoclusters enriched in La, TiO and O.

Keywords: High energy ball milling; La_2O_3-bearing nanostructured ferritic alloys; Oxide dispersion strengthened steels

2.1. Introduction

Nanostructured ferritic steels (NFSs) are being considered for a number of advanced nuclear reactor applications because of their excellent high temperature strength and radiation damage tolerance [1]. These alloys are produced via mechanical alloying (MA) of a ferritic matrix and yttrium oxide (Y_2O_3) using high energy ball milling and generally consolidated via hot isostatic pressing (HIP) or hot extrusion [2]. A high number density (~10^{24} m^{-3}) of Y–Ti–O nanofeatures (NFs) with the average size of less than 5 nm dispersed in the matrix improves high temperature as well as irradiation properties of NFS by pinning of the mobile dislocations and trapping of helium atoms and / or vacancies [2-4]. Many studies have been carried out on yttria containing NFS. However, little is known on the role of other potential alternative rare earth (RE) oxides.

Lanthanum has no solubility in iron at all temperatures [5] and a very high affinity to oxygen to form La–O bond [6]. Based on the density functional theory calculations, lanthanum oxide clusters are calculated to have the same general structure as the corresponding yttrium species; however, the bond distances are generally larger. These structures presumably maximize the number of strong RE–O bonds. Interestingly, the bond energies for the yttrium oxide clusters are generally close but lower than those for the lanthanum oxide clusters, especially in smaller clusters [6]. Also, La_2O_3 is more abundant (25–38 wt.%) in the main rare earth mineral of bastnasite compared to yttria (only ~0.2 wt. %) [7].

A few studies on doping molybdenum wire with La_2O_3 [8,9] have been carried out. It has been reported that the addition of La_2O_3 to molybdenum-based alloys leads to higher ultimate tensile strength compared to that of yttria [8-10]. In this study, 0.5 wt.% La_2O_3 is

added to the elemental powder mixture of Fe–14Cr–1Ti–0.3Mo (named as 14LMT hereafter) and mechanically alloyed via high energy ball milling. The model alloy developed in this study represents a variant of yttria bearing MA957 alloy. The goal of the present study is to focus on understanding the microstructural and morphological evolution of 14LMT powder during ball milling, which is expected to serve as the basis for understanding the effect of ball milling parameters on the properties of consolidated 14LMT powders in future studies.

2.2. Experimental

Elemental powders of Fe, Cr, Ti, Mo and La_2O_3 with purity of 99.99% were procured from American Elements Inc. The elemental powder mixture was poured in vials in argon atmosphere glove box and then mechanical alloying was performed in a SPEX 8000M high energy ball mill with a speed of 1725 rpm. The ball to powder ratio (BPR) was 10:1. Mechanical alloying experiments were carried out for 2, 5, 10, 15 and 20 h.

X-ray diffraction (XRD) of the ball milled powders were performed using a Siemens 5000D diffractometer with Cu $K\alpha$ radiation (wavelength = 0.154439 nm). Modifications such as adaptive smooth, $k\alpha_2$ Rachinger and background correction by Sonnerveld method were applied to XRD patterns using Powder–X software [11]. Lattice parameter was calculated based on Nelson – Riley relation [12] and the crystallite size and lattice strain were calculated by applying Williamson – Hall (W – H) formula [13].

Microhardness measurements were carried out on the milled powders mounted in phenolic resin (polished down to a 0.05 μm diamond finish) using a Leco LM100 Vickers microhardness tester at a load of 50 g_f (~0.5 N).

Microstructure of the milled powders was examined using a Zeiss Supra Field Emission SEM and a Tecnai TF30 FEG – STEM. Energy dispersive spectroscopy (EDS) experiments were carried out in the STEM. Local electrode atom probe (LEAP) experiments were performed using CAMECA Instruments LEAP 4000X HR using voltage pulsing (20% pulse fraction) at a specimen temperature of 50 K. Focused ion beam (FIB) – SEM was used to prepare TEM and LEAP specimens investigated in this study.

2.3. Results and discussion

XRD patterns of 14LMT powder ball milled for different hours are illustrated in Fig. 2.1. In the XRD pattern of the un-milled powder, Fe and Cr show overlapped peaks, and La_2O_3 and Ti peaks are barely observable due to their low content. The Fe–Cr peaks shift to lower diffraction angles as a result of Cr dissolution in the Fe matrix, and the intensity of both La_2O_3 and titanium peaks decreases and disappears completely after 5 h of milling due to their incorporation into the Fe matrix. Significant α(Fe–Cr) peak broadening was observed up to 5 h of milling and did not change with further milling. Table 2.1 summarizes relevant microstructural quantities and microhardness values of 14LMT powder for various milling times.

Significant lattice expansion and higher density of defects due to milling are the evidence of incorporation of alloying elements into the Fe matrix. The lattice parameter increased from 0.2864 to 0.2879 nm and the crystallite size was as low as 24 nm after 10 h of ball milling. Hardness of ~ 970 HV obtained after 10 h of ball milling is found to be similar to that of gas atomized 14WT (Fe–14Cr–3W–0.4Ti) powder after adding $0.25Y_2O_3$ and 8 h of ball milling in a SPEX mill [14]. Hall – Petch strengthening due to nanocrystallite size, work hardening, increasing lattice strain and solid solution strengthening and formation

of highly stable nanoclusters, all contribute to the high hardness obtained in the mechanically alloyed powder [15].

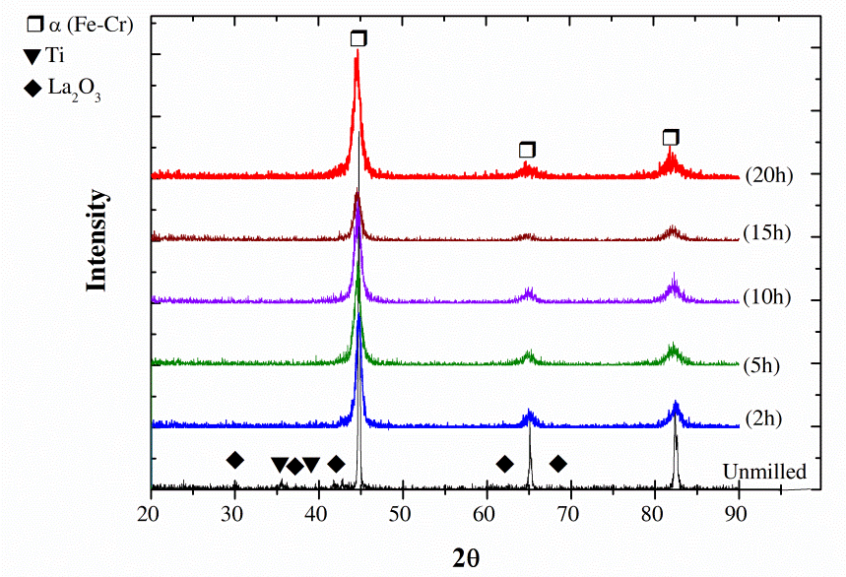

Figure 2.1. XRD patterns of ball milled 14LMT powders as a function of milling time

Table 2.1. Summary of microstructural characteristics and microhardness values of ball milled 14LMT powders as a function of milling time

Milling Time (h)	Lattice Parameter (nm)	Crystallite Size (nm)	Lattice Strain (%)	Microhardness (HV)	Particle Size (μm)
0	0.2864±0.0003	388±13	0.10±0.02	330±24	14.1±1.1
2	0.2870±0.0002	150±12	0.50±0.04	591±12	16.6±1.5
5	0.2878±0.0003	76±9	0.66±0.03	851±10	26±2.1
10	0.2881±0.0001	24±8	0.77±0.04	970±20	5.5±1.1
15	0.2881±0.0002	18±5	0.82±0.02	1011±12	7.5±1.2
20	0.2880±0.0002	14±3	0.79±0.02	929±20	24.1±2

The high energy SPEX mill was highly effective in reducing the crystallite size of the powder to the nanometric range and introduced a significant amount of lattice strain in the powder particles due to severe plastic deformation. At the early stages of ball milling, a broad range of powder particle sizes developed; a fraction of which were larger than the starting particles. With continued deformation via high energy ball milling up to 10 h,

accumulating severe plastic deformation caused work hardening in the powder particles, and consequently particle fracture started occurring mainly by a fatigue failure mechanism as well as fragmentation of brittle flakes [16]. Beyond 10 h of milling, the particle size increases again due to cold welding of powder particles in order to decrease the overall surface energy of the many fine powder particles. For this reason, powder mechanically milled for 10 h was deemed as optimum and characterized further.

Figure 2.2(a–b) shows a bright field TEM image and corresponding selected area diffraction (SAD) pattern of the milled (10 h) powder, respectively. The general microstructure shows a uniform distribution of nanograins (average grain size of ~ 22 nm). A high dislocation density is observed as a result of severely deformed crystallites. All the rings in the SAD pattern are from the ferritic matrix phase and no diffraction from the other elements was observed. The ring diffraction pattern with features shows the evidence of a polycrystalline microstructure with randomly oriented fine grains. Both equiaxed and slightly elongated grain morphology are observed in different regions of the microstructure, which is plausibly due to the very nature of local milling conditions that were not uniform throughout the whole volume of the material.

Figure 2.2(c) shows a high resolution TEM (HRTEM) micrograph of the as milled powder. Two particles named A and B of about 10 nm in diameter were found to be composed of mainly Fe–Cr oxide that has formed during the milling process while picking up excess oxygen. In Fig. 2.2(c) several number of 2–5 nm scale features are evident and marked by white arrows. The observed poor contrast of nanoscale features is the result of under focusing to make them distinguishable from the matrix.

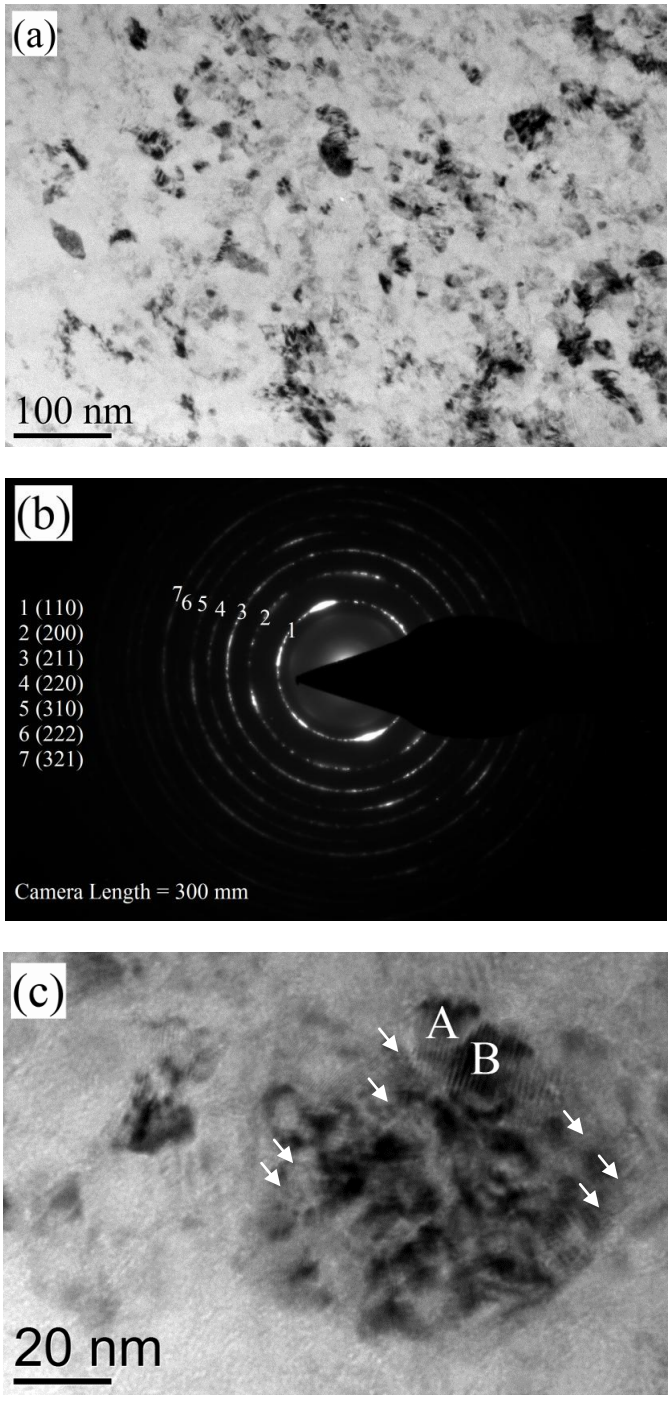

Figure 2.2. (a) A bright field TEM micrograph of ball milled 14LMT powder, (b) a diffraction pattern of ball milled 14LMT powder, and (c) a HRTEM image of nanoscale features

These nanoscale features are extremely difficult to detect by EDS due to the influence of the matrix. Hence, EDS line scan experiment was performed across a 100 nm line in the matrix containing several features with different contrasts in the STEM mode, as discussed later. The STEM mode image of a FIBed powder is shown in Fig. 2.3(a). There are not many significantly different contrasts observed implying a reasonably homogeneous distribution of solute elements after 10 h of milling; however, there are some features with brighter contrast that are enriched with more Fe based on EDS results. No large oxide particles were observed; however, some nanoscale oxide particles were found. Furthermore, the FIBed powder does not have exactly equal thickness throughout the sample, which should be taken into account while explaining the observations. Overall the HRTEM and STEM results are found to be largely complementary. Figure 2.3(b) shows concentration in atom% for Cr, Ti, Mo and La along a 100 nm EDS line scan. It can be noted that some regions within the line scan show significantly increased Cr concentration while Ti presents a marked decrease, suggesting presence of Cr oxide. Some regions with the opposite behavior indicate the presence of Ti oxide. There are some regions where both Cr and Ti are present in higher amounts. In Fig. 2.3(b), along a 2 nm-length scan (contrast feature #1 in Fig. 2.3(a)) the concentration of La increases whereas those of Ti and Cr decrease. This indicates the presence of a La containing oxide nanofeatures with more Cr and Ti at those nanofeatures. For second brighter contrast feature (#2 in Fig. 2.3(a)), the concentrations of Cr, Ti and La increase from the matrix to the nanofeatures. It is plausible that the addition of Ti changes the chemical equilibrium from the formation of Cr oxides towards that of Ti oxides because of a greater affinity of Ti for O [17]. From the knowledge of respective phase diagrams, Cr, Mo and Ti can be easily incorporated into the ferritic solid solution

during mechanical alloying. However, Fe and La_2O_3 are immiscible [5]. Thus, a practical approach to incorporating La_2O_3 into the ferritic matrix is via high energy ball milling. High energy ball milling results in severe plastic deformation and fatigue / fragmentation of fine powders by energetic impacts during milling process.

Two ways can be envisioned for La_2O_3 incorporation. One possibility is that La_2O_3 is taken up in the metal powders as highly refined oxides, and the other possibility is that La_2O_3 is mechanically dissolved in the matrix due to fragmentation and severe plastic deformation [14]. Dissolution of La_2O_3 can be explained by powder particle crushing to very small (nanometric) size and the formation of new grain boundaries during severe plastic deformation [18].

Figure 2.4(a–b) shows atom maps of La, O, Ti and TiO of the milled powder and 1-D concentration profile along the direction of analysis, respectively. It can be noted that Ti is found more as Ti oxide due to its high oxygen affinity. It can also be understood that nanoclusters with diameters of 2–5 nm with complex interfaces are found in the as milled powder and are enriched with O–, La– and TiO–. These nanoclusters are expected to have significantly increased the hardness of the as milled powder.

Nucleation of stable oxygen enriched clusters in the as milled Fe has been suggested by Fu *et al.* [19]. According to the mechanism proposed by them, the binding of O to Fe is rather weak compared to C and N such that O has a relatively stronger affinity for vacancies. It is likely that during the milling process a high concentration of lattice vacancies is produced, and Ti and La alloying elements in the ferritic matrix bind strongly with oxygen – vacancy complexes. Free energy of formation for La–, Ti–, and O-rich

nanoclusters can become lower than that of the stable oxide phases since both Ti and La can form strong bonds with oxygen – vacancy pairs.

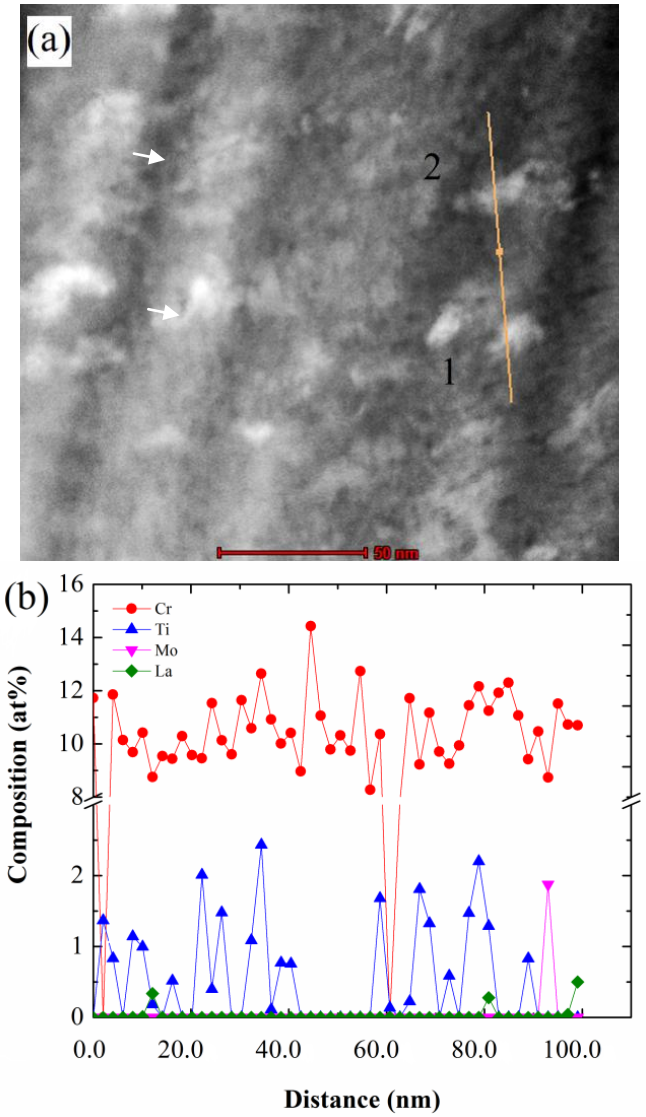

Figure 2.3. (a) A STEM image of milled 14LMT powder, and (b) EDS line scan concentration profile for Cr, Ti, Mo and La

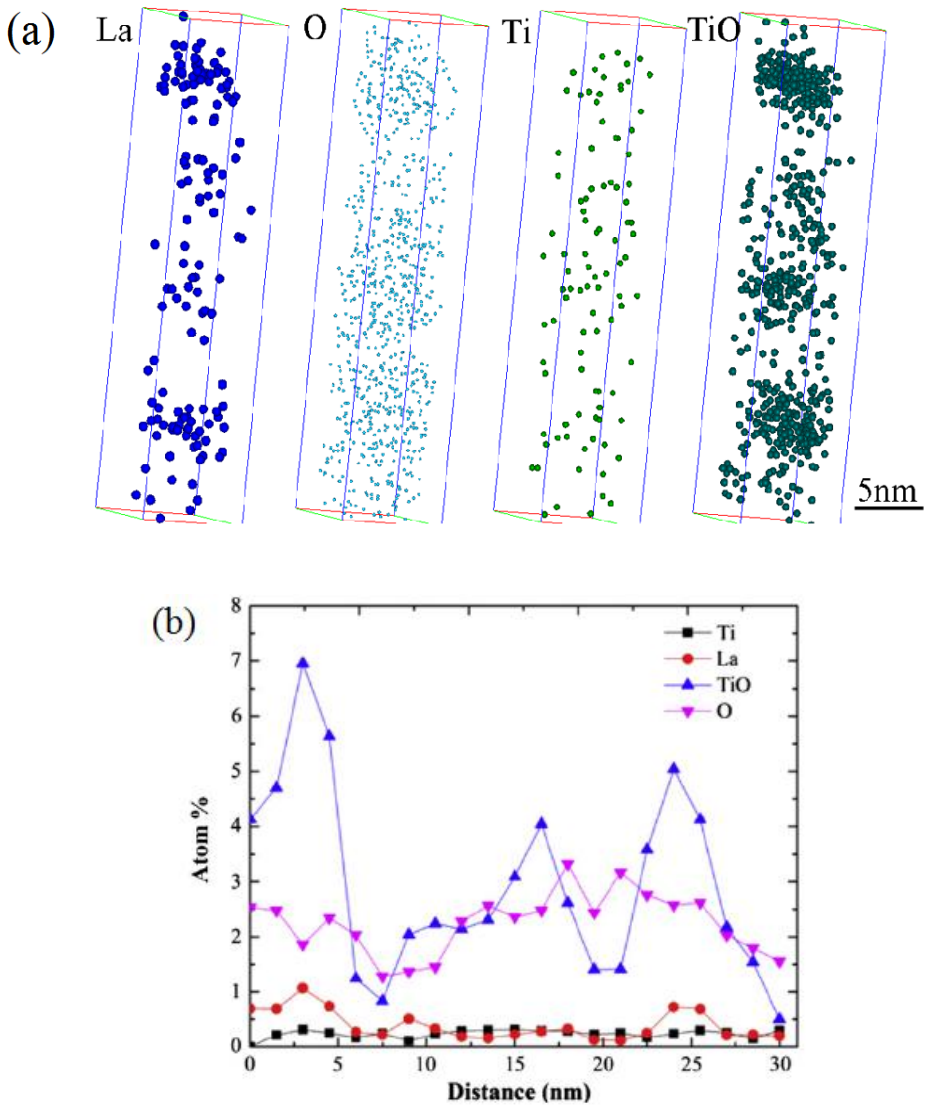

Figure 2.4. (a) Atom probe maps of La, O, Ti and TiO in ball milled 14LMT powder, and (b) 1-D concentration (atom%) profile along the direction of analysis

2.4. Conclusions

Mechanical alloying of high chromium steel with La_2O_3 (14LMT) was carried out by high energy ball milling of elemental powders for different milling times. Microstructural, morphological and mechanical characteristics of powders were investigated in order to determine the optimum milling time. After 10 h of milling, the crystallite size was reduced to 24 nm and a reasonably uniform distribution of solute elements was achieved. TEM and

LEAP studies showed that in the ferritic solid solution matrix there exist features of 2–5 nm diameters, which are complex nanoclusters of TiO–, La– and O formed during the milling process.

Acknowledgments

This work was supported partly by the Laboratory Directed Research and Development Program of Idaho National Laboratory, Contract DE–AC07–05ID14517, and partly by a grant of the Advanced Test Reactor National Scientific User Facility (ATRNSUF). We would also like to acknowledge the help of Yaqiao Wu and Jatuporn Burns for experimental assistance.

References

[1] P. Pareige, M.K. Miller, R.E. Stoller, D.T. Hoelzer, E. Cadel, B.P. Radiguet, Stability of nanometer-sized oxide clusters in mechanically-alloyed steel under ion-induced displacement cascade damage conditions, J. Nucl. Mater. 360 (2007) 136–142.

[2] G.R. Odette, M.J. Alinger, B.D. Wirth, Recent developments in irradiation-resistant steels, Annu. Rev. Mater. Res. 38 (2008) 471–503.

[3] M.J. Alinger, G.R. Odette, D.T. Hoelzer, The development and stability of Y–Ti–O nanoclusters in mechanically alloyed Fe–Cr based ferritic alloys, J. Nucl. Mater. 329–333 (2004) 382–386.

[4] K. Yutani, H. Kishimoto, R. Kasada, A. Kimura, Evaluation of helium effects on swelling behavior of oxide dispersion strengthened ferritic steels under ion irradiation, J. Nucl. Mater. 367–370 (2007) 423–427.

[5] ASM handbook, Vol. 3, ASM International, Materials Park, Ohio, 1992.

[6] Z. D. Reed, M. A. Duncan, Photodissociation of yttrium and lanthanum oxide cluster cations, J. Phys. Chem. A. 112 (2008) 5354–5362.

[7] http://www.molycorp.com

[8] M. Endo. K. Kimura, T. Udagawa, S. Tanabe, S. Hiroyuki, Effects of doping molybdenum wire with rare earth elements, High Temperatures–High Pressures, 22 (1990) 129−137.

[9] D. Poerschike, Mechanical properties of oxide dispersion strengthened molybdenum alloys, Master thesis, Case Western Reserve University, 2009.

[10] J. Cho, M. Harmer, H. Chan, J. Rickman, A.M. Thompson, Effect of yttrium and lanthanum on the tensile creep behavior of aluminum oxide, J. Am. Ceram. Soc. 80 (1997) 1013–1017.

[11] C. Dong, PowderX: Windows 95-based program for powder X-ray diffraction data processing, J. Appl. Cryst. 32 (1999) 838.

[12] J.B. Nelson, D.P. Riley, An experimental investigation of extrapolation methods in the derivation of accurate unit cell dimensions of crystals, Proc. Phys. Soc. 57(1945) 160–177.

[13] G.K. Williamson, W.H. Hall, X-ray line broadening from filed aluminium and wolfram, Acta Metall. 1 (1953) 22–31.

[14] Z. Guojun, Z. Yi, L. Bin, W. Ruihong, L. Gang, S. Jun, Microstructure and mechanical properties of molybdenum alloy strengthened by lanthanum oxide and silicon, Key Eng. Mater. 479 (2011) 22–26.

[15] M.J. Alinger, G.R. Odette, D.T. Hoelzer, On the role of alloy composition and processing parameters in nanocluster formation and dispersion strengthening in nanostructured ferritic alloys, Acta Mater. 57 (2009) 392–406.

[16] C. Suryanarayana, Mechanical alloying and milling, Prog. Mater. Sci. 46 (2001) 1–184.

[17] P. He, M. Klimenkov, R. Lindau, A. Möslang, Characterization of precipitates in nano structured 14% Cr ODS alloys for fusion application, J. Nucl. Mater. 428 (2012) 131–138.

[18] Y. Kimura, S. Takaki, S. Suejima, R. Uemori, H. Tamehiro, Ultra grain refining and decomposition of oxide during super heavy deformation in oxide dispersion ferritic steel power, ISIJ Int. 39 (1999) 176–182.

[19] C. L. Fu, M. Kremar, G. S. Painter, X. Q. Chen, Vacancy mechanism of high oxygen solubility and nucleation of stable oxygen-enriched clusters in Fe, 99 (2007) 2255021–4.

CHAPTER 3: Mechanical Alloying of Lanthana-Bearing Nanostructured Ferritic Steels

Somayeh Pasebani [a,d], *Indrajit Charit* [a,d], *Yaqiao Wu* [b,d], *Darryl P. Butt* [b,d]

and James I. Cole [c,d]

[a] Department of Chemical and Materials Engineering, University of Idaho, Moscow, ID 83844, USA

[b] Department of Materials Science and Engineering, Boise State University, Boise, ID 83725, USA

[c] Idaho National Laboratory, Idaho Falls, ID 83401, USA

[d] Center for Advanced Energy Studies, Idaho Falls, ID 83401, USA

(*Published in the Journal of Acta Materialia, Volume 61 (2013) pages 5605–5617*)

Abstract

A novel nanostructured ferritic steel powder with a nominal composition of Fe–14Cr–1Ti–0.3Mo–0.5La_2O_3 (wt.%) was developed via high energy ball milling. La_2O_3 was added in this alloy instead of traditionally used Y_2O_3. The effects of varying ball milling parameters such as milling time, steel ball size and ball to powder ratio on the mechanical properties and microstructural characteristics of the as-milled powder were investigated. Nanocrystallites of a body centered cubic ferritic solid solution matrix with a mean size of approximately 20 nm were observed by transmission electron microscopy. Nanoscale characterization of the as-milled powder by local electrode atom probe tomography revealed formation of Cr–Ti–La–O-enriched nanoclusters during mechanical alloying. The Cr:Ti:La:O ratio is considered “non-stoichiometric”. The average size (radius) of the nanoclusters was about 1 nm, with number density of 3.7×10^{24} m^{-3}. The mechanism for

formation of nanoclusters in the as-milled powder is discussed. La_2O_3 appears to be a promising alternative rare earth oxide for future nanostructured ferritic steels.

Keywords: Mechanical alloying; Nanostructured ferritic steels; Oxide dispersion strengthened steels; Lanthanum oxide

3.1. Introduction

Nanostructured Ferritic Steels (NFSs) with 12–14 wt.% Cr have attracted significant interest for potential high temperature structural and fuel cladding applications in advanced nuclear reactors. These steels are a sub-class of oxide dispersion strengthened (ODS) alloys and attractive because of their excellent high temperature mechanical properties and high resistance to irradiation-induced damage.

The properties of the NFSs depend on the composition that mainly consists of Cr, Ti, W or Mo, and Y_2O_3 as alloying constituents. An ultra high number density (10^{24} m^{-3}) of Y–Ti–O-enriched nanofeatures (NFs) with 2–5 nm diameter along with ultrafine grains and high dislocation densities lead to high tensile, creep and fatigue strength [1-4].

Furthermore, understanding of the exact formation sequence of these Y–Ti–O-enriched nanoclusters (NCs) is still evolving. The prevailing hypothesis in the published literature is that high energy ball milling creates a homogenized, highly alloyed ferritic solid solution, and the formation of these Y–Ti–O-enriched NCs only takes place afterwards during the hot consolidation process (e.g., hot extrusion, hot isostatic pressing (HIP), or hot rolling).

However, Brocq *et al.* [5] processed Fe–14Cr–2W–1Ti–0.8Y–0.2O (wt.%) ODS steel by reactive-inspired ball milling with Fe–Cr–W–Ti, YFe_3 and Fe_2O_3 followed by annealing at

800^{o}C for 5 min. They observed a dense dispersion of nanoclusters enriched in titanium, yttrium and oxygen with an average radius of about 1 nm by APT in the as-milled ODS steel and concluded that ball milling initiated the NC nucleation that will be enhanced by annealing.

A comprehensive characterization of the milled powder with a composition of Fe–14Cr–2W–0.3Ti–0.3Y_2O_3 (wt.%) by APT and TEM was performed by Williams *et al.* [6]. In that work, the formation of Y–Ti–Cr–O nanoparticles was observed during the MA, and the initially formed particles maintained a similar ratio of Cr:Ti:Y:O during the processing.

In this study, an alternative rare earth (RE) oxide was dispersed in the ferritic matrix instead of traditionally used Y_2O_3. Lanthanum oxide (La_2O_3) has no solubility in iron at all temperatures under normal conditions [7], and has a high affinity for oxygen to form the La–O bond [8]. Based on the density functional theory calculations by Reed and Duncan [8], lanthanum oxide clusters have the same general structure as the corresponding yttrium species; however, the bond distances are generally larger. These structures presumably maximize the number of strong RE–O bonds. Interestingly, the bond energies for the yttrium oxide clusters are generally close but lower than those for the lanthanum oxide clusters, especially in smaller clusters.

Furthermore, La_2O_3 is more abundant (25–38 wt.%) in one of the main US RE minerals (Bastnasite) compared to yttria (only 0.2 wt.%) (http://www.molycorp.com) [9]. Hence, this study is driven not only by mere scientific curiosity but also strategic importance. Even though there is no published report on La_2O_3 containing NFSs except the preliminary study published by the authors [10], Endo *et al.* [11] studied the mechanical and microstructural

characteristics of molybdenum (bcc) alloys doped with various RE oxides such as Y_2O_3, La_2O_3, Nd_2O_3, Sm_2O_3, and Gd_2O_3. Creep behavior was determined using high temperature sag tests, which showed that La_2O_3 provided the highest strength and creep resistance to the molybdenum matrix. Mueller *et al.* [12] investigated the oxide dispersion strengthening effect of La_2O_3, Y_2O_3 and ZrO_2 in molybdenum and found that La_2O_3 doping produced the highest ultimate tensile strength (UTS) and significantly higher creep rupture properties than the other doping oxides. Thus, an alloy with a nominal composition of Fe–14Cr–1Ti–0.3Mo–0.5La_2O_3 (wt.%), named 14LMT has been developed using mechanical alloying (MA) of the constituent powders.

The presence of chromium in NFSs greatly improves the corrosion resistance by forming a thin, protective oxide film. Chromium also stabilizes the ferritic (bcc) structure of the matrix even at elevated temperatures. Titanium and molybdenum are added in small quantities to improve the ductility and oxidation resistance, and impart solid solution strengthening in the ferritic matrix. Furthermore, Ti and Mo are believed to trap the carbon and nitrogen atoms present in the matrix, and prevent the formation of chromium carbides or nitrides, and thereby prevent possible grain boundary embrittlement. Titanium is also known to play an important role in stabilizing complex RE–Ti–O-enriched nanofeatures [3].

Detailed microstructural characteristics of the as-milled powder of 14LMT composition, as a function of various MA variables, such as milling time, steel ball size, and ball to powder ratio (BPR), were carried out in this study. A combination of microstructural characterization tools and hardness measurements were used to obtain the optimum milling parameters amenable for later powder consolidation.

3.2. Experimental procedure

3.2.1. Starting powder source

The starting constituent powders including Fe (99.9 wt.% Fe, average particle size of 40 μm), Cr (99.8 wt.%, average particle size of 5 μm), Ti (99.7 wt.% Ti, average particle size of 26 μm) and La_2O_3 (99.99 wt.% La_2O_3, average particle size of 40 nm) were procured from the American Elements Inc., and Mo (99.9 wt.% Mo, average particle size of 1–2 μm) powder was acquired from the Micron Metal Powder Inc.

3.2.2. High energy ball milling

The elemental powders were mixed in the nominal proportion of Fe–14Cr–1Ti–0.3Mo–0.5La_2O_3 (wt.%), referred to as 14LMT hereafter. The powder blend was poured into a hardened steel milling vial inside a glove box operated under a high purity argon atmosphere. Thompson 52100 chrome steel balls (with a composition of Fe–1.0C–0.35Mn–0.25Si–1.5Cr–0.1Mo–0.35Cu, wt.%) of different dimensions were used in this study. The powder mass in each milling batch was 10 g due to limited capacity of the milling vial, and no process control agent was used during the milling process.

High energy ball milling was performed in an air-cooled SPEX 8000M high energy ball mill at the speed of 1725 rpm with lateral movements. The vial was vibrated with amplitude of 50 mm and frequency of 20 Hz during milling. Milling was carried out for 2, 5, 10, 15 and 20 h using a ball to powder ratio (BPR) of 10:1 and steel ball diameter of 8 mm. The BPR is defined as the mass ratio of the milling media (e.g. steel balls) to the powder. Two different steel ball size configurations, one with steel balls with 5 mm diameter and another with a combination of 5 mm (25 wt.%) and 8 mm (75 wt.%) diameter steel balls, were also

used while the BPR and milling time were 10:1 and 10 h, respectively. In order to investigate the effect of BPR on the characteristics of the as-milled powder, three different BPRs, 5:1, 10:1 and 15:1, were used with a milling time and steel ball diameter were 10 h and 8 mm.

3.2.3. Microstructural characterization

X-ray diffraction (XRD) of the as-milled powders was performed using a Siemens 5000D diffractometer with Cu K_{α} radiation (wavelength of 0.15406 nm). Modifications such as $K_{\alpha 2}$ Rachinger and background correction by Sonnerveld were applied to XRD patterns using the Powder–X software [13]. Lattice parameters were calculated based on the Nelson-Riley extrapolation [14]. The crystallite size and lattice strain were calculated by the Williamson – Hall (W – H) formula [15].

The morphology and size distribution of the as-milled powder were analyzed using a Zeiss Supra 35 field emission gun scanning electron microscope (FEG–SEM). A focused ion beam (FIB) was used to prepare specimens from the as-milled powder for both transmission electron microscopy (TEM) and atom probe tomography (APT) studies. The FIB effort was carried out using a Quanta 3D FEG instrument with a Ga-ion source. TEM studies along with energy dispersive spectroscopy (EDS) were performed using a Tecnai TF30–FEG STEM operating at 300 kV.

The APT analysis carried out using an Imago LEAP 4000X HR operating in voltage mode at the specimen temperature of 50–60 K and 20% of the standing voltage pulse fraction. The atom maps were reconstructed using CAMECA IVAS 3.6 software. The maximum separation cluster algorithm was used to identify the composition of the NCs.

The maximum separation between solute atoms is defined as d_{max} whereas L is the maximum separation of additional elements, N_{min} is the minimum size of a cluster (in terms of solute atoms that constitute a significant cluster) and E is the erosion distance for removal of atoms near the cluster matrix interface [16]. A N_{min} value of 5, d_{max} of 0.5–0.7 nm, L of 0.4–0.5 nm and E of 0.2–0.4 nm were chosen based on the procedure explained in the relevant literature [6,16-19].

The size of NCs was estimated from the radius of gyration (R_g) that is the average distance between each cluster atom and the center of mass of the cluster [20-21]. This was applied to the APT datasets each containing 20–30 M ions in this study. The extent of clustering of each individual ion type was investigated where Ti–O, Cr–O and La showed clustering according to χ^2 values [22]. The contribution of matrix was removed and artificially set to zero in this work using a method outlined in Ref. [6] to estimate other matrix elements (Cr, Mo, Ti and La). The calculated composition of the clusters by not assessing matrix contribution was quoted as "matrix corrected" introduced by Williams *et al.* [6, 22].

3.2.4. Hardness testing

Microhardness measurements were carried out on the as-milled powders mounted in phenolic resin (polished to a 0.05 μm diamond finish) using a Leco LM100 Vickers microhardness machine. A load of 50 g_f (0.5 N) was applied over a period of 15 s. The microhardness tester was calibrated against the low load using a standard steel specimen with a known hardness.

3.3. Results and discussion

3.3.1. Effect of milling time

A SEM micrograph in Fig. 3.1 shows the variation in morphology and size of the blended (unmillled) and as-milled powder batches for different milling times (2–20 h). The particles of the blended powder (Fig. 3.1(a)) were mainly non-spherical with variable sizes. Figure 3.1(b) shows the surface of some blended powder particles uniformly covered by nanoparticles of La_2O_3 based on the EDS results. At the early stages of ball milling, the matrix powder particles were soft, and their tendency to weld together and forming large particles was high. As the powder particles were becoming flat and cold welded together the brittle particles of the La_2O_3 were trapped between lamella of the ductile Fe particles. A broad range of powder sizes developed with some larger than the starting powder particles as shown in Fig. 3.1(c). The morphology of the 5 h as-milled powder in Fig. 3.1(d) exhibited mostly large agglomerated powder particles with irregular shapes, and several cracks started to appear on their surfaces. It is suggested that agglomeration started to occur at the early stage of ball milling (0–2 h), and after that, it was superseded by fracture and fragmentation. Beyond 5 h due to the continued impact of the milling balls, the structure of the powder particles was steadily refined and the powder size continued to decrease in the absence of strong agglomerating forces. After 10 h, the particle shapes became more spherical and the particle size distribution was more uniform. Accumulation of severe plastic deformation caused a great amount of work hardening in the particles, and consequently, particle fracture occurred because of fatigue and fragmentation of the brittle flakes [23]. The average particle size of the agglomerated powder was 5.5 μm (Fig. 3.1(e)); however, the size of the individual powder particles was 200 nm (Fig. 3.1(f)). The smaller powder particle size is an

advantage during hot consolidation as the larger surface to volume ratio generally improves the densification. With further milling (15 and 20 h), the powder particle size increased due to cold welding, as shown in Figs. 3.1(g–h).

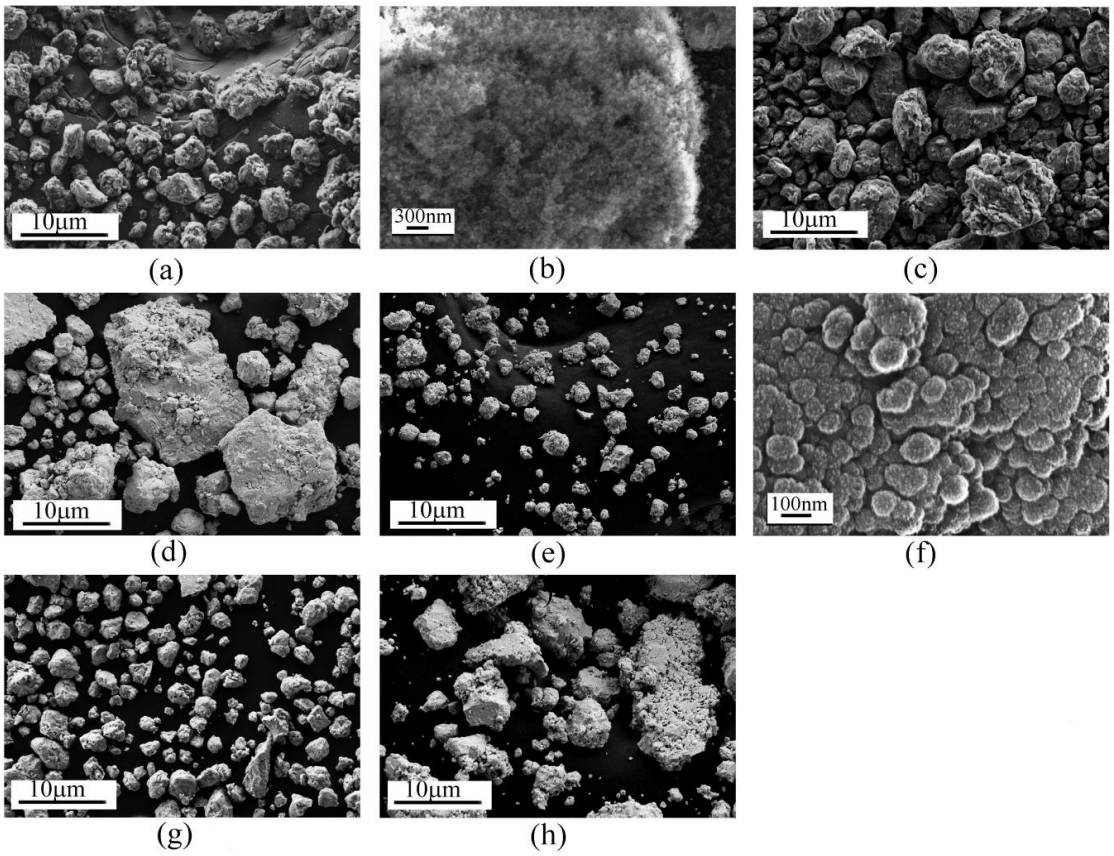

Figure 3. 1. SEM micrographs of 14LMT alloy: (a) blended powder under low magnification showing particle morphology, (b) at higher magnification showing La_2O_3 nanopowder particles cover the particles surface; milled powder morphology for (c) 2 h, (d) 5 h, (e) 10 h, (f) 10 h at higher magnifications, (g) 15 h, and (h) 20 h

The XRD patterns of the as-milled 14LMT alloy, milled for 2–20 h are shown in Fig. 3.2(a). A BPR of 10:1 and steel ball diameter of 8 mm were used for ball milling of these powder batches. In the XRD pattern of the blended powder, Fe and Cr show overlapped peaks, while the peaks of elements such as Mo, Ti and La_2O_3 were barely

observable due to their relatively low concentrations. After 2 h of milling, the Fe–Cr peaks shifted to lower diffraction angles as a result of increasing lattice parameter and dissolution of Cr in the Fe, forming Fe–Cr as the matrix. The Fe–Cr peaks started exhibiting significant broadening and a decrease in intensity after 2 h of milling. Table 3.1 summarizes the microstructural characteristics and microhardness values of the as-milled 14LMT alloy as a function of milling time. The lattice parameters of the bcc Fe–Cr matrix increased with increasing milling time up to 10 h. Significant lattice expansion and complete disappearance of peaks pertaining to alloying constituents Ti, Mo and La_2O_3 after 10 h of milling were associated with their incorporation into the matrix. Beyond 10 h milling time, the lattice parameter did not show any significant change, because solid solutionizing effect reached a saturation level. Similar observations have been made in yttria containing NFSs [24]. The peak broadening effect as shown in Fig. 3.2(a) can be attributed to the progressive reduction in crystallite size (i.e. grain refinement) and increase in lattice strain arising from crystal imperfections and severe plastic deformation caused by high energy ball milling.

As the milling time increased, the average crystallite size decreased from 380 nm in the blended powder to 24 nm after 10 h of milling, and thereafter slightly decreased with further milling. The high energy SPEX mill was found to be effective in reducing the crystallite size of the powder down to the nanoscale range while introducing a significant amount of lattice strain. It was noted that milling for 10 h was enough to reach a mean crystallite size of 24 nm and saturation of the lattice strain. Further milling decreased the crystallite size, but it led to an increase in the powder size as evident in the powder size of 15 h and 20 h as-milled batches.

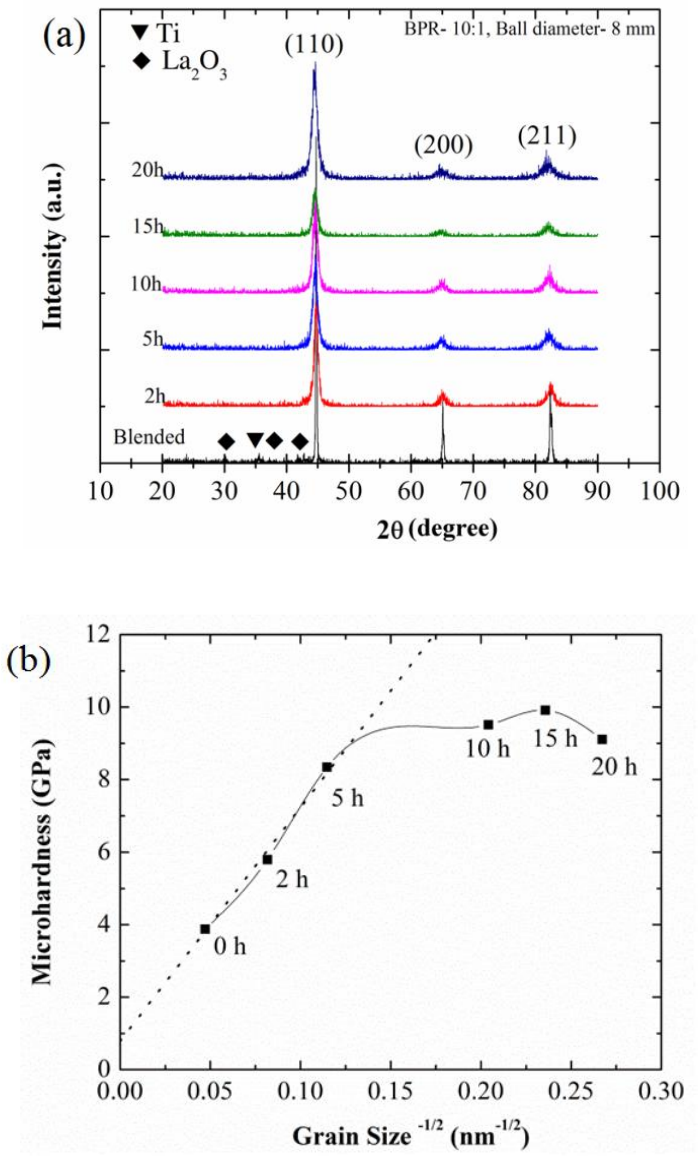

Figuer 3.2. (a) XRD patterns of the 14LMT alloy as a function of milling time, and (b) Hall–Petch behavior in the as-milled 14LMT alloy

Table 3.1. Summary of microstructural characteristics and microhardness of 14LMT powder batches as a function of milling time

Milling Time (h)	Lattice Parameter (nm)	Crystallite Size (nm)	Lattice Strain (%)	Microhardness (HV)	Mean Particle Size (μm)
0	0.2864±0.0003	388±13	0.10±0.02	330±24	14.1±1.1
2	0.2870±0.0002	150±12	0.50±0.04	591±12	16.6±1.5
5	0.2878±0.0003	76±9	0.66±0.03	851±10	26 ±2.1
10	0.2881±0.0001	24±8	0.77±0.04	970±20	5.5±1.1
15	0.2881±0.0002	18±5	0.82±0.02	1011±12	7.5±1.2
20	0.2880±0.0002	14±3	0.79±0.02	929±20	24.1±1.8

The microhardness of the blended powder (no milling) was 330 HV. However, with decreasing crystallite size and increasing lattice strain, the microhardness values increased due to significant amount of plastic deformation and work hardening, high density of dislocations and other crystal imperfections. After 10 h of milling, the microhardness of the as-milled powder was 970 HV that was roughly equivalent to a uniaxial strength level of 3000 MPa. Alinger *et al.* [24] reported the microhardness of the gas atomized 14WT (Fe–14Cr–3W–0.4Ti, wt.%) powder to be 1000 HV after adding 0.25 wt.% Y_2O_3 and 8 h of ball milling in a SPEX mill. The Hall – Petch strengthening due to grain refinement, strain hardening due to high dislocation density, solid solution strengthening and possibly formation of nanosized La–Ti–O-enriched clusters (as discussed later) all may contribute to the very high hardness obtained in the mechanically alloyed 14LMT powder just after 10 h of milling. The microhardness increased slightly after 15 h and leveled off thereafter due to saturation in dislocation density and crystallite refinement. A negative Hall – Petch slope at small grain sizes (10 h and beyond) has been observed in the case of the 14LMT alloy produced by the MA as shown in Fig. 3.2(b). The literature explanation of a negative Hall – Petch slope generally depends on the phenomena of Coble creep or grain boundary sliding [25].

Since 14LMT was a complex alloy system, studying solubility of each alloying element in bcc Fe lattice was not easy considering the small amounts of alloying constituents of Ti, Mo and La_2O_3. Therefore, in an experiment as a check confirmation of dissolution of low concentration elements, 14 wt.% Cr, 1–5 wt.% Ti, 0.3–5 wt.% Mo and 0.5–5 wt.% La_2O_3 were separately added to Fe and then ball milled for 10 h under the same other milling

conditions described before. This was done to confirm that 10 h ball milling time was optimum for dissolution of all the alloying constituents in the ferritic matrix.

The XRD patterns of blended and as-milled Fe–14Cr, Fe–5Ti, and Fe–5La_2O_3 are illustrated in Fig. 3.3. After milling for 10 h, the diffraction peaks of Cr, Ti, Mo and La_2O_3 completely disappeared and only broadened peaks of the bcc Fe-based matrix phase were observed.

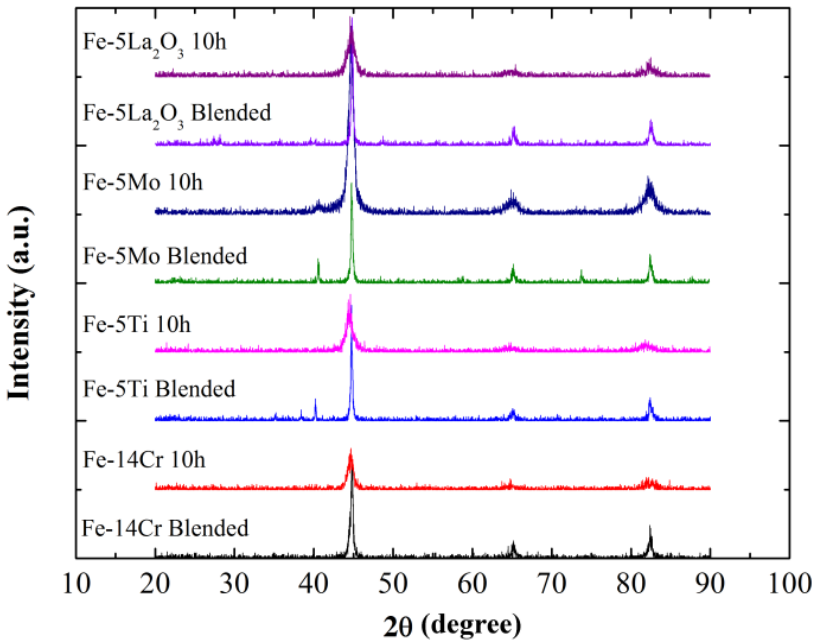

Figuer 3.3. XRD patterns for Fe–14Cr, Fe–5Ti, Fe–5Mo and Fe–5La_2O_3 (wt.%) before and after milling for 10 h

Disappearance of Ti and Mo peaks is due to dissolution of these elements into the ferritic (bcc) matrix. However, considering the starting powder size of La_2O_3 (40 nm) and its immiscibility with the Fe matrix, the disappearance of La_2O_3 peaks could be due to two possible phenomena: (1) La_2O_3 is decomposed to O and La dissolving into the ferritic matrix

and is distributed homogenously forming a solid solution, (2) La_2O_3 remains as particles that become much finer due to ball milling, and therefore peaks are not observed. Whether or not La and O are dissolved in the bcc matrix lattice can be judged from an increase in the observed lattice parameter of the bcc Fe [18-19]. Experimentally determined lattice parameters of the bcc Fe lattice after adding each element and milling for 10 h are given in Table 3.2. The lattice parameter for un-milled Fe was calculated based on Fe powder annealed under vacuum at 950 ^{o}C for 2 h. The theoretical values of the lattice parameters calculated using Vegard's law [26] is also included for comparison.

Table 3.2. Theoretical and experimental lattice parameters of Fe–14Cr, Fe–1Ti, Fe–5Ti, Fe–0.3Mo, Fe–5Mo, Fe–0.5 La_2O_3 and Fe–5La_2O_3 (wt.%) after milling for 10 h

Lattice Parameter (nm)	Fe	Fe–14Cr	Fe–1Ti	Fe–5Ti	Fe–0.3Mo	Fe–5Mo	Fe–0.5La_2O_3	Fe–5La_2O_3
Theoretical (Vegard's law)	0.2870	0.2871	0.2870	0.2874	0.2870	0.2882	0.2874	0.2914
Experimental	0.2868	0.2878	0.2876	0.2888	0.2875	0.2881	0.2880	0.2882

From a knowledge of respective phase diagrams, Cr, Mo and Ti can be easily incorporated in the ferritic solid solution during mechanical alloying, but La_2O_3 in Fe is insoluble [6]. Thus, a practical approach to incorporating La_2O_3 into the ferritic matrix is via high energy ball milling. High energy ball milling resulted in severe plastic deformation and fragmentation of powders by energetic impacts during the milling process. Based on the calculated lattice parameter given in Table 3.2, decomposition of La_2O_3 (0.5 wt.%) to La and O could happen during milling. The required energy for decomposition of 0.5 wt.% La_2O_3 was calculated to be 60.40 J (ΔG = 393.6 kJ.mol^{-1}). The energy dissipation per impact was 7.2 J where the vibration frequency, milling time and the mean energy per impact were 20 Hz, 10 h and 10^{-5} J, respectively [27]. Since in this study 50 steel balls per milling batch

were used (each steel ball mass with a mass of 2 g) along with a powder mass of 10 g, a BPR of 10:1, and steel ball diameter of 8 mm, the theoretical estimate of the total energy from all of the steel balls compacting the La_2O_3 particles were 360 J that was higher than the required amount of energy. In the case of 5 wt.% La_2O_3 addition, the lattice parameter did not show any increase. The disappearance of La_2O_3 peaks in current XRD pattern is likely due to reduction in the particle size of La_2O_3, or possible operation of other suggested mechanisms such as grain boundary amorphization that needs to be verified by high resolution transmission electron microscopy (HRTEM) imaging [28].

The elemental distribution maps as obtained by EDS and given in Fig. 3.4 suggest that all the alloying elements were distributed homogenously throughout the matrix. The chemical compositions of the blended and 10 h as-milled powder are given in Table 3.3. The extra Cr content observed in the as-milled powder comes from the milling media. Because EDS does not provide a good quantitative estimate of the light elements such as C and N, a standard combustion analysis was carried out on the 10 h as-milled powder and C and N concentrations were measured to be 0.03 and 0.01wt.%, respectively. This means that no significant pick-up of C or N occurred during ball milling from the steel vial/steel balls (for C) or any entrapped air (for N) occurred during ball milling.

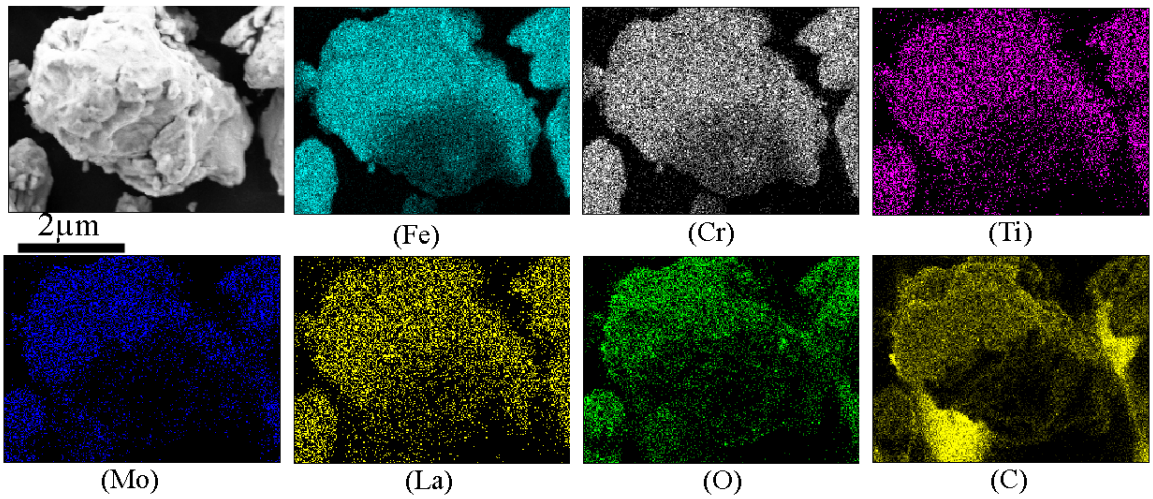

Figuer 3.4. SEM elemental distribution maps in the as-milled 14LMT alloy (10 h, BPR – 10:1, ball diameter – 8 mm)

Table 3.3 Chemical composition (wt.%) of the 14LMT alloy before milling and after milling for 10 h

Chemical composition (wt.%)	La_2O_3	Ti	Mo	Cr	Fe
Blended (nominal composition)	0.5	1.0	0.3	14	Bal.
Milled for 10 h	0.49±0.21	1.04±0.09	0.284±0.1	15.23±0.33	Bal.

3.3.2. Effect of steel ball size

The size of the steel balls (milling media) plays a certain role in the milling efficiency. The steel ball size also determines the steady state powder particle size, where smaller steel balls yield smaller powder particles. The rate of grinding (or mechanical milling) is proportional to four parameters:

(1) The total number of contact points between steel balls that is proportional to D^{-3}, where D is steel ball diameter; (2) the collision frequency of steel balls that is proportional to v/D, where v is the translational velocity speed of a steel ball at collision and the mean free path varies with D; (3) the volume of particles nipped into a contact point area for grinding that is proportional to Db^2, where b is the powder particle size and (4) the stress

acting on the particles fragmented by steel balls that is proportional to $D^2\rho\,\alpha/b$, where ρ and α are the powder density and acceleration due to collision, respectively [27].

The steel ball diameter was varied, i.e., 5 mm diameter, 8 mm diameter, and a mixture of 5 and 8 mm diameter, and the BPR and milling time were 10:1 and 10 h, respectively. Figure 3.5 shows SEM micrographs of the as-milled 14LMT alloy using steel balls with different size configurations. Table 3.4 summarizes the microstructural parameters and microhardness of the as-milled powder as a function of the milling media characteristics.

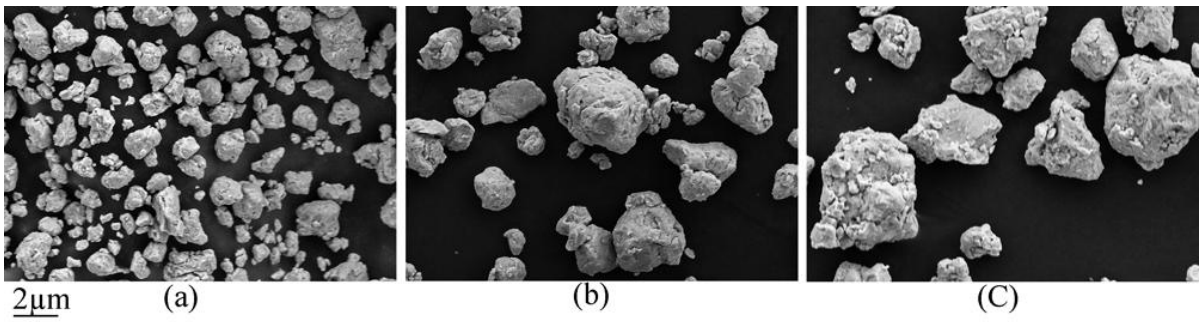

Figuer 3.5. SEM micrographs of the as-milled 14LMT alloy as a function of the steel ball size (a) 5 mm, (b) 8 mm, and (c) a mixture of 5 and 8 mm in diameter (10 h, BPR – 10:1)

Table 3.4. Summary of microstructural characteristics and microhardness values of the as-milled 14LMT powders (milling time: 10 h, BPR: 10) as a function of steel ball size

Steel ball Size (mm)	Lattice Parameter (nm)	Crystallite Size (nm)	Lattice Strain (%)	Microhardness (HV)	Mean Particle Size (µm)
5	0.2879	64±2	0.52±0.05	613±10	4.4±2.7
8	0.2881	24±8	0.77±0.04	970±20	5.5±1.1
Mixed of 5 and 8	0.2882	18±3	0.80±0.02	984±16	7.2±2.3

The lattice parameter increased, but the crystallite size decreased when larger steel balls were used. This is because smaller steel balls are less efficient in solid solutionizing and in reducing the crystallite size. This can be explained in the following reasons: (1) lower stress and the smaller amount of energy is transferred to the powder during collisions. (2) when larger steel balls are used, temperature raises, and enhances the diffusion of atoms, solid solutionizing increasing the lattice parameter [29]. Similarly, with increasing steel ball size, the microhardness values increased.

Using two different steel ball sizes in the milling media randomizes the steel ball motion by preventing the steel balls from moving in the same trajectories throughout the milling cycle. Larger steel balls transfer higher impact energy per impact and smaller steel balls provide higher collision frequency [30]. It may also increase the shear forces between surfaces during collisions, and remove powder coating from the steel ball surfaces.

Furthermore, the occupancy level is less and more volume in the vial is free for the powder movement, and the number of contact points in a collision is more (the smaller steel balls can be placed in the vacant areas of the larger steel balls). As a result, the efficiency in reducing the crystallite size and increasing the microhardness became more when a mixture of the steel balls was used. The morphology of the powder for all steel ball size conditions was equiaxed. The average particle size of the powder milled decreased when smaller steel balls were used because of higher collision frequency. So, based on the data given in Table 3.4, an optimum situation to achieve both smaller crystallite size and particle size is by using steel balls with 8 mm diameter. That is because steel balls with 5 mm diameter did not provide the smaller crystallite size and the mixture of steel balls did not achieve smaller

powder size. Smaller powder particles will accelerate the densification rate during further consolidation and hence are desirable.

3.3.3. Effect of ball to powder ratio (BPR)

Figure 3.6 shows SEM micrographs of the as-milled powders using different BPRs. Table 3.5 summarizes the morphological and microstructural parameters of the as-milled 14LMT alloy using BPR of 5, 10 and 15. The lattice parameter increased at a higher BPR due to smaller mean free path of the steel balls and higher collision frequency. As a result, more energy was transferred to the powder particles and led to faster alloying and more lattice expansion. It is also possible that due to higher energy more heat is generated and this could raise the powder temperature and accelerate the kinetics of alloying. Table 3.5 shows that the crystallite size decreased with increasing BPR.

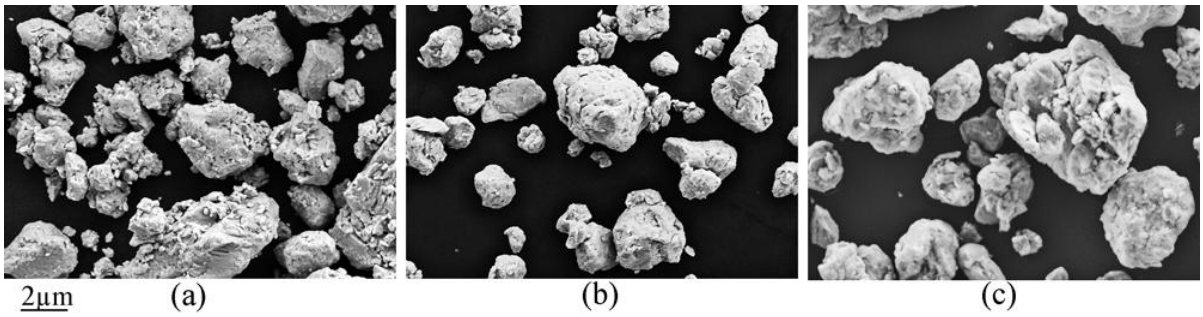

Figuer 3.6. SEM micrographs of the as-milled 14LMT alloy as a function of BPR; (a) 5:1, (b) 10:1 and (c) 15:1 10 h, steel ball diameter – 8 mm)

Table 3.5. Summary of microstructural characteristics and microhardness values of the as-milled 14LMT alloy (milling time of 10 h and steel ball size of 8 mm) as a function of BPR

BPR	Lattice Parameter (nm)	Crystallite Size (nm)	Lattice Strain (%)	Hardness (HV)	Mean Particle Size (μm)
5	0.2877	72±10	0.61±0.05	832±17	8.4±2.7
10	0.2881	24±8	0.77±0.04	940±20	5.5±1.1
15	0.2884	12±2	0.85±0.03	1006±11	6.7±2.3

The microhardness of the as-milled 14LMT alloy using a BPR of 10:1 was higher than BPR 5:1. This is due to an enhanced plastic deformation of the powder particles milled using higher BPR. The microhardness value decreased at BPR 15:1 because of lower amount of the synthesized powder and remnants of the unprocessed powder particles. In general, with lower BPR the number of collisions decreases, but the number of particles caught between steel balls increases. Consequently, both the vial and the individual particles temperature are reduced [31].

Increasing the BPR from 5 to 10 resulted in decrease of the average powder particle size, and the morphology of the powder particles changed from flaky to more spherical. On the other hand, with increasing BPR from 10 to 15 the powder morphology remained equiaxed. The particle size slightly increased due to more agglomeration caused by accelerated plastic deformation and faster steel ball milling at higher BPR. Figure 3.7 illustrates the powder yield (%) and powder contamination (%) as a function of BPR. Powder yield was estimated as the ratio of the actual mass of the powder after milling with the mass filled in the vial, while the degree of contamination was estimated using the following equation,

$$C = (M_1 - M_2) / M_1 \quad (3.1)$$

where C is the degree of contamination, M_1 is the mass of steel balls filling the vial and M_2 is the mass of the steel ball after milling [31]. With increasing BPR from 5 to 15, the powder yield decreased, and the powder contamination progressively increased. At higher BPR, the high frequency of collisions resulted in significant adhesion of the powder to the milling

media, and this caused less mass of the as-milled powder and reduction in powder yield. Meanwhile, higher BPR caused more contamination due to a larger mass of the steel balls colliding with each other resulting in extensive wear and more carbide and oxide pickup from the milling media. Based on the results presented in this section, a BPR of 10:1 was used for further ball milling experiments.

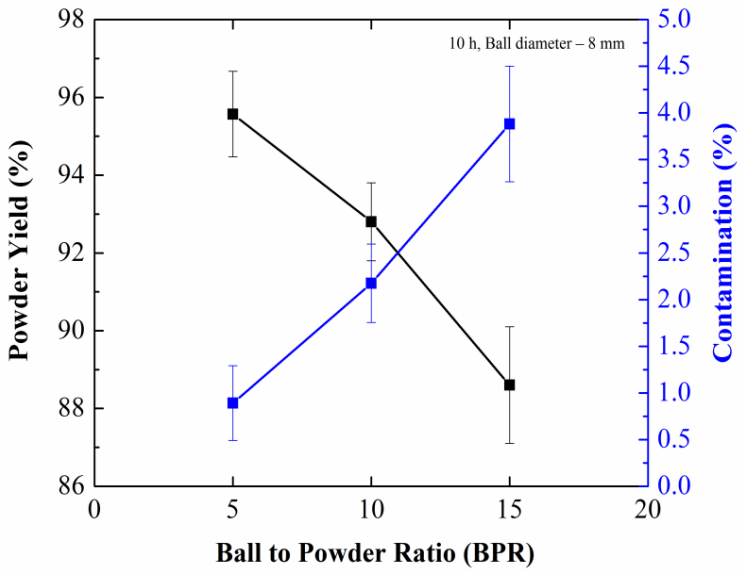

Figuer 3. 7. Powder yield (%) and powder contamination (%) in 14LMT alloy as a function of BPR

3.3.4. Microstructural studies

Further microstructural characterization was carried out on the 14LMT powder milled for 10 h using steel balls with 8 mm in diameter and a BPR of 10:1. TEM bright field micrographs of 14LMT alloy are shown in Figs. 3.8(a–b). The microstructure was nanocrystalline with a significant reduction in crystallite size during ball milling. Severely

deformed nanograins were found in two morphologies: equiaxed and elongated pancake shaped. The dislocation density was significantly high as revealed by the complicated diffraction contrast, but it was difficult to quantify the dislocation density due to the small size of the crystallites. During ball milling, the powder particles are heavily deformed, forming a dislocation cell structure and reducing the grain size. The dislocation cell structure becomes saturated and finally transforms to high angle boundaries [32]. In this study, it was difficult to distinguish grains and subgrain dislocation structures since both could be referred as crystallites. The crystallite size varied between 5–30 nm with an average diameter of 20 nm that was reasonably consistent with the XRD data showing a crystallite size of 24 nm. No oxide particles were observed due to incorporation of Ti and La in the bcc ferritic matrix as a solid solution.

Figure 3.8(c) shows a selected area diffraction (SAD) pattern corresponding to the region shown in Fig. 3.8(a). Analysis of Debye rings revealed that the nanograins were distributed in a crystallographically random orientation. Some variation in intensity of rings was observed in Fig. 3.8(c). This was because of localized and inhomogeneous deformation, significant lattice distortion and fracture by shear deformation [32]. The SAD pattern rings were consistent with bcc Fe. No evidence of La or Ti diffraction could be detected in the SAD pattern. Based on the TEM and XRD findings, it can be argued that La_2O_3 was dissolved into the nanograins of the ferritic matrix.

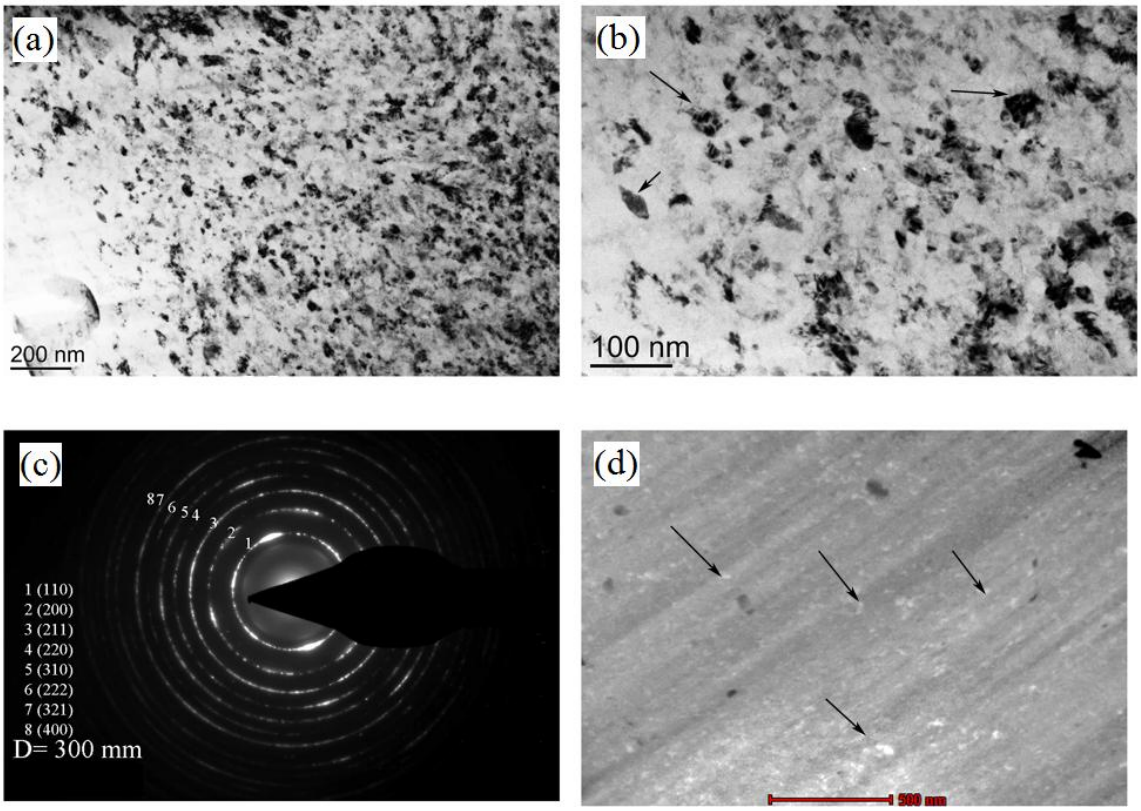

Figuer 3.8. (a) A TEM Bright field image of the as-milled 14LMT alloy (b) A TEM bright field micrograph at a higher magnification, (c) A SAD pattern showing nanocrystalline bcc Fe rings, (d) A STEM image of the microstructure

The uniform contrast in the Z-contrast STEM image of 14LMT alloy shown in Fig. 3.8(d) suggests an overall qualitatively homogeneous distribution of the solute elements after 10 h of milling. There were a few features with brighter contrast that were mostly enriched with Fe and depleted of the solutes (Ti or Cr) as examined by the EDS. The darker contrast features were due to segregation of the solute atoms from the matrix. The size of the bright features was close to the size of crystallites in the matrix, and the contrast was due to Z-contrast and was not due to any diffraction contrast.

The EDS line scan was performed along a 100 nm distance in the matrix containing several features with different contrasts. Corresponding STEM image and concentration

profiles of Cr, Ti, Mo and La are shown in Fig. 3.9(a–b), respectively. It can be noted that some regions within the line scan (e.g., between distance 45 nm and 60 nm) were enriched in Cr concentration and depleted from Ti. The Cr concentration varied between 9–14 at.% along the 100 nm line scan. Ti concentration was not homogeneously constant along the line scan and some regions were found to be locally enriched in Ti. It was difficult to quantify La content due to its low concentration and nano-sized particles, yet a few regions with 0.5 at.% La were detected in Fig. 3.9(b) with La:Ti ratio found between 0.5–0.25.

Figure 3.10 shows a HRTEM micrograph of the as-milled 14LMT alloy with two identified regions or two squares and the corresponding FFT images. Inside the squares shown in Fig. 3.10, NFs were observed (1–2 nm), but the EDS experiment was extremely difficult to do because of the matrix influence. These nanofeatures were indicated by the black arrows in this micrograph. The FFT patterns did not correspond to either to the bcc matrix or to the remnants of La_2O_3 particles.

The reconstructed APT maps of the as-milled 14LMT alloy are illustrated in Fig. 3.11. A uniform distribution of Cr–Ti–La–O-enriched nanoclusters was evident in the as-milled powder. These nanoclusters were distributed semi-homogeneously and were not associated with the solute segregation regions, such as at grain boundaries or dislocation lines. It can be noted that Mo did not show any clustering and was uniformly distributed in the matrix. The overall (bulk) compositional measurements averaged over a number of analyzed volumes are summarized in Table 3.6. The bulk composition was calculated by counting the total number of atoms of each element in a complete APT analysis, and the values were averaged over several datasets. The matrix composition was calculated by excluding the clustering atoms in a similar manner using a method explained by Williams *et al.* [6].

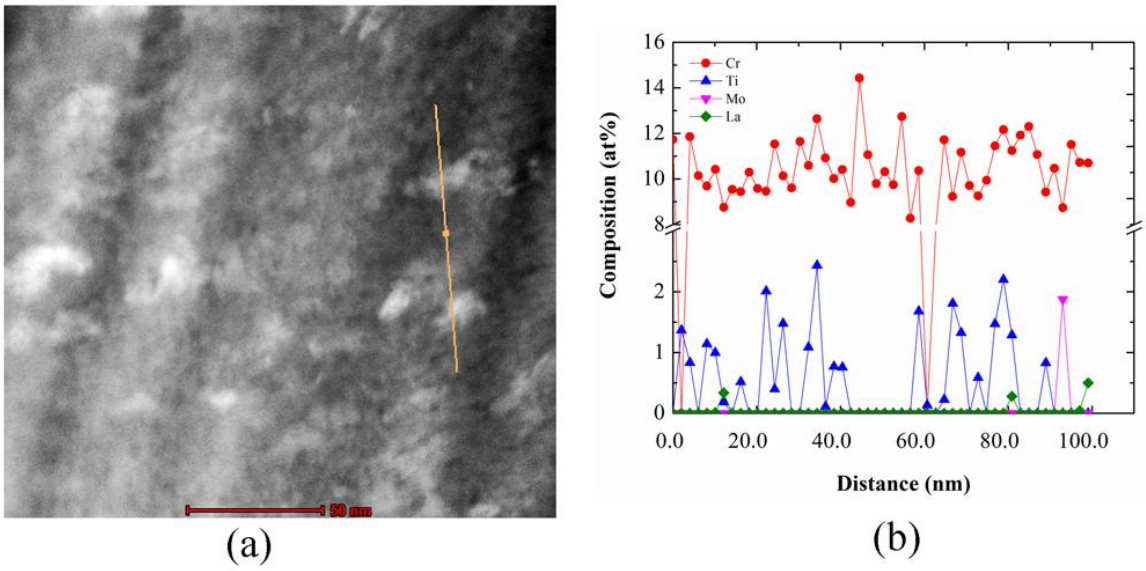

Figuer 3.9. (a) A STEM image of the as-milled 14LMT alloy, (b) EDS line scan concentration profile for Cr, Ti, Mo and La

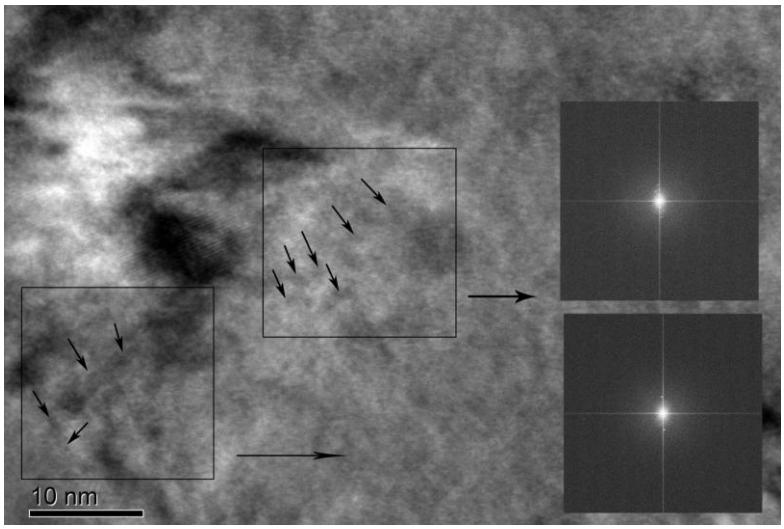

Figuer 3.10. A HRTEM image along with FFT images of the as-milled 14LMT alloy

The bulk composition did not show any significant differences with the nominal composition; however, the amount of C, O and N in the bulk composition were higher than the expected values due contamination of powder particles as a result of MA. In the matrix composition, due to low solubility of C and N, it can be assumed that majority of these

elements could segregate to the boundaries or formed carbides / nitrides [20] that were not observed in the analysis volume in the current study. Most Ti and La atoms were found to be in the nanoclusters based on the results shown in Table 3.6 and Fig. 3.11.

The data was collected from 10–20 million ions and no remnant of the original La_2O_3 powder particles was found in multiple specimens implying incorporation of La_2O_3 in to the matrix. This could be associated with two possibilities: (1) La_2O_3 was taken up in the metal powders as highly refined oxides and (2) the solubility of O and La was greatly enhanced by high energy ball milling causing O and La super saturation in the ferritic phase [33]. The first possibility was not true in this case since no LaO or remnant of initial La_2O_3 particles was found either in the reconstructed analysis or in TEM observations.

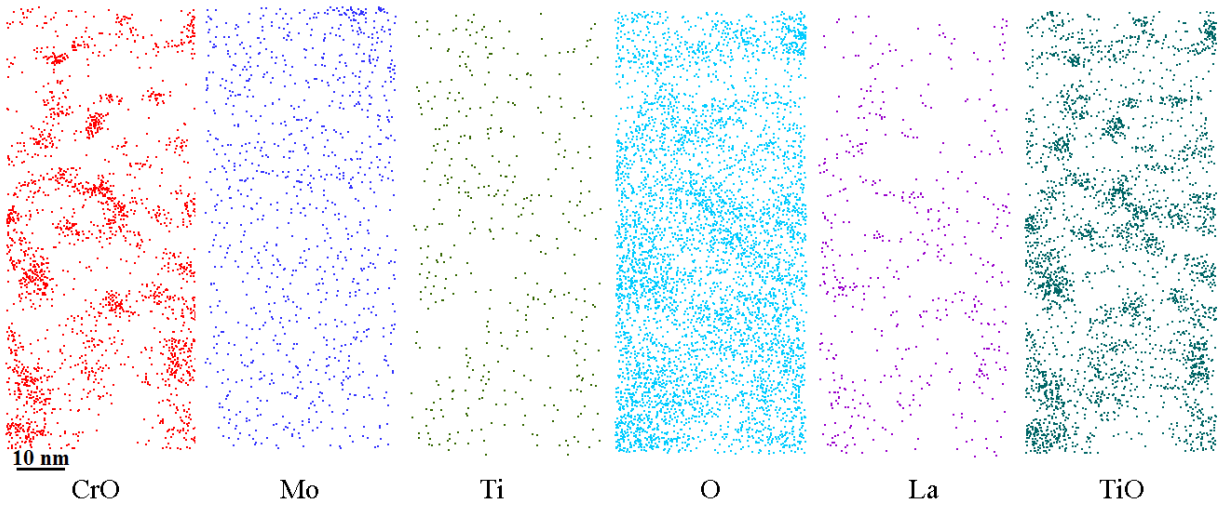

Figuer 3.11. Reconstructed APT maps of the as-milled 14LMT alloy showing the distribution maps of CrO, Mo, Ti, O, La and TiO (the total analyzed volume is 45×45×95 nm^3)

Table 3.6. Bulk and matrix composition (at.%) measurements in the APT analysis

Element	Nominal Composition	Bulk Composition	Matrix Composition
C	–	0.22±0.03	0.06±0.05
Cr	14.8	14.92±0.45	13.59±0.3
Fe	83.71	81.50±0.1	85.23±0.7
Ti	1.0	1.29±0.05	0.53±0.08
O	0.19	1.63±0.12	0.32±0.13
Mo	0.17	0.24±0.04	0.20±0.05
N	–	0.11±0.09	0.07±0.09
La	0.13	0.09±0.04	0. 05±0.03

Several analysis volumes were studied to detect any segregation of Cr or Mo; however, no solute segregation was observed in the one-dimensional (1-D) concentration profile shown in Fig. 3.12. The analysis was carried out in a cylinder of 5 nm diameter through a region showing grain boundary characteristics and the results were consistent with the analysis of the as-milled Fe–14 Cr–2 W–0.3 Ti–0.3Y_2O_3 (wt.%) powder reported by Williams *et al.* [6]. Figure 3.13 shows a small analysis volume with clear clustering of CrO, TiO and La. The analysis volume was 5×5×35 nm^3.

Table 3.7 shows the averaged chemical composition of the nanoclusters using maximum separation algorithm. Both raw and "matrix corrected" compositions were calculated using several steps explained in Ref. [16-20]. A significant concentration of Cr, Ti and O were calculated in the composition of nanoclusters and no exact stoichiometric composition was found. So it can be assumed that the formation of Cr–Ti–La–O-enriched nanoclusters has taken place during MA. The raw concentration composition showed a M:O equal to 0.75±0.05 whereas M:O in "matrix corrected" composition was equal to 0.49±0.04 that is consistent with ~ Cr_2O_3 but La:Ti ratio is considered as "non-stoichiometric". The number density of the nanoclusters was estimated to be about (3.7±0.6)×10^{24} m^{-3} with average R_g = 0.97±0.07 nm.

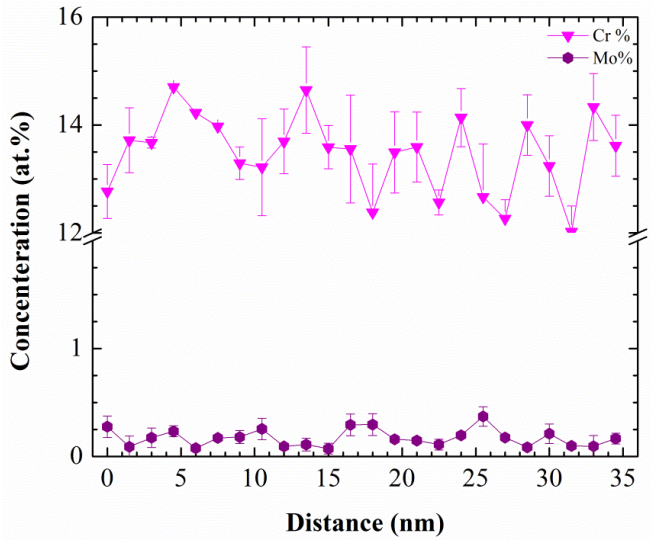

Figuer 3.12. 1-D concentration profiles of Cr and Mo from an APT analysis volume with a cylindrical shape with a diameter of 5 nm

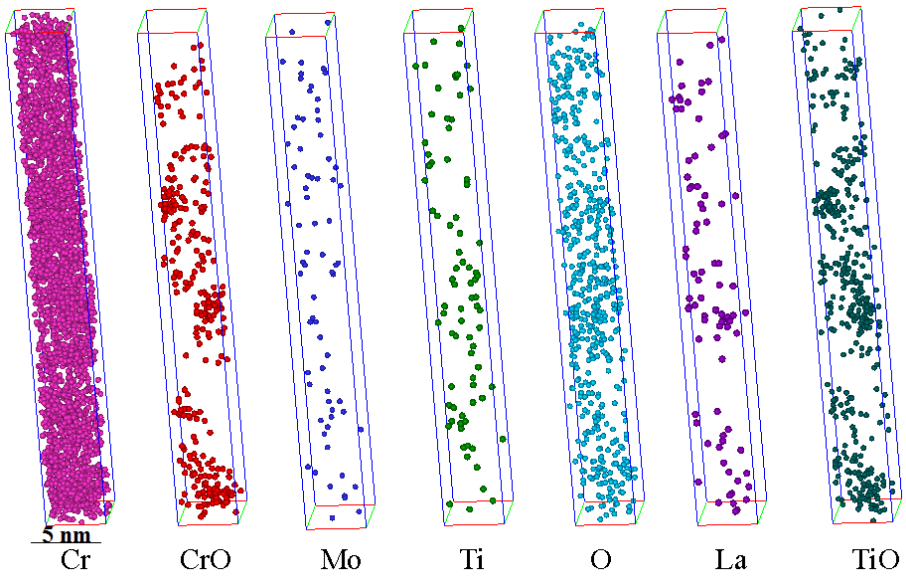

Figuer 3.13. (a) APT 3-D reconstructions of Cr, CrO, Mo, Ti, O, La and TiO distribution maps in the as-milled 14LMT powder (the total analyzed volume is $5\times5\times35$ nm^3)

Table 3.7. Composition (at.%) measurements of nanoclusters showing both raw and "matrix corrected" values in the as-milled powder

Element	Raw Concentration	Matrix Corrected
C	0.05±0.05	0.26±0.1
Cr	12.11±0.25	30.82±0.68
Fe	57.02±1.1	0
Ti	9.07±0.55	16.51±0.65
O	17.43±1.2	45.47±1.3
Mo	0.08±0.05	1.02±0.3
N	0.08±0.06	0.09±0.03
La	4.05±0.91	5.8±0.98
Mn	0.11±0.05	0.21±0.06
M:O	0.75±0.05	0.49±0.04

The mechanism of nanocluster formation is still under debate but it is generally thought to be composed of two steps: dissolution of solute elements into the matrix during ball milling and re-precipitation of the nanoclusters during annealing or hot consolidation processes [5]. The presence of the nanoclusters with mean radius of 0.8±0.2 nm in the as-milled powder was first reported by Brocq *et al.* [5] in ball milling of Fe–14Cr–2W–1Ti mixed with YFe_3 and Fe_2O_3. Brocq *et al.* [5] suggested that the role of high energy ball milling was not only limited to the dissolution of alloying constituents into the ferritic matrix. It could also be an initiation step for nucleation of the nanoclusters that could grow and become more enriched during the hot consolidation. They reported that at the end of milling the nucleation was far from being complete and 94% of Ti, Y and O were left in the matrix as solutes. Laurent – Brocq *et al.* [34] suggested a two-step mechanism during ball milling in specific conditions: first, reactants are dissolved into the metallic matrix until an oversaturated solid solution is formed; and second, nanocluster nucleation begins. Increasing milling intensity or temperature hastens the dissolution of reactants during ball milling, and the nanocluster density increases with increasing temperature during hot consolidation.

The mechanism of the nanocluster nucleation during the MA was recently studied by Fu *et al.* [35]. First principles studies identified a vacancy mechanism underlying the unusually high O solubility and nucleation of stable O-enriched nanoclusters in defect–containing Fe. Oxygen, confined as an interstitial, shows an exceptionally high affinity for vacancies, an effect enhanced by spin polarization. If vacancies preexist, the O–vacancy pair formation energy essentially vanishes, allowing the O concentration to approach that of the vacancies. This O–vacancy mechanism enables the nucleation of the O-enriched nanoclusters that attract solutes with high O affinities (Ti and Y) and strengthen Fe-based alloys. Based on the mechanism suggested by Fu *et al.* [35] in the neighborhood of an O–vacancy pair, some lattice sites are energetically favorable for La atoms. Therefore, highly stable O–vacancy pairs enable the nucleation of O-enriched nanoclusters that attract solutes with high affinity for oxygen, such as La.

The formation enthalpies of various oxides of some selected species are listed in Table 3.8. It can be assumed that expected nanocluster in the 14LMT composition will be mainly based on La because of its larger enthalpy of formation for lanthanum oxide. However, based on the results given in Table 3.7, Cr and Ti–oxide were part of the nanocluster composition. More work is required to identify the shell / core existence and its composition, but APT studies on ODS – Eurofer 97 steel [20] and Fe–14Cr–2W–0.3Ti–$0.3Y_2O_3$ [6] showed that Cr and Ti are predominantly found in the particle – matrix interface.

Since the level of O is significantly high in the as-milled powder, and O has a very low solubility in Fe, the formation of the oxide particles from the supersaturated matrix is likely

possible during MA. Therefore, the precipitation of nanoclusters is driven by the low equilibrium solubility of O in the Fe matrix, and oxidation reaction could happen in the as-milled powder and lower the free energy by nanoclusters formation [6]. Despite the high enthalpy of formation for La–O, formation of Cr–oxide and Ti–oxide are encouraged because the kinetics of nanoclusters will depend on the concentration and diffusivity of high oxygen affinity elements (such as Cr and Ti here). Based on the mechanism suggested by Williams *et al.* [6,20], Ti and Cr are always part of the oxide clusters in the as-milled powder and assist in the further nucleation of Y–O. This is because the initial oxides to form are Cr-based oxides due to high concentration of O in the Fe matrix that is far above the equilibrium level and due to the high concentration of Cr.

Hence, kinetics of oxidation will form Cr–O and similarly Ti–O that will assist further nucleation of La–O. Moreover, the atomic radius of La (195 pm) is bigger than the Y atomic radius (180 pm), and thus larger misfit is induced into the bcc ferritic matrix and formation of nanoclusters with interfacial phases like TiO / CrO is favorable. Ball milling atmosphere and purity of reactants influence the excess amount of O and possibly have an effect on the nanoclusters formation during ball milling.

Table 3.8. The formation enthalpies of various oxides [6,36]

Element	Composition	$-\Delta H_f$ (kJ mol^{-1} (oxide))
Cr	Cr_2O_3	583
	CrO_2	1130
Fe	Fe_3O_4	1118
	Fe_2O_3	822
Ti	TiO	543
	TiO_2	944
	Ti_2O_3	1522
	Ti_3O_5	2475
Y	Y_2O_3	1907
	$YCrO_3$	1493
	$Y_2Ti_2O_7$	3874
La	La_2O_3	1791
	$La_2Ti_2O_7$	3855

3.4. Conclusions

In this study, a novel NFS with a nominal composition of Fe–14Cr–1Ti–0.3Mo–0.5La_2O_3 (wt.%), was developed using MA of the constituent powders. This alloy contained La_2O_3 instead of Y_2O_3 and was named 14LMT. The objective of this study was to study the effect of ball milling parameters on developing of the alloy as well as optimize the ball milling parameters for subsequent consolidation.

1. Using the SPEX high energy ball mill, the optimal milling conditions for 14LMT alloy were determined to be 10 h, BPR of 10:1 and a milling medium containing steel balls of 8 mm diameter.

2. TEM studies revealed nanocrystallites with average diameter of 20 nm and crystallographically random orientation in the as-milled 14LMT alloy. No remnants of original La_2O_3 were detected in the TEM micrographs or SAD pattern. La_2O_3 got decomposed, and La and O were incorporated in the ferritic matrix substitutionally and interstitially, respectively. The decomposition was suggested to be due to the repeated fracture and shearing of the fragmented oxide particles.

3. APT data analysis revealed number density of 3.7×10^{24} m^{-3} of nanoclusters with a mean radius of ~1 nm in the as-milled powder. These nanoclusters were enriched in Cr–Ti–La–O atoms and were very similar to the nanoclusters observed in ODS steels and NFSs that contained Y_2O_3. The nanoclusters showed "non-stoichiometric" composition and had significant concentration of Cr and Ti possibly due the faster kinetics of their formation.

4. La_2O_3 could serve as a promising alternative RE oxide for Y_2O_3 in future NFS compositions. The potential of this RE oxide will require further investigations, but as a first advantage it was beneficial to initiate nucleation of nanoclusters during ball milling. These nanoclusters are expected to appear more in number and evolve in composition and morphology during hot consolidation. Future studies will be focused on consolidation of the ball milled 14LMT alloy by SPS.

Acknowledgments

This work was supported partly by the Laboratory Directed Research and Development Program of the Idaho National Laboratory, Contract DE–AC07–05ID14517, and partly by a grant of the Advanced Test Reactor National Scientific User Facility. TEM and APT were done at the Microscopy and Characterization Suite (MaCS), Center for Advanced Energy Studies (CAES). We would also like to acknowledge the help of Mrs. Jatuporn Burns and Dr. Kerry N. Allahar. Furthermore, we would like to thank the reviewers for the helpful comments.

References

[1] Ukai S, Fujiwara M, J Nucl Mater 2002; 307–311:749.

[2] Sokolov MA, Hoelzer DT, McClintock DA, J Nucl Mater 2007; 67–370:213.

[3] Oksiuta1 Z, Baluc N, J Mater Res 2009; 59:308.

[4] Odette GR, Alinger MJ, Wirth BD, AR Mater Res 2008; 38:471.

[5] Brocq M, Radiguet B, Poissonnet S, Cuvilly F, Pareige P, Legendre F, J Nucl Mater 2011; 409:80.

[6] Williams CA, Unifantowicz P, Baluc N, Smith GD, Marquis EA, Acta Mater 2013; 2219:2235.

[7] ASM handbook, third ed. Ohio: ASM International; 1992.

[8] Reed ZD, Duncan MA, J Phys Chem A 2008; 112:5354.

[9] http://www.molycorp.com

[10] Pasebani S, Charit I, Butt DP, Cole JI, J Nucl Mater 2013; 434:282.

[11] Endo M, Kimura K, Udagawa T, Tanabe S, Seto H, High Temp–High Press 1990; 20:129.

[12] Mueller AJ, Shields JA, Buckman RW, In: Proceedings of 15th International Plansee Seminar, Plansee Holding AG, Vol.1 2001:485.

[13] Dong C, J Appl Cryst 1999; 32:838.

[14] Nelson JB, Riley DP, Proc Phys Soc 1945; 57:160.

[15] Williamson GK, Hall WH, Acta Metall 1953; 1:22.

[16] Hyde JM, Marquis EA, Wilford KB, Williams TJ, Ultramicroscopy 2011; 111:440.

[17] Vaumousse D, Cerezo A, Warren PJ, Ultramicroscopy 2003; 95:215.

[18] Leigh T, Moody MP, Liddicoat PV, Ringer SP, Microsc Microanal 2007;13:448.

[19] Cerezo A, Davin L, Surf Interface Anal 2007; 39:184.

[20] Williams CA, Marquis EA, Cerezo A, Smith GD, J Nucl Mater 2010; 400:37.

[21] Miller MK, Atom Probe Tomography, Kluwer Academic/Plenum, New York, 2000.

[22] Williams CA, Haley D, Marquis EA, Smith GD, Moody MP, Ultramicroscopy 2013; dx.doi.org/10.1016/j.ultramic.2012.12.011

[23] Suryanarayana C, Prog Mater Sci 2001; 46:1.

[24] Alinger MJ, Odette GR, Hoelzer DT, Acta Mater 2009; 57:392.

[25] Trichy GR, Master's Thesis, North Carolina State University, Raleigh, 2005.

[26] Lubarda VA, Mech Mater 2003; 35:53.

[27] Tanaka T, Advanced Powder Technol 1995; 6:125.

[28] Kimura Y, Takaki S, Suejima S, Uemori R, Tamehiro H, ISIJ Int 1999; 39:176.

[29] Cunningham NJ, Master's Thesis, University of California, Santa Barbara, 2008.

[30] Shelekhov EV, Tcherdyntsev VV, Pustov LY, Kaloshkin SD , Tomilin IA, Mater Sci Forum 2000; 343–346:603.

[31] Yao Z, Xiong W, Yuan M, Peng Q, J Nucl Mater 2010; 403:198.

[32] Srinivasarao B, Ohishi K, Ohkubo T, Hono K, Acta Mater 2009; 57:3277.

[33] Miller MK, Hoelzer DT, Kenik EA, Russell KF, J Nucl Mater 2004; 329–333:338.

[34] Brocq LM, Legendre F, Mathon MH, A. Mascaro A, Poissonnet S, Radiguet B, Pareige P, Loyer M, Leseigneur O, Acta Mater 2012; 60:7150.

[35] Fu CL, Kremar M, Painter GS, Chen XQ, Phys Rev Lett 2007; 99:225502.

[36] Gale W, Totemeier T, Smithells Metals Reference Book. Amsterdam: Elsevier;2004.

CHAPTER 4: Effect of Milling Time on Densification Behavior and Microstructure of Spark Plasma Sintered Nanostructured Ferritic Steels

Somayeh Pasebani[1,4], Indrajit Charit[1,4], Darryl P. Butt[2,4], James I. Cole[3,4], Yaqiao Q. Wu[2,4] and Jatuporn Burns[2,4]

[1] Department of Chemical and Materials Engineering, University of Idaho, Moscow, ID 83844, USA

[2] Department of Materials Science and Engineering, Boise State University, Boise, ID 83725, USA

[3] Idaho National Laboratory, Idaho Falls, ID 83401, USA

[4] Center for Advanced Energy Studies, Idaho Falls, ID 83401, USA

(*In Revision with the Journal of Metallurgical and Materials Transaction A*)

Abstract

The Fe−14Cr−1Ti−0.3Mo−0.5La_2O_3 (wt.%) was mechanically alloyed for 0–20 h and subsequently consolidated by spark plasma sintering at 950 ^oC (1223 K) for 7 min leading to the development of a nanostructured ferritic steel (14LMT). The effect of milling time on the densification behavior was investigated, and the relative density and microhardness of the sintered 14LMT alloys were measured. Milling enhanced the densification behavior by initiating sintering at lower temperatures and lowering the activation energy for both grain boundary and volume diffusion. However, the activation energy for volume diffusion was less than that for grain boundary diffusion in the milled alloys. Milling also provided a higher microhardness in the sintered specimens mainly by providing solid solution and precipitation strengthening. The microstructural studies performed on the sintered materials revealed a heterogeneous microstructure with a large proportion of highly deformed

nanocrystalline grains surrounded by microcrystalline grains formed due to recovery and recrystallization facilitated by high amount of stored energy. The bimodal grain structure was a result of milling and not only to sintering. The diameter of the precipitates varied between 2–70 nm and the morphology from spherical to faceted. Faceted precipitates smaller than 10 nm were found to be La–Ti–Cr-enriched complex oxides that could control further recrystallization and grain growth phenomena in the sintered alloy.

Keywords: Mechanical alloying; Spark plasma sintering; Milling time; Nanostructured ferritic steel; Lanthanum oxide; Bimodal grain structure

4.1. Introduction

Nanostructured ferritic steels (NFSs), a novel type of oxide dispersion strengthened (ODS) steels, are considered promising candidates for high radiation environment and high temperature applications. These alloys generally contain a high number density of Y–Al–O- or Y–Ti–O-enriched nanoprecipitates and high dislocation densities [1]. Uniformly dispersed nanoprecipitates act as the pinning sites inhibiting dislocations movement and stabilize the grain boundaries leading to improvement in creep resistance [2]. The NFSs also have a high dimensional stability under irradiation, i.e. high resistance to swelling and irradiation creep [3].

The NFSs are typically processed via mechanical alloying (MA) of the powder mixture of Fe–(12–20)Cr–Ti–W / Mo (rapidly solidified pre-alloyed or blended elemental powder) followed by a hot consolidation route such as hot isostatic pressing (HIP) or hot extrusion [3]. The most widely used oxide constituent for NFSs is yttria (Y_2O_3) [4]. Generally, yttria is added to the pre-alloyed powders and dissolved in solid solution during MA, allowing the

Y–Ti–O-enriched nanoclusters (NCs) to form during consolidation. It has been reported that adding Ti reduces the size and enhances the stability of the nanoparticles, by forming of complex oxide precipitates [5].

Recently, an advanced pressure assisted sintering technique utilizing a pulsed current (1000–5000 A) called spark plasma sintering (SPS) has been utilized by researchers to consolidate ODS milled powders [6-10]. Typical sintering time can be greatly reduced from several hours in conventional sintering to a few minutes in the SPS, thereby minimizing or eliminating propensity for grain growth [8, 11, 12]. One of the keys to preparing high performance NFSs lies in minimizing the size of the precipitates and improve the uniformity in their distribution [11]. Therefore, SPS would be beneficial by maintaining the fine microstructure allowing the densification at lower temperature and time compared to conventional techniques. For example, in processing the milled 14YWT (Fe–14Cr–0.4Ti–3W–0.25Y_2O_3) powder via HIP at 850, 1000 and 1150 ^oC for 3 h under pressure of 200 MPa, the volume fractions and number densities of NCs decreased and their size increased with increasing HIP temperature as reported by Alinger *et al.* [13].

In this study, the role of La_2O_3 as a potential alternative to Y_2O_3 dispersoids is evaluated. A nominal composition of Fe–14Cr–1Ti–0.3Mo–0.5La_2O_3 (wt.%), referred to as 14LMT hereafter, is developed via MA and SPS (here L, M and T stand for La_2O_3, Mo and Ti, respectively). The reason for using La_2O_3 is that lanthanum oxide is more abundant (25–38 wt.%) in one of the main US rare earth (RE) minerals (Bastnasite) compared to yttria (only ~0.2 wt.%) [14]. Furthermore, lanthanum has negligible solubility in solid iron at all temperatures [15] as well as a high affinity for oxygen [16].

There is no published report on the La_2O_3-containing NFSs except the studies published by the authors [10, 17, 18]. However, La_2O_3 is added as dispersoids to Mo-based ODS alloys. For example, Endo *et al.* [15] studied the mechanical and microstructural characteristics of molybdenum (bcc) alloys doped with the RE oxides including Y_2O_3, La_2O_3, Nd_2O_3, Sm_2O_3 and Gd_2O_3. In their study, La_2O_3 addition provided the highest strength and creep resistance to the molybdenum matrix.

In processing NFSs, several parameters such as milling conditions, chemical compositions, sintering parameters as well as post sintering parameters have a great influence on the microstructural evolutions and mechanical properties. In our previous work, mechanical alloying [18] and the effect of alloying elements [10] on the microstructure and mechanical properties of lanthana-bearing NFSs were studied. Hence in this work, the focus was to study the effect of milling time on densification behavior and microstructural evolution in 14LMT alloy consolidated via SPS.

4.2. Experimental procedure

4.2.1. High energy ball milling

The starting constituent powders including Fe (99.9 wt.% Fe, average particle size of 40 µm), Cr (99.8 wt.%, average particle size of 5 µm), Ti (99.7 wt.% Ti, average particle size of 26 µm) and La_2O_3 (99.99 wt.% La_2O_3, average particle size of 40 nm) were procured from American Elements Inc., and Mo (99.9 wt.% Mo, average particle size of 1–2 µm) powder was acquired from Micron Metal Powder Inc. The elemental powders were mixed in the nominal proportion of Fe–14Cr–1Ti–0.3Mo–0.5La_2O_3 (wt.%). The powder blend was poured into a hardened steel grinding vial (SPEX 8001) inside a glove box operated under a high purity argon atmosphere and sealed properly. High energy ball milling was performed

in an air-cooled SPEX 8000M shaker mill at the speed of 1725 (rpm) using Thompson chromium steel balls (Grade 52100) with a diameter of 8 mm. Milling was carried out for 0 h (unmilled), 5 h, 10 h, 15 h and 20 h using a ball to powder ratio (BPR) of 10:1 (here 100 g steel balls were used for milling of 10 g powder mixture).

A powder blend with nominal proportion of Fe–14Cr–1Ti–0.3Mo (wt.%) was milled for 10 h and then was mixed with La_2O_3 (no milling on La_2O_3 particles) to investigate the role of ball milling on dispersion of La_2O_3. For comparison between the role of La_2O_3 and Y_2O_3 in the NFSs, a powder blend with nominal proportion of Fe–14Cr–1Ti–0.3Mo–0.3Y_2O_3 (wt.%) was also milled for 10 h.

4.2.2. Spark plasma sintering

A Dr. Sinter Lab SPS-515S (SPS Syntex Inc., Kanagawa, Japan) available at the Center for Advanced Energy Studies (CAES), Idaho Falls, was used to consolidate the milled powder. A Tri-Gemini cylindrical graphite die with an inner diameter of 12.7 mm and outer diameter of 38 mm was used. The inner surface of the die was covered with a graphite foil with a thickness of 0.25 mm to facilitate sample removal. The milled powder was first cold-compacted inside the graphite die, and a 0.2 mm thick graphite foil was placed between the powder and punches. In order to inhibit the diffusion of carbon from the graphite, a thin niobium foil (thickness of 0.06 mm) was placed between the powder and the graphite foils.

The die was wrapped in a 4 mm thick layer of graphite felt to minimize heat loss by thermal radiation. Degassing was carried out by continually purging argon gas and pumping the chamber down to 7×10^{-3} Torr (9.33×10^{-7} MPa) and repeated at least thrice before starting the sintering process. All the milled powder batches were heated in the vacuum chamber to 950 ^{o}C (1223 K) at a rate of 100 ^{o}C/min and then held at that temperature for 7

min. The temperature was monitored with a K-type thermocouple that was inserted through a hole in the die. A constant uniaxial pressure of 80 MPa (~10 kN force) was applied to the milled powder during both heating and dwell time. The samples were then cooled to room temperature in the vacuum chamber by the rate of 50 ^{o}C/min. The final product was in the form of a disk with dimensions of 12.5 mm diameter and 4.8 mm thickness.

To study the sintering kinetics in SPS, constant heating rate has been utilized and the model proposed by Young and Cutler [19] is the mostly used technique. They have modified the non-isothermal equations for volume and grain boundary diffusion individually that represent the relationship between the shrinkage (Y) and diffusion coefficient (D) as shown in Equations 1 and 2, respectively, where c represents the heating ramp rate in units of K.s^{-1}.

$$\ln(YT\frac{dY}{dT}) = \ln(\frac{2.63\gamma\Omega D^{0}{}_{v}}{ka^{3}c}) - \frac{Q_{v}}{RT} \quad (4.1)\ [19]$$

$$\ln(Y^{2}T\frac{dY}{dT}) = \ln(\frac{0.71\gamma b\Omega D^{0}b}{ka^{4}c}) - \frac{Q_{b}}{RT} \quad (4.2)\ [19]$$

where Y is the linear shrinkage ($\Delta l/l_o$); Ω, the volume of vacancy (m^3); γ, the surface energy (J/m^2); D_V, the volume diffusion coefficient given by $D_V = D_0{}^V \exp(-Q_V/RT)$ (m^2.s^{-1}); bD_B, the product of the grain boundary thickness 'b' and grain boundary diffusion coefficient 'D_B' given by $D_B = D_0{}^B \exp(-Q_B/RT)$ (m^3.s^{-1}); k, the *Boltzmann* constant (J/K); T, the temperature (K); a, the particle radius (m) and t is time (s), Q_V and Q_B are the activation energy for volume diffusion and grain boundary diffusion, respectively. The activation energies for volume diffusion and grain boundary diffusion can be obtained from the slope of the plots between ln (YT(dY/dT)) versus 1/T and ln (Y^2T(dY/dT)) versus 1/T, respectively.

4.2.3. Microstructural and mechanical characterization

The density of the sintered specimens was measured by Archimedes method using nano-pure deionized water. At least six measurements were made for each specimen. The final relative density was determined as the ratio between the measured and the theoretical density of 14LMT alloy (~7.7 g/cm^3). The sample surface for microhardness testing was mechanically polished using standard metallographic procedures involving grinding and polishing down to 0.5 μm. The Vickers microhardness tests were performed with a Leco LM100 microhardness tester at 1 kg (9.81 N) load for the sintered samples. The microhardness tests were repeated on random spots in the center of each specimen up to 10 times.

Microstructural characteristics of the sintered specimens were examined using a LEO Supra 35 VP FESEM. The unmilled and milled specimens that were sintered were prepared for electron back scatter diffraction (EBSD) characterization by grinding on 120 to 1200 grit SiC papers, followed by a final polish in a Buehler Vibromet–2 vibratory polisher using 0.05 μm alumina slurry for 6 to 24 h. The EBSD analysis was performed on a JEOL SEM Model JSM–6610LV equipped with an EDAX / TSL Hikari EBSD system operated at an accelerating voltage of 20 kV. The automated scan was performed with a 0.1 μm step size at 2000 X magnification on a total area of 50×50 μm^2. The EBSD data were analyzed using TSL Orientation Imaging Microscopy (OIM™) Data Collection version 5.31.

For preparing TEM specimens, electropolishing technique and focused ion beam (FIB) technique were used. Electropolishing was carried out in CH_3OH–HNO_3 (80:20 by vol.%) electrolyte at –40 ^oC and voltage of 25 V using a Fischione Model 110 Twin Jet Electropolisher. For FIB experiments, a FEI 3D Quanta SEM was utilized. The TEM

specimens were studied using a FEI Tecnai TF30–FEG STEM operating at an accelerating voltage of 300 kV.

4.3. Results and discussion

4.3.1. Sintering kinetics

The effect of milling times on the displacement profiles during SPS is shown in Fig. 4.1(a). The temperature at which densification begins (T_s) and the temperature at which maximum densification rate occurs (T_{max}) can be calculated from the displacement curve and its first derivative, respectively [20]. The T_s and T_{max} were calculated and their variation as a function of milling time is shown in Fig. 4.1(b).

Figure 4.1(a) shows the differences between the profile of the un-milled powder and milled powder; the displacement profile of the un-milled powder had a large displacement before the sintering began and this behavior was not observed for any of the milled powders. The rate of sintering for the un-milled powder was lower than the sintering rate for all of the milled powders.

Furthermore, sintering started at a higher temperature and ended at a lower temperature compared to all of the milled powders and the total displacement of the un-milled powder was lower than that for the milled powders. These differences will likely lead to lower density and higher amount of residual porosity in the un-milled powder as will be shown later. The displacement profile of the powder milled for 5 h was similar to powder milled for 10 h. The difference between the profiles of 5 and 10 h milling time was that the densification began at lower temperature in case of 10 h milled powder. The profile of 10

and 20 h milling time was similar but with slightly higher densification rate and larger displacement for the powder milled for 20 h.

Lower hardness and less complicated geometrical shape of the un-milled powder particles facilitated rearrangement of the particles in a more random and packed powder compact leading to an intense displacement before T_s as shown in Fig. 4.1(a). This large displacement for the un-milled powder was also reported by Guyon *et al.* [20]. On the contrary, the ball milled powders had a complicated geometrical shape and higher hardness [18] and thus showed a lower displacement before T_s. Lower density of dislocations, grain boundary surfaces and other microstructural defects in the un-milled powder particles as shown in a previous work [18] were likely the reasons for higher T_s and lower total displacement values during sintering [21].

In Fig. 4.1(b), the T_s value showed a decrease with milling time whereas the value of T_{max} constantly increased with milling time. This variation in T_s and T_{max} could provide a wider sintering temperature region with increasing milling time. Theoretically, high diffusivity paths created during heavy plastic deformation would also enhance sintering efficiency and contribute to lower T_s. As the milling time increased and the powder crystallite and particle size decreased [18], the interfacial area increased leading to an increase in the total number of the particles.

A very important factor in sintering the nanocrystalline powder is the presence of a very high specific surface area acting as a driving force in densification process. A high specific surface area could easily activate the surface diffusion mechanism compared to grain boundary and volume diffusion especially at the initial stage of sintering before the necks

between powder particles are formed [25]. This could contribute to lower T_s at longer milling times. Once the necks are formed, the surface diffusion is not the dominant mechanism anymore and other diffusion-based mechanism will be activated

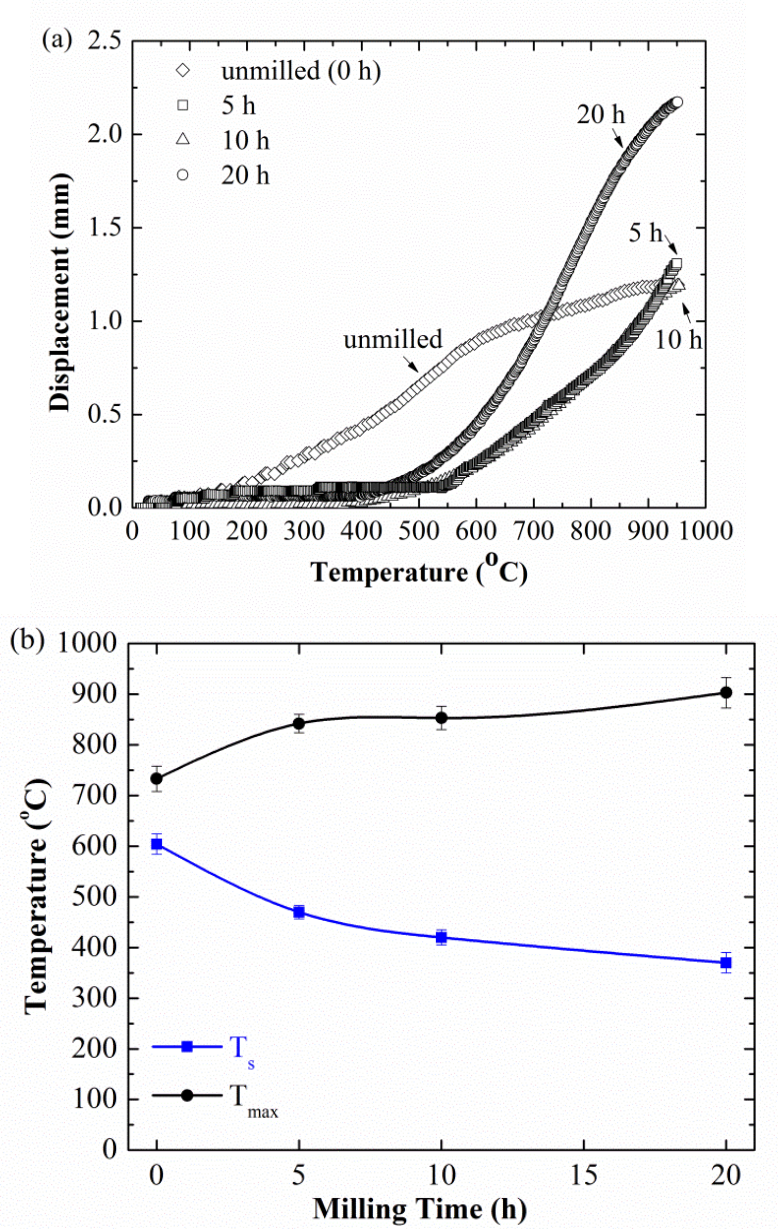

Figure 4.1. (a) The effect of milling time on the displacement profile, and (b) the estimated T_s and T_{max} as a function of milling time for 14LMT alloy sintered at 950 °C (1223 K) for 7 min

To quantify the sintering behavior as a function of milling time, one should consider the role of volume diffusion or grain boundary diffusion in driving the sintering process. For this purpose the activation energy profiles for volume diffusion and grain boundary diffusion in 14LMT powder milled for 0–20 h were estimated and plotted in Figs. 4.2(a–b), respectively.

From the slope of the ln (YT dY/dT) versus 1/T plots shown in Fig. 4.2(a), the volume diffusion activation energy for the 0 h, 10 h and 20 h milled 14LMT sintered at 950 ^{o}C (1223 K) was estimated to be 247±6, 98±4 and 64±6 kJ./mol, respectively. From the slope of the ln (Y^2T dY/dT) versus 1/T plots shown in Fig. 4.2(b), the grain boundary diffusion activation energy for the 0 h, 10 h and 20 h milled 14LMT alloy was estimated to be 153±5, 164±4 and 144±15 kJ/mol, respectively. The activation energy for volume diffusion and grain boundary diffusion of pure α–Fe was 251 and 174 kJ/mol, respectively [22].

Matrenin *et al.* [23] estimated the activation energy of volume diffusion in coarse grained and fine grained Fe powder to be 58 and 29 kJ/mol, respectively. The nanograin boundary diffusion for Fe powder was estimated to be 187 kJ/mol according to Lee *et al.* [24].

In sintering of 14LMT alloy, the activation energy of both grain boundary diffusion and volume diffusion constantly decreased with increasing milling time. In case of the unmilled powder, the volume diffusion had higher activation energy than the grain boundary diffusion and hence the volume diffusion was not most likely the dominant sintering mechanism. The applied uniaxial pressure on the unmilled powder during SPS, would enhance the grain boundary diffusion compared to surface diffusion according to Chiam *et al.* [25].

The activation energy of grain boundary diffusion in the milled alloys was higher than that of the volume diffusion implying that the grain boundary diffusion is most likely not the preferred sintering mechanism.

The lower activation energy of volume diffusion in the milled alloy could be related to high density of vacancies, other point defects and dislocations that are produced during high energy ball milling as well as thermal vacancies produced during sintering. The reason for higher T_{max} in sintering of alloys longer milled for longer hours, is not clarified for the authors, however larger particle size and higher hardness in the alloy milled for 20 h [18] could influence on T_{max} value and increase it to higher temperatures.

Similarly, Chaim *et al.* [25] reported that the increase in particle size would lead to decrease in the total number of the particles, as well as particle necks and full densification would happen at higher temperatures.

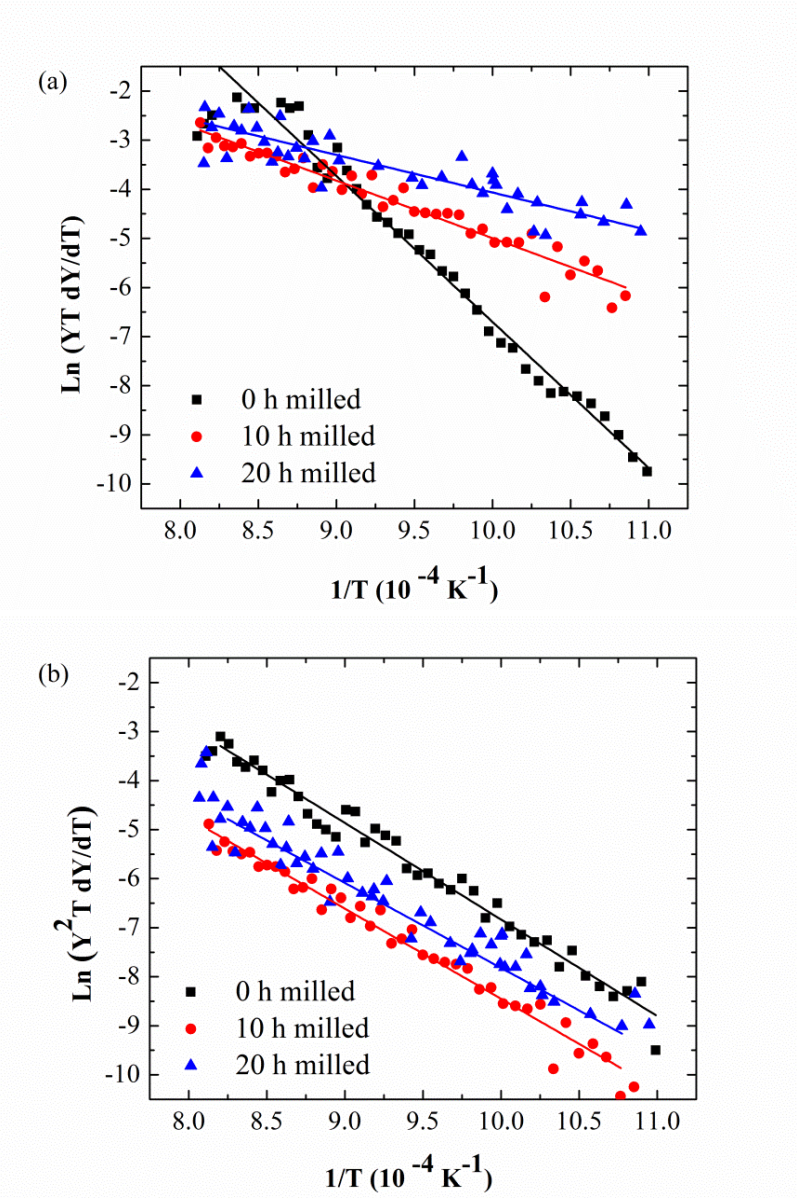

Figure 4.2. Activation energy profiles for (a) volume diffusion, and (b) grain boundary diffusion after 0–20 h milling and SPS (at 950 ^{o}C (1223 K) for 7 min) of 14LMT alloy

4.3.2. Density and microhardness

The relative density and microhardness values of the SPSed samples are illustrated in Fig. 4.3. The density of the sintered samples increased with increasing milling time up to 10 h and decreased thereafter. With milling beyond 10 h, both density and hardness values of the SPSed samples decreased because of saturation in the crystallite size and lattice strain

[18]. In addition, a high level of carbon and oxygen contents from oxide and carbide impurities likely produced a higher residual porosity with longer milling times. The relative density of 98.7% and microhardness value of 505 HV were achieved after sintering the 14LMT alloy milled for 10 h. Achieving full density was only possible by applying a very high pressure (higher than the yield stress of 14LMT alloy at 950 ^{o}C (1223 K). This was practically impossible to achieve in the SPS process in this study due to the mechanical limit of the graphite die and punches. The other option is increasing the sintering temperature and / or time at the expense of grain growth and coarsening of the nano-sized oxide precipitates. As it will be shown in the microstructural section, the presence of high number of oxide precipitates and work hardening during sintering of the nanostructured milled powder, would contribute to higher hardness bringing new challenges to achieve the full densification in NFSs.

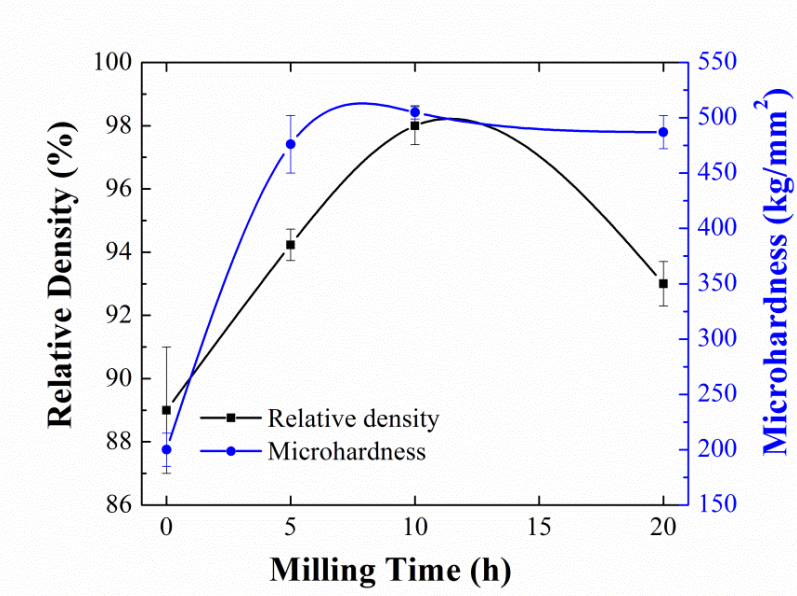

Figure 4.3. Relative density and microhardness after 0–20 h milling and SPS (at 950 ^{o}C (1223 K) for 7 min) of 14LMT alloy

An alloy with the nominal composition of Fe–14Cr–1Ti–0.3Mo–0.3Y_2O_3 was also processed in this study using the same milling and SPS parameters. The density and hardness of this alloy were measured to be 98.5% and 460 HV, respectively. In a study by Alinger *et al.* [13], the hardness of the milled and HIPed 14YWT (Fe–14Cr–0.4Ti–3W –0.25Y_2O_3) alloy was reported to be 500 HV (under the same hardness test conditions as this study). So, La_2O_3 containing dispersoids could provide a higher hardness in sintered NFSs. Table 4.1 compares the relative density and microhardness values between 14LMT alloy milled for 0 and 10 h, and 14LMT alloy with no milling of La_2O_3 (La_2O_3 was added but not milled) sintered at 950 ^oC (1223 K). Solid solution and precipitation hardening contributed to high hardness in 14LMT alloy milled for 10 h.

Table 4.1. The effect of milling La_2O_3 in 14LMT alloy sintered at 950 ^oC (1223 K) for 7 min on the relative density and microhardness

Milling Condition	Relative Density (%)	Microhardness (kg. mm^{-2})
Unmilled powder	89.0±2.0	200±15
Milled for 10 h	98.7±0.6	505±6
Blended La_2O_3 (La_2O_3 was not milled)	97.5±1.6	328±2

4.3.3. Microstructural characteristics of the SPSed 14LMT Alloy

The SEM back scattered electron (BSE) micrographs of the SPSed specimens milled for 0 h, 5 h, 10 h and 20 h are shown in Figs. 4.4(a–d). As shown in Fig. 4.4(a), the un-milled powder contained a significant volume fraction of large pores which were mostly irregular in shape. Increasing the milling time from 0 to 5 h resulted in a more uniform microstructure with smaller spherically shaped pores that were mostly present on the boundaries of the powder particles (Fig. 4.4(b)). With further milling up to 10 h, a significant improvement in density was observed (relative density of 98.7%), and only few nano porosity was observed

(the volume fraction of porosity was less than 1.0%) in Fig. 4.4(c). The pores had an irregular morphology but were mostly interconnected in the sintered microstructure of the 20 h milled powder shown in Fig. 4.4(d).

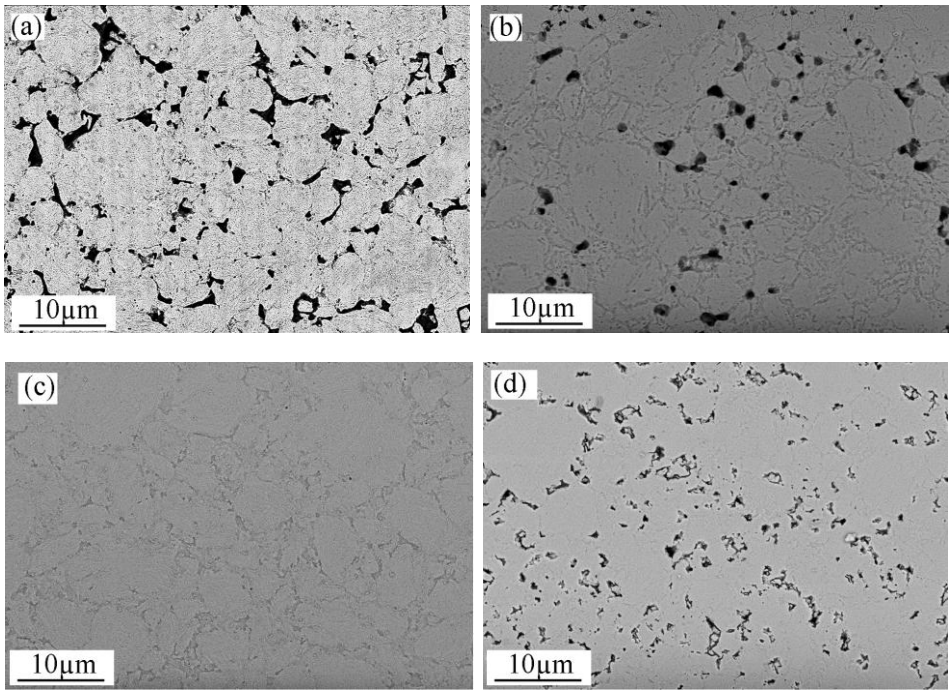

Figure 4.4. SEM – BSE micrographs of 14LMT alloy after (a) 0 h, (b) 5 h, (c) 10, and (d) 20 h of milling and SPS at 950 ^{o}C (1223 K) for 7 min

Larger agglomerated powder particles (average size of 24.1±1.8 μm) of 20 h milled powder led to larger necking joints and more interconnected porosity. In addition, high level of oxygen and carbide contamination could cause inefficiency during sintering, leading to more porosity and lower hardness in 20 h milled / sintered sample [26]. The average porosity size in the sintered14LMT alloys milled for 0 h, 5 h, 10 h and 20 h was measured to be 1.6±0.3 μm, 1.1±0.2 μm, 100±30 nm and 0.9±0.1 μm, respectively. The porosity volume percentage for the 14LMT alloys milled for 0 h, 5 h, 10 h and 20 h was measured to be

10.5±2.3, 5.8±1.4, 1.1±0.3 and 3.9±0.4, respectively. The EBSD micrographs of the sintered alloys milled for 0 h, 5 h, 10 h and 20 h are shown in Figs. 4.5(a–d). The grains in the un-milled 14LMT alloy (shown in Fig. 4.5(a)) were coarse and equiaxed and La_2O_3 particles were mostly located at the powder boundaries. No nanograin or bimodal grain structure was observed in Fig. 4.5(a).

In Fig. 4.5(b), majority of the observed grains were difficult to be resolved and indexed due to their nanoscale size and only few micron-sized grains were present. A higher volume fraction of the micron-sized grains were observed after 10 h and 20 h of milling as shown in Figs. 4.5(c–d). The EBSD micrographs presented random crystallographic orientations in the micron-sized grains, and no evidence of strong texture or elongated grains were observed. In the EBSD micrographs, individual nanograins and associated grain boundaries were difficult to distinguish due to the beam size limit. Consequently, here the EBSD micrographs were used only to analyze the micron-sized grains and not the nanograins.

The grain size distribution histograms obtained from Figs. 4.5(a–d) were plotted in Figs. 4.6(a–d). Under the sintered state, the grain size distribution exhibited micron sized grains in the unmilled alloy, nanograins in 5 h milled alloy, and bimodal grain structure in 10 and 20 h milled 14LMT alloy. Although the EBSD micrographs of the 14LMT alloy milled for different durations (5 h, 10 h and 20 h) exhibited a bimodal distribution consisted of coarse grains with a few micron level grains and nanograins with 200–500 nm size, the presence of such heterogeneous microstructure is not limited only in the alloys consolidated via SPS. Such bimodal microstructure were also observed in the ODS alloys consolidated via HIP [27] and hot forging [28]. In fact, the absence of a bimodal microstructure in the

unmilled alloy and yet its presence after longer milling times would suggest that a bimodal microstructure could develop as a result of the milling process.

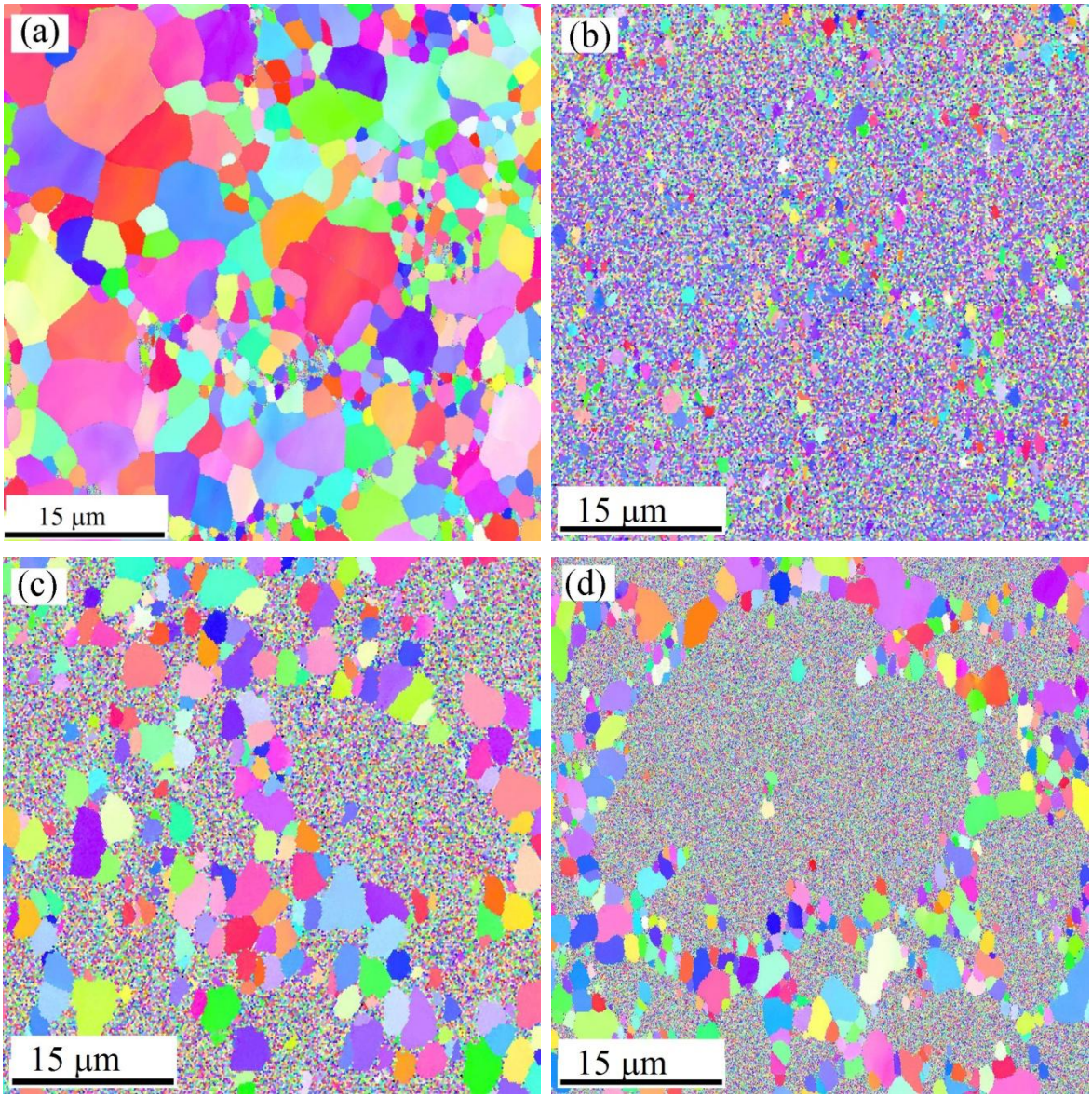

Figure 4.5. The EBSD micrographs of 14LMT alloy after (a) 0 h, (b) 5 h, (c) 10 h, and (d) 20 h of milling and SPS at 950 ^{o}C (1223 K) for 7 min

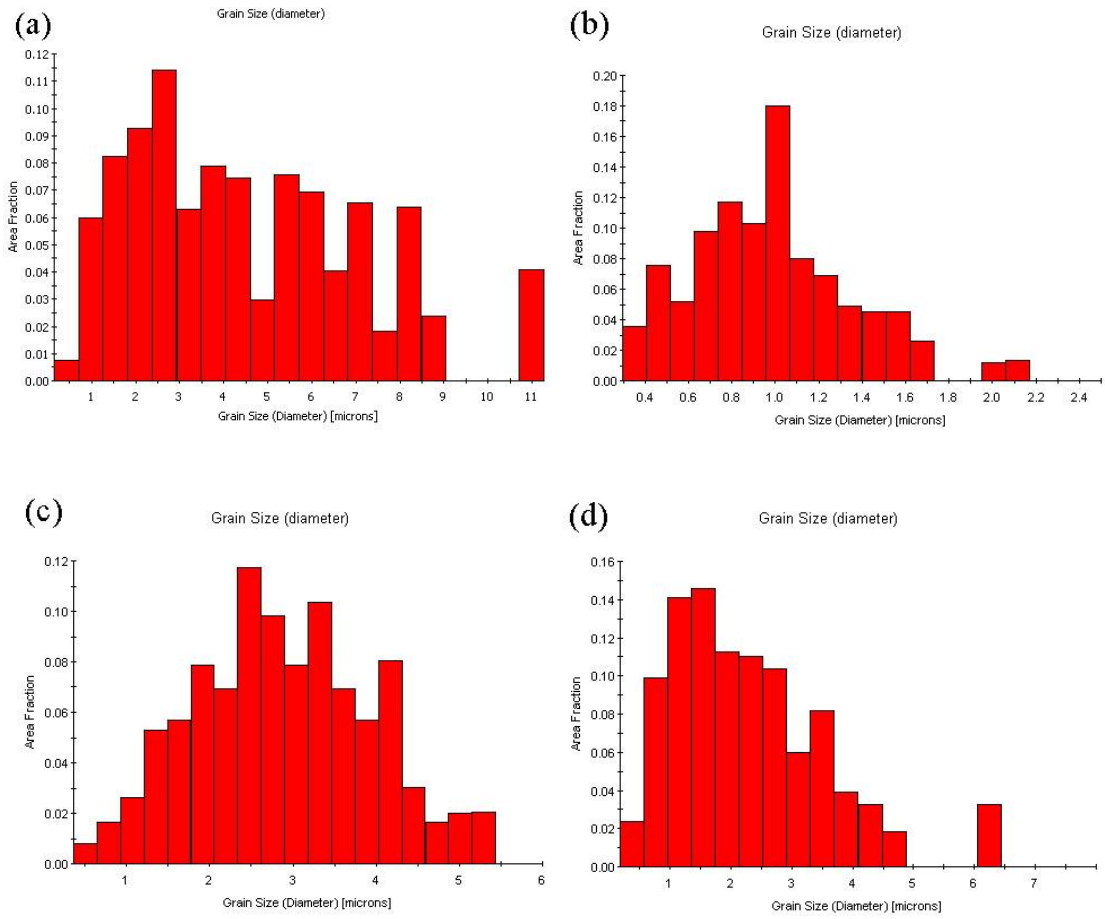

Figure 4.6. The grain size distribution histograms of 14LMT alloy obtained from EBSD results after (a) 0 h, (b) 5 h, (c) 10 h, and (d) 20 h of milling and SPS (950 ^{o}C (1223 K) for 7 min) 14LMT alloy

Because high dislocation density and dislocation cells that are created in the nanograins regions during high energy milling could lead to extended recovery or recrystallization initiation in some of these grains [23, 24] even at the early stages of sintering. Besides, during SPS pulsed DC current directly passes through the die and the powder, creating rapid Joule heating. The localized temperature gradient created within the heavily deformed nanostructured milled powder would assist in further developing of a bimodal microstructure [8]. Therefore, heavy plastic deformation during MA, and thermal gradient

from the electric field during SPS can produce grains of different orientations and different sizes. However once the alloy is consolidated, any further grain growth through the movement of high angle grain boundaries would be impeded by the presence of nano-sized precipitates [29].

The TEM overview micrographs of the 14LMT alloy milled for 0 h, 10 h and 20 h and sintering at 950 ^{o}C (1223 K) for 7 min are displayed in Figs. 4.7(a–c), respectively. No bimodal microstructure and nanograins were observed in Fig. 4.7(a). Instead, the grains with an average diameter of 2.5 μm and small La_2O_3 particles were observed heterogeneously with no nano-oxide precipitates.

Two major types of grain structures were observed in Fig. 4.7(b): nanograins (50–200 nm) embedded in a heavily deformed matrix containing nano precipitates, and micron-sized grains (>500 nm and <2 μm) containing larger precipitates. This was consistent with the broad grain size distribution for this specimen as shown in Fig. 4.6. Once the bimodal microstructure is formed, it is going to be very stable. Odette *et al.* [3] suggested this type of microstructure is likely due to a heterogeneous distribution of nano-oxide precipitates formed during hot consolidation. The heterogeneous distribution of the oxide NCs in the milled 14LMT alloy has been previously reported by the authors [18], and therefore the initiation of a stable bimodal microstructure is likely to be formed during milling. The nanograins showed a darker contrast due to high dislocation density as will be shown in STEM micrographs; however, the micron-sized grains did not exhibit a high dislocation density due to the recrystallization process during SPS. The nano-oxide precipitates were smaller and higher in number inside the nanograins.

The micron sized grains had smaller number and lager size of oxide precipitates. The high density of oxide precipitates would contribute to stabilizing the grain boundaries and control the recrystallization process during sintering. In Fig. 4.7(b), the nano precipitates were observed in sub-grains and it may lead to a complex interaction between the processes of precipitation and further recrystallization [29]. This is consistent with the results of other studies and formation of nanoparticles in ODS steels even during MA [17, 30-32].

The significant difference in processing time between SPS and other consolidation techniques (such as HIP) suggests that precipitation reaction is accelerated during SPS. Similar microstructure was also observed in Fig. 4.7(c) after milling the 14LMT alloy for 20 h and sintering at 950 ^{o}C (1223 K) for 7 min.

The high angle annular dark field (HAADF) micrographs from the 14LMT alloy milled for 10 and 20 h and sintered at 950 ^{o}C (1223 K) for 7 min are shown in Figs. 4.8(a–b), respectively. Both Figs. 4.8(a−b) exhibited nanograins with nano-precipitates smaller in size but higher in number density whereas coarser (micron-sized) grains had nano-precipitates larger in size but lower in number density. A high dislocation density was observed in nanograins of 14LMT alloy milled for 10 h and sintered at 950 ^{o}C (1223 K) for 7 min, as shown in Fig. 4.8(c). Dislocation density in this specimen was estimated to be 6.5×10^{14} m^{-2} estimating the foil thickness to be approximately 50 nm using FIB. For comparison, Klueh *et al.* [33] reported the dislocation density of milled / extruded 12YWT (Fe–12Cr–2.5W–0.4Ti–0.25Y_2O_3 manufactured by Kobe Special Tube Co. Ltd.) to be 10^{15}–10^{16} m^{-2}

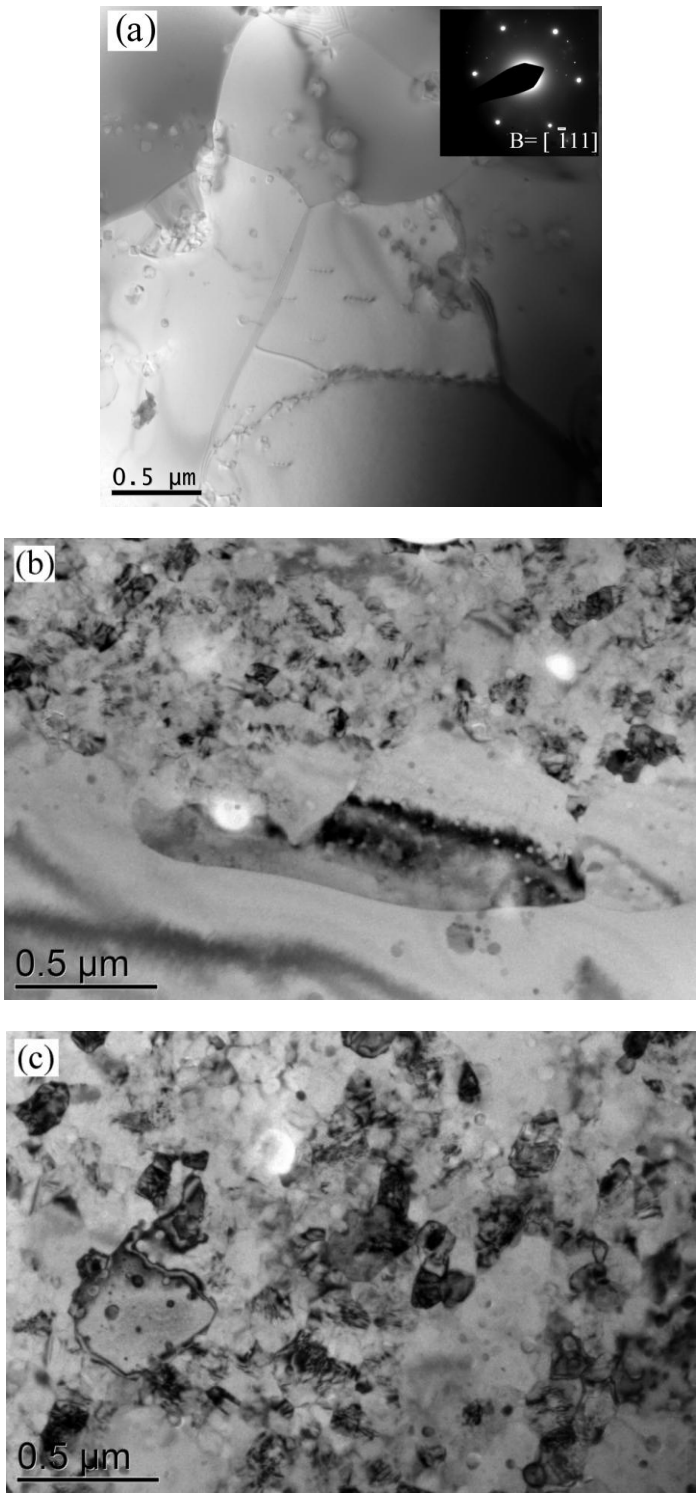

Figure 4.7. Bright Field TEM micrographs of 14LMT alloy after (a) 0 h, (b) 10 h, and (c) 20 h of milling and SPS at 950 ^{o}C (1223 K) for 7 min

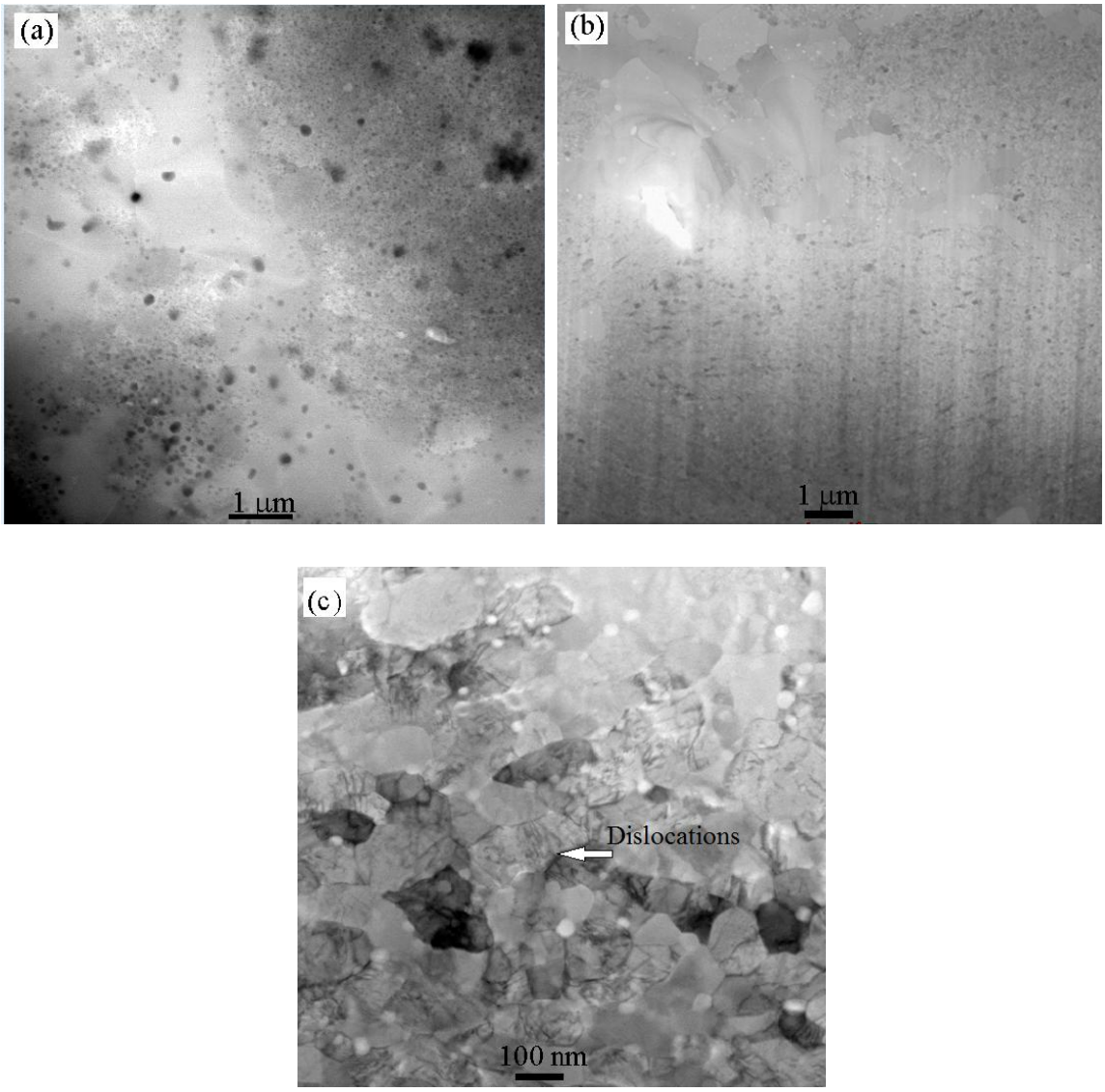

Figure 4.8. The HAADF STEM images of 14LMT alloy (SPSed at 950 ^{o}C (1223 K) for 7 min) showing nanograins, coarse grains and precipitates after milling for (a) 10 h, (b) 20 h, and (c) dislocations in nanograins after 10 h of milling

High amount of stored energy in the milled powder and less efficient oxide precipitates in larger subgrains would facilitate a fast recovery and recrystallization. However, no further recrystallization could occur because the interaction between dislocations and precipitates would hinder the recrystallization process.

A high resolution TEM micrograph from the small precipitates is shown in Fig. 4.9(a). Those precipitates that were mostly found at the grain interiors were as small as 2 nm with faceted morphology. However, those larger particles with quasi-spherical morphology were mostly located at the grain boundaries. A HAADF micrograph of the sintered 14LMT alloy is shown in Fig. 4.9(b). The corresponding energy dispersive spectroscopy (EDS) spectrum obtained from a nano-precipitate is shown in Fig. 4.9(c).

The EDS results showed that precipitates larger than 10 nm were enriched in Cr and mostly spherical whereas precipitates smaller than 10 nm were enriched in La and Ti. Due to the significant influence of the matrix, EDS was not very efficient in analyzing the small precipitates. The Cr concentration in the matrix was in the range of 12–15 at.%, and no significant Ti or La was detected in the matrix. The concentrations of Cr, Ti and La in the precipitates smaller than 10 nm were found to be 8 at.%, 8 at.% and 4−6 at.%, respectively, with Fe as remaining. The Ti / La ratio was found to be 2–2.5 which does not correlate to a stoichiometric compound. It can be seen that the faceted precipitate was non-stoichiometric La–Ti–C-enriched oxide. Due to inefficiency of EDS in analyzing nano-precipitates, more powerful characterization tool such as atom probe tomography (APT) will be used in future work to study the chemical composition of these precipitates.

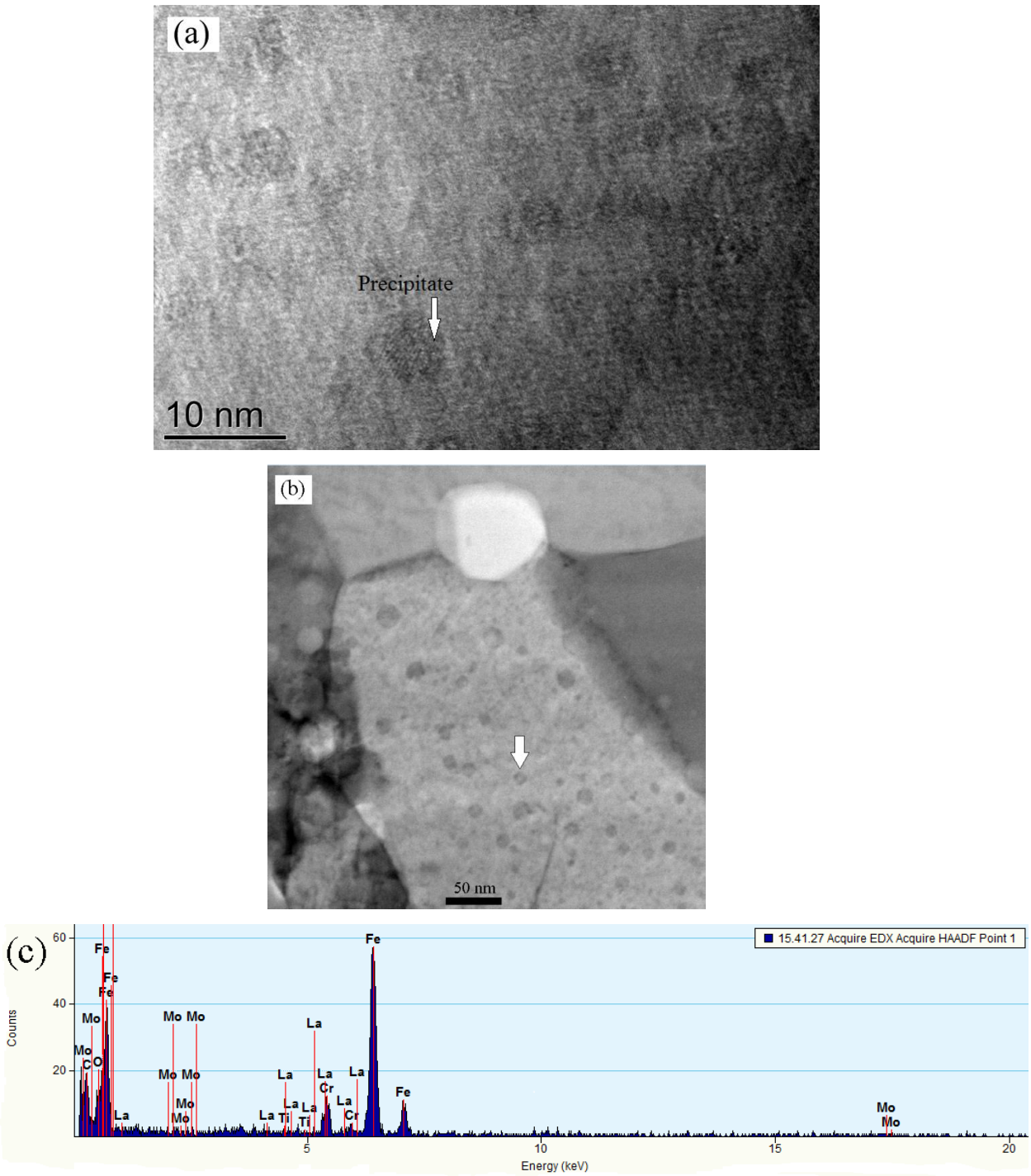

Figure 4.9. (a) A HRTEM image of 14LMT (10 h milled, SPSed 950 ^{o}C (1223 K) for 7 min), (b) the HAADF STEM micrograph showing the grains and precipitates in a nanograin, and (c) the EDS spectrum from a precipitate with diameter of 10 nm shown by an arrow in Fig. 4.9(b)

4.4. Conclusions

This work has examined the effect of milling on the densification behavior, density, hardness and microstructure of a La-bearing NFS processed via SPS. The MA followed by SPS created a heterogeneous microstructure with a bimodal grain size distribution. The main conclusions made are summarized as follows:

1. The role of ball milling was more complex than just the dissolution of the solute elements and had a significant impact on the densification behavior. Ball milling would enhance the rate of densification by lowering the sintering start temperature.

2. The activation energy of both volume and grain boundary diffusion decreased with increasing milling time. For the unmilled alloy, the activation energy of the volume diffusion was higher than that of grain boundary diffusion. For the milled alloy, the activation energy of volume diffusion was estimated to be less due to vacancies and point defects incorporated in the alloy as a result of high energy ball milling.

3. The density and hardness of the sintered 14LMT alloys milled for 10 h were measured to be 98.7% with a hardness of 505 HV. In order to achieve significant dispersion hardening in 14LMT alloy, La_2O_3 particles have to be mechanically milled; only mixed powder will not lead to the desired properties.

4. The microstructure of the sintered unmilled alloy showed significant porosity. The size and number of pores decreased after 5 h, and only few nano-pores were observed after SPS of 10 h milled powder. With further milling beyond 10 h, the number of residual porosity increased again, and they became interconnected.

5. The microstructure of the 10 h and 20 h milled powder after SPS revealed a bimodal grain size distribution with micron-sized grains (> 500 nm, < 2 μm) surrounded by nanograins (200 – 500 nm). The majority of the microstructure contained high concentration of nano-precipitates. The bimodal grain size distribution was due to ball milling and subsequent SPS. No bimodal grain structure was observed in unmilled alloy.

6. High microhardness of the milled / SPSed samples was due to the presence of the solid solution strengthening, nanograins, high dislocation density and high number density of nano-oxide precipitates. The precipitates act efficiently as pinning sites against the dislocation movement and also inhibit grain boundary sliding and grain growth.

Acknowledgments

This work was supported partly by the Laboratory Directed Research and Development Program of Idaho National Laboratory, Contract DE–AC07–05ID14517, and partly by a grant of the Advanced Test Reactor National Scientific User Facility (ATRNSUF). The help of the Boise State University (BSU) and the Center for Advanced Energy Studies (CAES) staff is greatly acknowledged.

References

[1] P. Unifantowicz, Z. Oksiuta, P. Olier, Y. de Carlan, and N. Baluc: *Fusion Eng. Des.*, 2011, vol. 86, pp. 2413–2416.

[2] E.A. Marquis: *App. Phys. Lett.*, 2008, vol. 93, pp. 181901–181903.

[3] G.R. Odette, M.L. Alinger, and B.D. Wirth: *Annu. Rev. Mater. Res.*, 2008, vol. 38, pp. 471–503.

[4] A. Kimuraa, H. Chob, N.Todab, R. Kasadaa, H. Kishimotoa, N. Iwataa, S. Ukaic, S. Ohtsukac, and M. Fujiwarad: *Proceedings of ICAPP '06 Reno*, 2006, pp. 2229–2237.

[5] H. Sakasegawa, L. Chaffron, F. Legendre, L. Boulanger, T. Cozzika, M. Brocq, and Y.D. Carlan: *J. Nucl. Mater*., 2009, vol. 384, pp. 115–118.

[6] K.N. Allahar, J. Burns, B. Jaques, Y. Wu, I. Charit, J.I. Cole, and D.P. Butt: *J. Nucl. Mater*., 2013, vol. 443, pp. 256–265.

[7] Y. WU, K.N. Allahar, J. Burns, I. Charit, D.P. Butt, and J.I. Cole: *Cryst. Res. Technol*., 2013, DOI: 10.1002/crat.201300173

[8] B. Srinivasarao, K. Ohishi, T.Ohkubo, and K. Hono: *Acta. Mater.*, 2009, vol. 57, pp. 3277–3286.

[9] G. Ji, F. Bernard, S. Launois, and T. Grosdidier: *Mater. Sci. Eng. A.*, 2013, vol. 559, pp. 566–573.

[10] S. Pasebani, and I. Charit: *J. Alloys. Compd.*, 2014, vol. 599, pp. 206–211.

[11] Y.P. Xia, X.P. Wang, Z. Zhuang, Q.X. Sun, T. Zhang, Q.F. Fang, T. Hao, and C.S. Liu: *J. Nucl. Mater.*, 2013, vol. 432, pp. 198–204.

[12] Y. Kim, K.H. Lee, E.P. Kim, D.I. Cheong, and S.H. Hong: *Int. J. Refract. Metals& Hard Maters.*, 2009, vol. 27, pp. 842–846.

[13] M.J. Alinger, G.R. Odette, and D.T. Hoelzer: *Acta. Mater.*, 2009, vol. 57, pp. 392–406.

[14] http:// www. Molycorp. Com.

[15] M. Endo, K. Kimura, T. Udagawa, S. Tanabe, and H. Seto: *High. Temp. High. Press.*, 1990, vol. 20, pp. 129–137.

[16] Z.D. Reed, and M.A. Duncan, *J. Phys. Chem.*: 2008, vol. 112, pp. 5354–5326.

[17] S. Pasebani, I. Charit, D.P. Butt, and J.I. Cole: *J. Nucl. Mater.*, 2013, vol. 434, pp. 282–286.

[18] S. Pasebani, I. Charit, Y.Q.Wu, D.P. Butt, and J.I. Cole: *Acta Mater.*, 2013, vol. 61, pp. 5605–5617.

[19] W.S. Young, and I.B. Cutler: *J. Am. Ceram. Soc.*, 1970, vol. 53, pp. 659–663.

[20] J. Guyon, A. Hazptte, J.P. Monchoux, and E. Bouzy: *Intermetallics.*, 2013, vol. 34, pp. 94–100.

[21] S. Libardi, M. Zadra, F. Casari, and A. Molinari: *Mater. Sci. Eng. A.*, 2008, vol. 478, pp. 243–250.

[22] H.J. Frost, and M.F. Ashby: *Fundamentals aspects of structural alloy design*, Plenum, 1977.

[23] S.V. Matrenin, A.P. Ilin, A.I. Slosman, and L.O. Tolbanova: *Russian J. Non-Ferrous Met.*, 2009, vol. 50, pp. 513–517.

[24] J.S. Lee, J.P. Choi, and G.Y. Lee: *Materials,* 2013, vol. 6, pp. 4046–4063.

[25] R. Chaim, and M.Margulis: *Mater. Sci. Eng. A.*, 2005, vol. 407, pp. 180–187.

[26] C.L. Chen, and Y.M. Dong: *Mater. Sci. Eng. A.*, 2011, vol. 528, pp. 8374–8380.

[27] Z. Oksiuta, A. Ozieblo, K. Perkowski, M. Osuchowski, and M. Lewandowska: *Fusion. Eng. Des.*, 2014, vol. 89, pp. 137–141.

[28] Z. Dapeng, L. Yong, L. Feng, W. Yuren, Z. Liujie, and D. Yuhai: *Mater. Lett.*, 2011, vol. 65, pp. 1672–1674.

[29] F.J. Humphreys, M. Hatherly: *Recrystallization and Related Annealing Phenomena*, 2nd ed., Elsevier, Oxford, 2004.

[30] C.A. Williams, P. Unifantowicz, N. Baluc, G.D. Smith, and E. M. Marquis: *Acta. Mater.*, 2013, vol.61, pp. 2219–2235.

[31] L.M. Brocq, F. Legendre, M.H. Mathon, A. Mascaro, S. Poissonnet, B. Radiguet, P. Pareige, M. Loyer, and O. Leseigneur: *Acta. Mater.*, 2012, vol. 60, pp. 7150–7159.

[32] L.M. Brocq, B. Radiguet, S. Poissonnet, F. Cuvilly, P. Pareige, and F. Legendre: *J. Nucl. Mater.*, 2011, vol. 409, pp. 80–85.

[33] R.L. Klueh, J.P. Shingledecker, R.W. Swindeman, and D.T. Hoelzer: *J. Nucl. Mater.*, 2005, vol. 341, pp.103–114.

CHAPTER 5: Spark Plasma Sintering of Lanthana-Bearing Nanostructured Ferritic Steels

Somayeh Pasebani[a,d], *Indrajit Charit*[a,d] , *Yaqiao Wu*[b,d], *Jatuporn Burns*[b,d]

Kerry N. Allahar[b,d], *Darryl P. Butt*[b,d] *and James I. Cole*[c,d]

[a] Department of Chemical and Materials Engineering, University of Idaho, Moscow, ID 83844, USA

[b] Department of Materials Science and Engineering, Boise State University, Boise, ID 83725, USA

[c] Idaho National Laboratory, Idaho Falls, ID 83401, USA

[d] Center for Advanced Energy Studies, Idaho Falls, ID 83401, USA

(*Submitted to the Journal of Materials Science and Engineering A*)

Abstract

A lanthanum-containing nanostructured ferritic steel was processed via mechanical alloying of Fe–14Cr–1Ti–0.3Mo–0.5La_2O_3 (wt.%) powder followed by spark plasma sintering. The effects of sintering temperature and dwell time were investigated on the microstructure, relative density, microhardness and shear yield strength of the sintered specimens. While the recrystallization nucleation occurred within some grains, the presence of a high number of nanoparticles impeded further recrystallization. This resulted in a bimodal grain size distribution observed in the microstructure of specimens sintered at 850–1050 ^{o}C for 45 min. Significant densification occurred at temperatures greater than 950 ^{o}C with a relative density higher than 98%. A variety of nanoparticles, some enriched in Fe and Cr oxides and copious nanoparticles smaller than 10 nm with faceted morphology and enriched in La and Ti oxide

were observed. After SPS at 950 ^{o}C, the number density of Cr–Ti–La–O-enriched nanoclusters with an average radius of 1.5 nm was estimated to be 1.2×10^{24} m^{-3}. The La+Ti:O ratio was close to 1 after SPS at 950 and 1050 ^{o}C; however, the number density of nanoclusters decreased at 1050 ^{o}C. With SPS above 950 ^{o}C, the density improved whereas the microhardness and shear yield values declined due to partial coarsening of grains and nanoparticles.

Keywords: Mechanical alloying; Powder metallurgy; Sintering; Steels; Nanostructured materials; Atom probe.

5.1. Introduction

Nanostructured ferritic steels (NFSs) are considered potential candidates for fuel cladding and structural applications in advanced nuclear reactors. These steels possess high creep and tensile strength along with excellent radiation damage tolerance [1-3]. The NFSs are distinguished from conventional oxide dispersion strengthened (ODS) steels because of the finer microstructure and smaller size of oxide dispersions. The unique properties of the NFSs such as 12YWT (Fe–12Cr–3W–0.4Ti–0.25Y_2O_3, wt.%) and 14YWT (Fe–14Cr–2W –0.3Ti–0.3Y_2O_3, wt.%) are derived from the presence of an ultrahigh density of Y–Ti–O-enriched nanoclusters (NCs). These NCs are formed via mechanical alloying (MA) of Fe–Cr–Ti powder with Y_2O_3 followed by a hot consolidation route [4-6]. The most commonly used Rare Earth (RE) oxide in ferritic ODS or NFSs is yttria, Y_2O_3; in the present study, the potential of using an alternative RE oxide in processing a new NFS was investigated by replacing the Y_2O_3 with lanthanum oxide, La_2O_3. This replacement can be rationalized by considering that La_2O_3 is thermally stable at high temperature and insoluble

in solid iron at all temperatures [7]. It also has a low diffusion rate in the ferritic matrix and a high affinity for oxygen [8]. Based on the density function theory calculations done by Reed *et al.* [8], La_2O_3 clusters should have the same general structure as the corresponding yttrium-enriched species. Furthermore, La_2O_3 is more abundant (25–38 wt.%) than Y_2O_3 (only 0.2 wt.%) in Bastnasite, a main RE mineral in the USA (http://www.molycorp.com). There is no study in the literature on dispersing of La_2O_3 to the bulk ferritic matrix to the best of our knowledge except for our study [9]. However, Mueller *et al.* [10] investigated the precipitation hardening effect of La_2O_3, Y_2O_3 and ZrO_2 in a Mo-based ODS alloy. They have reported that La_2O_3 produced the highest ultimate tensile strength (UTS) and significantly better creep rupture properties than the other oxides.

In current study, La_2O_3 (0.5 wt.%) was added to the nominal composition of Fe–14Cr–1Ti–0.3Mo (wt.%), to give approximately equal atomic fraction to 0.3 wt.% Y_2O_3 in Fe–14Cr–1Ti–0.3Mo–0.3Y_2O_3 (wt.%) or nominal composition of a commercially produced MA957 alloy. The novel NFS with nominal composition of Fe–14Cr–1Ti–0.3Mo–0.5La_2O_3 (wt.%) is termed 14LMT, hereafter. In addition to altering the RE addition in the chemical composition, the traditional consolidation methods such as hot extrusion and hot isostatic pressing (HIP) were replaced by spark plasma sintering (SPS).

Compared to hot extrusion and HIP, the SPS technique allows sintering at lower temperatures and shorter dwell times. In SPS, the powder mixture is being uniaxially pressed while a DC pulse voltage is applied to the compact simultaneously. In the case of electrically conductive materials, heating is mainly due to the Joule effect. Although the occurrence of electrical discharges (plasma discharge) is widely mentioned in the literature [11], its existence is yet a matter of speculation. [12]. In addition to the ambiguous plasma

occurrence, several phenomena such as local melting, evaporation of oxide layers, surface and volume diffusion would enhance the neck formation between the powder particles and eventually the final densification [13].

There have been only a limited number of studies on the application of SPS in consolidating the ODS steels and NFSs [9, 14-17]. For example, Srinivasarao *et al.* [17] processed a commercially pure nanocrystalline iron by milling and SPS. Its microstructure consisted of nanograins (< 100 nm) as well as coarse grains (> 1 μm) with uniform dispersion of nano-sized chromium oxide particles. Similar heterogeneous nanostructured ODS Fe–Al alloys were produced by Ji *et al.*[16]. Heintze *et al*. [18, 19] consolidated ODS Fe–9Cr model alloys including (Fe–9 Cr, Fe–9Cr–0.3Y_2O_3 and Fe–9Cr–0.6Y_2O_3, wt.%) using SPS and studied mechanical properties as well as microstructural characteristics of these alloys. Hardness values for the Fe–9Cr ODS alloys with 0.3 wt.% and 0.6 wt.% Y_2O_3 were in the range of 216–322 HV. The combined microstructural characterization done by small angle neutron scattering (SANS), atom probe tomography (APT) and transmission electron microscopy (TEM) demonstrated that the Y–O-enriched NCs were 4.2 nm in diameter and the ratio of Y:O between 1:3 and 2:3.

Allahar *et al.* [14] used SPS to consolidate Fe–16Cr–3Al (wt.%) powder by sequentially adding Y_2O_3 and Ti powders to produce Fe–16Cr–3Al–0.5Y_2O_3 (wt.%) and Fe–16Cr–3Al–0.5Y_2O_3–1Ti (wt.%) alloys, respectively. The hardness of the alloy increased from 200 HV in Fe–16Cr–3Al matrix to 350 HV after adding 0.5Y_2O_3 and finally 480 HV after adding 0.5Y_2O_3–1Ti. The microstructure of the consolidated ODS alloys contained both ultrafine and coarse grains associated with recrystallization occurrence during SPS at 1000 ^oC. The TEM and APT studies revealed Y–O- and Y–Ti–O-enriched NCs with Y:O:Ti ratio of

3:10:8 and M:O (metal to oxygen) ratio close to 1:1, which were similar to those obtained in the ODS alloys sintered by conventional hot extrusion method [14].

A preliminary investigation [20] on the mechanically alloyed 14LMT powder revealed the presence of NCs in the nanocrystalline ferritic matrix. Subsequently, a study on the mechanically alloyed lanthana-bearing 14LMT powder was carried out [21]. The effect of alloying elements on the microstructure and mechanical properties that was reported elsewhere [9]. The present study focuses on consolidation of the mechanically alloyed 14LMT powder via SPS. Furthermore, it demonstrates the effects of SPS parameters such as temperature and dwell time on the microstructure and mechanical properties of the 14LMT steel.

5.2. Experimental procedure

5.2.1. High energy ball milling

The starting constituent powders including Fe (99.9 wt.%, average particle size of 40 μm), Cr (99.8 wt.%, average particle size of 5 μm), Ti (99.7 wt.%, average particle size of 26 μm), La_2O_3 (99.99 wt.%, average particle size of 40 nm) and Mo (99.9 wt.%, average particle size of 1–2 μm) were mixed in the nominal proportion of Fe–14Cr–1Ti–0.3Mo–0.5La_2O_3 (wt.%). The Mo powder was obtained from the Micron Metal Inc and the remaining powders (Fe, Cr, Ti and La_2O_3) were procured from American Elements Inc. High energy ball milling was performed in an air-cooled SPEX 8000M mixer / mill for 10 h using 316 stainless steel balls (8 mm in diameter) as the milling media. A milling batch consisted of 100 g steel balls and 10 g powder giving a ball to powder ratio (BPR) of 10:1.

5.2.2. Spark plasma sintering

A Dr. Sinter Lab SPS-515S machine (SPS Syntex Inc., Kanagawa, Japan) was used to consolidate the as-milled powder. A Tri-Gemini cylindrical graphite die with an inner diameter of 12.7 mm and an outer diameter of 38 mm was used. The inner surface of the die and radial surfaces of punches were covered with a graphite foil (thickness of 0.25 mm) to facilitate the removal of the sintered specimens. In order to inhibit the diffusion of carbon from the punches and graphite foil to the powder mixture, a thin niobium foil was placed between the powder and the graphite foils. The die was wrapped in a graphite felt (thickness of 4 mm) to minimize heat loss by thermal radiation. The as-milled powder was sintered under vacuum (7×10^{-3} Torr or 0.9 Pa) at temperatures ranging from 850 to1100 ^{o}C and various dwell times of 0, 2, 20 and 45 min. A pulsed DC current with pattern of 12–2 (current on for 12 ms and off for 2 ms), a heating rate of 100 ^{o}C/min and a pressure of approximately 80 MPa (10 kN force) were used. The temperature was monitored with a K-type thermocouple that was inserted in a hole in the die such that the tip was located 6 mm away from the sintering powder. The sintered samples were cooled to room temperature in the vacuum chamber at approximately 50 ^{o}C/min. The final product was in the form of a disk with dimensions of 12.5 mm diameter and 8 mm thickness. Some taller samples with 20 mm in height were also produced for tensile tests in the future work. The temperature, applied current, voltage, applied pressure and the vertical displacement of the lower punch were monitored and recorded during the sintering process.

5.2.3. Microstructural and compositional characterization

Microstructural characteristics of the sintered specimens were examined using a Zeiss LEO Supra 35 VP FESEM at accelerating voltages of 15–20 kV. Some specimens were also

prepared for electron back scatter diffraction (EBSD) characterization by polishing sequentially from 120 through 1200 grit SiC papers, followed by a final polish in a Buehler Vibromet-2 vibratory polisher using 0.05 μm alumina slurry for 6 to 24 h. The EBSD analysis was performed on a JEOL JSM–6610LV scanning electron microscope (SEM) equipped with an EDAX / TSL Hikari EBSD system. The SEM was operated at an accelerating voltage of 20 kV. The automated scan was performed with a 0.1 μm step size on a total area of 50×50 μm^2. The EBSD data were analyzed using the TSL Orientation Imaging Microscopy (OIM™) Data Collection version 5.31 software.

After SPS, disks with 3 mm in diameter were mechanically thinned and electropolished in an electrolyte of CH_3OH–HNO_3 (80:20 by vol.%) at a temperature of –30 ^oC using a Fischione Model 110 Twin-Jet Electropolisher. Transmission electron microscopy (TEM) studies along with energy dispersive spectroscopy (EDS) experiments were performed using a FEI Tecnai TF30 FEG STEM operating at 300 kV. A focused ion beam (FIB) was used to prepare specimens for atom probe tomography (APT) studies. The FIB effort was carried out using an FEI Quanta 3D – FEG instrument with a Ga-ion source. The APT analysis was carried out using a CAMECA LEAP 4000X HR operating in voltage mode at the specimen temperature of 50–60 K and 20% of the standing voltage pulse fraction. The atom maps were reconstructed using CAMECA IVAS 3.6 software. The maximum separation cluster algorithm was used to identify the composition of NCs. The maximum separation between solute atoms is defined as d_{max} whereas L is the maximum separation of additional elements, $N_{\min}$ is the minimum size of a cluster and E is the erosion distance for removal of atoms near the cluster−matrix interface. An N_{min} value of 10–15, d_{max} values of 0.6–0.8 nm, L values of 0.4–0.5 nm and E values ranging from 0.3–0.5 nm were chosen based on procedures

described comprehensively in the literature [6, 22-25]. The bulk composition was calculated based on the total number of atoms of each element in a complete analysis volume and was averaged over at least three different tip coupons. A background noise correction was applied to the mass spectrum and the matrix composition was calculated by excluding those atoms defined as a cluster based on the maximum separation method. The size of NCs was estimated from the radius of gyration (R_g) that is the average distance between each atom and center of a corresponding cluster [26, 27]. This was applied to APT datasets each containing 20–30 million ions. The clustering of each individual oxide-type was investigated, and Ti–O, Cr–O along with La showed clustering (according to the reduced Chi square (χ^2) values) [27]. The quantity of matrix was artificially set to zero using a model outlined by Williams *et al.* [6] in order to remove the matrix contribution. The cluster composition calculated this way was termed "matrix corrected"

5.2.4. Density and mechanical characterization

The density of the sintered specimens was measured by Archimedes' method. At least six measurements were made for each specimen. The final relative density was expressed in percentage and determined as the ratio between the measured and the theoretical density (~7.7 g/cm^3) of 14LMT alloy. The Vickers microhardness tests were performed using a Leco LM100 microhardness tester at a 1 kg (9.81 N) with a dwell time of 15 s. Shear punch experiments were carried out on an Instron 5967 electromechanical test frame. Several shear-punch disk specimens with 3 mm in diameter were punched out from the foils with an average thickness of 250–350 μm. Tests were conducted at room temperature using a displacement rate of 240 μm / min (or 4 μm / s) and repeated three to four times for each processing condition. The shear punch fixture included a 1 mm diameter flat-end punch,

which sheared a portion of a 3 mm diameter specimen into a 1.02 mm diameter hole in the receiving die. Punch displacement was measured using a linear variable differential transformer (LVDT) with a range of ±3.2 mm. Shear punch data were obtained in terms of the punch load and displacement. Then the shear yield strength was determined using the following equation:

$$\tau = \frac{p}{2\pi r t} \quad (5.1)$$

where p is the load, r is the average of the hole and punch radii, and t is the specimen thickness [28].

5.3. Results

5.3.1. Effect of the SPS temperature and time on the microstructural evolution

5.3.1.1. SEM and EBSD studies

The SEM micrographs along with the EBSD maps as insets from the various 14LMT specimens are shown in Figs. 5.1(a–f). The grain structure was not clearly revealed in any of the SEM micrographs presented in Figs. 5.1(a–f) due to the nanograins. The EBSD micrograph in Fig. 5.1(a) showed the combination of nanograins and coarse grains (mixture of ultrafine and micron-sized grains) in the consolidated microstructure. The area fraction of the coarse grains increased in Fig. 5.1(b) at longer dwell times. The porosity in Figs. 5.1(a–b) was observed as regions with a darker contrast. The area fraction of porosity generally decreased with increasing SPS temperature and time. The area fraction of porosity was calculated close to 6.4±2.3% (Fig. 5.1(a)) and 5.1±2.1% (Fig. 5.1(b)) after SPS at 850^{o}C for 7 and 45 min, respectively.

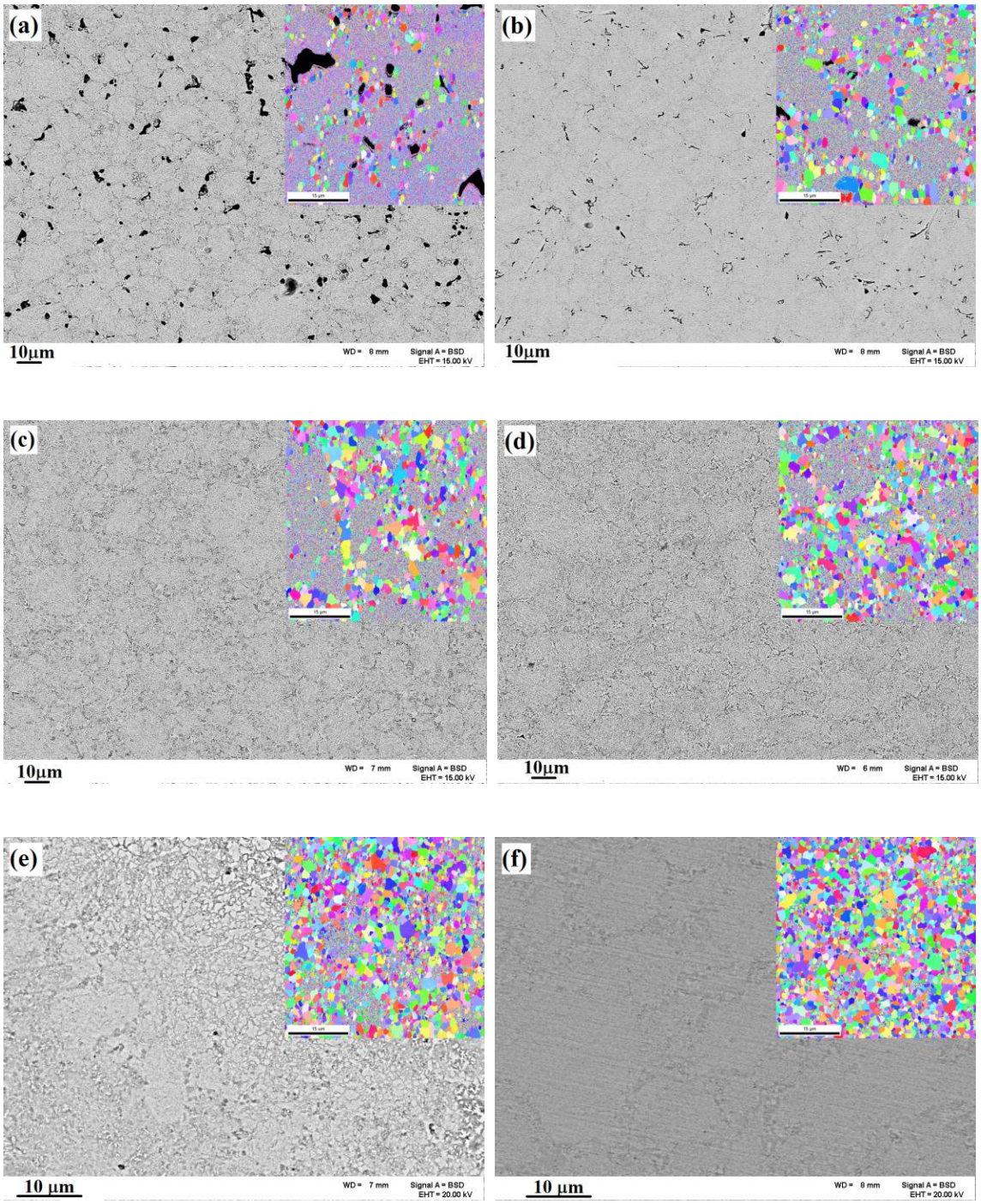

Figure 5.1. SEM and EBSD micrographs of the specimens SPSed at (a) 850 ^{o}C for 7 min, (b) 850 °C for 45 min, (c) 950 °C for 7 min, (d) 950 °C for 45 min, (e) 1050 °C for 7 min, and (f) 1050 °C for 45 min

Increasing the dwell time from 7 min to 45 min at 950^{o}C improved densification to some extent (e.g. the area fraction of porosity decreased from 1.1±0.3% to 0.8±0.3%) and increased the area fraction of coarse grains. The area fractions of porosity in Figs. 5.1(e–f) were estimated to be 0.7±0.4% and 0.7±0.2%, respectively. The area fraction of coarse grains was higher at the SPS temperature of 1050 ^{o}C and very much dependent on the dwell time. Higher SPS temperature and longer dwell time improved the densification but led to a higher proportion of coarse grains. Furthermore, it is evident that the main densification occurred at 950 ^{o}C.

5.3.1.2 TEM studies

The TEM bright field images from the microstructure and nanoparticles in the 14LMT alloy sintered at 850 ^{o}C for 45 min are shown in Figs. 5.2(a–c). A non-homogeneous distribution of ultrafine grains with a broader grain size distribution (~ 100 nm to 1 μm) and nanograins (100 nm) was revealed in Fig. 5.2(a). The type of non-homogenous distribution of grains is similar to the bimodal grain size distribution as revealed in other studies [14, 17]. The boundaries of these ultrafine grains were pinned by either larger nanoparticles or by the triple-junction of the grain boundaries themselves. As will be demonstrated, these nanoscale particles were determined to be mainly oxides. The presence of the oxide particles on the boundary and interior of the ultrafine grains implied that these particles could have a significant role in controlling the dynamic recrystallization and dependent microstructural evolution. The average diameter of nanograins and ultrafine grains in the 14LMT alloy after SPS at 850 ^{o}C for 45 min was calculated to be 76±10 nm and 470±30 nm, respectively. The area fraction of ultrafine grains was approximately 37% with the remaining attributed to nanograins.

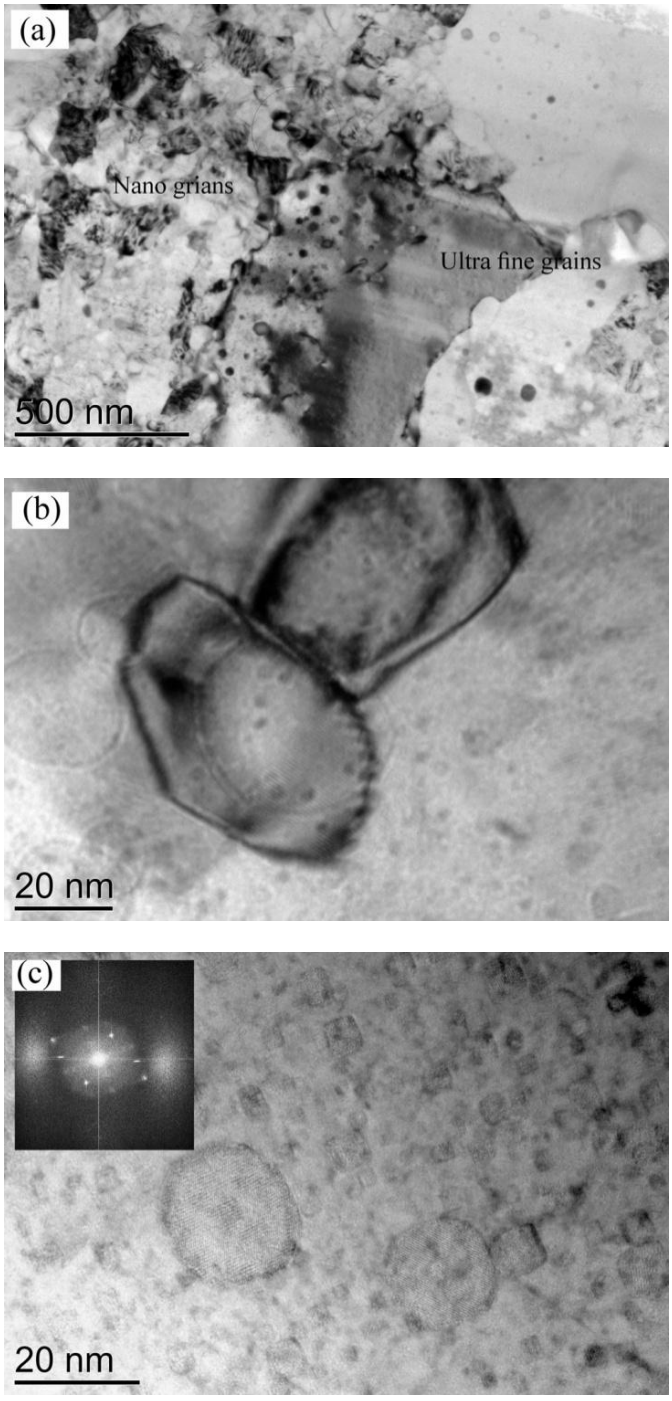

Figure 5.2. TEM micrographs of the 14LMT alloy SPSed at 850 °C for 45 min: (a) a bright field micrograph of a bimodal grain size distribution, (b) recrystallization nuclei in the circle shown in (a) with nanoparticles in the interior, and (c) nanoparticles with diameters varying between 3–20 nm

A higher magnification micrograph from the black circle shown in Fig. 5.2(a) is presented in Fig. 5.2(b). A few nanograins with a high number of particles as small as 2–3 nm were observed. No dislocations were observed in these nanograins (even after tilting in different two beam condition) suggesting that these are possibly the nuclei for the recrystallized grains most likely originated on the deformed grains. Nanoparticles with faceted morphology and diameter between 2–30 nm were clearly observed as shown in Fig. 5.2(c). Further EDS analysis demonstrated that these faceted nanoparticles contained La and Ti along with matrix elements and oxygen. The microstructure of the 14LMT alloy sintered at 950 ^{o}C for 45 min is shown in Figs. 5.3(a–c). The bimodal distribution of nano and ultrafine grains was revealed in Fig. 5.3(a). The microstructure contained a high number of dislocations, nanoparticles and nanograins. The recrystallized ultrafine grains were surrounded by nanograins and non-homogeneously distributed in the microstructure. The average diameter of nanograins and ultrafine grains in the 14LMT alloy after SPS at 950 ^{o}C for 45 min was calculated to be 112±10 nm and 539±30 nm, respectively. Approximately 45% of the area contained the ultrafine grains. Ultrafine grains with a high number density of nanoparticles in the interior and on the boundaries were observed as shown in Fig. 5.3(b). The evidence of subgrain formation was observed in Fig. 5.3(c). It can imply the possibility of recovery and recrystallization occurring simultaneously during SPS at 950 ^{o}C. Meanwhile, coarser particles induced more dislocations and facilitated recovery and sub-grain formation. The nanoparticles as small as 2–3 nm were observed and are shown in Fig. 5.3(c). They did not show any notable coarsening with increasing sintering temperature or dwell time.

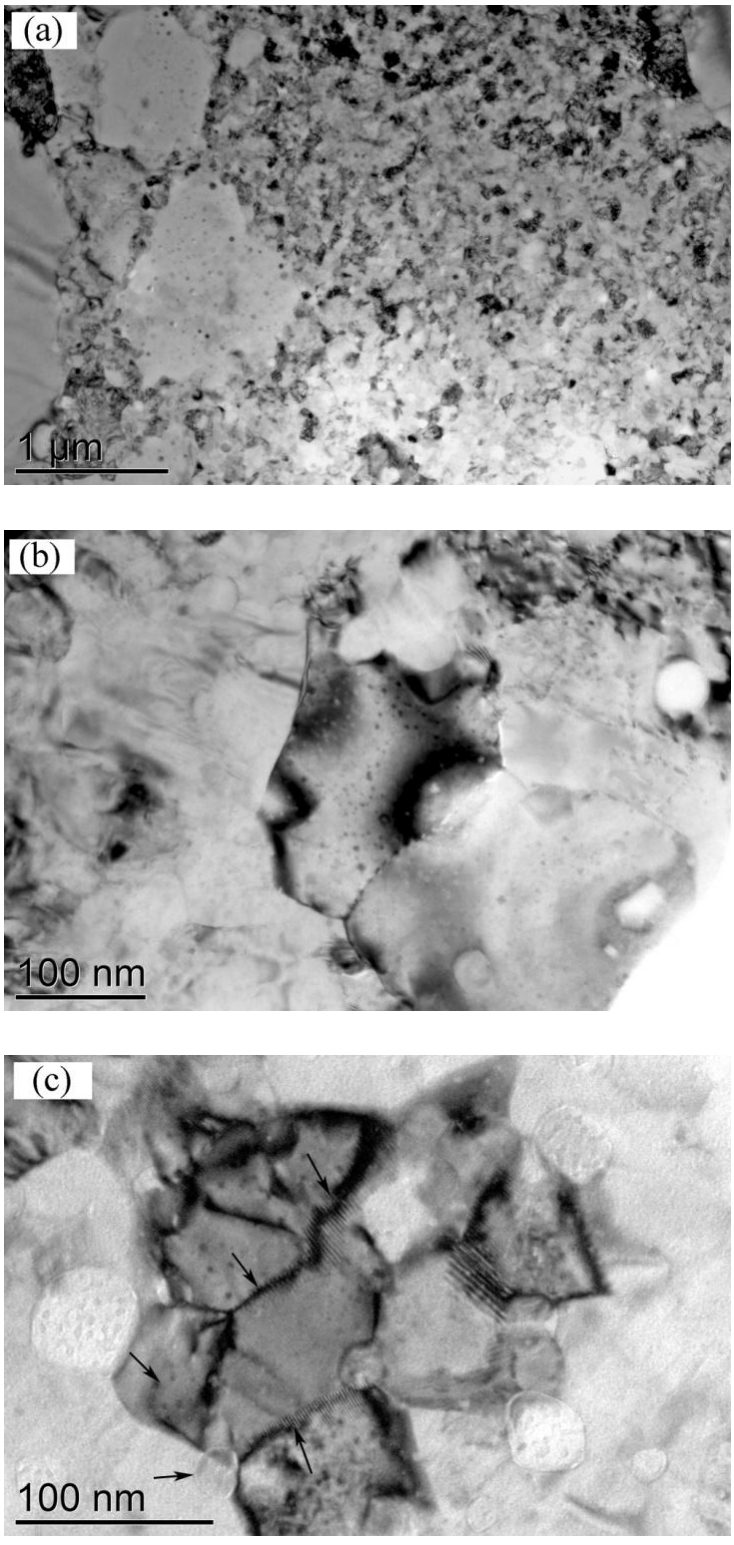

Figure 5. 3. TEM micrographs of the specimen SPSed at 950 ^{o}C for 45 min: (a) a bright field micrograph of a bimodal grain size distribution, (b) ultrafine grains with high number of particles, and (c) subgrain formation

Nanoparticles with different Z-contrast could be distinguished from the matrix due to a difference in the chemical composition. Several EDS analyses on a large area located in the matrix revealed a chemical composition of Fe–1.1Ti–14.1Cr–0.2Mo–0.5La (wt.%). Detailed EDS analysis of the 14LMT alloy sintered at 950 ^{o}C for 45 min was carried out. Three different nanoparticles were marked as 1, 2 and 3 in the high angle annular dark field (HAADF) micrograph shown in Fig. 5.4(a). These particles were different in diameter and Z contrast. The EDS analysis on particle 1 (with a dark contrast and spherical morphology with diameter of 40 nm) revealed a composition of Fe–27.9±1.1Cr–16±0.86Ti, wt.% (Fe–28.6±1.5Cr–17.8±0.9%Ti, at.%). No La or Mo was detected in the chemical composition of this particle. The light element concentrations could not be statistically quantified and therefore are not reported here. The EDS analysis on particle 2 (bright contrast and spherical morphology with diameter of 60 nm) revealed a composition of Fe–25.07±0.48Cr–3.92±0.2Ti, wt.% (Fe–26.3±0.5Cr–4.5±0.3Ti, at.%). The EDS analysis showed a higher content of Fe and lower content of Ti in particle 2 compared to particle 1. Particle 3 in Fig. 5.4(a) was a spherical particle with dark contrast and a diameter of over 100 nm, and was located in the vicinity of a grain boundary. Particle 3 had a higher Cr and Ti content compared to particles 1 and 2. EDS analysis on particle 3 revealed a composition of Fe–64.2±1.4Cr–23±0.9Ti, wt.% (Fe–64±1.0Cr–25±1Ti, at.%). Four particles with a faceted morphology and an average diameter of 10 nm are highlighted in Fig. 5.4(b) with a scan line running across them. The corresponding EDS line-scan profile is plotted in Fig. 5.4(c).

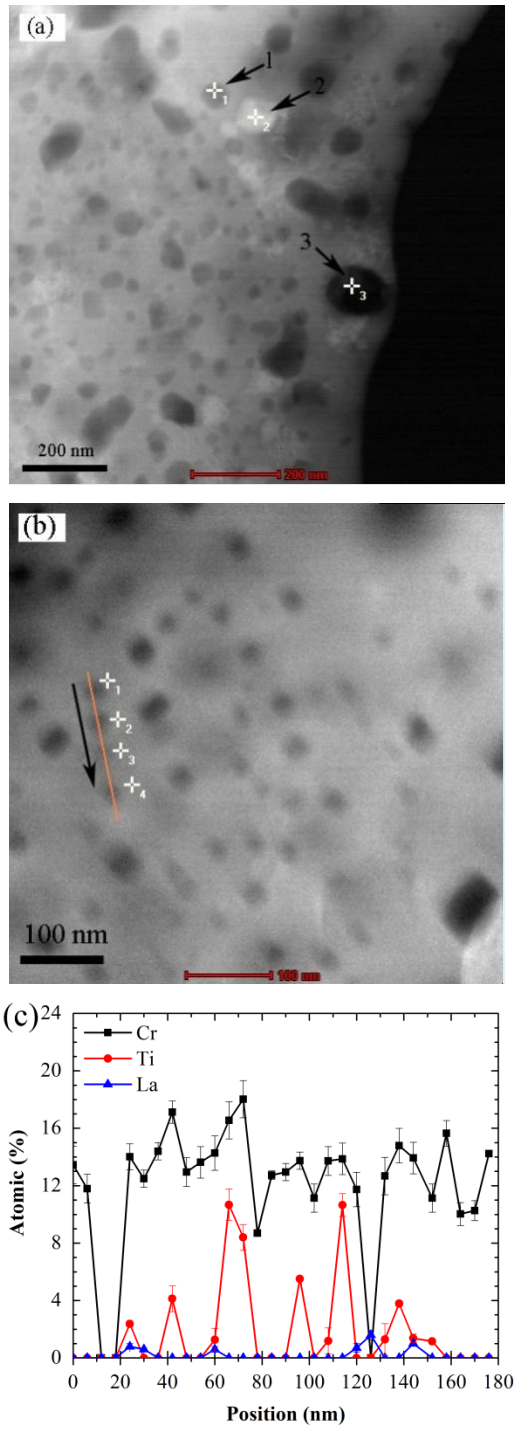

Figure 5.4. (a) STEM HAADF micrograph showing three various particle with different size and Z-contrast, (b) STEM HAADF micrograph of four particles with faceted morphology, and (c) the concentration profile for Fig. 5.4(b) as a function of position

It is evident that the Ti and La were mostly concentrated only in the particles rather than the ferritic matrix. The foregoing examples of EDS analyses shown in Figs. 5.4(a–c) implied that the concentration of Cr, Ti and La varied within the particles and particle – matrix interface.

The EFTEM elemental composition micrographs from the particles are presented in Figs. 5.5(a–f). In Fig. 5.5(a), the signals from the Fe–$L_{2,3}$ peak became weaker in the particles and showed a darker contrast identifying less iron content in them. Chromium, however, showed some enrichment in those larger particles (Fig. 5.5(b)).

In Fig. 5.5(c), Ti was clearly distinguishable in particles; however, Mo revealed a darker contrast in the EFTEM map shown in Fig. 5.5(d) meaning of no Mo was found in the particles. In EDS results, larger particles did not contain any La, and similarly in EFTEM elemental map in Fig. 5.5(e), no La enrichment was observed in larger particles. It was difficult to obtain an EFTEM image from 2–3 nm particles due to relatively large thickness of the specimen and large excitation volume. Therefore, La mapping could not be clearly realized in small particles, as shown in Fig. 5.5(e), due to insufficient sensitivity, lower spatial resolution and lower signal to noise ratio. The signals from O were enriched in the particles as shown in Fig. 5.5(f). However, the oxygen in the smaller particles could not be unequivocally revealed likely because oxygen was already present on the sample surface. The EFTEM maps in Fig. 5.5(a–f) imply the presence of Cr, Ti and O in the particles. Despite the absence of La in the larger particles in EFTEM maps, its presence in the smallest particles also could not be clearly resolved.

The microstructure of the 14LMT alloy sintered at 1050 ^{o}C for 45 min is shown in Fig. 5.6(a–c). A combination of nanograins, ultrafine grains and micron-sized grains were

present as shown in Fig. 5.6(a). The area fraction of recrystallized grains was estimated to be approximately 60%. The average diameter of nanograins and ultrafine grains in the 14LMT alloy after SPS at 1050 ^{o}C for 45 min was calculated to be 154±15 nm and 785±60 nm, respectively. The recrystallized grains as shown in Fig. 5.6(a) had nanoparticles and a few dislocations. In contrast, the nanograins showed a higher density of the nanoparticles. An example of a micron-sized grain containing a high number of nanoparticles interacting with dislocations in grain interior is shown in Fig. 5.6(b). The HRTEM image shown in Fig. 5.6(c) revealed the oxide particles with a diameter in the range of 2–5 nm. The increased SPS temperature (1050 ^{o}C) did not cause any significant coarsening in nanoparticles, specifically those that were smaller than 5 nm.

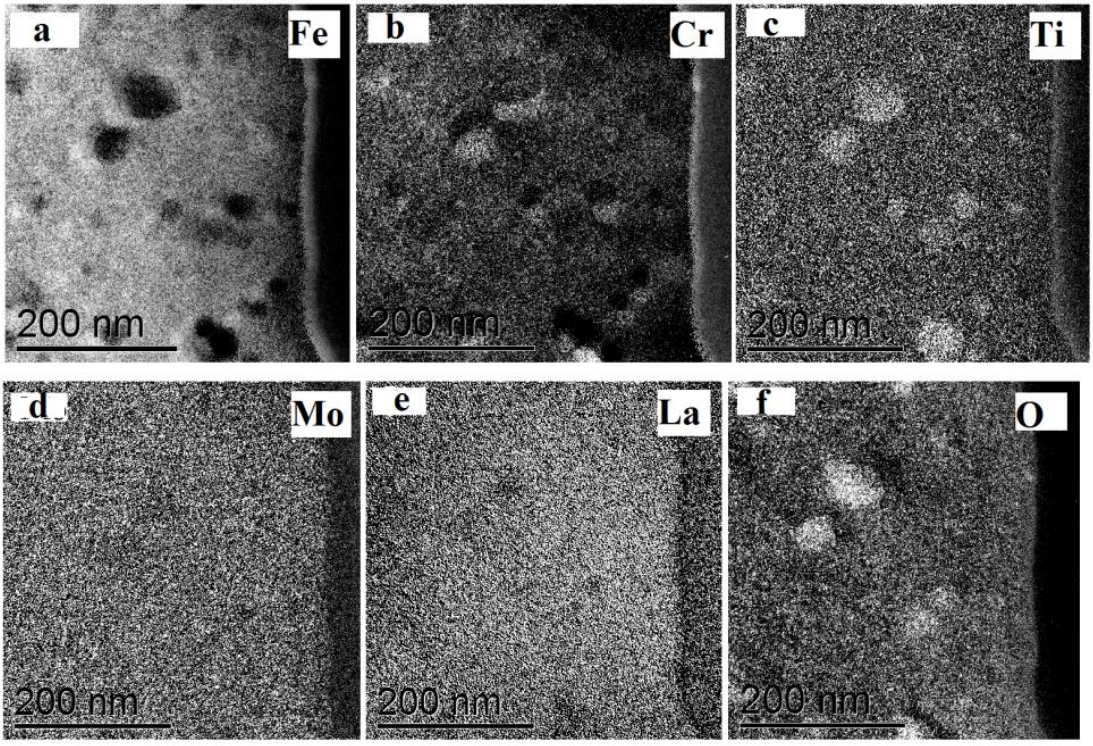

Figure 5.5. EFTEM elemental maps from raw data showing (a) Fe, (b) Cr, (c) Ti, (d) Mo, (e) La, and (f) O in 14LMT alloy SPSed at 950 ^{o}C for 45 min

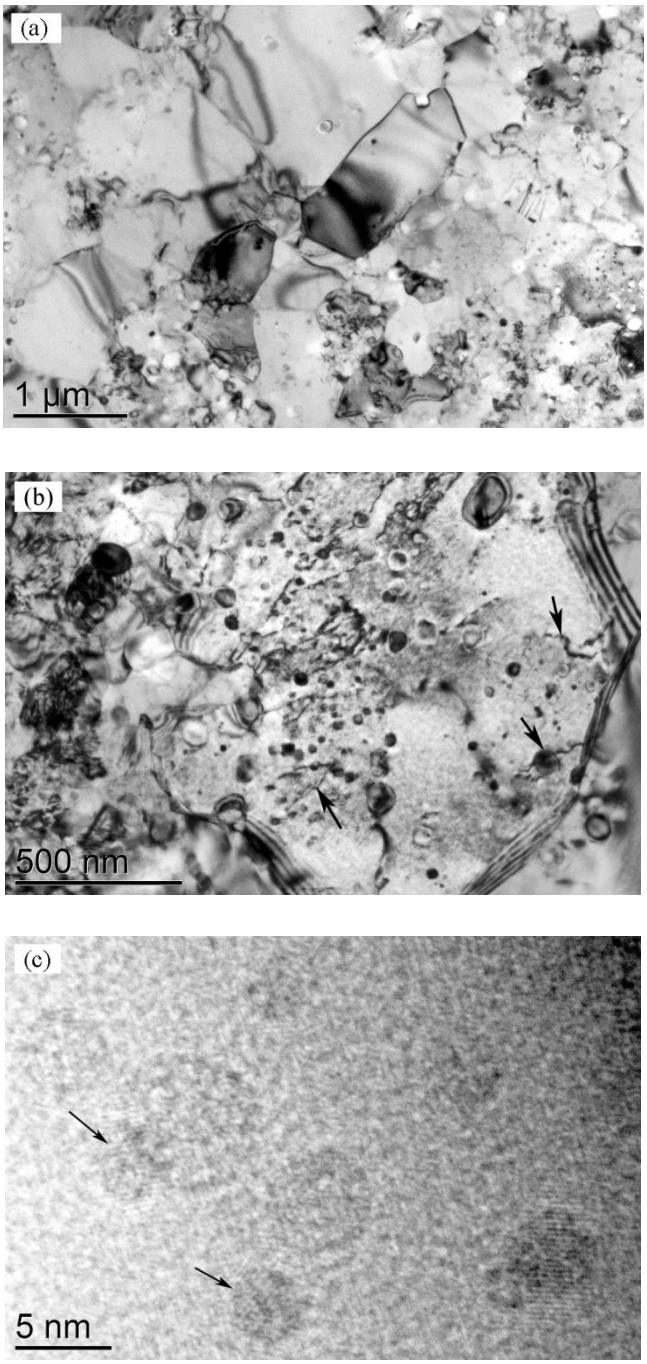

Figure 5.6. TEM micrographs of the specimen SPSed at 1050 °C for 45 min: (a) a bright field image showing the recrystallized grains free of dislocations and lower number of particles, (b) a micron-sized grain with arrows showing the interaction of nanoparticles with dislocations, and (c) arrows in the HRTEM micrograph point to the nanoparticles

Grain size histograms of the 14LMT alloy SPSed at 850, 950 and 1050 ^{o}C for 45 min are plotted in Figs. 5.7(a–c), respectively. As the SPS temperature increased, the number of ultrafine and micron-sized grains increased at the expense of nanograins. In the microstructure of 14LMT alloy after SPS at 850 ^{o}C for 45 min, more than 65% of the grains were smaller than 100 nm as shown in Fig. 5.7(a). This number decreased to approximately 55% after SPS at 950 ^{o}C for 45 min and 30% after SPS at 1050 ^{o}C for the same dwell time as shown in Figs. 5.7(b–c), respectively.

The particle size distribution histograms of 14LMT alloy after SPS at 850, 950 and 1050 ^{o}C for 45 min are shown in Fig. 5.8. Approximately 1,000 particles were counted from corresponding micrographs for each SPS temperature in order to construct the histogram. The percentage of particles with diameters smaller than 5 nm was estimated to be 83%, 64% and 50% at the SPS temperatures of 850, 950 and 1050 ^{o}C, respectively. Greater fractions of coarse particles were obtained at higher SPS temperatures. The frequency of 5–10 nm particles was higher at the SPS temperature of 950 ^{o}C than at 850 ^{o}C and at 1050 ^{o}C, whereas the proportion of particles larger than 10 nm was higher at 1050 ^{o}C than at the other two SPS temperatures.

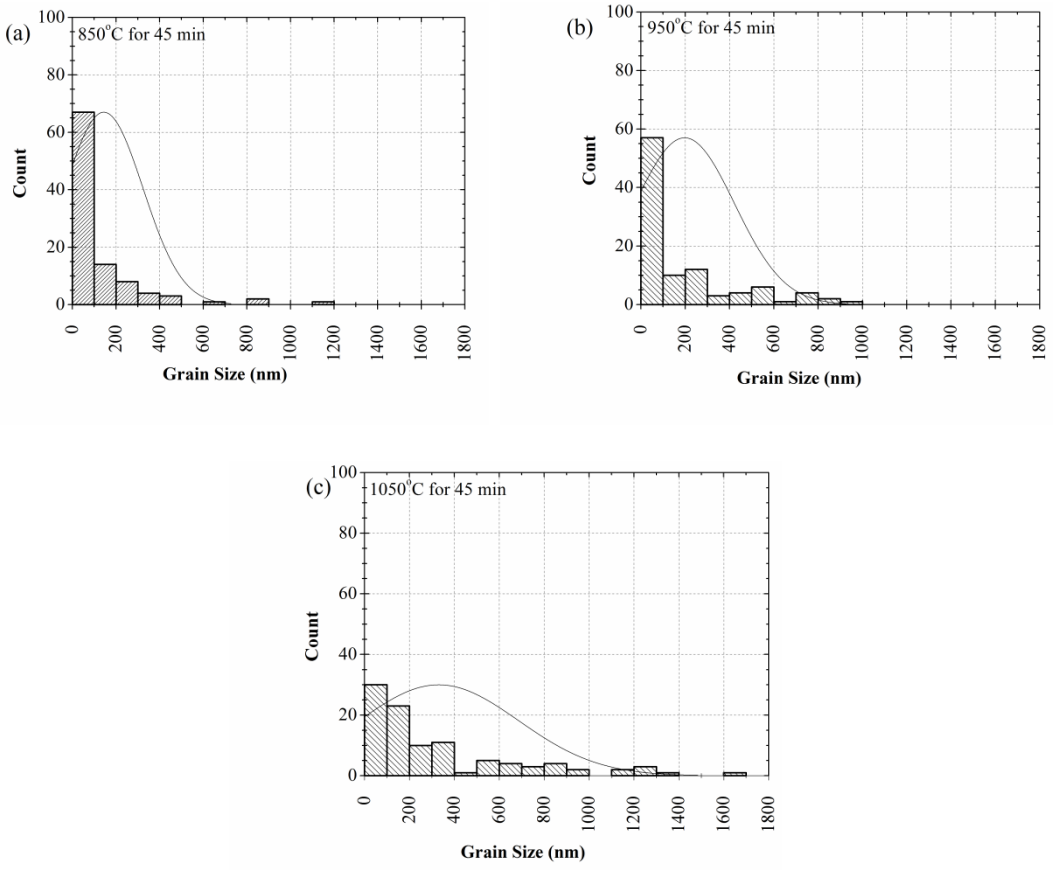

Figure 5.7. Grain size histogram of 14LMT alloy after SPS at (a) 850 °C for 45 min, (b) 950 °C for 45 min, and (c) 1050 °C for 45 min

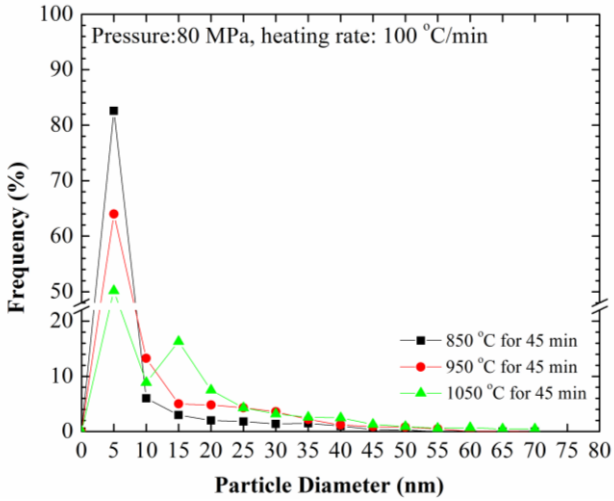

Figure 5.8. Particle size distribution plot of 14LMT alloy after SPS at 850, 950 and 1050 °C for 45 min

5.3.1.3. APT studies

Figure 5.9 illustrates the distribution of solutes in a small volume (18×18×50 nm^3) of the 14LMT alloy specimen sintered at 950 ^oC for 45 min. It revealed clustering of Cr–, Ti–, La– and O-enriched particles. The presence of Cr and Ti ions as oxide ions is due to their strong affinity for O. The O atoms showed a broader distribution than TiO and La possibly due to the irregular oxygen evaporation from the tip [25]. Most of Mo atoms were distributed uniformly throughout the matrix. The bulk composition, matrix average composition, clusters average composition and matrix corrected composition 14LMT alloy SPSed at 950 °C for 45 min are calculated and summarized in Table 5.1. The cluster composition was calculated using the maximum separation algorithm [29]. Here, core atoms of La, O and TiO were selected using a maximum separation distance (d_{max}) of 0.6–0.8 nm, and clusters were found to be composed of at least 10 core atoms (N_{min}=10–15) within d_{max}. The Guinier radius (R_G) of nanoclusters that exhibits the size was estimated by using the radius of gyration (R_g) and the following equation [25, 26]:

$$R_G = \sqrt{\frac{5}{3}} R_g \qquad (5.2)$$

The number density of Cr–, Ti–, La–, O-enriched NCs in 14LMT alloy sintered at 950 ^oC for 45 min was estimated to be 1.2×10^{24} m^{-3} with an average Guinier radius of 1.5±0.3 nm. The average cluster composition was 9±2 at.% Cr, 18±2 at.% Ti, 6±1 at.% La, 35.2±3 at.% O along with Fe as the balance. The matrix-corrected cluster composition indicated that the particles were enriched in Cr, Ti, La and O and was depleted in Mo and Fe with a stoichiometry of (La+Ti):O being about 0.98.

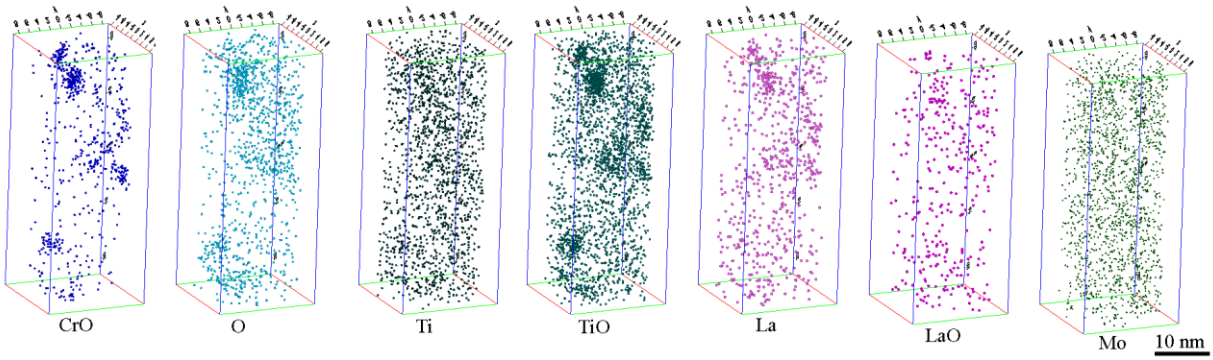

Figure 5.9. 3-D APT reconstruction maps of the 14LMT alloy after SPS at 950 ^{o}C for 45 min

Table 5.1. Composition measurements based on the APT data obtained from 14LMT alloy after SPS at 950 ^{o}C for 45 min

Element	Compositional Measurements			
	Bulk (at.%)	Matrix (at.%)	Cluster (at.%)	Matrix Corrected (at.%)
Cr	13.88±0.5	10.73±0.3	8.9±2.2	29.82±3.2
O	0.39±0.1	0.12±0.06	35.25±3.2	34.2±4.3
Ti	1.09±0.09	0.25±0.1	17.8±2.0	25.5±2.1
C	0.1±0.05	0.10±0.05	0.05±0.04	0.09±0.05
N	0.09±0.04	0.10±0.05	0.04±0.02	0.04±0.05
La	0.14±0.06	0.05±0.04	7.89±0.84	10.31±0.1
Mo	0.17±0.05	0.16±0.05	0.06±0.03	0.04±0.04
Fe	84.14±0.5	88.49±0.3	32.01±6.4	0.0

The effect of SPS temperature on the distribution, chemical composition and NCs size was studied by conducting APT analyses on the 14LMT alloy sintered at 1050 ^{o}C for 45 min. The corresponding APT 3D-maps are shown in Fig. 5.10. The Cr–, Ti–, La–, O-enriched NCs with an average Guinier radius of 2.0±0.2 nm and a number density of 0.66×10^{24} m^{-3} were detected in this sintered alloy. With increasing SPS temperature, the NCs became slightly larger in size and less in number but not significantly changed. The average cluster composition was found to be 14±1 at.% Cr, 23±3 at.% Ti, 11±0.5 at.% La, 30.0±5 at.% O along with Fe as the balance. The matrix corrected cluster composition indicated that the particles were enriched in Cr, Ti, La and O and depleted in Mo and Fe

with a stoichiometry of (La+Ti):O being 1.03. The bulk composition, matrix average composition, clusters average composition and matrix corrected composition for 14LMT alloy SPSed at 1050 °C for 45 min are calculated and summarized in Table 5.2.

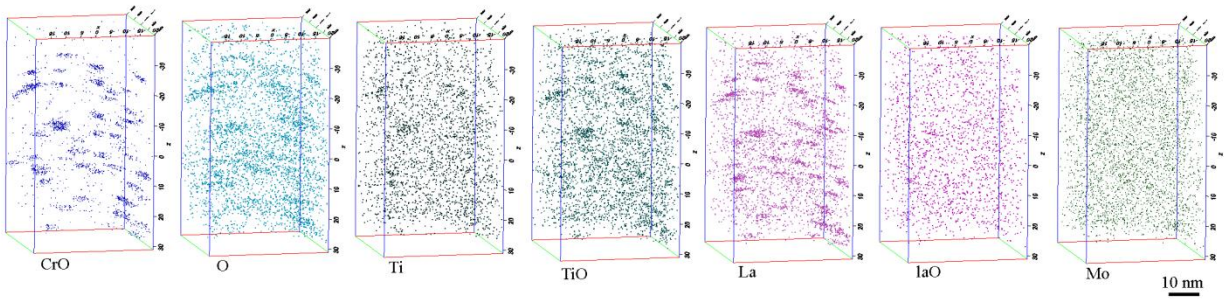

Figure 5.10. Three dimensional reconstruction maps of APT data showing clustering of CrO, TiO and La from the 14LMT alloy after SPS at 1050 °C for 45 min

Table 5.2. Composition measurements based on the APT data obtained from 14LMT alloy after SPS at 1050 ^{o}C for 45 min

Element	Compositional Measurements			
	Bulk (at.%)	Matrix (at.%)	Cluster (at.%)	Matrix Corrected (at.%)
Cr	14.56±0.7	11.12±0.5	14.14±1.2	15.4±3.3
O	0.45±0.1	0.15±0.06	30.0±5.5	41.63±2.5
Ti	0.9±0.2	0.12±0.1	23.3±3.1	27.77±0.5
C	0.12±0.05	0.08±0.06	0.05±0.03	0.05±0.05
N	0.10±0.04	0.08±0.05	0.04±0.04	0.02±0.02
La	0.16±0.05	0.05±0.05	11.1±0.5	15.11±1.5
Mo	0.14±0.1	0.12±0.03	0.06±0.03	0.02±0.02
Fe	83.57±1.2	88.28±2.2	21.31±3.5	0

5.3.2. Effect of SPS temperature and time on densification and mechanical properties

The sintering experiments were performed in the temperature range of 850 to 1100 ^{o}C for dwell times of 0 and 2 min at a constant heating rate of 100 ^{o}C/min and an applied pressure of 80 MPa. The measured density values are plotted in Fig. 5.11 for the dwell times of 0 (i.e., no dwelling) and 2 min and designated as plot 1 and plot 2, respectively. The

relative density values in Fig. 5.11–plot 1 increased with increasing SPS temperatures from 850 to 1100 ^{o}C, with a significant increase at 950 ^{o}C and a slight increase at temperatures above 950 ^{o}C. The final relative density of 98.5% was achieved after sintering at 1100 ^{o}C. Similarly, the relative density in Fig. 5.11–plot 2 increased with increasing dwell time from 0 to 2 min at temperatures below 950 ^{o}C and did not show significant dependence on dwell time at temperatures above 950 ^{o}C.

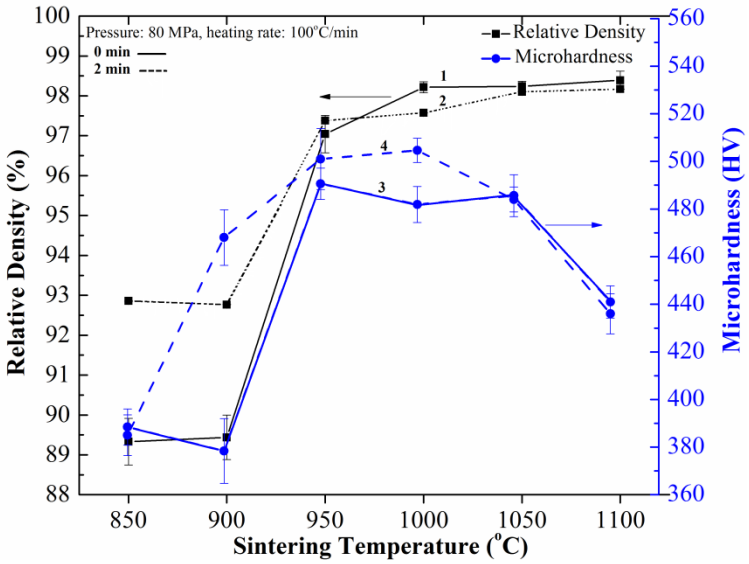

Figure 5.11. The variation of relative density and microhardness of 14LMT alloys as a function of sintering temperatures; plot 1 the relative density for dwell time of 0 min, plot 2 the relative density for dwell time of 2 min, plot 3 the microhardness values for dwell time of 0 min and plot 4 the microhardness values for dwell time of 2 min

The microhardness values for dwell times of 0 and 2 min are presented in Fig. 5.11–plots 3–4, respectively. The microhardness values shown in Fig. 5.11–plot 3 progressively increased from 389 HV at 850 ^{o}C to 491 HV at 950 ^{o}C and remained unchanged up to 1050 ^{o}C and decreased down to 441 HV at 1100 ^{o}C. The microhardness values shown in Fig. 5.11–plot 4 were consistently higher for 2 min dwell time than 0 min

dwell time at SPS temperatures below 1000 ^{o}C. The relative density and microhardness data for 2 min dwell time (Fig. 5.11–plots 2–4) revealed three distinct stages of the sintering process as a function of SPS temperature. In the temperature range of 850 to 900 ^{o}C, significant hardening occurred without much densification improvement; at 900 to 1000 ^{o}C range both densification and hardening occurred; and above 1000 ^{o}C the extent of densification did not change notably although microhardness values declined. In order to study the combined effect of SPS temperature and time, the three temperatures 850, 950 and 1050 ^{o}C were selected from Fig. 5.11 and the dwell time was varied between 0 and 45 min isothermally. The density and microhardness values were measured and presented in Figs. 5.12(a–b), respectively. The relative density of the sintered specimens increased with increasing SPS temperature from 850 to 1050 ^{o}C at all dwell times. The relative density values did not change significantly after 20 min at 850 ^{o}C and after 7 min at 950 and 1050 ^{o}C. The relative density values after SPS at 850, 950 and 1050 ^{o}C for 45 min were 94.3%, 97.8% and 98.3%, respectively. Microhardness values of the 14LMT alloys sintered at 850 and 950 ^{o}C increased consistently with increasing dwell time from 0 to 45 min, however, the microhardness showed a decrease at 1050 ^{o}C after 2 min and longer dwell time. The microhardness values were 489, 561 and 324 HV, after SPS at 850, 950 and 1050 ^{o}C for 45 min, respectively. The shear yield values of the 14LMT alloys processed for different sintering times and temperatures are shown in Fig. 5.12(c). A 0.01 offset shear strain was used to calculate the shear yield stress in the punch displacement traces according to literature [30, 31]. The shear yield stress values were higher for 14LMT alloys processed at 950 ^{o}C for 7 and 45 min than those processed at 850 and 1050 ^{o}C. The shear yield stress values revealed a similar trend to the microhardness values of the same materials.

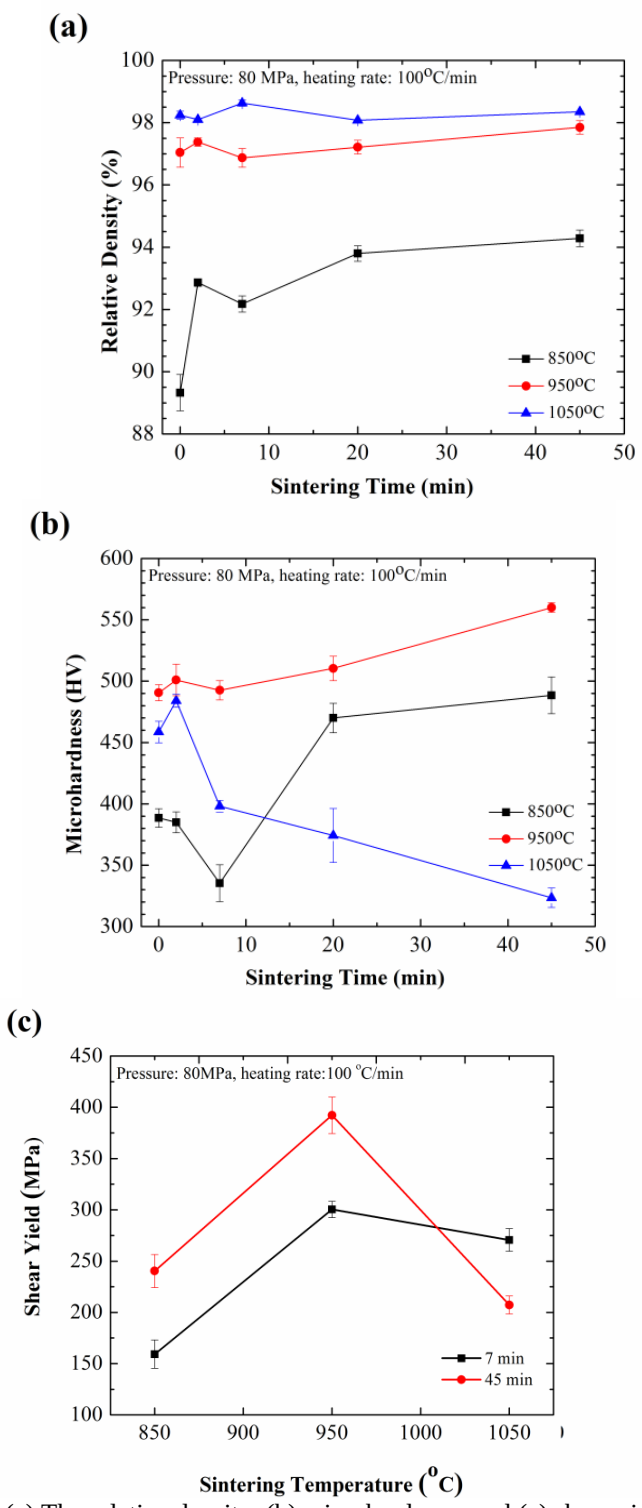

Figure 5.12. (a) The relative density, (b) microhardness, and (c) shear yield values at SPS temperatures between 850–1050 °C for various sintering times

Table 5.3 compares the microstructure and mechanical properties of different NFS specimens processed with HIP or SPS with current study.

Table 5.3. The summary of microstructure and mechanical properties for some ODS alloys and NFS reported in other studies

Alloy	Composition	Processing Method	Microstructure	Mechanical Properties	Ref.
MA957	Fe–13.7Cr–0.98Ti–0.3Mo–0.28 Y_2O_3	Hot extrusion at 850 ^oC	A uniform microstructure of elongated grains, some cavities and a low number density of micron-sized particles	Room temperature UTS 1400 MPa	[39, 44]
14YWT	Fe–14Cr–3W–0.4Ti–0.3Y_2O_3	HIP at 1000 ^oC for 3 h and 200 MPa	roughly 50–50% fine and coarse ferrite mixture of ferrite grains with diameter of ~200 nm	500 HV	[45]
Commercially Pure Fe	Commercially pure Fe (99+%)	SPS at 800 ^oC for 20 min and 484 MPa	Nanograined (<100 nm) as well as coarse grained regions (>1 lm) with uniform dispersion of nanosized chromium oxide particles (10 nm)	Room temperature UTS 1480 MPa	[17]
Fe–9Cr ODS	Fe–9Cr–0.3Y_2O_3	SPS at 1250 ^oC for 10 s and 314 kN	Y–O–rich clusters with Y–O ratio between 1:3 and 2:3	293±9 HV	[18, 46]
16YAT	Fe–15.83Cr–2.97Al–0.05 Y_2O_3–1.0Ti	SPS at 1000 ^oC For 60 min and 80 MPa	A bimodal structure with fine and coarse grains	480 HV	[14, 15]
High Chromium Ferritic Steel	Fe–14.5Cr–1.01W–0.16Y–0.15O–0.32Ti-0.18Si	SPS+HIP	large recrystallized grains, ultrafine grains substructured with low-angle grain boundaries	Room temperature YS 1000 MPa	[36, 47]
14LMT	Fe–14Cr–1Ti–03Mo–0.5 La_2O_3	SPS at 950 ^oC for 45 min and 80 MPa	Approximately 45% of the area contained the ultrafine grains	561 HV	Current work

5.4. Discussion

5.4.1. Microstructural evolutions

Most of the mechanically alloyed powders are composed of non-equilibrium phase constituents with a very large amount of stored energy. Formation of a supersaturated solid solution consisting of Cr, Ti, La, O and Mo in a ferritic matrix via high energy ball milling of elemental powders practically occurs when the powder particles become fragmented and smaller until eventually disappearing into a super saturated solid solution. This can be done by inducing an immense quantity of dislocations as well as vacancies that actually act as "*solute-pumping stations*" to introduce the solutes (here Cr, Ti, Mo and La) into the crystalline lattices [32].

As ball milling proceeds, the interfacial energy increases with the refinement of the powder particles providing a sufficient driving force for any recrystallization and second phase precipitation during further consolidation [33]. Often during consolidation, the mechanically alloyed powder may recrystallize to a sub-micron grain size which is representative of the grain structure found immediately after consolidation [34].

The porosity in the 14LMT alloy sintered at 850 ^{o}C for 45 min was about 5.1% as shown in Fig. 5.1(b). The relatively large area fraction of porosity may remain in the specimen plausibly because plastic flow is required to produce a fully dense material via SPS. The presence of nano and ultrafine grains in bimodal grain structured observed in Fig. 5.2(a) is attributed to partial recrystallization facilitated in some regions with higher dislocation densities such as in the vicinity of larger Cr–Fe oxide particles, or prior grain or crystallite boundaries. The high number of nanoparticles in the microstructure shown in Fig. 5.2(b–c) can have a complex effect on the recrystallization process through Zener pinning effect [35].

The partial recrystallization can be explained by applying a model initially proposed by Bhadeshia [34]. In this model, grain junctions act as the pinning points during the formation of nuclei and thus retard the recrystallization. With this model, it is plausible that the nucleation of recrystallized grains shown in Fig. 5.2(b) occurred through formation of grain boundary bulges but grain junctions were the pinning points and made it difficult for bulge nuclei to grow [34]. Furthermore, at 950 ^{o}C, the recrystallization rate was controlled by a high number density of nanoparticles as illustrated in Figs. 5.3(a–b). The recrystallization is hindered in the presence of nanoparticles as long as $F_v/r > 0.2$ μm^{-1} where F_v is the volume fraction of the particles and r is the particle radius [35]. In the SPSed material, F_v/r is larger than 0.2 μm^{-1} if use 0.0055 for the F_v and 35–40 nm in diameter for the particles. Residual pores for example as visible in Fig. 5.1(d), may also play a role in pinning boundaries and hindering the recrystallization process [35]. Subgrains shown in Fig. 5.3(c) were formed by the re-arrangement of dislocations and controlled by nanoparticles. Meanwhile, due to recovery in these grains, the driving force for recrystallization would be possibly no longer sufficient and further recrystallization initiation would be delayed. Allahar *et al.* [14] reported the development of a similar bimodal grain size distribution in the SPSed Fe–16Cr–3Al–0.5Y_2O_3–1Ti (wt.%) ODS alloy. It was also attributed to the occurrence of partial recrystallization. Boulant *et al.* [36] implied that the heterogeneous plastic deformation which is characteristic of any high energy ball milling process is the main reason of a heterogeneous recrystallization or “abnormal grain growth” during sintering. However, the oxide nanoparticles pin the recovered grains and impede further recrystallization by providing significant thermal stability.

By combining the alloying elements and processing parameters, it is possible to control the distribution of the oxide particles in the NFSs and the grain size evolutions to a relatively optimized condition. In conventional sintering process such as HIP or hot extrusion, due to the higher operating temperatures and indirect heating of the non-equilibrium powder, recrystallization is likely to be completed before the precipitation occurs and therefore the particles will not have a great influence on the recrystallization process. In SPS, a lower sintering temperature and shorter dwell time does not cause a significant coarsening in nanoparticles that are already nucleated during milling [18] and solute enriched during sintering. This can increase the influence of nanoparticles on the grain structure at higher temperature once the primary consolidated microstructure formed during recovery and subsequent recrystallization.

Although nanoparticles smaller than 5 nm did not significantly coarsen at 1050 ^{o}C as shown in Fig. 5.6(c), the frequency of these particles was noticeably reduced at the higher SPS temperature. The fraction of the nanoparticles smaller than 5 nm was estimated to be 83%, 64% and 50% at 850, 950 and 1050 ^{o}C, respectively (Fig. 5.8.). The lower fraction of the smaller particles and coarsening of the particles at higher SPS temperature likely facilitated the recrystallization at 1050 ^{o}C. To summarize the microstructural evolution during sintering of the milled powder in SPS process, a hypothesis is suggested in a form of a schematic as illustrated in Fig. 5.13.

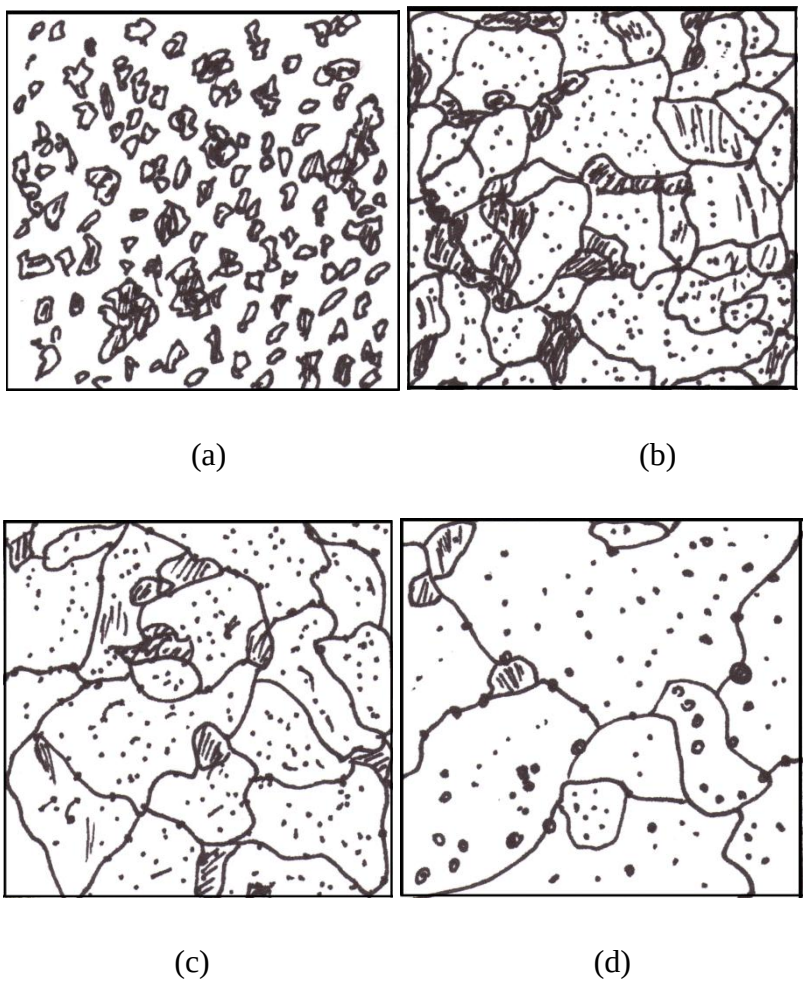

Figure 5.13. A schematic illustration of the microstructural evolutions from (a) milling to sintering at different stages of sintering, (b) 850 ^{o}C, (c) 950 ^{o}C, and (d) 1050 ^{o}C

A supersaturated milled powder with nanocrystalline domains with high number of vacancies, dislocations and grain boundaries, vacancies–O atoms pairs [37], has a very high amount of stored energy for a possible fast recovery process to form subgrains. During sintering, milling vacancies annihilation, thermal vacancies generation, dislocations recovery and subgrain formation lead to recrystallized nuclei, recovered grains and formation of precipitates. For example; after SPS at 850 ^{o}C, nanograins with the smallest oxide nanoprecipitates were observed along with recrystallized ultrafine grains with larger precipitates. Although the precipitation formation and recrystallization are two competing

processes, there is not enough evidence which one occurs earlier if they are not occurring simultaneously. However, it is more likely true that recrystallization will be more dominant than precipitation formation at higher SPS temperature (e.g. 1050 ^{o}C) due to higher mobility of grain boundaries and coarsening of the oxide nano-precipitates.

The APT maps in Figs. 5.9 and 5.10 showed that NCs in this alloy are non-stoichiometric and Cr–, Ti–, La– and O-enriched. In order for NCs to nucleate during ball milling, a super saturated solid solution has to be formed first. This meta-stable state can be achieved by continuous particle shearing and thermally activated jumps. The numerous O–vacancies pairs are created in a ball milled Fe system and attract atoms with high affinity for O such as Cr, Ti and La [38]. Nucleation of Y–O [6] and similarly La–O can be facilitated by the presence of Cr and Ti in part of the oxide clusters. The nucleation of a high number density of Cr–, Ti–, La–, O-enriched NCs have been formerly reported in the ball milled 14LMT ferritic matrix [21]. Despite more negative enthalpy of La–O formation, the initial oxides were Cr– and Ti– based due to the higher concentration of O, Cr and Ti, larger La atoms and lower diffusion rate of La in the Fe lattice. During initial stages of consolidation, remaining vacancies and dislocations created from milling, along with thermally activated vacancies and excess vacancies induced by different diffusion rates of solutes are presumed to greatly enhance NCs formation through a fast vacancy-based diffusion mechanism. However, Brocq *et al*. [38] have reported that at 800 ^{o}C, most of the milling-generated vacancies were annihilated in a Fe-based matrix and further nucleation of NCs did not happen. In 14LMT alloy system, the atomic radius of La (195 pm) is greater than that of Y (180 pm), and thus a greater misfit is introduced into the bcc ferritic matrix and the formation of NCs with interfacial phases such as TiO and CrO are preferred. Hence,

the oxidation kinetics will result in the formation of Cr–O and Ti–O, which may assist in further nucleation of La–O [39]. With increasing SPS temperature from 950 ^{o}C to 1050 ^{o}C, the number density of NCs decreased to almost 50% but the r_G increased. A higher SPS temperature could provide more thermally activated vacancies in the Fe-based system and compensate for the large misfit of La–O by rapid diffusion of solute–vacancy pair. This is likely the reason for the higher La content in composition of NCs at higher SPS temperatures.

5.4.2. Mechanical properties

A high hardness (561 HVN) was achieved in 14LMT alloy after SPS at 950 ^{o}C for 45 min that can be attributed to the following strengthening contributions: (1) dispersion strengthening from the RE oxide particles such as La_2O_3 particles and the presence of the Ti–Cr–rich phase, (2) grain boundary strengthening due to grain refinement (Hall – Petch relationship), (3) solid solution strengthening and (4) dislocation strengthening [40]. Thus, the yield strength (σ_y) can be given by the following relation:

$$\sigma_y = \sigma_o + \sigma_s + \sigma_d + \sigma_{GB} + \sigma_p \quad (5.3)$$

where σ_o is the friction stress representing the overall resistance of the crystal lattice to dislocation movement (28 MPa for pure annealed iron) [17], σ_s is the solid solution strengthening, σ_d is the dislocation strengthening, σ_{GB} is grain boundary strengthening, and σ_p is the particle strengthening. Although no tensile yield values were reported in this study, the shear values were given in Fig. 5.12(c). Toloczko *et al.* [30] have shown that the shear punch traces can be compared to the corresponding tensile traces by considering that in a shear punch test reduction in load bearing area is increasingly controlled by cutting of the material as the punch displacement becomes large. Thus, for materials which display low

uniform elongation, the reduction in loading area is probably most strongly controlled by the same processes which control it in a tensile test. For polycrystalline specimens, the uniaxial tensile stress is related to the critical resolved shear stress by the Taylor factor (*M*):

$$\sigma = M \times \tau \quad (5.4)$$

where *M* equals 2.7 for *bcc* metals [41]. Since the average shear yield value of 14LMT alloy SPSed at 950 ^{o}C was measured to be 392 MPa, a rough estimation for tensile yield would be 1058 MPa. The strength of material can be improved by addition of solutes to the matrix by introducing a strain field due to the atomic misfit. The nominal composition of the present alloy is Fe–14Cr–1Ti–0.3Mo–0.5La_2O_3 (wt.%). Solid solution strengthening contributions due to the addition of chromium and molybdenum has only been considered since most of Ti and La are present in the oxide particles based on the TEM and APT results. The solid solution strengthening contribution can be expressed as:

$$\sigma_{ss} = \sum AC_i \quad (5.5)$$

where C_i is the element concentration in wt.% and *A* is a coefficient. For Cr, Mo and C or N, *A* is equal to 8.5, 57.9, and 5544 MPa / (wt.%), respectively [42, 43]. The carbon and nitrogen content in the matrix solid solution came from the milling media and were unavoidable. The resulting contribution from the solid solution strengthening was estimated to be 190 MPa. In a bimodal grain size distribution, σ_{GB} can be expressed by [17]:

$$\sigma_{GB} = k\,[(1 - V_f)\,D_{nano}^{-0.5} + V_f\,D_{coarse}^{-0.5}] \quad (5.6)$$

where *k* is the Hall – Petch constant, V_f is the volume fraction of coarse-grained regimes, and D_{nano} and D_{coarse} are the average size of the nanograins (here 110 nm) and coarse grains (here 850 nm), respectively. The grain boundary contribution is calculated by assuming the Hall – Petch relation is valid and is a single constant for the observed nano grain size range.

The constant k was estimated to be 260 MPa μm $^{0.5}$ [17], and the value for σ_{GB} is roughly estimated to be 328 MPa. The precipitation hardening part [17] can be expressed as:

$$\sigma_p = k'\lambda_s^{-0.5} \quad (5.7)$$

$$\lambda_s = 1.22\{[\pi/(4f_v)]^{0.5} - 1\}d \quad (5.8)$$

where λ_s is the surface to surface interparticle spacing, k' is a constant (roughly estimated to be 395 MPa μm$^{0.5}$), f_v is the volume fraction of oxide particles and d is the average diameter of oxide particles. The σ_p is roughly estimated to be 450 MPa by having 0.0055 for the f_v, and 35–40 nm for d in the equation. The contribution of dislocation strengthening was estimated to be 62 MPa. From the preceding calculations, it is clear that almost 42% of the yield strength comes from due to the precipitation hardening effect and , the contribution of solid solution strengthening and grain boundary strengthening were roughly 18% and 31%, respectively, and the rest is comprised of dislocation strengthening and friction stress.

5.5. Conclusions

In this study, the potential use of an alternative RE oxide in processing a NFS was investigated by adding 0.5 wt.% La_2O_3 to Fe–14Cr–1Ti–0.3Mo (wt.%). The mechanically alloyed powder was consolidated via SPS at 850, 950 and 1050 ^{o}C with a dwell time of 0–45 min. The influence of sintering parameters such as sintering temperature and dwell time on the microstructure, density, microhardness and shear yield strength was studied.

1. Oxide nanoparticles formed before and during the SPS, and hence the interaction of nanoparticles with dislocations and grain boundaries could be complex and impede further recrystallization.

2. Larger nanoparticles were Fe–Cr-enriched oxide particles but smaller nanoparticles with faceted morphology were La–Ti-enriched oxides and highly stable at elevated temperatures.

3. The APT analysis of the specimen sintered at 950^{o}C revealed high number density of 1.2×10^{24} m^{-3} of NCs with the average radius of 1.5 nm, enriched in Cr–, Ti–, La– and O. The La+Ti:O ratio was close to 1. At 1050 ^{o}C, the number density of NCs decreased to $0.66\times10^{24}m^{-3}$ and the average radius increased slightly.

4. The presence of high number of NCs along with Hall – Petch mechanism, dislocation hardening and solid solution hardening led to a significant hardening in the sintered NFSs. The relative density values increased with SPS temperature and dwell time. The densification after SPS at 950 ^{o}C and improved with longer dwell time.

Acknowledgments

This work was supported partly by the Laboratory Directed Research and Development Program of Idaho National Laboratory (INL), Contract DE–AC07–05ID14517, and partly by a grant of the Advanced Test Reactor National Scientific User Facility (ATRNSUF). The authors greatly acknowledge staff of Microscopy and Characterization Suite (MaCS) facility at Center of Advanced Energy Studies (CAES).

References

[1] Y. Wu, E.M. Haney, N.J. Cunningham, G.R. Odette, Acta Mater. 60 (2012) 3456−3468.

[2] H. Kishimoto, M.J. Alinger, G.R. Odette, T. Yamamoto, J. Nucl. Mater. 329–333 (2004) 369−371.

[3] G.R. Odette, M.L. Alinger, B.D. Wirth, Annu. Rev. Mater. Res. 38 (2008) 471−503.

[4] S. Ukai, T. Okuda, M. Fujiwara, T. Kobayashi, S. Mizuta, H. Nakashima. J. Nucl. Sci. Tech. 39 (2002) 872−879.

[5] S. Ukai, M. Fujiwara, J. Nucl. Mater. 307–311 (2002) 749−757.

[6] C.A. Williams, P. Unifantowicz, N. Baluc, G.D.W. Smith, E.A. Marquis, Acta Mater. 61 (2013) 2219−2235.

[7] ASM Handbook, ASM International, 3rd ed., Materials Park (OH), 1992

[8] Z.D. Reed, M.A. Duncan, J. Phys. Chem. 112 (2008) 5354−5362.

[9] S. Pasebani, I. Charit, J. Alloys Compd. 599 (2014) 206−211.

[10] A.J. Mueller, R. Bianco, R.W. Buckman, Int. J. Refract. Met. Hard Mater. 18 (2000) 205-211.

[11] R.S. Mishra, A.K. Mukherjee, K. Yamazaki, K. Shoda, J. Mater. Res. 11 (1996) 1144−1148.

[12] M. Gendre, A. Maitre, G. Trolliard, Acta Mater. 58 (2010) 2598−2609.

[13] A.M. Locci, R. Orru, G. Cao, Z.A. Munir, Mater. Sci. Eng. A 434 (2006) 23−29.

[14] K.N. Allahar, J. Burns, B. Jaques, Y.Q. Wu, I. Charit, J. Cole, DP Butt, J. Nucl. Mater. 443 (2013) 256−265.

[15] Y.Q. Wu, K.N. Allahar, J. Burns, B. Jaques, I. Charit, D.P. Butt, J.I. Cole, Cryst. Res. Technol. (2013) DOI 10.1002/crat.201300173:1−8.

[16] W.S. Young, I.B. Cutler. J. Am. Ceram. Soc. 53 (1970) 659−663.

[17] B. Srinivasarao, K. Ohishi, T. Ohkubo, K. Hono, Acta Mater. 57 (2009) 3277−3286.

[18] C. Heintze, A.H. Mayoral, A. Ulbricht, F. Bergner, A. Shariq, T. Weissgarber, H. Frielinghaus, J. Nucl. Mater. 428 (2012) 139−146.

[19] C. Heintze, F. Bergner, A. Ulbricht, M. Hernandez, U. Keiderling, R. Lindau, T. Weissgarber, J. Nucl. Mater. 416 (2011) 35−39.

[20] S. Pasebani, I. Charit, D.P. Butt, J.I. Cole, J. Nucl. Mater. 434 (2013) 282−286.

[21] S. Pasebani, I. Charit, D.P. Butt, J.I. Cole, Acta Mater. 61 (2013) 5605−5617.

[22] D. Vaumousse, A. Cerezo, P.J. Warren, Ultramicroscopy 95 (2003) 215−221.

[23] T. Leigh, M.P. Moody, P.V. Liddicoat, S.P. Ringer, Microsc. Microanal. 13 (2007) 448−463.

[24] A. Cerezo, L. Davin, Surf. Interface Anal. 39 (2007) 184−188.

[25] C.A. Williams, E.A. Marquis, A. Cerezo, G.D.W. Smith, J. Nucl. Mater. 400 (2010) 37−45.

[26] M.K. Miller, Atom Probe Tomography, Kluwer Academic / Plenum, New York, 2000.

[27] C.A. Williams, D. Haley, E.A. Marquis, G.D. Smith, M.P. Moody, Ultramicroscopy 132 (2013) 271−278.

[28] G.L. Hankin, M.B. Toloczko, M.L. Hamilton, R.G. Faulkner, J. Nucl. Mater. 1651 (1998) 258−263.

[29] L.T. Stephenson, M.P. Moody, P.V. Liddicoat, S.P. Ringer, Microsc. Microanal. 13 (2007) 448−463.

[30] M.B. Toloczko, R.J. Kurtz, A. Hasegawa, K. Abe, J. Nucl. Mater. 307−311 (2002) 1619−1623.

[31] V. Karthik, P. Visweswaran, A. Vijayraghavan, K.V. Kasiviswanathan, B. Raj, J. Nucl. Mater. 393 (2009) 425−432.

[32] A.Y. Badmos, H.K.D.H. Bhadeshia, Metall. Mater. Trans. A 28 (1997) 2189−2194.

[33] L.M. Brocq, F. Legendre, M.H. Mathon, A. Mascaro, S. Poissonnet, B. Radiguet, P. Pareige, M. Loyer, O. Leseigneur, Acta Mater. 60 (2012) 7150−7159.

[34] H.K.D.H. Bhadeshia, Mater Sci Eng A 223 (1997) 64−77.

[35] F.J. Humphreys, M. Hatherly, Recrystallization and Related Phenomena, Pergamon, London, 1995.

[36] X. Boulant, M. Perez, D. Fabregue, T. Douillard, M.H. Mathon, Y.D. Carlan, Metall. Mater. Trans. A 45A (2014) 1485−1497.

[37] C.L. Fu, M. Kremar, G.S. Painter, Physc. Rev. Lett. 99 (2007) 225502−225504.

[38] L.M. Brocq, B. Radiguet, S. Poissonnet, F. Cuvilly, P. Pareige, F. Legendre, J. Nucl. Mater. 409 (2011) 80−85.

[39] M.K. Miller, D.T. Hoelzer, E.A. Kenik, K.F. Russell, J Nucl. Mater. 329−333 (2004) 338−333.

[40] R. Song, D. Ponge, D. Raabe, Scripta Mater. 52 (2005) 1075−1080.

[41] U.F. Kocks, Metall. Mater. Trans. A 1 (1970) 1121−1143.

[42] J. Wang, W. Yuan, R.S. Mishra, I. Charit, J. Nucl. Mater. 432 (2013) 274−280.

[43] G.E. Totten, L. Xie, K. Funatani, Handbook of Mechanical Alloy Design. New York: CRC Press;2003

[44] R. L. Klueh, J.P. Shingledecker, R.W. Swindeman, D.T. Hoelzer, J. Nucl. Mater. 341 (2005) 103−114.

[45] M.J. Alinger, G.R. Odette, D.T. Hoelzer, Acta Mater. 57 (2009) 392−406.

[46] P. Franke, C. Heintze, F. Bergner, T. Weibgarber, Material prufung. Materials testing 52 (2010) 133−138.

[47] X. Boulant, D. Fabergue, M. Perez, M.H. Mathon, Y. Decarlan, Metall. Mater. Trans. A 44 (2013) 2461−2465.

CHAPTER 6: On the Role of Alloying Elements in Developing Nanostructured Ferritic Steels via Spark Plasma Sintering

Somayeh Pasebani [a], *Indrajit Charit* [a]

[a] Department of Chemical and Materials Engineering, University of Idaho, Moscow, ID 83844, USA

(*Published in the Journal of Alloys and Compounds, Volume 599 (2014) pages 206–211*)

Abstract

Several Fe–14Cr based alloys with varying compositions were processed using mechanical alloying and spark plasma sintering. Lanthanum oxide (0.5 wt.%) was added to Fe–14Cr leading to improvement in the microstructural stability and mechanical properties mainly due to a high number density of La–Cr–O-enriched nanoclusters (NCs). The combined addition of La, Ti (1 wt.%) and Mo (0.3 wt.%) to the Fe–14Cr base composition enhanced the microstructural stability and mechanical properties even further. Nanoclusters enriched in Cr–Ti–La–O with a number density of 1.4×10^{24} m^{-3} were found in this alloy with a bimodal grain size distribution. A higher density (1.5×10^{24} m^{-3}) of Cr–Ti–Y–O-enriched NCs with smaller size was detected after adding Y (0.3 wt.%), Ti and Mo to Fe–14Cr matrix. Formation mechanism of these nanoclusters can be explained through the concentrations and diffusion rates of the initial oxide species formed during milling process and initial stages of sintering as well as the thermodynamic nucleation barrier and their enthalpy of formation.

Keywords: Nanostructured ferritic steels; Spark plasma sintering; Mechanical alloying; Nanoclusters

6.1. Introduction

Nanostructured ferritic steels (NFSs), a subcategory of oxide dispersion strengthened (ODS) steels, have outstanding high temperature strength, creep strength [1, 2] and excellent radiation damage resistance [3]. These enhanced properties of NFSs have been attributed to the high number density of Y–Ti–O-enriched NCs with diameter of 1–2 nm [4]. The Y–Ti–O-enriched NCs have been found to be stable under irradiation and effective in trapping helium [5]. These NCs are formed due to the mechanical alloying (MA) of Fe–Cr–Ti powder with Y_2O_3 followed by hot consolidation route such as hot isostatic pressing (HIP) or hot extrusion [6-8]. Alinger *et al.* [4] have investigated the effect of alloying elements on the formation mechanism of NCs in NFSs processed by hot isostatic pressing (HIP) and reported both Ti and high milling energy were necessary for the formation of NCs. Miller and Parish [9] found that the excellent creep properties in NFSs result from the pinning of the grain boundaries by a combined effect of solute segregation and precipitation.

Although HIP and hot extrusion are commonly used to consolidate the NFS powder, anisotropic properties and processing costs are considered as challenging issues. Recently, spark plasma sintering (SPS) has been utilized to sinter the powder at a higher heating rate, lower temperature and shorter dwell time. This can be done by simultaneously applying a uniaxial pressure and direct current pulses to a powder sample contained in a graphite die [10]. Except for a few studies on consolidating simple systems such as Fe–9Cr–(0.3–0.6) Y_2O_3 [11] and Fe–14Cr–0.3 Y_2O_3 [10], the SPS process has not been extensively utilized to consolidate the NFSs with complex compositions. Recently, the role of Ti and Y_2O_3 in processing of Fe–16Cr–3Al–1Ti–0.5Y_2O_3 (wt.%) via MA and SPS was investigated by

Allahar *et al*. [12]. A bimodal grain size distribution in conjunction with Y–Ti–O-enriched NCs were obtained [12, 13].

In current study, Fe–14Cr (wt.%) was designed as the base or matrix alloy, and then Ti, La_2O_3 and Mo were sequentially added to the ferritic matrix and ball milled. This approach allowed us to study the effect of individual and combination of solutes on the formation of NCs along with other microstructural evolutions. Furthermore, SPS was used to consolidate the NFS powder. The mixture of Fe–Cr–Ti–Mo powder with Y_2O_3 was also MAed and SPSed for comparison.

6.2. Experimental procedure

Table 6.1 presents the chemical compositions of a series of alloys developed in this study, by sequentially adding elements to the ferritic matrix. High energy ball milling was performed in a SPEX 8000M shaker mill for 10 h using argon atmosphere, steel balls with 8 mm in diameter and a ball to powder ratio (BPR) of 10:1. A Dr. Sinter Lab SPS-515S was used to consolidate the as-milled powder at different temperatures (850, 950 and 1050 ^{o}C) for 7 min using the pulse pattern 12–2 ms, a heating rate of 100 ^{o}C/min and a pressure of 80 MPa (10 kN force). The samples were disks with 8 mm height and 12 mm in diameter. The density of the sintered specimens was measured by Archimedes' method. The Vickers microhardness tests were performed by a Leco LM100 microhardness tester at a 1000 g_f (9.8 N). A Fischione Model 110 Twin-Jet Electropolisher operating at about –40 ^{o}C and mixture of CH_3OH–HNO_3 (80:20 by vol.%) as electrolyte were used to prepare specimens for transmission electron microscopy (TEM). A FEI Tecnai TF30–FEG STEM operating at 300 kV was used. A Quanta 3D FEG instrument with a Ga-ion source focused ion beam (FIB) was used to prepare specimens for atom probe tomography (APT) studies.

The APT analysis was carried out using a CAMECA LEAP 4000X HR instrument operating in the voltage mode at 50–60 K and 20% of the standing voltage pulse fraction. The atom maps were reconstructed using CAMECA IVAS 3.6 software and the maximum separation algorithm to estimate the size and chemical composition of NCs. This was applied to APT datasets each containing 20–30 million ions for each specimen. Lower evaporation field of the nanoparticles and trajectory aberrations caused estimation of higher Fe atoms in the nanoclusters. Although, the contribution of Fe atoms from the matrix was examined here the accurate examination was not addressed in current study.

Table 6.1. The alloy compositions and processing conditions (milled for 10 h and SPSed at 850–1050 ^{o}C for 7 min)

Alloy ID	Elements (wt.%)					
	Cr	Ti	La_2O_3	Y_2O_3	Mo	Fe
14Cr-unmilled	14	0	0	0	0	Bal.
14Cr	14	0	0	0	0	Bal.
14T	14	1	0	0	0	Bal.
14L	14	0	0.5	0	0	Bal.
14Y	14	0	0	0.3	0	Bal.
14LM	14	0	0.5	0	0.3	Bal.
14LT	14	1	0.5	0	0	Bal.
14LMT(0.3)	14	1	0.3	0	0.3	Bal.
14LMT	14	1	0.5	0	0.3	Bal.
14LMT(0.7)	14	1	0.7	0	0.3	Bal.
14YMT	14	1	0	0.3	0.3	Bal.

6.3. Results and discussion

The TEM bright field micrographs for the various alloys SPSed at 950 ^{o}C for 7 min are illustrated in Figs. 6.1(a–d). The microstructure of 14Cr alloy shown in Fig. 6.1(a) revealed a complex microstructure with submicron sub grain cell structure, relatively high density of dislocations and lower number density of oxide nanoparticles. The nanoparticles were relatively large (25–65 nm) and found to have chemical compositions close to Cr_2O_3 and

$FeCr_2O_4$. The microstructure of the consolidated 14L alloy is shown in Fig. 6.1(b). The microstructure consisted of more ultra fine grains (< 1μm), a few nano grains with sharp boundaries and a higher number of nanoparticles mainly in the grain interiors. The number density of nanoparticles was higher than that of 14Cr alloy shown in Fig. 6.1(a) but lower than 14LMT (Fig. 6.1(c)) and 14YMT (Fig. 6.1(d)). In 14L alloy, the nano particles with 2–11 nm in diameter were found inside the grains (hard to be observed at magnification given in Figs. 6.1(b–a) micrograph at higher magnification was used for this purpose) whereas the nanoparticles with 50–80 nm in diameter were located at the boundaries regions. The particles on the boundaries were mainly Cr_2O_3 and $LaCrO_3$, but the chemical analysis on those smallest particles could not be done precisely due to the significant influence of the ferritic matrix.

Figure 6.1. (c) shows the microstructure of SPSed 14LMT alloy, consisting of ultra fine grains (≤ 1 μm) and nano grains (≤ 100 nm). The nanoparticles were complex oxides of Fe, Cr and Ti. The nanoparticles with faceted morphology and smaller than 10 nm in diameter were enriched in La and Ti. No evidence of stoichiometric La_2TiO_5 or $La_2Ti_2O_7$ particles was observed based on EDS and diffraction data. A similar microstructure was revealed after SPS of 14YMT alloy as shown in Fig. 6.1(d).

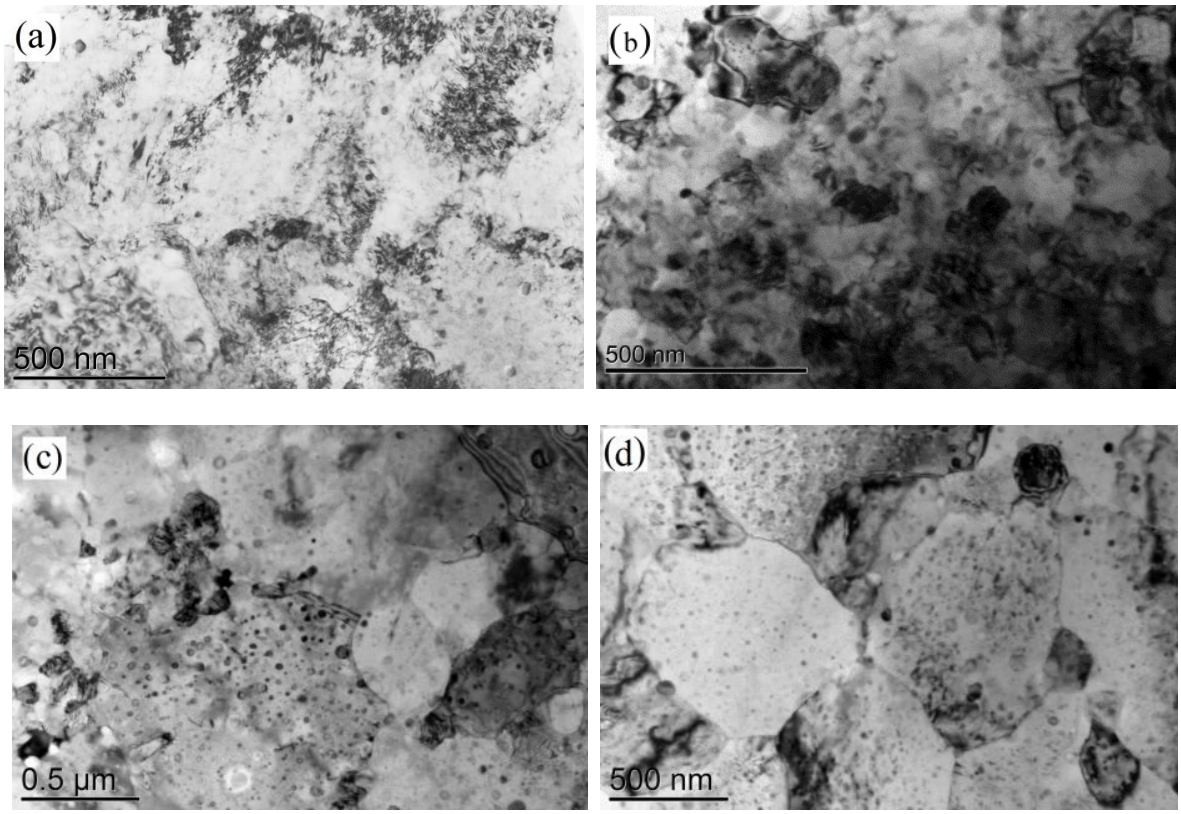

Figure 6.1. TEM bright field micrographs for various alloys (a) 14Cr, (b) 14L, (c) 14LMT and (d) 14YMT

The particle size distribution histograms of the 14Cr, 14L, 14LMT and 14YMT alloys are plotted in Figs. 6.2(a–d), respectively. Approximately 1000 particles were screened from each alloy to develop the histograms. The average particle size decreased in order of 14Cr, 14L, 14LMT and 14YMT. The highest fraction of the particle size as shown in the histograms of 14Cr, 14L, 14LMT and 14YMT was found to be associated with 25±5 nm (18±2.5%), 10±5 nm (28±3%), 5±1 nm (40±6%) and 5±1 nm (46±5%) in diameter, respectively. The number density of nanoparticles smaller than 5±1 nm was higher in 14YMT than 14LMT alloy. This is expected because of the smaller atom size and higher diffusion rate of Y in the ferritic matrix than La to facilitate nucleation of more nanoparticles under the same processing parameters.

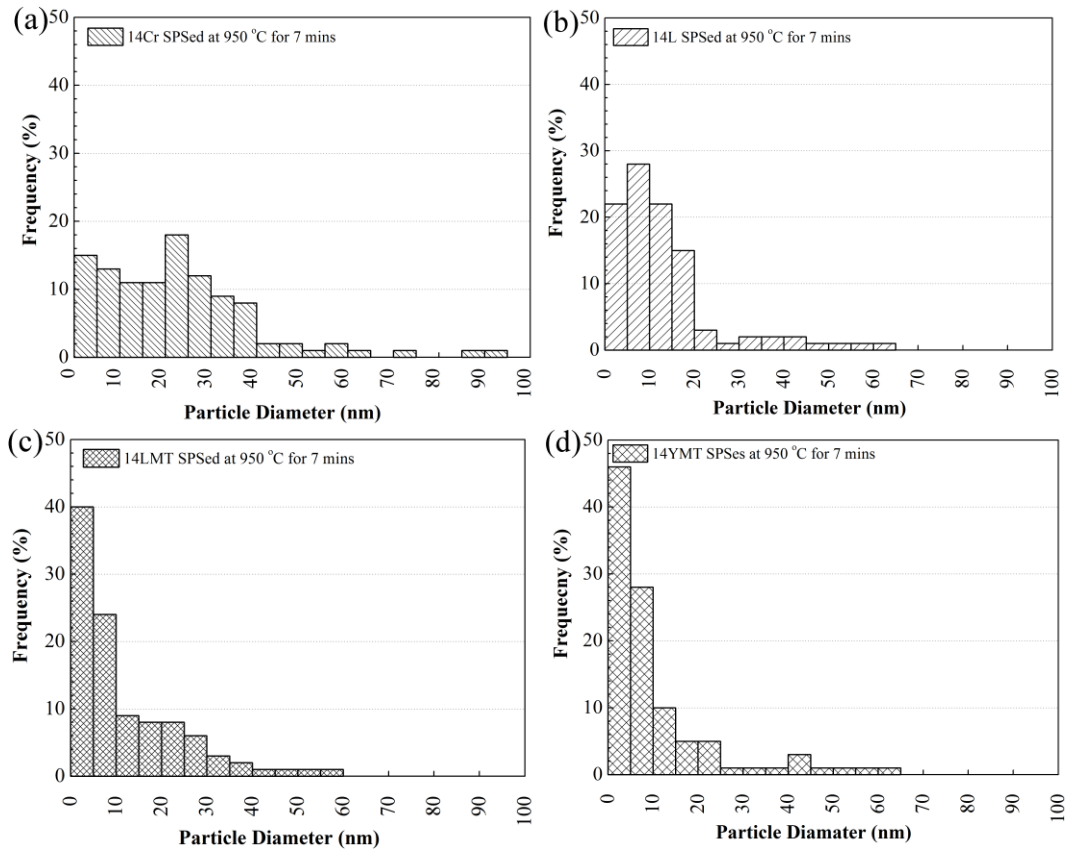

Figure 6.2. Particle size frequency histogram for (a) 14Cr, (b) 14L, (c) 14LMT and (d) 14YMT alloys

The 3-D APT maps for 14L alloy revealed a number density (≈3×10^{22} m^{-3}) of CrO–La–O-enriched NCs. The average Guinier radius of these NCs was approximately 1.9±0.6 nm. The average composition of the NCs in 14L was estimated by using the maximum separation algorithm to be Fe–17.87±3.4Cr– 32.61±3.2O–8.21±1.1 La (at.%).

A higher number density (≈1.4×10^{24} m^{-3}) and smaller NCs with average Guinier radius (r_G) of 1.43±0.2 nm were observed in the APT maps for 14LMT alloy as shown in Fig. 6.3(a). The NCs were Cr–Ti–La–O-enriched with the average composition of Fe–10.89±2.8Cr–30.85±3.1O–17.34±2.5Ti–8.15±2.2% La (at.%). According to the LEAP measurements, the chemical composition of NCs differed considerably from stoichiometric oxides. A large amount of Fe and Cr was detected inside the NCs, and La:Ti and La:O ratios

were not consistent with La_2TiO_5 or $La_2Ti_2O_7$ as expected based on thermodynamic calculations, rather the ratios were sub-stoichiometric. The 3-D APT maps for 14YMT alloy were similar to 14YMT alloy as shown in Fig. 6.3(b). The NCs with an average radius of 1.24±0.2 nm and a number density of 1.5×10^{24} m^{-3} were Cr–Ti–Y–O-enriched. The chemical composition of NCs was estimated close to Fe–8.52±3.1Cr–37.39±4.5O–24.52±3.1Ti–10.95±3.1 Y (at.%).

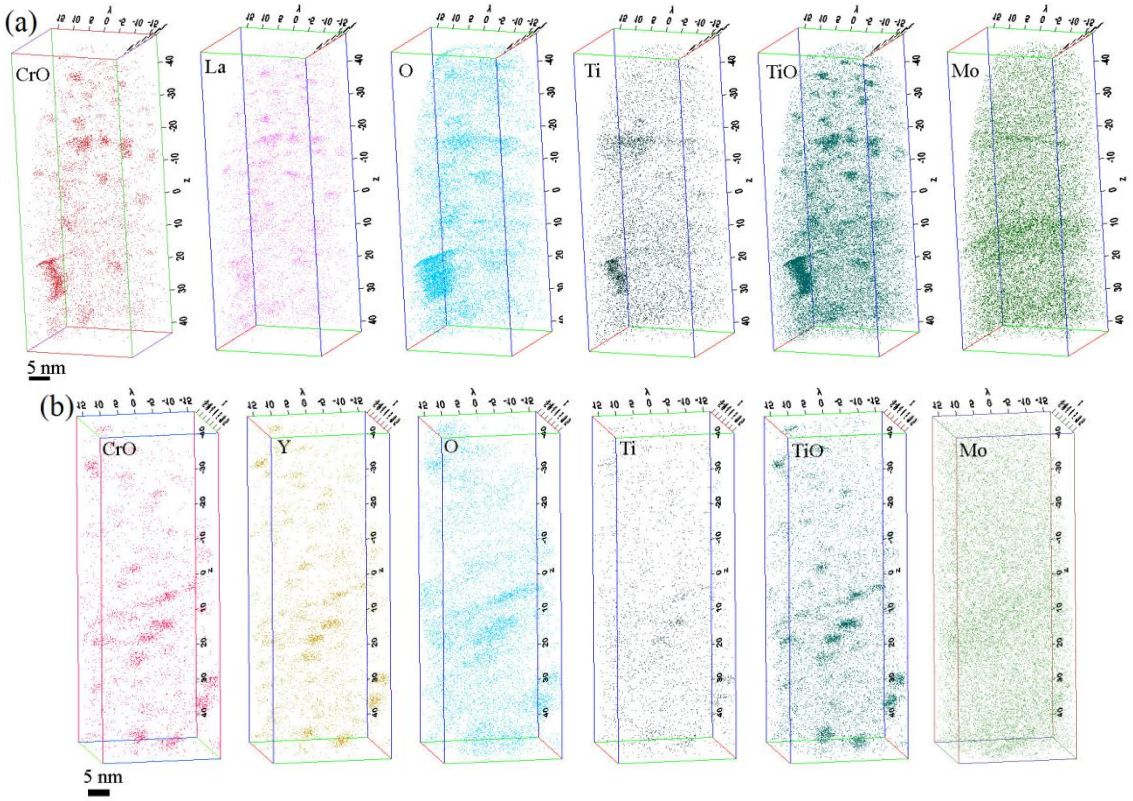

Figure 6.3. Three dimensional atom maps showing NCs for (a) 14LMT–91×34×30 nm^3 , and (b) 14YMT (93×30×30 nm^3)

The relative density of various alloys sintered at 850–1050 ^oC is shown in Fig. 6.4(a). Generally, a higher density was obtained in the specimens sintered at higher temperatures. At 850 and 950 ^oC, the density of unmilled 14Cr specimen (97.2% and 97.5%) was higher

than milled and SPSed 14Cr (92.8% and 95.5 %); because the unmilled powder particles were less hard (due to absence of strain hardening) and plastically deformed to a higher degree than the milled powder leading to a higher density. As a result, a higher density was achieved after sintering of the unmilled powder. Adding 0.5 and 0.7 wt.% of La_2O_3 and 0.3 wt.% Y_2O_3 to the 14Cr matrix significantly decreased the density of the specimen especially at 850 and 950 ^oC however, adding Ti to 14L and 14Y improved the density to some extent. The microhardness data of various alloys processed at different temperatures are shown in Fig. 6.4(b). In general, the microhardness increased with higher SPS temperature up to 950 ^oC and then decreased. Both Y and La increased the hardness due to dispersion hardening.

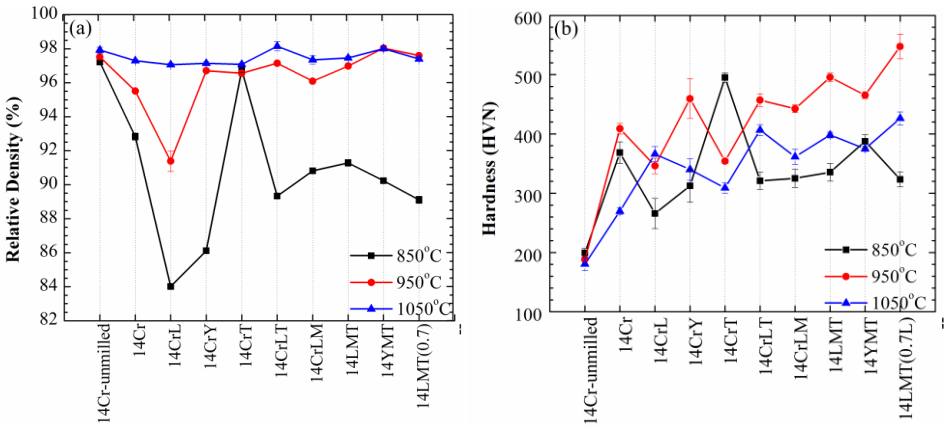

Figure 6.4. (a) The relative density and (b) microhardness values for different SPSed alloys at different SPS temperatures

The hardness increased at higher content of La due to the greater effect of dispersion hardening. Adding Ti separately to the 14Cr matrix improved the hardness due to the dispersion hardening but only at lower temperature (850 ^oC). The coarsening of Ti-enriched particles at above 850 ^oC plausibly decreased the hardness. Higher hardness (457 HV) was achieved by a combined addition of La and Ti to the 14Cr matrix to produce 14LT. Further

addition of Mo to 14LT improved the hardness through solid solution strengthening in 14LMT (495 HV) and similarly in 14YMT (465 HV) alloy. No microstructural evidence was provided to explain drop in microhardness values of 14Y and 14LM alloys and the reason is not clear at this point. High dislocation density and no well defined grain boundaries were characteristic of 14Cr alloy as shown in Fig. 6.1(a). The presence of a low number density and larger oxide particles ($FeCr_2O_4$ and Cr_2O_3) at the boundaries could not create an effective pinning effect during sintering. As a result, some of these particles became confined within the grain interiors. The coarse grains had the capacity to produce and store high density of dislocations that subsequently resulted in the strain hardening effect. The hardening mechanism in 14Cr alloy can thus be attributed to greater dislocation activities and strain hardening mechanism. The grain boundary or precipitation hardening cannot be the dominant mechanism because of larger particles, greater inter-particle spacing and weakened Zener drag effect at the temperature of sintering. Such strain hardening capability in nanocrystalline Fe consolidated via SPS was reported by other researchers too [14, 15]. Interestingly, the high hardness in Fe–14Cr alloy consolidated via SPS at 1100 ^oC for 4 minutes by Auger *et al.* [10] was attributed to the formation of martensite laths caused by higher carbon content diffusing from the die, possible Cr segregation and rapid cooling during SPS. It is noteworthy to mention that no martensite lath was observed in the consolidated 14Cr alloy in the present study.

The level of solutes in the bcc matrix could be much greater than the equilibrium level, associated with a large number of vacancies created during milling. Our recent study [16] has shown that high energy ball milling has a complex role in initiating nucleation of La–Ti–O-enriched NCs in 14LMT alloy powder, with a mean radius of ≈ 1nm, a number

density of 3.7×10^{-24} m^{-3} and a composition of Fe–12.11Cr–9.07Ti–4.05La (at.%). The initiation of NCs during ball milling of NFSs has also been investigated by other researchers [8, 17, 18]. According to Williams *et al*. [8], due to a low equilibrium solubility of O in the matrix, the precipitation of nanoparticles is driven by an oxidation reaction, subsequently resulting in reduction of the free energy. As the SPS proceeds, the number density of NCs would decrease and larger grain boundary oxides would form with the grain structure developing simultaneously during the sintering process [8]. Formation of larger grain boundary oxides in Fig. 6.1(a) could have been preceded by segregation of O and Cr to grain boundaries leading to a decrease in the level of the solutes in the ferritic matrix. The initial oxides forming in a chromium-rich matrix can be Cr_2O_3 as suggested by Williams *et al.* [8]. However formation of $LaCrO_3$ in 14L alloy (shown in Fig. 6.1(b)) was associated with a higher reduction in the free energy according to the enthalpy of formation of various oxides given in Table 6.2.

Table 6.2. The standard enthalpies of formation of various oxide compounds at 25 ^{o}C [8, 22, 23]

Element	Composition	$-\Delta H_f$ (kJ.mol^{-1}(oxide))
Cr	Cr_2O_3	1131
	CrO_2	583
Fe	Fe_3O_4	1118
	Fe_2O_3	822
Ti	TiO	543
	TiO_2	944
	Ti_2O_3	1522
	Ti_3O_5	2475
Y	Y_2O_3	1907
	$YCrO_3$	1493
	$Y_2Ti_2O_7$	3874
La	La_2O_3	1794
	$La_2Ti_2O_7$	3855
	$LaCrO_3$	1536

The presence of nanoparticles inside the grains caused grain boundary pinning and subsequently stabilized the nanocrystalline grains. The high density of defects (dislocations and vacancies) in a supersaturated solid solution, such as 14LMT and 14YMT alloys, could dramatically increase the driving force for accelerated sub-grain formation during the initial stage of sintering. At the initial stage, the vacancies created during the milling are annihilated [8, 17]. Meanwhile, the temperature is not high enough to produce a significant number of thermal vacancies; subsequently, any nucleation of new NCs will be prevented. As the SPS proceeds with no nucleation of new NCs, the high concentrations of extra solutes in the matrix are thermodynamically and kinetically required to precipitate out to form larger oxide particles. The larger solute-enriched oxide particles can be formed more favorably on the grain boundaries due to a higher diffusivity. On the other hand, it should be considered that there is a dynamic plastic deformation occurring within the powder particles during SPS. The interaction of larger particles and dislocations introduced by dynamic hot deformation can explain the coarsening in some grains; because larger particles could not effectively pin the dislocations and the grain boundary migration could be facilitated following the orientation with lower efficiency of Zener drag mechanism [19]. Once the extra solutes present in the matrix precipitated out, the microstructure will remain very stable because of the grain boundary pinning by triple-junctions of the grain boundaries themselves [20], along with the high density of NCs and oxide particles [8].

Further coarsening of the grains will be prevented even at longer dwell times at 950 ^{o}C. Therefore, a bimodal grain size distribution emerged as shown in Figs. 6.1(d–e). The hardening of 14LMT and 14YMT alloys were attributed to solid solution strengthening, Hall – Petch strengthening and precipitation hardening.

Based on the APT studies of the as-milled powder [16] and formation mechanism of the oxide particles suggested by Williams *et al.* [8] it could be speculated that in 14LMT and 14YMT alloys, Cr–O species form first and then absorb Ti and La / Y. This is associated with a change in the interfacial energy of Cr–O species even though it is not thermodynamically the most favorable oxide. It has been established that the driving force for the oxide precipitations to form is the low solubility limit of oxygen in the ferritic matrix. The change in free energy due to oxidation reaction and nucleation of oxide nanoparticles is the primarily the leading mechanism [8].

The majority of the oxygen required to generate the oxide nanoparticles may be provided from the surface oxide during milling process. Furthermore, higher concentrations of Cr led to greater nucleation of Cr–O by influencing the kinetics of oxide formation. Concentrations and diffusivities of the oxide species along with the energy barrier for nucleation will control the nucleation of oxide nanoparticles. After the Cr–O formed during sintering, the Ti–O and Y / La-enriched clusters could form. The sub-stoichiometric NCs in 14LMT and 14YMT alloys were not due to insufficient level of O in the matrix [8]. Formation of stoichiometric $Y_2Ti_2O_7$ and Y_2TiO_5 requires very high temperatures [8] that were not used in this study. Slightly higher number density of NCs was detected in 14YMT (1.5×10^{24} m^{-3}) than in 14LMT (1.4×10^{24} m^{-3}), possibly due to the greater diffusivity of Y than that of La in the ferritic matrix [21]. However, the microhardness values of 14YMT were slightly lower than 14LMT; the reason for this is unclear at this point, but is likely due to other factors such as a higher fraction of nanograins in the 14LMT alloy.

6.4. Conclusions

In summary, Fe–14Cr was found to have a higher hardness at room temperature due to the strain hardening. The stability of its microstructure at high temperatures was improved by addition of La forming the Cr–La–O-enriched NCs. Adding La and Ti to Fe–14Cr matrix significantly improved the mechanical behavior and microstructural stability even further due to the high number density of Cr–Ti–La–O-enriched NCs in 14LMT alloy. However, the number density and size of NCs in 14YMT alloy was estimated to be slightly more. It can be concluded that the potential capability of La in developing new NFSs is promising but more investigation on its thermal stability and irradiation stability will be required.

Acknowledgements

This work was supported partly by the Laboratory Directed Research and Development Program of Idaho National Laboratory (INL), and by the Advanced Test Reactor National Scientific User Facility (ATRNSUF), Contract DE–AC07–05ID14517. The authors gratefully acknowledge the assistance of the staff members at the Microscopy and Characterization Suite (MaCS) facility at Center for Advanced Energy Studies (CAES).

References

[1] M. J. Alinger, G. R. Odette, G. E. Lucas, J. Nucl. Mater. 307–311 (2002) 484.

[2] R. L. Klueh, J. P. Shingledecker, R. W. Swindeman, D. T. Hoelzer, J. Nucl. Mater. 341 (2005) 103.

[3] M. J. Alinger, G. R. Odette, D. T. Hoelzer, J. Nucl. Mater. 329–333 (2004) 382.

[4] M.J. Alinger, G.R. Odette, D.T. Hoelzer, Acta Mater. 57 (2009) 392.

[5] G. R. Odette, M. L. Alinger, B. D. Wirth, Annu. Rev. Mater. Res. 38 (2008) 471.

[6] S. Ukai, T. Okuda, M. Fujiwara, T. Kobayashi, S. Mizuta, Nakashima, H., J. Nucl. Sci. Tech. 39 (2002) 872.

[7] S. Ukai, M. Fujiwara, J. Nucl. Mater. 307–311 (2002) 749.

[8] C.A. Williams, P. Unifantowicz, N. Baluc, G.D. Smith, E.A. Marquis, Acta Mater. 61 (2013) 2219.

[9] M.K. Miller, C.M. Parish, Mater. Sci. Tech. 27 (2011) 729.

[10] M.A. Auger, V. De Castro, T. Leguey, A. Muñoz, Pareja, R., J. Nucl. Mater. 436 (2013) 68.

[11] C. Heintze, M. Hernández-Mayoral, A. Ulbricht, F. Bergner, A. Shariq, T. Weissgärber, H. Frielinghaus, J. Nucl. Mater. 428 (2012) 139.

[12] K.N. Allahar, J. Burns, B. Jaques, Y.Q. Wu, I. Charit, J.I. Cole, D.P. Butt, J. Nucl. Mater. 443 (2013) 256.

[13] Y.Q. Wu, K.N. Allahar, J. Burns, B. Jaques, I. Charit, D.P. Butt, Cole, J. I., Cryst. Res. Technol. DOI 10.1002/crat.201300173 (2013) 1.

[14] K. Oh-Ishi, H.W. Zhang Hw, T. Ohkubo, K. Hono, Mater. Sci. Eng. A 456 (2007) 20.

[15] B. Srinivasarao, K. Ohishi, T. Ohkubo, K. Hono, Acta Mater. 57 (2009) 3277.

[16] S. Pasebani, I. Charit, Y.Q. Wu, D.P. Butt, J.I. Cole, Acta Mater. 61 (2013) 5605.

[17] M.L. Brocq, F. Legendre, M.H. Mathon, A. Mascaro, S. Poissonnet, B. Radiguet, P. Pareige, M. Loyer, O. Leseigneur, Acta Mater. 60 (2012) 7150.

[18] M. Brocq, B. Radiguet, S. Poissonnet, F. Cuvilly, P. Pareige, Legendre, F., J. Nucl. Mater. 409 (2011) 80.

[19] H.K.D.H. Bhadeshia, Mater. Sci. Eng. A 223 (1997) 64.

[20] H.K.D.H. Bhadeshia, Mater. Sci. Technol. 16 (2000) 1404.

[21] A.J. Mueller, R. Bianco, Buckman, R. W., Int. J. Refract. Met. Hard. Mater. 18 (2000) 205.

[22] W. Gale, T. Totemeier, Smithells Metals Reference Book, Amsterdam, Holland, 2004.

[23] T.J. Kallarackel, S. Gupta, P. Singh, J. Am. Ceram. Soc. DOI: 10.1111/jace.12435 (2013) 1.

CHAPTER 7: Microstructural Stability of a Self-Ion Irradiated Lanthana-Bearing Nanostructured Ferritic Steel

Somayeh Pasebani[a,d], Indrajit Charit[a,d], Darryl P. Butt[b,d], James I. Cole[c,d], Lloyd Price[e] and Lin Shao[e]

[a] Department of Chemical and Materials Engineering, University of Idaho, Moscow, ID 83844, USA

[b] Department of Materials Science and Engineering, Boise State University, Boise, ID 83725, USA

[c] Idaho National Laboratory, Idaho Falls, ID 83401, USA

[d] Center for Advanced Energy Studies, Idaho Falls, ID 83401, USA

[e] Department of Nuclear Engineering, Texas A&M University, College Station, TX 77843, USA

(To be submitted to the Journal of Nuclear Materials)

Abstract

Nanostructured ferritic steels (NFSs) are a potential candidate for fuel cladding applications and structural components in the advanced nuclear reactors. The high number density of thermally stable nanofeatures with complex composition is expected to provide excellent high temperature strength and irradiation stability in NFSs. A lanthana–bearing NFS was developed via mechanical alloying and spark plasma sintering of Fe–14Cr–1Ti–0.3Mo–$0.5L_2O_3$ (wt.%), termed 14LMT. The sintered samples were irradiated by Fe^{+2} ions for 10, 50 and 100 dpa at 30 °C and 500 °C. The microstructural stability and mechanical characteristics of the irradiated samples were studied using different microscopy techniques and nanoindentation. The overall grain structure and dislocations configuration did not reveal significant changes after irradiation up to 100 dpa, and no dislocation loops were

observed. Similarly, morphology, number density of the nanofeatures remained unchanged after irradiation. The average radius of the irradiated sample (100 dpa at 500 °C) was slightly smaller than that of the unirradiated sample. A notable irradiation hardening and enhanced dislocation activity occurred after irradiation. Samples irradiated at 30 °C showed a saturation peak in hardness values at 50 dpa and above. However, samples irradiated at 500 °C did not reveal any saturation hardening, and hardness increased monotonically with irradiation dose. Nanoparticles and nanoclusters (NCs) enriched in Ti–La–Cr with number density of 1.3×10^{24} $m^{-3}$and average radius of 1.2 nm were likely responsible for microstructural stability after irradiation up to 100 dpa at 30 and 500 °C. In addition, high density of grain boundaries in a nanostructured 14LMT alloy as well as high density of dislocations can also provide a sink effect for irradiation-induced point effects.

Keywords: Nanostructured ferritic steels; ODS steels; Lanthanum oxide; Spark plasma sintering; Heavy ion irradiation

7.1. Introduction

Successful improvements in efficiency, safety and sustainability of the advanced nuclear reactors will be achieved if fuel cladding materials or structural components present superior mechanical properties and sustain microstructural stabilities after prolonged operation under extreme conditions of higher radiation dose (200 displacement per atom or dpa) and higher temperatures (700 °C) [1-4].

The oxide dispersion strengthened (ODS) steels are considered as potential candidate materials for fuel cladding applications in Gen-IV fission reactors due to their radiation

resistance and creep strength at elevated temperatures [5, 6]. Classical ODS steels such as MA957 (Fe–14Cr–1Ti–0.25Mo–0.25Y_2O_3) [7] and NFSs such as 14YWT (Fe–14Cr–0.4Ti–3W–0.25 Y_2O_3) [3] have been typically produced by mechanical alloying (MA) of pre-alloyed or elemental powder mixture and consolidated via hot extrusion or hot isostatic pressing (HIP).

Microstructure of the NFSs contain an ultra high number density of thermally stable dispersion strengthening nanofeatures (also known as nanoclusters or NCs) enriched in Y–Ti–O or Y–Al–O that are resistant to radiation damage up to 800 °C [8]. These nanofeatures with 2–5 nm in diameter would provide a high tensile and creep strength at elevated temperatures and also trap helium in fine bubbles suppressing void swelling in NFSs [3, 9, 10]. A comprehensive review on the development of irradiation resistant steels can be found in Ref. [9]. Microstructure, mechanical properties, thermal and irradiation stability of the developed ODS steels and NFSs under heavy ion irradiation have been studied by researchers, and the irradiation tolerance of these materials have been found to be promising [1, 6, 11, 12].

In our previous studies [13] the potential of using an alternative rare earth (RE) oxide in processing a new NFS was investigated by replacing Y_2O_3 with La_2O_3 and as a result, an alloy with nominal composition of Fe–14Cr–1Ti–0.3Mo–0.5La_2O_3 (wt.%) termed as 14LMT was developed. In addition to altering the RE constituent in the chemical composition, the traditional consolidation methods such as HIP and extrusion were replaced by spark plasma sintering (SPS) [14].

Field activated sintering technique (FAST) also known as pulsed electric current sintering (PECS) and commercially known as SPS is a processing technique utilizing

uniaxial force and pulsed (on–off) direct electrical current (DC) under low atmospheric pressure or vacuum to rapidly sinter the powder. Due to direct heating by Joule mechanism, high heating rate and cooling rate can be obtained. This would enhance densification over grain growth and accelerate diffusion mechanisms while maintaining the intrinsic properties of nanopowders in their fully dense compact [15]. The SPS has many advantages over the HIP including ease of operation and accurate control of sintering energy as well as fast sintering speed, high reproducibility, safety and reliability [16].

The microstructure and mechanical properties of 14LMT alloy sintered at 950 °C for 7 min have been previously investigated, and a high number density (1.4×10^{24} m^{-3}) of Cr–Ti–La–O–enriched NCs with average radius of 1.4±0.2 nm was observed in the 3-D atom probe tomography (APT) maps [14]. The stability of these NCs under irradiation is critical, and collision cascades can eject solute atoms from these NCs and change the characteristics of them [17, 18]. Hence, irradiation experiments are required to examine stability of NCs. Neutron irradiation experiment was out of scope of this study and self-ion irradiation was applied instead. Was *et al.* [19] have recently reported that ion irradiation experiments, especially at high doses, can be tailored through controlling He production and damage rate in such a way to emulate radiation damage in reactor. Therefore, in the current study the self-ion (Fe^{+2}) irradiation experiments were conducted on the developed 14LMT NFS specimens at both room (30 °C) and elevated temperature (500 °C) for different doses (0, 10, 50 and 100 dpa). The current study is intended to examine the irradiation response of lanthana-bearing NFS developed via SPS to heavy ion irradiation at low and elevated temperatures. In order to do so, the mechanical properties and microstructural characteristics of numerous ion-irradiated samples are investigated.

7.2. Experimental

7.2.1. Material processing

The starting constituent powders including Fe (99.9 wt.%, average particle size of 40 μm), Cr (99.8 wt.%, average particle size of 5 μm), Ti (99.7 wt.%, average particle size of 26 μm), La_2O_3 (99.99 wt.%, average particle size of 40 nm) and Mo (99.9 wt.%, average particle size of 1–2 μm) were mixed in the nominal proportion of Fe–14Cr–1Ti–0.3Mo–0.5La_2O_3 (wt.%). Except for Mo powder that was procured from the Micron Metal Powder Inc., the rest of the powders were procured from the American Elements Inc.

High energy ball milling was performed in an air-cooled SPEX 8000M mixer / mill for 10 h using 316 stainless steel balls (8 mm in diameter) as the milling media. A milling batch consisted of 100 g steel balls and 10 g powder giving a ball to powder ratio (BPR) of 10:1.

The milled powder was consolidated via SPS by using a Dr. Sinter Lab SPS-515S machine (SPS Syntex Inc., Kanagawa, Japan). A Tri-Gemini cylindrical graphite die with an inner diameter of 12.7 mm and an outer diameter of 38 mm was used. The inner surface of the die and radial surfaces of punches were covered with a graphite foil (0.25 mm in thickness) to facilitate the removal of the sintered specimens. In order to inhibit the diffusion of carbon from the punches and graphite foil to the powder mixture, a thin niobium foil (thickness of 0.06 mm) was placed between the powder and the graphite foils. The die was wrapped in a graphite felt (thickness of 4 mm) to minimize heat loss by thermal radiation.

The milled powder was sintered at 950 ^{o}C for 45 min under vacuum (7×10^{-3} Torr or 0.9 Pa). A pulsed DC current with pattern of 12–2 (current on for 12 ms and off for 2 ms), a heating rate of 100 ^{o}C/min and a pressure of approximately 80 MPa (10 kN force) were used

here. The final product was in the form of a disk with diameter of 12.5 mm and thickness of 8 mm.

7.2.2. Heavy Ion Irradiation

Prior to irradiation experiments, thin disk specimens with diameter of 12 mm and thickness of 1 mm were cut and mechanically polished using standard metallographic procedures of grinding and polishing followed by a final polish in a Buehler Vibromet 2 vibratory polisher using 0.05 μm alumina slurry for up to 48 h. The irradiation experiments using Fe ion (Fe^{+2}) ion beam were conducted at the Texas A&M Ion Beam Laboratories using IoneX 1.7 MV Tandetron accelerator with a source of negative ions cesium sputtering (SNICS) at temperatures of 30 °C and 500 °C. The specimens were irradiated to doses of 10, 50 and 100 dpa (1dpa was equal to 5.75×10^{14} ions.cm^{-2}) with an ion flux of 1.88×10^{12} ions.cm^{-2} sec.

For irradiation tests at 30 °C, specimens were attached to an electrically isolated stage by double sided copper tape. This stage was able to read beam current directly and was hooked to a current integrator. This allowed for direct current measurement during the experiment.

For irradiation tests at 500 °C, specimens were mounted to a heated stage using silver paint and heated from a resistance heater (Firestick) while the temperature was measured by a thermocouple near the edge of the stage. A temperature calibration was performed to know the temperature at the center of the stage in comparison to the temperature at the edge of the stage, so that the sample temperature could be precisely known from that measurement. Since the stage emits electrons when it is heated, current cannot be directly measured. Instead, a current measurement was taken from the Faraday cup directly in front of the

sample stage periodically (every 15–30 min). This was allowed due to the high stability of the sputter source over very long time scales, and gave accurate results.

In order to extract Fe ions, the sputter ion source was started to maximum power after turning on the ionizer which had a tungsten filament with a ceramic coating. Heating process had to be conducted slowly as the thermal expansion of tungsten was different relative to the ceramic coating. Once filament became hot, it started producing electrons. In order to extract the ion species from the target cathode (purity of Fe 99.95 %), various voltages were needed. Then, Cs reservoir was heated to allow its vapors to transfer into the source head. When Cs reservoir reached the proper temperature, Fe ions were extracted.

The radiation damage profile (i.e. dpa as a function of depth) is estimated using the Stopping and Range of Ions in Matter (SRIM) 2008.04 software [20] and displayed in Fig. 7.1. The peak of the profile was observed at 0.9 μm distance (depth) from specimen surface. Table 7.1 summarizes the irradiation parameters for raster scanning iron ion (Fe^{+2}) irradiation on 14LMT steel in current study. At 30 °C, three different doses (10, 50 and 100 dpa), and the control sample (unirradiated) were considered. Similarly for irradiation at 500 °C three different doses (10, 50 and 100 dpa) and a control sample (unirradiated at 500 °C) were studied. The control sample at 500 °C was taken from the unirradiated area after exposure at 500 °C for almost 8 hours to include the effect of temperature and time.

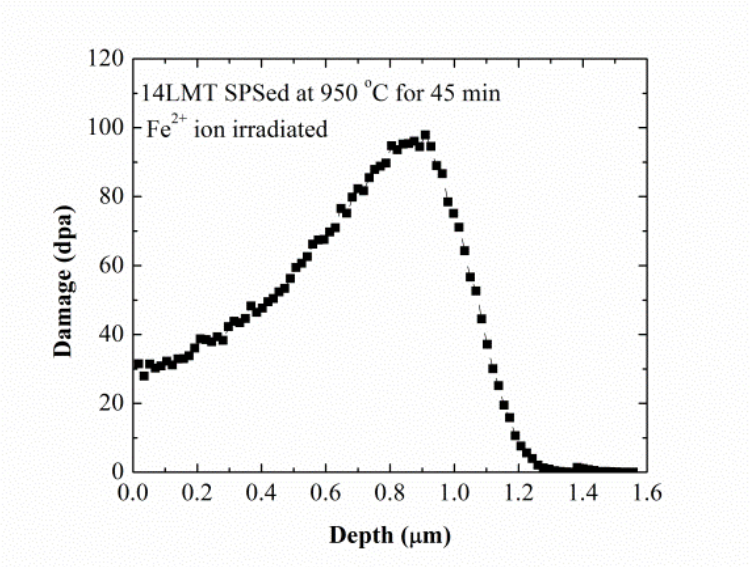

Figure 7.1. The Fe^{+2} irradiation damage profile (SRIM profile) of 14LMT alloy

Table 7.1. The irradiation parameters for raster scanning for iron ion (Fe^{+2}) irradiation on 14LMT steel

Condition	Rastering Area (mm^2)	Fluence ($ion.cm^{-2}$)	Time Under Irradiation (min)
10 dpa at 30 °C	10×10	5.86×10^{15}	95
50 dpa at 30 °C	10×10	2.93×10^{16}	417
100 dpa at 30 °C	10×10	5.86×10^{16}	369
10 dpa at 500 °C	7×7	5.86×10^{15}	95
50 dpa at 500 °C	7×7	2.93×10^{16}	417
100 dpa at 500 °C	7×7	5.86×10^{16}	512

7.2.3. Microstructural studies

7.2.3.1. Transmission electron microscopy

Since the irradiated layer in the specimens was not thicker than 1 μm, a focused ion beam (FIB) FEI Quanta 3D FEG instrument with a Ga-ion source was used to prepare samples for transmission electron microscopy (TEM) studies.

During FIB process, a protective layer of Pt with thickness of 3 μm was deposited on the specimen surface area of 20 μm × 2 μm using a voltage of 5 kV and current of 3.0 nA.

Bulk milling (using 30 kV and 7.0 nA) and rough cleaning (using 30 kV and 3.0 nA) were conducted on each edge of the protected area; then lamella was welded on a needle using an Omniprobe tip with Pt and lifted out. Following that, lamella was mounted on a copper grid and milled sequentially with 3.0 nA, 1.0 nA, 0.3 nA and 0.1 nA at voltage of 10 kV. Final cleaning was performed using 48.0 pA current at a voltage of 5 kV and 27.0 pA at a voltage of 2 kV to remove gallium contamination and damage from the specimen. The final thickness of lamella varied between 50–100 nm in different specimens. For TEM studies, a FEI Tecnai TF30 FEG STEM operating at 300 kV was utilized.

7.2.3.2. Atom probe tomography studies

A focused ion beam (FIB) was used to prepare specimens for atom probe tomography (APT) studies. The FIB experiment was carried out using an FEI Quanta 3D FEG instrument with a Ga-ion source. The APT analysis was carried out using a CAMECA LEAP 4000X HR operating in voltage mode at the specimen temperature of 50–60 K and 20% of the standing voltage pulse fraction. The atom maps were reconstructed using CAMECA IVAS 3.6 software.

The maximum separation cluster algorithm was used to identify the composition of NCs. The maximum separation between solute atoms is defined as d_{max} whereas L is the maximum separation of additional elements and E is the erosion distance for removal of atoms near the cluster / matrix interface. An N_{min} (the minimum size of a cluster) value of 10–15, d_{max} values of 0.6–0.8 nm, L values of 0.4–0.5 nm and E values ranging from 0.3–0.5 nm were chosen based on procedures described comprehensively in the literature [12, 21].

A background noise correction was applied to the mass spectrum and the matrix composition was calculated by excluding those atoms defined as a cluster based on the

maximum separation method. The size of NCs was estimated from the radius of gyration (r_G) which is the average distance between each atom and the center of a corresponding cluster [22]. This was applied to APT datasets each containing 8–10 million ions.

7.2.4. Nanoindentation

A Hysitron Nanoindenter (model TI–950 TriboIndenter) with a Berkovich tip (radius of 200 nm and tip angle of 142.35°) was used for the hardness measurements at room temperature. Prior to indentation, a fused silica reference material was used to calibrate the tip geometry with a total of 100 indents.

The indentations were made on the irradiated area for all six specimens (30 °C for 10, 50 and 100 dpa and 500 ^{o}C for 10, 50 and 100 dpa) and also on un-irradiated part of the specimens. Samples were mounted on a magnet without using any hot wax. Indents were produced in a direction normal to the sample surface with constant time segment using a multi-cycling method. A total of 100 cycles were obtained with 2 s holding time.

For each condition, more than 15 arrays of indentations were collected for accuracy in order to estimate the damage profile. Then 5 best data sets were plotted as variation of hardness (GPa) as a function of indentation depth (nm). The data sets obtained from the depth below 100 nm were ignored and not plotted due to ambiguity deriving from the tip complication. The total depth of penetration was 1000 nm, and the distance between the indents was approximately 50 μm.

7.3. Results and discussion

7.3.1. Microstructural examination and analyses

7.3.1.1. Transmission electron microscopy

The TEM bright field (BF) micrograph in Fig. 7.2(a) exhibits a representative view of the irradiation damage layer, protective Pt layer and the analyzed region in 14LMT alloy. The TEM BF micrographs in Figs. 7.2(b–g) show the overall microstructures of 14LMT alloy unirradiated, irradiated at 30 °C for 100 dpa, unirradiated at 500 °C; and irradiated at 500 °C for 10 dpa, 50 dpa and 100 dpa, respectively.

The microstructure in Figs. 7.2(b–g) consisted of mainly nanograins, high density of grain boundaries, dislocations and precipitates. The grain structure including grain size remained unchanged after irradiation at 30 and 500 °C up to 100 dpa, and no recrystallization or grain growth were observed after irradiation at higher temperature. The analysis of selected area diffraction (SAD) patterns did not indicate formation of any radiation induced particles or phase. No voids, amorphization, and hallo ring formation were observed in the micrographs shown in Figs. 7.2. (b–g).

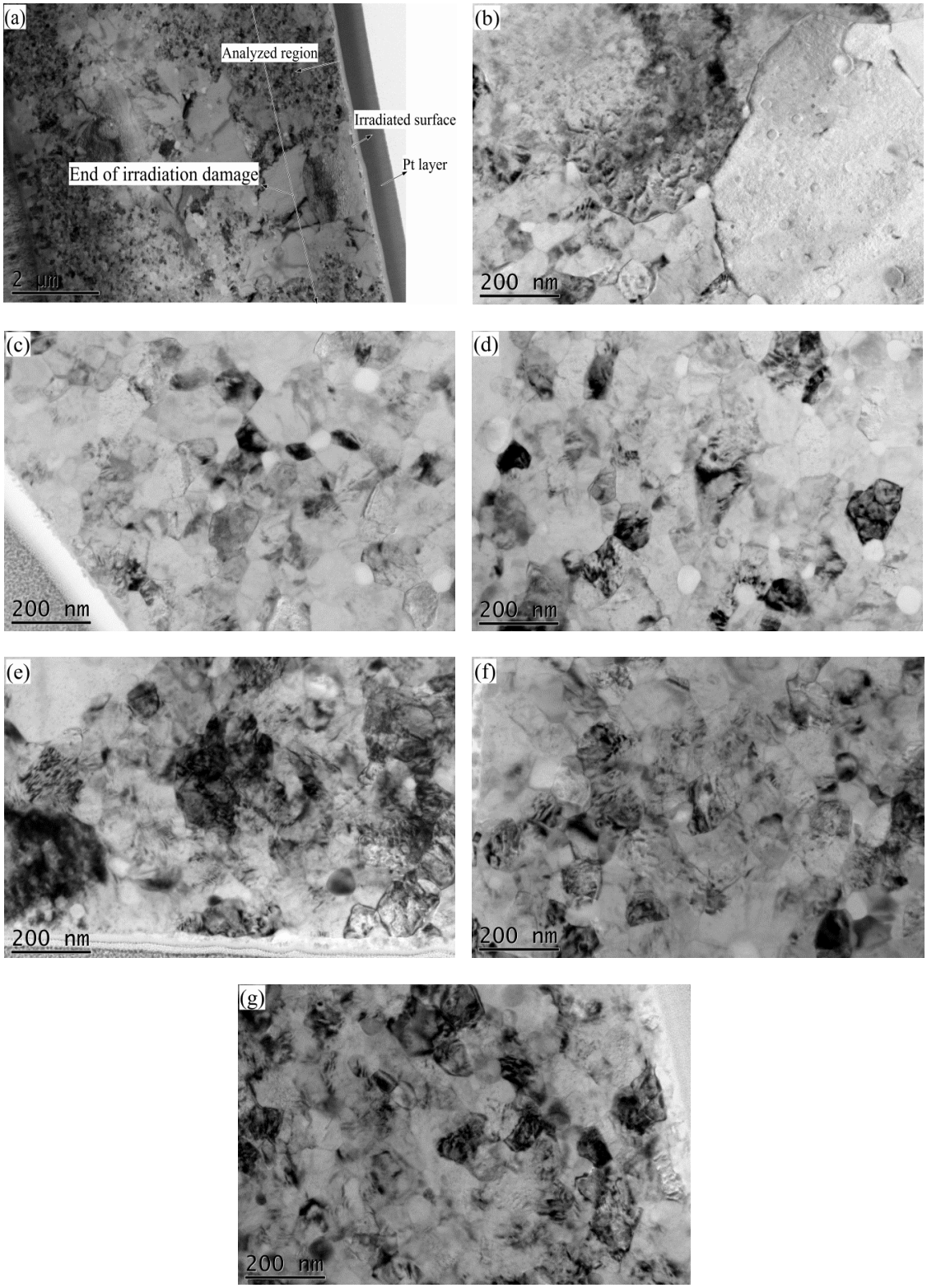

Figure 7.2. The overview of the microstructure of 14LMT alloy: (a) the irradiation damage and analyzed region, (b) unirradiated, (c) irradiated at 30 °C for 100 dpa, (d) unirradiated at 500 °C, (e) irradiated at 500 °C for 10 dpa, (f) irradiated at 500 °C for 50 dpa, and (g) irradiated at 500 °C for 100 dpa

The dislocation structures in the unirradiated condition, irradiated conditions at 30 °C for 100 dpa, unirradiated at 500 °C and irradiated at 500 °C for 10, 50 and 100 dpa are shown in Figs. 7.3(a–f), respectively. The micrographs were obtained under two-beam conditions and close to a major zone axis. High density of dislocations and nano-sized black dots without evidence of small loops or tangled networks were identified in the micrographs shown in Figs. 7.3(a–f). All the micrographs were obtained at similar beam conditions (g = [011]), and this was a challenging task to do due to nanocrystalline and magnetic intrinsic properties of the samples. The "black dots" in the unirradiated sample shown in Fig. 7.3(a) could be due to FIB artifacts. Higher number of 'black dot' damage was observed in Fig. 7.3(b) after irradiation at low temperature (30 °C). The black dots were expected to occur after irradiation at relatively low temperature (< 300 °C) [23]. Lower number of black dots was observed after irradiation at 500 °C as shown in Figs. 7.2(d–f) which could be due to sample preparation and FIB artifacts. The dislocation density was estimated for all the micrographs shown in Figs. 7.3(a–f) and measured to be ($3.7\pm0.3\times10^{14}$ m^{-2} for unirradiated sample, $6.0\pm0.2\times10^{14}$ m^{-2} for sample irradiated at 30 °C for 100 dpa, $2.7\pm0.3\times10^{14}$ m^{-2} for unirradiated at 500 °C sample (i.e. annealed at 500 °C for 8 h), $2.8\pm0.8\times10^{14}$ m^{-2} for sample irradiated at 500 °C for 10 dpa, $4.2\pm0.4\times10^{14}$ m^{-2} for sample irradiated at 500 °C for 50 dpa and $5.1\pm0.2\times10^{14}$ m^{-2} for sample irradiated at 500 °C for 100 dpa. The dislocation density increased at higher doses regardless of irradiation temperature. The changes in dislocation density under irradiation are attributed to the high surface stresses caused by the high dose of implanted surfaces during the ion irradiation process [24]. In unirradiated samples, a slight reduction occurred in dislocation density at 500 °C due to thermal dislocation annihilation but the recovery was not extensive since the dislocations were pinned by

nanoparticles as will be shown later. High density of dislocations that are effectively pinned by nanoparticles along high density of grain boundaries could provide strong sink sites for radiation-induced point defects such as vacancies and interstitial defects [4, 25].

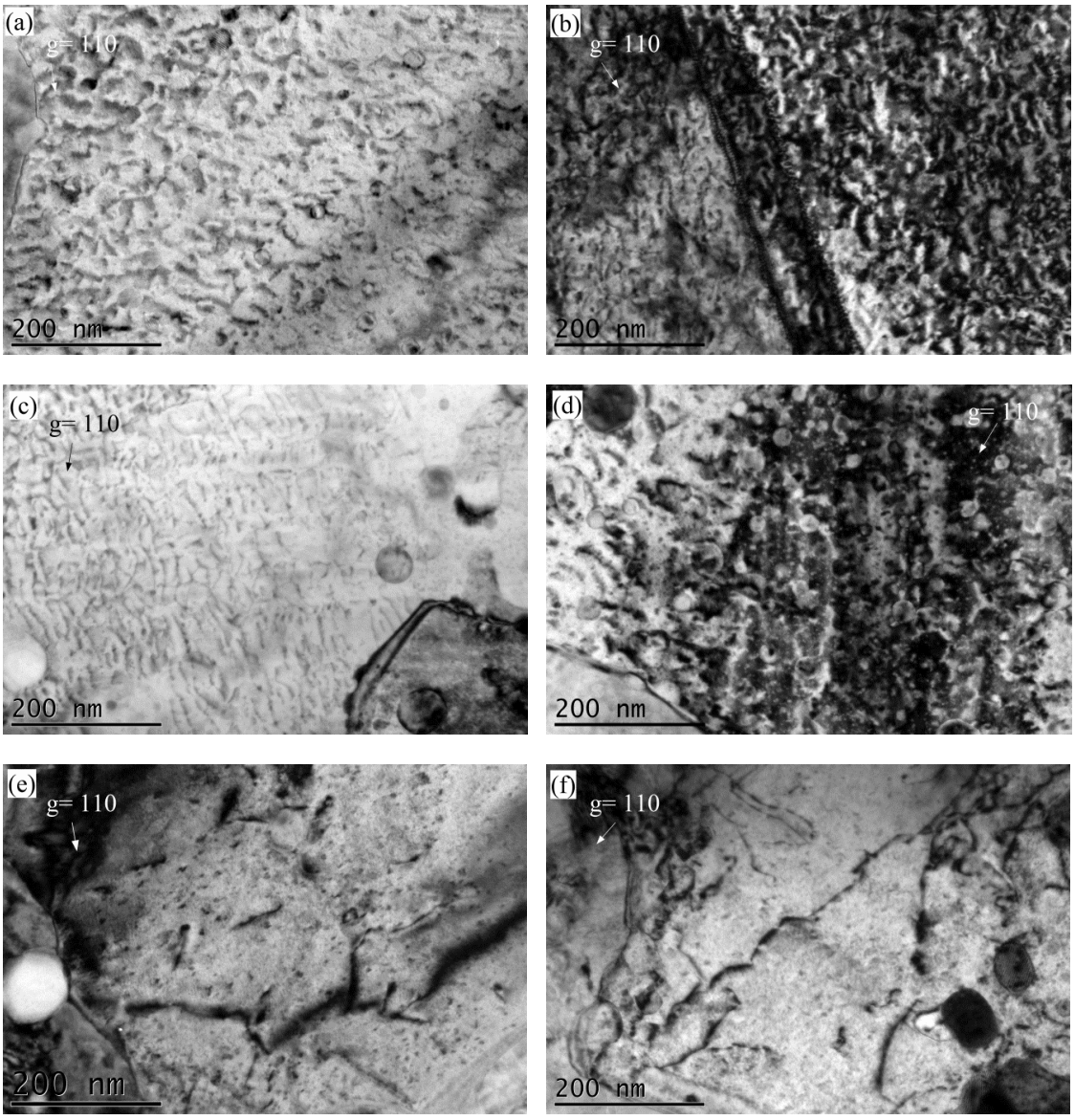

Figure 7.3. The dislocations configurations in 14LMT alloy: (a) unirradiated, (b) irradiated at 30 °C for 100 dpa, (c) unirradiated at 500 °C, (d) irradiated at 500 °C for 10 dpa, (e) irradiated at 500 °C for 50 dpa, and (f) irradiated at 500 °C for 100 dpa

The oxide particles of 14LMT alloy, unirradiated, irradiated at 30 °C for 100 dpa, unirradiated at 500 °C, irradiated at 500 °C for 10 dpa, 50 dpa and 100 dpa can be observed in Figs. 7.4(a–f), respectively. The micrographs did not reveal a strong contrast between the nanoparticles and the matrix in the BF mode; however, the particle size did not undergo any significant irradiation coarsening or refining. No halo of small particles surrounding larger oxide particles was observed in TEM micrographs shown in Figs. 7.4(a–f). So, the matrix / particles interface, shape, morphology and size of the particles did not show significant changes under irradiation condition up to 100 dpa.

The particle size distribution histograms for the samples 0 dpa (unirradiated), 100 dpa at 30 °C, and 0 dpa, 10, 50 and 100 dpa at 500 °C are illustrated in Figs. 7.5(a–f), respectively. In order to provide a better statistical data, approximately 300 particles were considered for each plot. Significant particle refining was not observed in Figs. 7.5(a–f). However, the fraction of particles smaller than 2 nm slightly increased at higher doses and appeared to be more obvious after irradiation at 500 °C than at 30 °C.

Higher magnification (here 295 kX) micrographs were utilized for constructing the plots in Figs. 7.5(a–f), mainly focusing on the smallest particles mainly. So, particles larger than 36 nm were not included in the plots even though they were observed in some of the micrographs obtained at lower magnification. Also, due to TEM resolution limit and FIB sample preparation, particles smaller than 1 nm were not detected well.

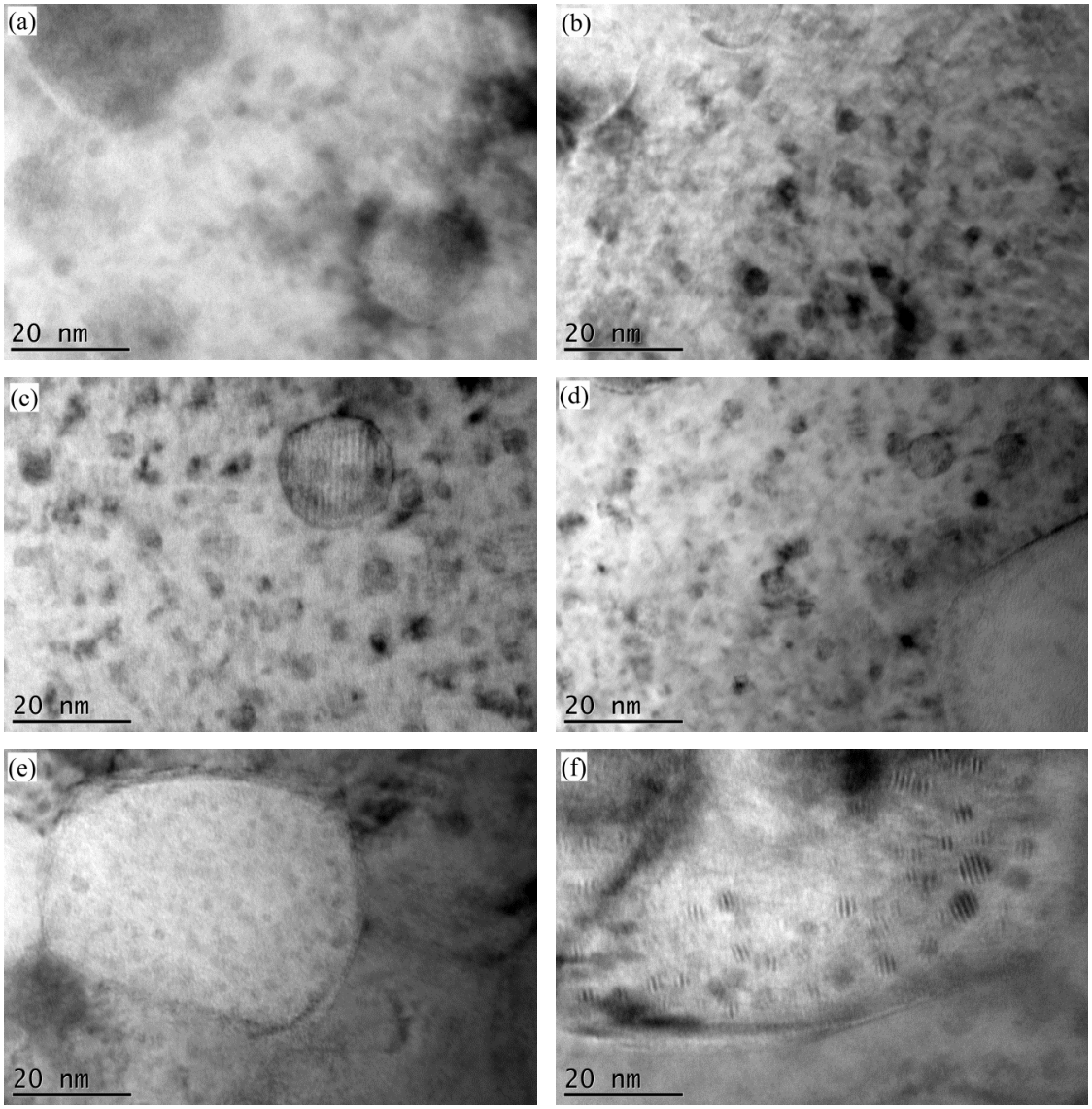

Figure 7.4. The oxide particles of 14LMT alloy: (a) unirradiated, (b) irradiated at 30 °C for 100 dpa, (c) unirradiated at 500 °C, (d) irradiated at 500 °C for 10 dpa, (e) irradiated at 500 °C for 50 dpa, and (f) irradiated at 500 °C for 100 dpa

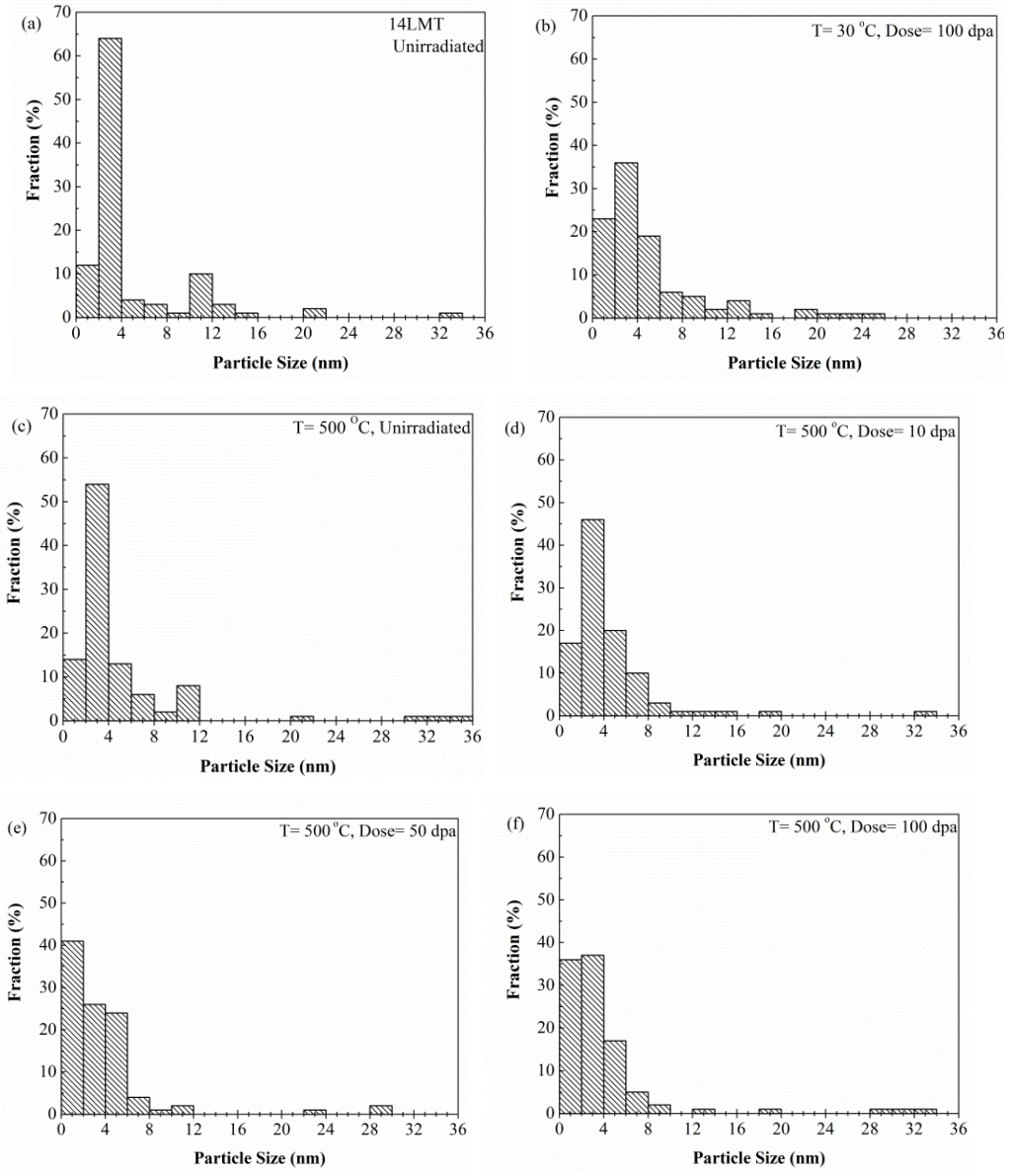

Figure 7.5. Particle size (radius) distribution for 14LMT samples: (a) unirradiated, (b) irradiated at 30 °C for 100 dpa, (c) unirradiated at 500 °C, (d) irradiated at 500 °C for 10 dpa, (e) irradiated at 500 °C for 50 dpa, and (f) irradiated at 500 °C for 100 dpa

Figure7. 6(a) shows a high angle annular dark field (HAADF) STEM micrograph obtained at a relatively lower magnification (34kX) from a large area of the sample showing the end of irradiation damage layer (with thickness of 1.6 μm), and the analyzed region. The nanoparticles distributed and irradiated samples were clearly observed in Z-contrast micrographs shown in Figs. 7.6(b–d). No significant changes in morphology or qualitative chemical composition of the particles were noted in the Z-contrast micrographs.

An energy dispersive X-ray spectroscopy (EDS) spectrum from a particle with diameter of 10 nm in the irradiated sample (100 dpa, 500 ^{o}C) is shown in Fig. 7.6(e). From the EDS spectrum, Fe, Cr, Ti, La and O were detected for this small oxide particle. Because the oxide particles were located in a foil thicker than the particle size, the EDS data included matrix information. Thus, due to inherent limitations of EDS and also relatively greater thickness of foil, no accurate comparable chemical composition data could be obtained from nanoparticles in the unirradiated and irradiated samples. Larger particles were mainly Cr-based oxide or Ti-based oxide and did not show any irradiation induced alteration in the chemical composition.

The energy filtered TEM (EFTEM) experiments were performed for 14LMT unirradiated sample (500 °C) and 14LMT irradiated at 500 °C for 100 dpa. The respective EFTEM micrographs are included in Figs. 7.7(a–h). The particles shown in EFTEM maps were mostly enriched with Ti and O and relatively poor of Fe. The particles smaller than 10 nm were enriched in La but was difficult to resolve in EFTEM due to thickness of the samples. This trend was similar for both unirradiated and irradiated samples implying that irradiation and thermal annealing did not significantly alter the qualitative chemical composition of nanoparticles.

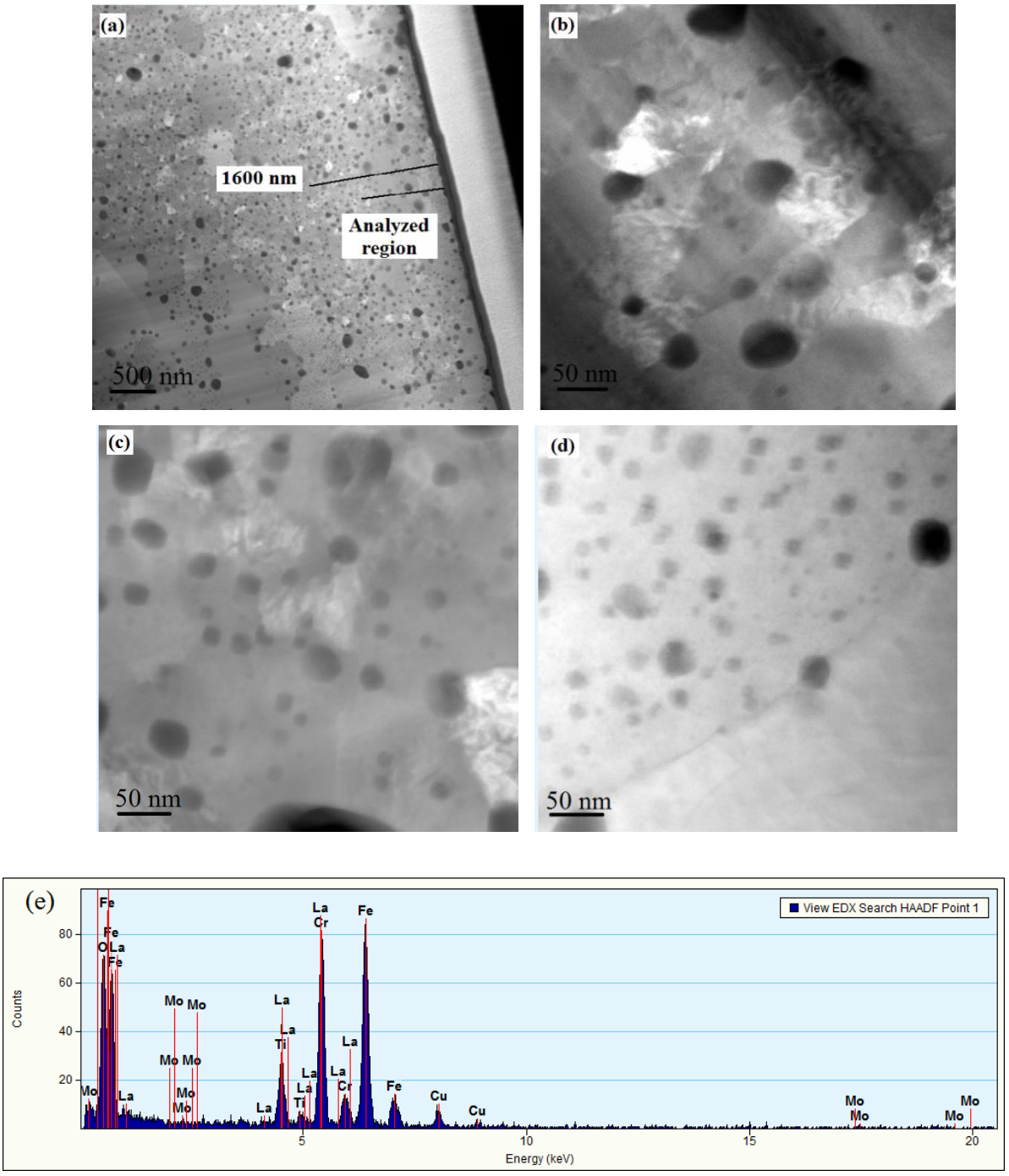

Figure 7.6. HAADF STEM micrograph overall view of the specimen: (a) the overview of the sample, (b) unirradiated, (c) unirradiated at 500 °C, (d) irradiated at 500 °C for 100 dpa and, (e) an EDS spectrum from oxide particles in sample irradiated at 500 °C for 100 dpa

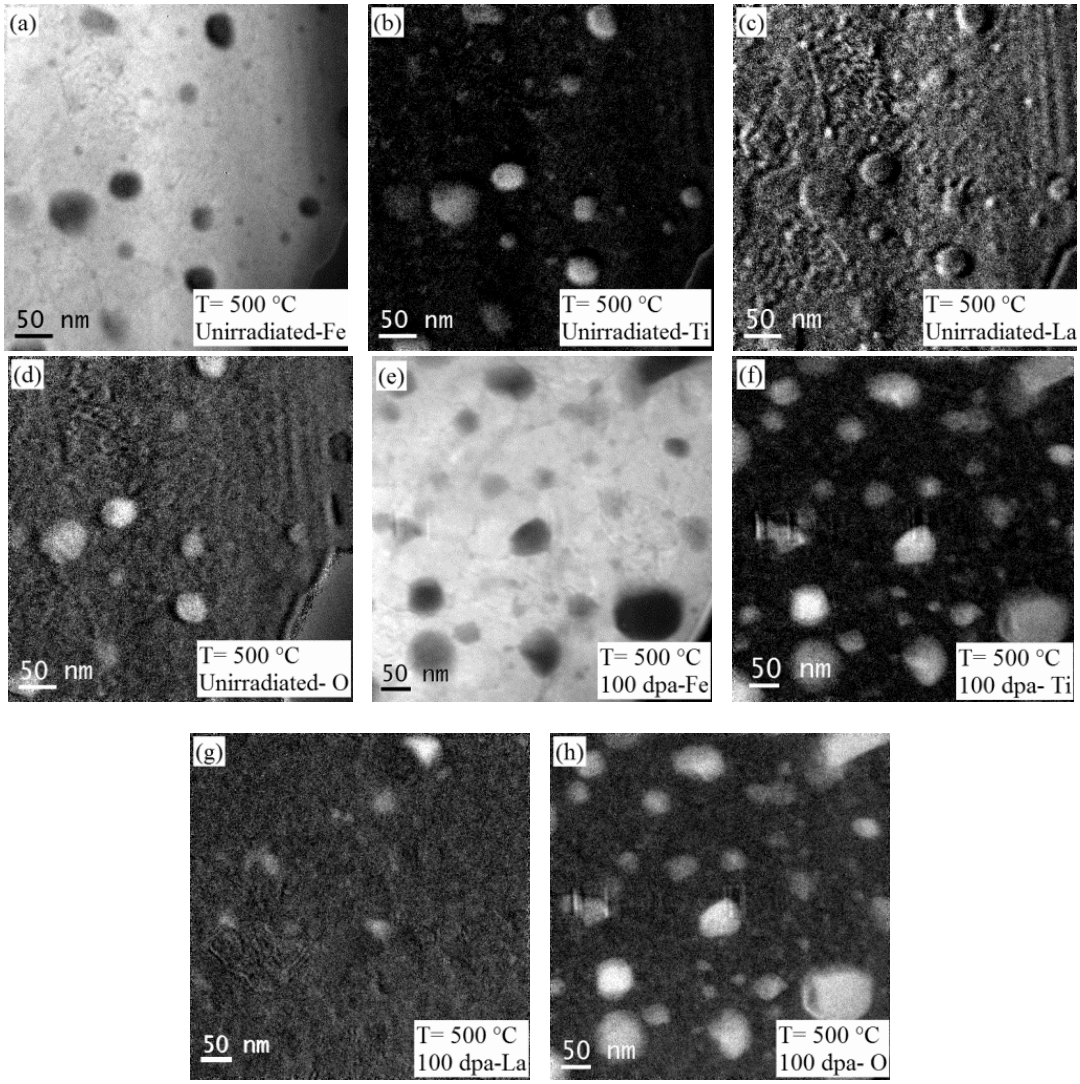

Figure 7.7. EFTEM maps for 14LMT alloy: (a) unirradiated – Fe, (b) unirradiated – Ti, (c) unirradiated – La, (d) unirradiated – O, (e) 100 dpa – Fe, (f) 100 dpa – Ti, (g) 100 dpa – La and, (h) 100 dpa – O (the temperature condition for all micrographs was at 500 °C)

Even though no void swelling was observed in the irradiated samples, the role of oxide particles in suppressing void are yet considered as secondary. While the main contribution of nanoparticles is on high temperature mechanical strength, stabilizing subgrains and dislocation configurations, the ferritic structure of the matrix would predominantly minimize the void swelling. Furthermore, the rastering mode of irradiation utilized in this study is not expected to produce detectable void swelling.

7.3.1.2. APT studies

The high resolution TEM (HRTEM) micrograph combined with APT maps of the NCs with diameter smaller than 5 nm of the unirradiated 14LMT alloy are shown in Figs. 7.8(a–e). The number density of Cr–, Ti–, La–, O-enriched NCs in 14LMT alloy (unirradiated) was estimated to be 1.2×10^{24} m^{-3} with an average Guinier radius of 1.5±0.3 nm. The HAADF STEM micrograph obtained from NCs and some larger oxide particles along with APT results of 14LMT sample irradiated at 500 °C for 100 dpa are shown in Figs. 7.8(f–j). The number density of Cr–, Ti–, La–, O–enriched NCs in 14LMT sample irradiated at 500 °C for 100 dpa was estimated to be 1.2×10^{24} m^{-3} with average Guinier radius of 1.3±0.2 nm. The summary of APT analysis results including average radius, number density and average compositions of the clusters for both unirradiated and irradiated 14LMT alloy are presented in Table 7.2.

The average chemical composition of NCs before and after irradiation did not exhibit significant changes. However, the concentration of Ti in NCs slightly decreased, and the concentration of Cr in NCs showed an increase after irradiation at 500 °C. Lanthanum, oxygen and iron concentration, however, remained approximately unchanged after irradiation at 500 °C up to 100 dpa. During formation of collision cascades, it is likely that some solute atoms like Cr and Ti get ejected from the NCs and re-diffuse from the matrix to the NCs given the high temperature (500 °C) and relatively long time (8 h).

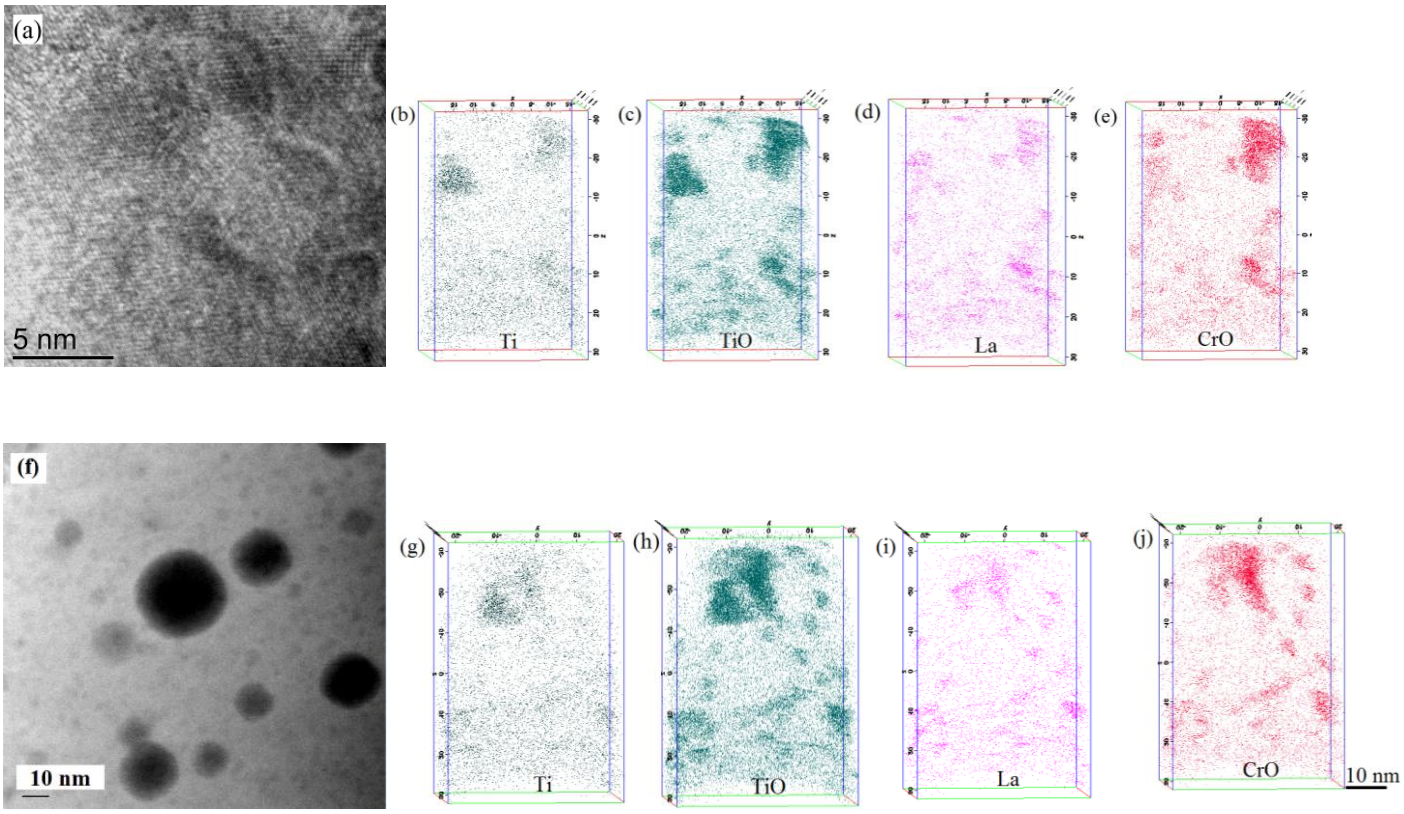

Figure 7.8. (a) HRTEM micrograph obtained from 14LMT unirradiated specimen prior to APT, corresponding (b) Ti map, (c) TiO map, (d) La map, (e) CrO map, (f) HAADF STEM micrograph obtained from 14LMT irradiated at 500 °C for 100 dpa prior to APT, corresponding (g) Ti map, (h) TiO map, (i) La map, and (j) CrO map (analyzed volume was 40×40×80 nm^3)

Table 7.2. Summary of the average radius, number density and average cluster composition obtained from APT results of 14LMT alloy samples unirradiated and irradiated at 500 °C for 100 dpa

Condition	Ave. Radius (nm)	No. Den. (10^{24} m^{-3})	Ave. Cluster Composition (at.%)					
			Cr	O	Ti	La	Mo	Fe
Unirradiated	1.5±0.2	1.2	8.9±2.2	35.25±3	17.8±2	6.89±0.8	0.06±0	31.1±6
100 dpa at 500 °C	1.3±0.2	1.2	12.2±3	36.6±2	15.4±3	8.8±2.1	0.2±0.5	26.8±5.2

Certain *et al.* [17] suggested that back-diffusion of solutes from the matrix to the NCs becomes possible under high temperature irradiation due to faster diffusion of atoms and this could lead to a "dynamic stability" in NCs. On contrary, the instability of NCs after

irradiation at –75 °C was associated with low or no diffusion of solute atoms implying that NCs could be more stable at higher temperatures rather than lower temperatures. The reason of higher Cr concentration and lower Ti concentration in NCs of the irradiated sample is not clear at this point and more investigations are necessary, but at 500 °C the diffusion coefficient of Cr in α–Fe is approximately 2.5 times more than that of Ti in α–Fe; for Cr diffusion in α–Fe, Q = 55,400±700 cal/mol and D_o = 0.64±0.07 cm^2s^{-1} [26] and for Ti diffusion in α–Fe, Q = 59,200 cal/mol and D_o = 3.15 cm^2s^{-1} [27]. In order to understand the role of diffusion in altering the chemical composition of NCs during the irradiation, more investigation especially at different temperatures is required.

The La+Ti:O ratio in NCS before and after irradiation was 0.98 and 1.15, respectively, implying a negligible increase in La+Ti:O ratio after irradiation. For calculating La+Ti:O ratio, the influence of matrix has been removed here. The number density of NCs remained unchanged after irradiation up to 100 dpa. The radius of NCs exhibited a slight refining after irradiation up to 100 dpa at 500 °C.

The APT maps and the size distribution histograms of NCs in a smaller volume of 14LMT alloy unirradiated and irradiated at 500 °C for 100 dpa are presented in Figs. 7.9(a–h). The size of NCs before and after irradiation did not show any remarkable changes, and only a slight refining after irradiation was identified. The NCs size distribution histograms for both unirradiated and irradiated 14LMT alloys are calculated from several APT data sets and illustrated in Fig. 7.9(d) and Fig. 7.9(h), respectively. The size distribution histogram for both unirradiated and irradiated at 500 °C for 100 dpa was similar; however, the latter histogram showed a slight decrease in the size of NCs. Pareige *et al.* [28] studied the stability of NCs in 12YWT after irradiation to 0.7 dpa with 150 keV Fe ions at

300 °C. The size, number density, and chemical composition of the NCs were similar to those observed in unirradiated specimens. However, under neutron irradiation, the instability of oxide particles in terms of morphology and crystallinity might be an issue as reported by Monnet *et al.* [29]. The fate of microstructural evolution including nanoparticles in different ODS alloys after ion and neutron irradiation are summarized in Table 7.3.

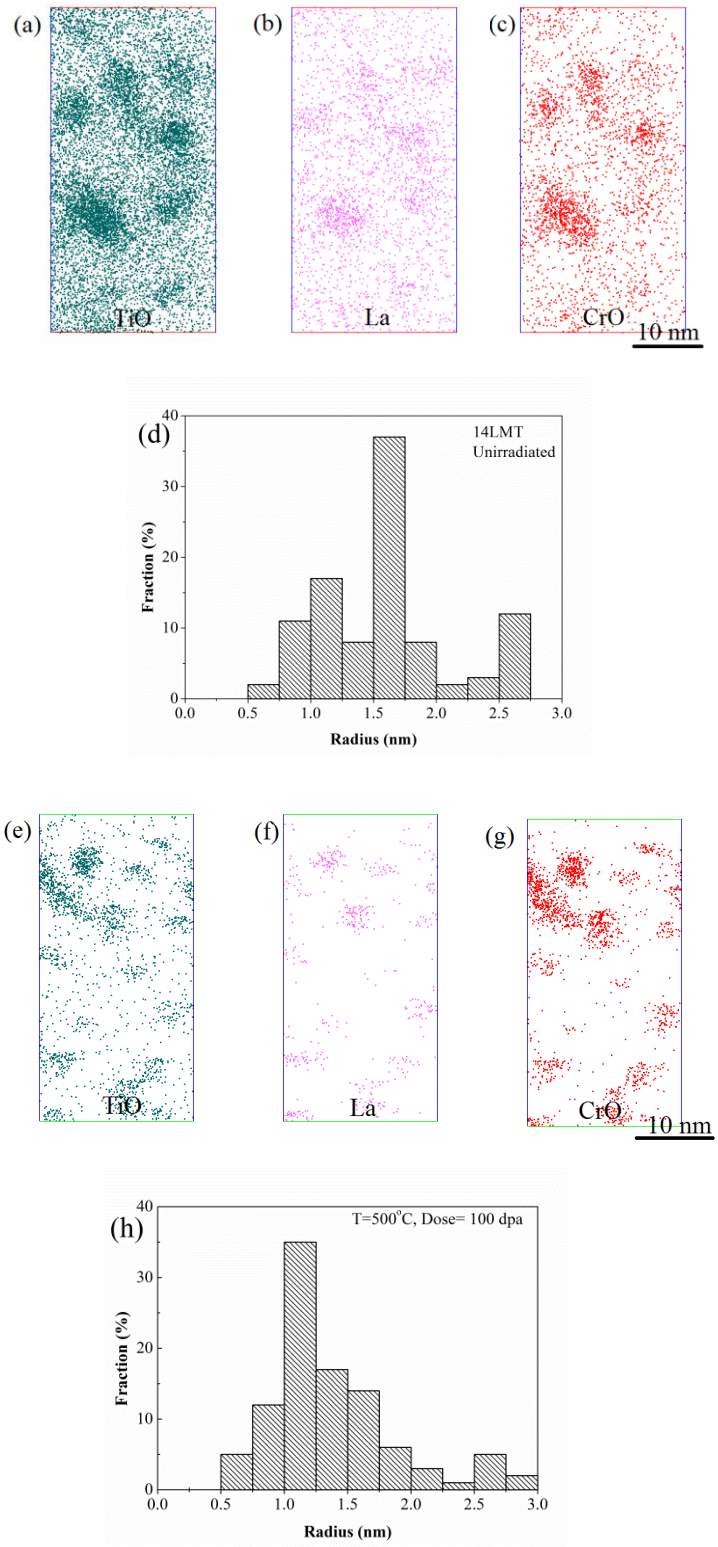

Figure 7.9. The APT maps of unirradiated specimen showing NCs enriched in: (a) TiO, (b) La, (c) CrO, (d) NCs radius distribution histogram for 14LMT unirradiated, (e) the APT maps of irradiated showing NCs enriched in (e) TiO, (f) La, (g) CrO, and (h) NCs radius distribution histogram for 14LMT irradiated at 500 °C for 100 dpa

Table 7.3. Summary of irradiation response of some ODS steels under ion and neutron irradiation

Alloy	Composition (wt.%)	Irradiation Conditions	Irradiation Response	Ref.
K1 K4	Fe–19Cr–0.3W–0.3Ti–0.35Y_2O_3 Fe–19Cr–2W–4Al–0.3Ti–0.35Y_2O_3	6.4 MeV Fe^{+3} Dose:50 dpa Temp: 670 °C	Grain morphology, grain size and fine dispersed oxides were unchanged. The complex Y–Ti–O-enriched and Y–Al–O-enriched particles were found to be stable.	[6]
9Cr–ODS	Fe–9.19Cr–2W–0.21Ti–0.33Y_2O_3	5 MeV Ni ions Dose: 5, 50 and 150 dpa Temp: 350–700 °C	The microstructre did not change and was dominated by dense dislocations, precipitates and yttrium oxide particles.	[1]
14YWT	Fe–14Cr–3W–4Al–0.4Ti–0.25Y_2O_3	5 MeV Ni^{+2} ions Dose: 5, 50 and 100 dpa Temp: –75, 300, 450 and 600 °C	The Y–Ti–O-enriched particles were stable after irradaitation at higher temperature due to dynamic stability; however, NCs were unstable at lower temperature due to low diffusion of the ejected solutes.	[17]
12YWT	Fe–12.3Cr–3W–0.39Ti–0.25Y_2O_3	150 keV Fe ions Dose: 0.7 dpa Temp: 300 °C	The size, number density and composition of NCs remained unchanged after irradiation. Neither dissolution nor coarsening of particles occurred.	[28]
MA957	Fe–14Cr–1Ti–0.3Mo–0.25Y_2O_3	300 keV of Fe ions Dose: 21 dpa Temp: 25 °C 1 MeV of Kr ions Dose: 200 dpa Temp: 500 °C	High density of black dot damage and developing loops as well as particle amorphization and degradation was reported.	[32]
MA957	Fe–14Cr–1Ti–0.3Mo–0.25Y_2O_3	Dual and single ion irradiation with 1 appm He Dose:150 dpa Temp:450 and 650 °C 3 MeV Ni^{+} Dose: 150 dpa Temp: 525 °C	The dislocation structure and dispersion was stable, especially under single-ion irradiation, while recovery was observed in dual-ion irradiated specimens. The oxide particles were stable under irradaition.	[33]
DT2203Y05	Fe–13Cr–2.2Ti–1.5Mo–0.5Y_2O_3	52 MeV Cr^{+6} and 4 MeV α particles Dose: 50 dpa and He 600 appm Temp: 475 °C	Yttria phase remained unchanged and dislocation density remained high and stable. There was a possibility of Laves phase and α' formation.	[34]
FeCrAl	Fe–20Cr–5.5Al–0.5Ti–0.5Y_2O_3	2.5 MeV Fe ions Dose: 31 dpa Temp: room temperature and 300 °C	Size and composition of Y–Al–O-enriched particles were stable and formation of nanocavities filled by He was observed.	[35]

Eurofer97	Fe–9.5Cr–0.65W–0.15Y–0.2Si–0.45Mn–0.21V–0.04Ta–0.65C	0.5–2 MeV Dose: 2 dpa Temp: 400 °C	The oxide particles were stable and siginificant Mn segregation was observed at dislocations and grainboundaries with less density of oxide particles. Mn segregation could possibly contribute to irradiation induced hardening.	[36]
16Cr	Fe–16Cr–0.1Ti–0.02C–0.35Y_2O_3	6.4 MeV Fe ions Dose: 60 dpa Temp: 650 °C	HRTEM and APT studies revealed that the size, shape and composition Y–Ti–O-enriched complex dispersoids were stable.	[37]
MA 956	Fe–19.4 Cr–4.8Al–0.38Ti–0.58Y_2O_3	123.4 MeV Ni ions Dose: 0.7– 1.8 dpa Temp: 440 °C	Small voids and stable oxide particles were observed.	[38]
12Cr–ODS	Fe–12.5Cr–2.5W–0.25Ti–0.4Y_2O_3	33 keV H ion 50 ppm/dpa Dose: 15 dpa Temp: 350, 450 and 550 °C	The oxide particles were stable but the interface between the dispersed oxide particle and the matrix became irregular due to the irradiation. Hydrogen irradiation caused void formation.	[39]
F94 ODS F 95 ODS	Fe–11.8Cr–0.3Ti–1.93W–0.24Y_2O_3 (MA in He) Fe–11.8Cr–0.3Ti–1.93W–0.24Y_2O_3 (MA in Ar)	Fast neutrons (JOYO) Dose: 7,2.5,14 and 15 dpa Temp: 330, 400, 450 and 500 °C	The oxide particles were stable during neutron irradiation with no evidence of growth and/or dissolution of the oxide particles. The heavier gas element in MA atmosphere is better than a lighter one in order to reduce irradiation-induced bubble coarsening. So, Ar was better than He in this study.	[4]
18Cr–ODS	Fe–18Cr–1W–0.3Ti–0.6Y_2O_3	150 keV in situ ion irradiation Dose: 4, 23, 45 and 48 dpa Temp: 500 °C	Y–Ti–O-enriched particles as small as 5 nm were stable up to 45 dpa. However, some larger oxides (> 20nm) seemed more affected by irradiation, showing evidences of interface and shape modifications.	[40]
316–ODS High Cr	Fe–16.2Cr–13.6Ni–0.35Y_2O_3	10.5 MeV ion or neutron? Dose: 20 dpa Temp: 250 and 380 °C	Irradiation-induced dislocations and dislcoation loops were extensive.	[31]
DY–ODS	Fe–13Cr–1.48Mo–0.08Mn–2Ti–0.45Y–0.3O	700 keV Kr^{2+} Dose: 100 dpa Temp: 500 °C	Amorphizatin occurred in the oxides. The spherical shape and particle surface morphology may be altered.	[41]

18Cr–ODS	Fe–18Cr–1W–0.3Ti–0.5Y_2O_3	92 MeV Xe ions Dose: 2.5 dpa (flunece of 3.5× $10^{14}cm^{-2}$) Temp:27 and 507 °C	Shape, composition and size of the oxide particles remained unchanged. No dissolution of the particles were observed. Possible amorphization after irradiation at low temperature was observed.	[42]
12Cr–ODS	Fe–12Cr–0.4Y_2O_3	Triple Fe^{+2}, He^{+}, H^{+} irradiation (JANNUS) Dose: 4.4 dpa Fe 2.23 × 10^{15} ions/cm^2 and 5.6 × 10^{15} ions/cm^2 He^{+} and H^{+} Temp:21 °C	Y–rich nanoparticles were stable and the crystalline structure was not altered.	[43]
KP4–ODS alloy	Fe–15Cr–4Al–2W–0.35Y_2O_3	700 MeV Bi ions: Dose: 1.2×10^{-3}, 4.8×10^{-4} dpa 167 MeV Xe ions Dose: 1.5×10^{-2} and 1×10^{-3} dpa Temp: 25 °C	Small oxide particles (<5 nm) remained crystalline in Bi irradiation, while subsurface regions in large (> 20 nm) particles were amorphized. Xe ion irradiation resulted in amorphization of small $Y_4Al_2O_9$ oxide particles while the amorphous bodies of large particles were found to contain small crystalline inclusions.	[44]
14YWT	Fe–14Cr–3W–0.4Ti–0.25Y_2O_3	5 MeV Ni^{+2} ions Dose: 100 dpa Temp: 300, 450 and 600 °C	Size and number density of NCs did not change especially at higher temperatures.	[45]
ODS ferrite–DT	Fe–13Cr–2.2Ti1.5Mo–0.5Y_2O_3	Neutron–Phenix Dose: 80 dpa Temp: 400–580 °C	Y_2O_3 dissolved under neutron irradiation with the dose of 80 dpa.	[46]
DY EM10+ Y_2O_3	Fe–12.9Cr–1.48Mo–2Ti–0.45Y–0.3O Fe–8.6Cr–1.15Mo–0.51Mn–0.38Si–0.18Y–0.13O	Neutrons Phenix Dose: 81 dpa 1 MeV He Dose: 0, 54.8, 75.6, 79.3, 78.8 and 30.5 Temp: 400, 435,484,508, 532 and 580 °C	Oxide particles were stable under He irradiation but a significant dissolution of oxides occurred under neutron irradiation (>60 dpa). The interfaces of oxide particles with the matrix became irregular, and a halo of fine oxides appeared around the larger oxides. The chemical composition of oxides altered losing Al and Ti from the NCs.	[29]

7.3.2. Nanomechanical characterization

Nanoindentation results for unirradiated and irradiated samples are included in Figs. 7.10(a–h). The hardness data were acquired at indentation depth of 100–1000 nm below the surface. All the samples showed constant increase in hardness with higher doses. Minor annealing effect on dislocation structures was likely to be the reason of lower hardness values at 500 °C compared to 30 °C, especially in unirradiated sample and in samples with lower doses. The sample irradiated at 500 °C for 100 dpa, the hardness values were close to those of the sample irradiated at 30 °C under the same dose, and radiation hardening effect became more dominant than annealing and dislocation annihilation effect. The estimated dislocation density for irradiated samples was consistent in relation to the nanoindentation results.

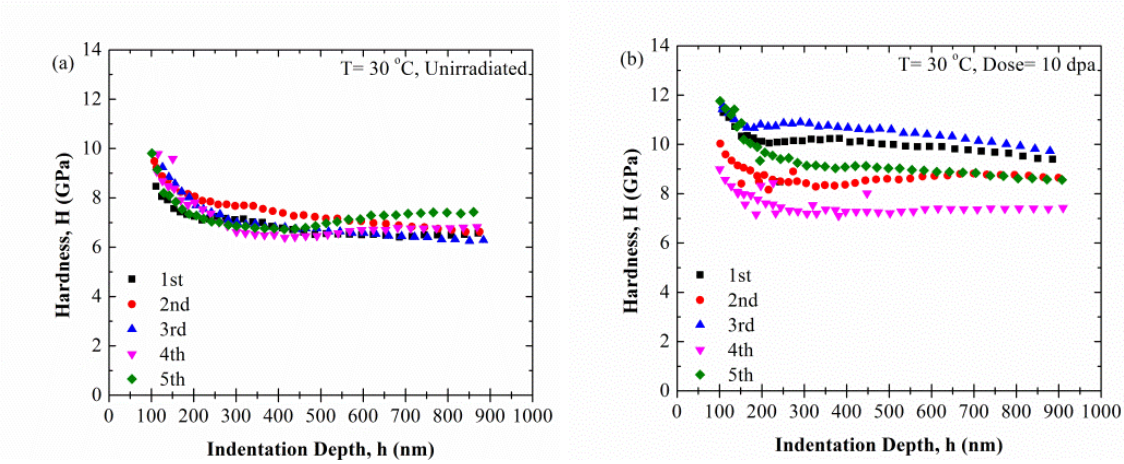

Figure 7.10. Nanoindentation results obtained by using the multi-cycling method: (a) unirradiated, (b) irradiated at 30 °C for 10 dpa, (c) unirradiated at 30 °C for 50 dpa, (d) irradiated at 30 °C for 100 dpa, (e) unirradiated at 500 °C, (f) irradiated at 500 °C for 10 dpa, (g) irradiated at 500 °C for 50 dpa, and (h) irradiated specimen at 500 °C for 100 dpa

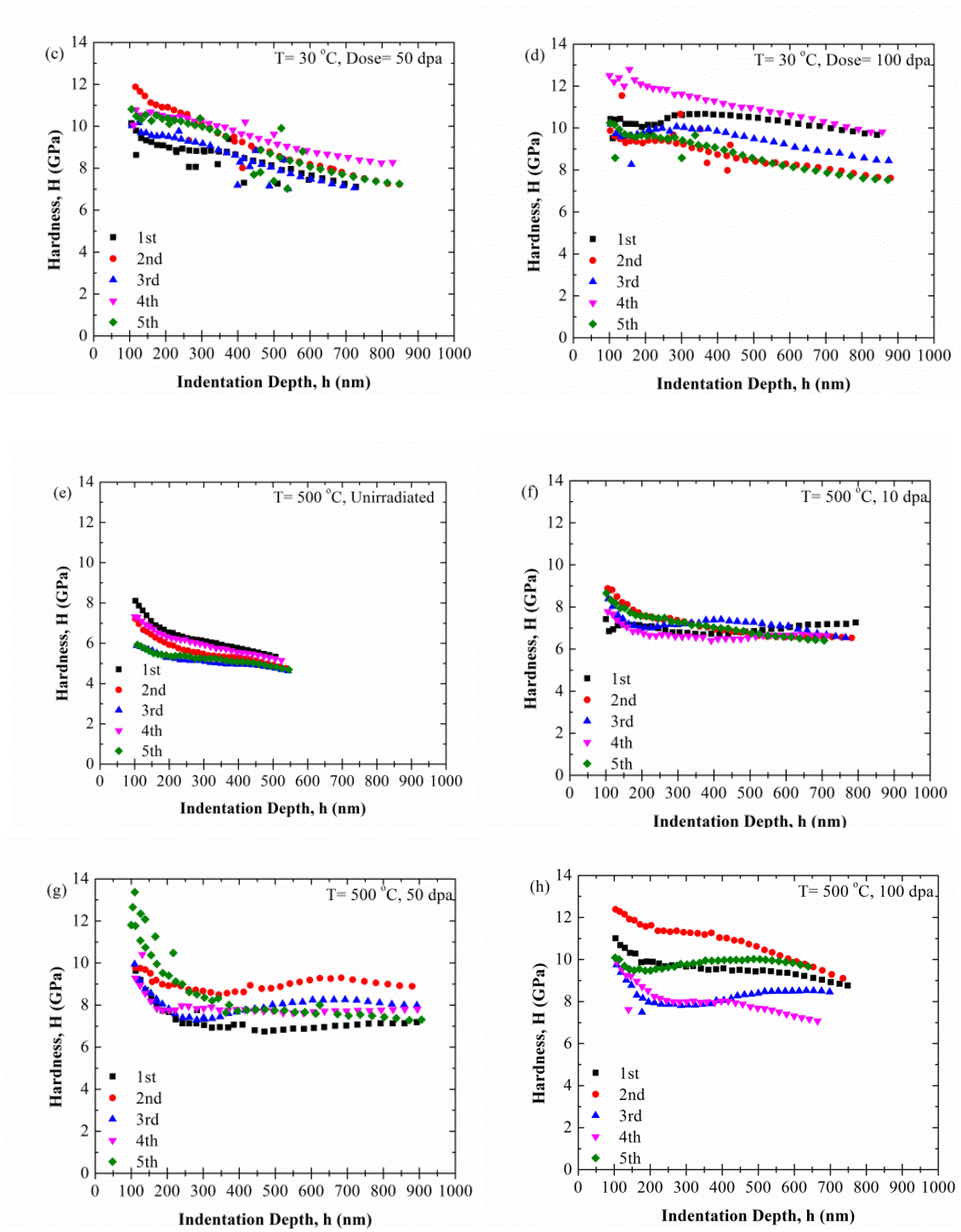

Continued Figure 7.11. Nanoindentation results obtained by using the multi-cycling method: (a) unirradiated, (b) irradiated at 30 °C for 10 dpa, (c) unirradiated at 30 °C for 50 dpa, (d) irradiated at 30 °C for 100 dpa, (e) unirradiated at 500 °C, (f) irradiated at 500 °C for 10 dpa, (g) irradiated at 500 °C for 50 dpa, and (h) irradiated specimen at 500 °C for 100 dpa

Figures 7.11(a–b) show the averaged nanoindentation hardness for samples 0, 10, 50 and 100 dpa at 30 and 500 °C, respectively. In Fig. 7.11(a), the averaged hardness values significantly increased after 10 dpa and then slightly increased after 50 and 100 dpa displaying saturation in hardness at 50 dpa and above. As illustrated in Fig. 7.11(b), the averaged hardness values constantly increased at higher doses. The dependence of the ratio of H_{irrad} and $H_{unirrad}$ (radiation hardening ratio) on indentation depth for irradiated samples at 30 °C for 100 dpa and at 500 °C for 10, 50 and 100 dpa is illustrated in Fig. 7.11(c). For irradiation at 30 °C, there was a peak in value of H_{irrad} / $H_{unirrad}$ at indentation depth of 200 nm. The peak was observed at about 20% of damaged layer thickness which is consistent with other reported studies [30, 31]. The ratio of H_{irrad} and $H_{unirrad}$ decreases when the implantation depth is less than the radius of hemispherical influence zone of the indentation. For irradiation at 500 °C, H_{irrad} / $H_{unirrad}$ constantly increased with indentation depth and radiation doses, and no peak was observed. This could be likely due to the lower hardness of unirradiated sample at 500 °C as a result of thermal annihilation of dislocations. The hardness of unirradiated samples at 500 °C was lower than the hardness of unirradiated sample at 30 °C and thus the ratio of H_{irrad} / $H_{unirrad}$ became greater. Since the implantation depth is approximately constant for all the samples, the radiation hardening ratio at 500 °C for 100 dpa was found to be higher than the radiation hardening ratio at 30 °C for 100 dpa. Another reason may be that partially dynamic dislocation annihilation at 500 °C allowed more dislocation storage capacity and more hardening to occur at the same irradiation dose.

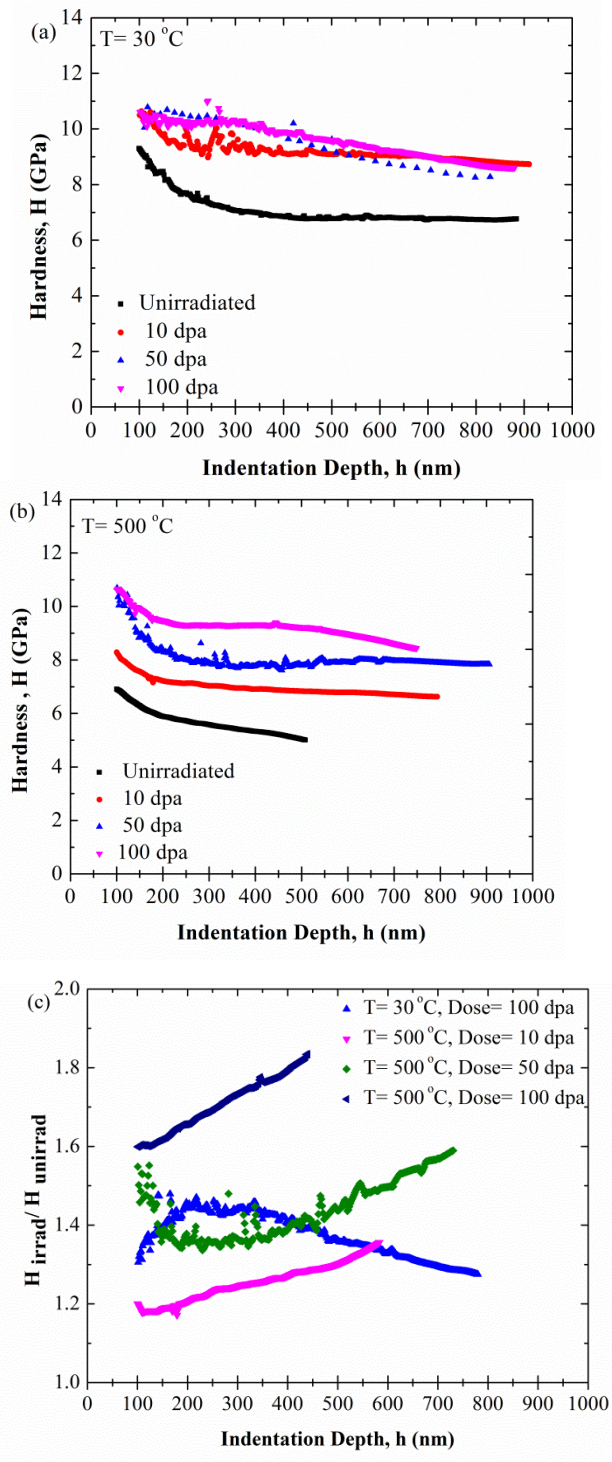

Figure 7.12. The averaged hardness results obtained by using the multi-cycling method: (a) 0, 10, 50 and dpa at 30 °C, (b) 0, 10, 50, and 100 dpa at 500 °C (each graph is averaged of 15 plots), and (c) $H_{irrad} / H_{unirrad}$ on indentation depth

The indent region in unirradiated and irradiated samples is shown in Fig. 7.12(a–b), respectively. A FIB lift-out was conducted at a region adjacent to the indent in the irradiated sample (500 ^{o}C, 100 dpa) shown in Fig. 7.12(b). The deformed microstructure was observed using TEM and included in Fig. 7.12(c). No clear evidence of localized deformation and dislocation channeling was observed, and the plastic deformation was found to be uniform. This could explain the absence of any saturation in hardening for the irradiated 500 ^{o}C sample. High dislocation activity including significant dislocation–particle interaction was observed in the deformed microstructure. A combination of nanoparticles interacting with the dislocations, and high density of grain boundary areas could efficiently provide sink sites for the dislocations. The deformed grain structure was similar to the undeformed one and no strain-induced grain growth was observed in the nanocrystalline region.

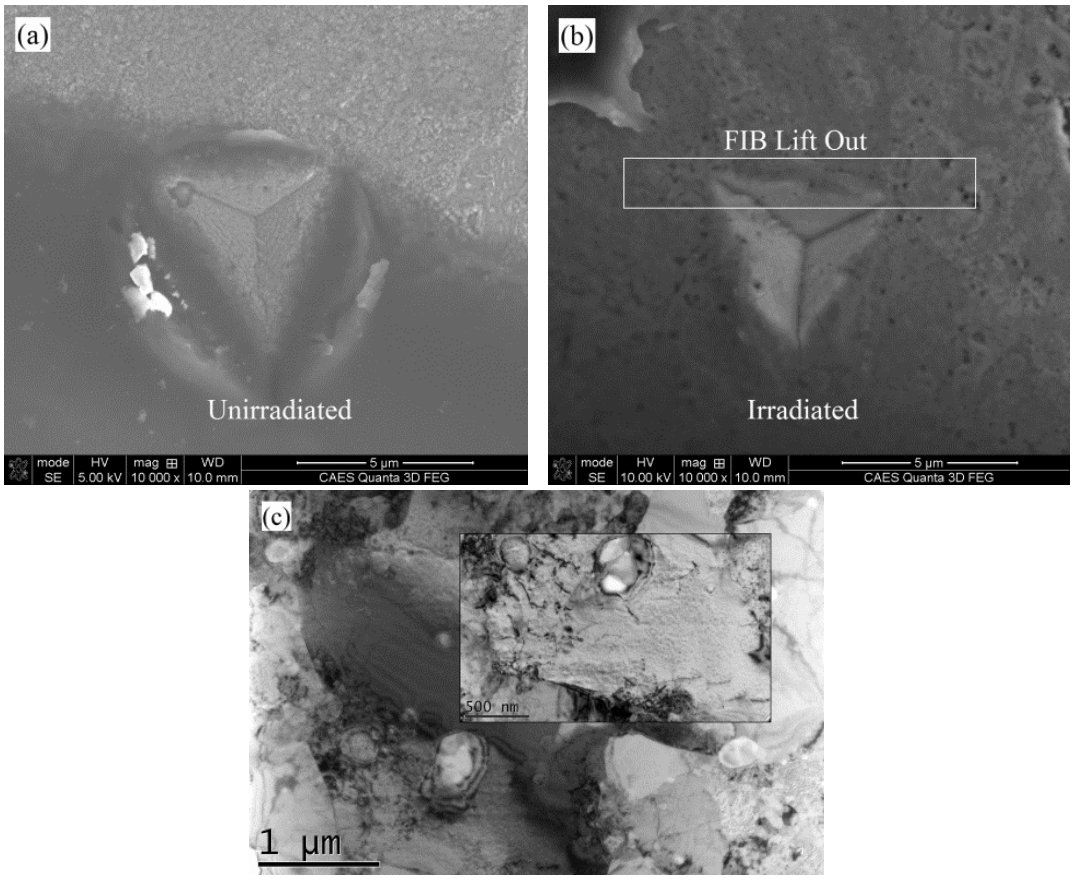

Figure 7.13. SEM micrographs showing the deformed region in the vicinity of an indent: (a) unirradiated sample and (b) irradiated at 500 °C for 100 dpa; the white rectangular region represntes the area for FIB lift-out and (c) the TEM BF micrograph from the FIB lift-out displaying the deformed microstructure in the vicinity of an indent as shown in Fig. 12(b)

7.4. Summary and conclusions

The heavy self-ion (Fe^{+2}) irradiation experiments were performed on lanthana-bearing nanostructured ferritic steel termed 14LMT alloy at 30 °C and 500 °C for different doses; 10, 50 and 100 dpa. The microstructure and nanoindentation properties of the irradiated samples were studied. An unirradiated control sample at each temperature was also studied. The overall grain structure and dislocation configuration did not exhibit any significant changes caused by thermal influence and irradiation damage. No clear evidence of dislocation loops or void swelling was detected in the irradiated samples. The dislocation

density constantly increased with increasing irradiation dose causing hardening across the entire irradiation damage depth. The high number density of La–Ti–O-enriched particles could play a big role in stabilizing the dislocation configurations under thermal and irradiation damage involved. The shape, morphology and number density of NCs did not reveal any significant changes after irradiation up to 100 dpa. The radius of NCs however slightly decreased after irradiation at 500 °C for 100 dpa in comparison with that of the unirradiated sample. The Cr concentration of NCs was found to be higher and Ti concentration of NCs was lower after irradiation at 500 °C for 100 dpa. The reason is not clear at this point but is likely due to different diffusion rates of ejected solute atoms while back-diffusing from the ferritic matrix to the host NCs. Significant irradiation hardening occurred in all the irradiated samples. The radiation hardening after irradiation at 30 °C showed saturation after 50 dpa and above. This saturation was not observed at 500 °C, and the irradiation induced hardening and dislocation density constantly increased at higher doses. The microstructural stability of 14LMT under heavy ion irradiation showed stability up to 100 dpa and more irradiation experiments with higher doses (200, 300 and 400 dpa) are planned for our future studies.

Acknowledgments

This work was supported partly by the Laboratory Directed Research and Development Program of Idaho National Laboratory (INL), Contract DE–AC07–05ID14517, and partly by a grant of the Advanced Test Reactor National Scientific User Facility (ATRNSUF). The authors greatly acknowledge the staff of Microscopy and Characterization Suite (MaCS) facility at the Center of Advanced Energy Studies (CAES) located at Idaho Falls.

References

[1] T.R. Allen, J. Gan, J.I. Cole, M.K. Miller, J.T. Busby, S. Shutthanand, S. Thevuthasan, J. Nucl. Mater., 375 (2008) 26−37.

[2] M.K. Miller, C.M. Parish, Mater. Sci. Technol., 27 (2011) 729−734.

[3] M.J. Alinger, G.R. Odette, D.T. Hoezler, Acta Mater., 57 (2009) 392−406.

[4] N. Akasaka, S. Yamashita, T. Yoshitake, S. Ukai, A. Kimura, J. Nucl. Mater., 329–333 (2004) 1053−1056.

[5] R.L. Klueh, P.J. Maziasz, I.S. Kim, L. Heatherly, D.T. Hoelzer, N. Hashimoto, E.A. Kenik, K. Miyahara, J. Nucl. Mater., 307 (2002) 773−777.

[6] H. Kishimoto, K. Yutani, R. Kasada, O. Hashitomi, A. Kimura, J. Nucl. Mater., 367-370 (2007) 179−184.

[7] J.J. Fisher, Patent, U.S.A. (1978).

[8] M.K. Miller, D.T. Hoelzer, E.A. Kenik, K.F. Russell, J. Nucl. Mater., 329–333, Part A (2004) 338−341.

[9] G.R. Odette, M.J. Alinger, B.D. Wirth BD, Annu. Rev. Mater. Res., 38 (2008) 471−503.

[10] S. Yamashita, S. Ohtsuka, N. Akasaka, S. Ukai, S. Ohnukiy, Phil. Mag. Let., 84 (2004) 525−529.

[11] C. Robertson, B.K. Panigrahi, S. Balaji, S. Kataria, Y. Serruys, M.H. Mathon, C.S. Sundar, J. Nucl. Mater., 426 (2012) 240−246.

[12] E.A. Marquis, S.L. Perez, V.D. Castro, J. Nucl. Mater., 417 (2011) 257−261.

[13] S. Pasebani, I. Charit, D.P. Butt, J.I. Cole, J. Nucl. Mater., 434 (2013) 282−286.

[14] S. Pasebani, I. Charit, J. Alloy. Compd., 599 (2014) 206−211.

[15] M. Suárez, A. Fernández, J.L. Menéndez, R. Torrecillas, H. U. Kessel, J. Hennicke, R. Kirchner, T. Kessel, Sintering Applications- Challenges and Opportunities for Spark Plasma Sintering: A Key Technology for a New Generation of Materials, In Tech, 2013.

[16] J.G. Juárez, D.V. Jaramillo, R.A. Cuenca, F. L. Juárez, Powder Technol., 221 (2012) 264−270.

[17] A. Certain, S. Kuchibhatla, V. Shutthanandan, D.T. Hoelzer, T.R. Allen, J. Nucl. Mater., 434 (2013) 311−321.

[18] H.J. Frost, K.C. Russle, Acta Metall., 30 (1982) 953−960.

[19] G.S. Was, Z. Jiao, E. Beckett, K. Sun, A.M. Monterrosa, S.A. Maloy, O. Anderoglu, B.H. Sencer, M. Hackett, Scipta Mater., http://dx.doi.org/10.1016/j.scriptamat.2014.06.003 (2014).

[20] R.E. Stoller, M. B. Toloczko, G. S. Was, A. G. Certain, S. Dwaraknath, F.A. Garner, Nucl. Instr. Meth. Phys. Res. B, 310 (2013) 75−80.

[21] C.A. Williams, D. Haley, E.A. Marquis, G.D. Smith, M.P. Moody, Ultramicroscopy 132 (2013) 271−278.

[22] M.K. Miller MK, Atom probe tomography, Kluwer Academic / Plenum Publishers, NewYork, 2000.

[23] S.J. Zinkle, P. J. Maziasz, R. E. Stoller, J. Nucl. Mater., 206 (1993) 266−286.

[24] G. Was, Fundamentals of Radiation Materials Science: Metals and Alloys, Springer, Berlin, 2007.

[25] R. Bullough, M.R. Hayns, C.H. Woo, J. Nucl. Mater., 84 (1979) 93−100.

[26] A.W. Bowen, G.M. Leak, Metal. Trans., 1 (1970) 2767−27723.

[27] G. B. Gibbs, Trans. TMS-AIME, 239 (1967) 236.

[28] P. Pareige, M.K. Miller, R.E. Stoller, D.T. Hoelzer, E. Cadel, B. Radiguet, J. Nucl. Mater., 360 (2007) 136−142.

[29] I. Monnet, P. Dubuisson, Y. Serruys, M.O. Ruault, O. Kaitasov, B. Jouffery, J. Nucl. Mater., 335 (2004) 311−321.

[30] P. Hosemann, D. Kiener, Y. Wang, S.A. Maloy, J. Nucl. Mater., 425 (2012) 136−139.

[31] C. Liu, C. Yu, N. Hashimoto, S. Ohnuki, M. Ando, K. Shiba, S. Jitsukawa, J. Nucl. Mater., 417 (2011) 270−273.

[32] D. Kaomi, A. Motta, M. Kirk, Transactions of the American Nuclear Society, Anaheim, CA., 98 (2008).

[33] K. Asano, Y. Kohno, A. Kohyama, T. Suzuki, H. Kusanagi, J. Nucl. Mater., 155–157 (1988) 928−934.

[34] E.A. Little, D.J. Mazey, W. Hanks, Scripta Metall. Mater., 25 (1991) 1115−1118.

[35] C.L. Chen, A. Richter, R. Kögler, J. Alloy. Compd., 586 (2014) S173−S179.

[36] C.A. Williams, M.J. Hyde, G.D. Smith, E.A. Marquis, J. Nucl. Mater., 412 (2011) 100−105.

[37] H. Kishimoto, R. Kasada, O. Hashitomi, A. Kimura, J. Nucl. Mater., 386–388 (2009) 533−536.

[38] C.H. Zhang, Y.T. Yang, Y. Song, J. Chen, L.Q. Zhang, J. Jang, A. Kimura, J. Nucl. Mater., 455 (2014) 61−67.

[39] Y. Zhanbing, H. Benfu, H. Kinoshita, H. Takahashi, S. Watanabe, J. Nucl. Mater., 398 (2010) 81−86.

[40] M.L. Lescoat, J. Ribis, A. Gentils, O. Kaïtasov, Y. de Carlan, A. Legris, J. Nucl. Mater., 428 (2012) 176−182.

[41] M.L. Lescoat, I. Monnet, J. Ribis, P. Dubuisson, Y. de Carlan, J.M. Costantini, J. Malaplate, J. Nucl. Mater., 417 (2011) 266−269.

[42] J. Ribis, M.L. Lescoat, Y. de Carlan, J.M. Costantini, I. Monnet, T. Cozzika, F. Delabrouille, J. Malaplate, J. Nucl. Mater., 417 (2011) 262−265.

[43] V.D. Castro, M. Briceno, S. Lozano-Perez, P. Trocellier, S.G. Roberts, R. Pareja, J. Nucl. Mater., 445 (2014) 157−161.

[44] V.A. Skuratov, V.V. Uglov, J. O'Connell, A.S. Sohatsky, J.H. Neethling, S.V. Rogozhkin, J. Nucl. Mater., 442 (2013) 449−457.

[45] J. He, F. Wan, K. Sridharan, T.R. Allen, A. Certain, V. Shutthanandan, Y.Q. Wu, J. Nucl. Mater., 455 (2014) 41−45.

[46] P. Dubusisson, R. Schill, M.P. Hugon, I. Grislin, J.L. Seran, R.K. Nanstad, M.L. Hamilton, F.A. Garner, A.S. Kumar, Effects of Radiation in Materials: 18th International Symposium, ASTM STP, West Conshohocken, PA . (1999).

CHAPTER 8: Nickel–Chromium Alloys: Engineered Microstructure via Spark Plasma Sintering

Somayeh Pasebani[1,a], Aniket K. Dutt[2,b], Indrajit Charit[1,c] and Rajiv S. Mishra[2,d]

[1]Department of Chemical and Materials Engineering, University of Idaho, Moscow, ID 83844-3024, USA

[2]Department of Materials Science & Engineering, University of North Texas, Denton, TX 76203, USA

(Proceeding of 8th International Conference on PROCESSING & MANUFACTURING OF ADVANCED MATERIALS; Processing, Fabrication, Properties, Applications, December 2-6, 2013, Las Vegas, USA)

(Published in the Journal of Materials Science Forum, Volume 783–786 (2014) pages 1099–1104)

Abstract

There is a need to enhance or develop high temperature capabilities of structural materials for advanced coal-fired power plants. These materials require a combination of high temperature strength, creep resistance and corrosion resistance in the oxygen-rich and hydrogen-rich high pressure environments. In this study, atomized Ni–20Cr (wt.%) powder was mechanically milled with Y_2O_3 nanopowder (30–40 nm powder size) to produce an alloy with a chemical composition of Ni–20Cr–1.2Y_2O_3 (wt.%) alloy using high energy ball milling. To minimize agglomeration during milling, 1 wt.% stearic acid was added to the powder mixture prior to milling. Microstructural characteristics of the powder were primarily characterized by the X-ray diffraction (XRD), scanning electron microscopy (SEM) and transmission electron microscopy (TEM). The crystallite size and lattice strain were measured by XRD, and powder morphology (powder size, shape) was studied by SEM. A milling time of 2 h was found to be optimal for the purpose that yttria particles are

not dissolved rather uniformly distributed in the Ni–20Cr matrix. Subsequently, the milled powder was consolidated into bulk specimens (12.5 mm in diameter) via spark plasma sintering (SPS) at 1100 ^{o}C for 30 minutes. Following SPS, the density and hardness of the specimens were measured. Microstructural characterization of the SPSed specimens was performed using SEM and TEM. The microstructural characteristics were correlated with the measured mechanical properties.

Keywords: Nickel–Chromium alloys; High energy ball milling; Spark plasma sintering; X-ray diffraction; Transmission electron microscopy

8.1. Introduction

High temperature structural materials are important for advanced fossil fuel fired power plants. Structural materials with enhanced high temperature capabilities can improve the efficiency of these power plants, thus decreasing the greenhouse gas emissions. One way of attaining that objective is to develop ultra super-critical power plants in which some of the components would need to withstand a high temperature close to 760 ^{o}C under stresses [1]. Nickel-based super alloys are the potential candidate materials for such applications. In this study, preliminary results on the development of nickel-based alloys are reported. The alloys were prepared by using a combined route of high energy ball milling and SPS. In SPS, direct current (DC) is passed through the powder mass for consolidation. This technique is also known as the pulsed electric current sintering (PECS). SPS has many advantages over conventional sintering processes, such as lower sintering temperature and time, and creation of near full density bulk materials in a wide variety of material classes [2]. While there is still an ongoing debate on the exact mechanism of SPS, its application has surpassed the

understanding of the SPS process fundamentals. To the best of our knowledge, there have been only a few studies on the SPS of Ni-based alloys. Nanko *et al.* [3] reported results of the consolidation of the unmilled Ni–20Cr powder via SPS at 650–725 ^{o}C for 0–1200 s under a uniaxial pressure of 13 MPa under vacuum. Their study was focused on the process kinetics analysis, and the creep deformation of the particles was found to be the predominant densification mechanism during SPS. While mechanical alloying studies on the Ni–20Cr and Ni–Y_2O_3 powders exist in the literature [4-5], there are very few studies [6,7] on the SPS of Ni-based alloys with no detailed discussion on the correlation of microstructure and mechanical properties.

This study was focused on the fundamental understanding of the microstructural characteristics and mechanical properties of the SPSed Ni–20Cr and Ni–20Cr–1.2Y_2O_3 alloys. Furthermore, this work will serve as a prelude to a broader effort to produce engineered microstructures as prescribed by a computational optimization (genetic algorithm) design scheme.

8.2. Experimental procedure

The atomized Ni–20Cr powder (a mean powder diameter of 20 μm) and Y_2O_3 nano-powder (a mean powder diameter of 30–40 nm) were procured from the American Elements Inc. The nominal composition of the Ni–20Cr powder was Ni–19.6Cr–0.2Fe–0.8Mn–0.9Si (wt.%) while the Y_2O_3 powder was of high purity (99.99%). The as-received powder batches were characterized using SEM, energy dispersive spectroscopy (EDS) and XRD for verifying the quality of the powder batches. The powder batch was prepared in a glove box under an argon atmosphere and poured into a chrome steel vial. The Ni–20Cr powder was ball milled with the Y_2O_3 nanopowder for 1, 2 and 4 h to produce the Ni–20Cr–1.2Y_2O_3

(wt.%) alloys. In order to minimize the powder agglomeration, 1 wt.% stearic acid was added to the powder mix prior to the ball milling process as a process control agent (PCA). The ball milling was carried out using a SPEX 8000M shaker mixer / mill using steel balls of 5 mm in diameter and a ball to powder ratio (BPR) of 10:1. The ball milled powder batches were characterized by the XRD, SEM / EDS and TEM.

The optimized (2 h) ball milled powder was consolidated via SPS using a Dr. Sinter SPS-515S machine available at the Center for Advanced Energy Studies (CAES) located in Idaho Falls, Idaho. All the SPS experiments were performed using a heating rate of 100 ^{o}C/min and 10 kN force (equals to about 80 MPa) under vacuum. An intermediate 15 min dwell at 450 ^{o}C (with 4.5 kN applied force) was provided for all the SPS runs in order to remove the stearic acid. Following that, the temperature was ramped up to 1100 ^{o}C and kept at that temperature for 30 min, and then cooled down in the vacuum chamber. The standard graphite die and punches were used; niobium foils were used as the diffusion barrier. Figure 8.1 shows one of the SPSed Ni–20Cr–1.2Y_2O_3 samples.

Upon SPS, the physical density of the bulk specimens was measured using Archimedes' principle. Subsequently, the physical density values were divided by the theoretical densities of the respective alloys to obtain the relative density of the SPSed specimens. Vickers microhardness measurement was carried out using a load of 0.5 kg-f (about 5 N) applied for 15 s. TEM studies were performed on the SPSed specimens using a JEOL–2010 TEM.

The 3-mm disk TEM specimens were mechanically thinned and electropolished at about –35^{o}C in a solution of nitric acid and methanol (10:90 vol.%) using a Fischione twin-jet polisher device.

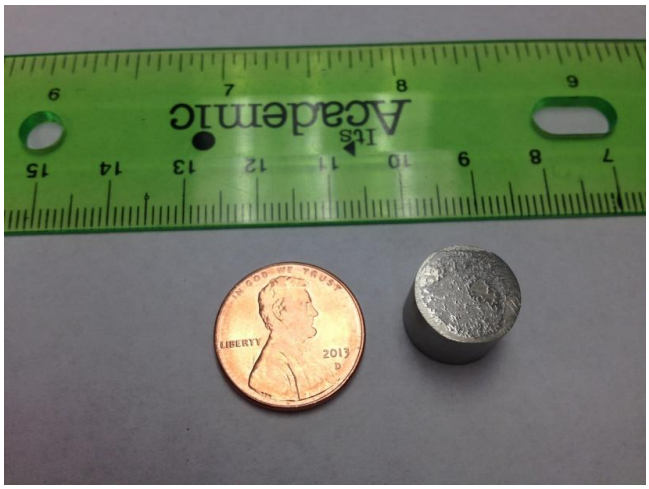

Figure 8.1. A macroscopic view of the SPSed Ni–20Cr–1.2Y_2O_3 specimen (sample mass – 10 g)

8.3. Results and discussion

8.3.1. Microstructural characteristics of the ball milled powder

The ball milled powder batches of Ni–20Cr–1.2Y_2O_3 were characterized using XRD. The XRD peak broadening was utilized to analyze the microstructural parameters. Unlike the crystal structure transformation of Y_2O_3 from cubic to monoclinic during milling of Ni–Y_2O_3 nanocomposite as reported by Park *et al.* [6,7], the original nano particles of Y_2O_3 with cubic crystal structure remained cubic in Ni–20Cr matrix after 2 h of milling and did not show any transformation. However, in the present study after 4 h of milling, the peaks of Y_2O_3 showed low intensity and were hardly detected due to the incorporation and dissolution of Y_2O_3 particles in the matrix.

The Nelson – Riley extrapolation method [8] was used to determine the lattice constants, whereas the crystallite size and lattice strain were evaluated using the Williamson – Hall formula [9]. The ball-milled powder size was determined by SEM. Table 8.1 lists all the microstructural parameters of the ball milled powder. The relevant parameters of the

blended powder mix (denoted by ‘0’ milling time) are also included in the table for comparison.

Table 8.1. Microstructural parameters of Ni–20Cr–1.2Y_2O_3 alloy as calculated by XRD and SEM

Milling Time (h)	Crystallite Size (nm)	Lattice Strain (%)	Lattice Constant (nm)	Mean Powder Size (μm)
0	44±12	0.03±0.001	0.3530±0.0002	23.6±1.1
1	17±9	0.03±0.001	0.3532±0.0003	39.2±2.2
2	14±7	0.03±0.001	0.3536±0.0003	33.6±1.5
4	4±2	0.15±0.003	0.3560±0.0004	39.4±3.1

Figure 8.2(a) shows the SEM image of the 2 h ball milled Ni–20Cr–1.2Y_2O_3 alloy. The average powder size of about 33.6 μm of the ball milled powder was found to be small enough for subsequent optimum sintering. Fig. 8.2(b) shows a TEM image of the ball milled Ni–20Cr–1.2Y_2O_3 powder showing nano particles of Y_2O_3 with an average diameter of about 10 nm in the nanocrystalline matrix of Ni–Cr solid solution. With increasing milling time, the crystallite size decreased. Milling for 4 h caused an increase in the lattice constant as an indication that Y_2O_3 dissolved in the matrix to a significant extent. However, because the purpose of this study was to distribute the yttria particles homogenously and not to dissolve them in the matrix, 2 h ball milled powder was used for subsequent SPS experiments.

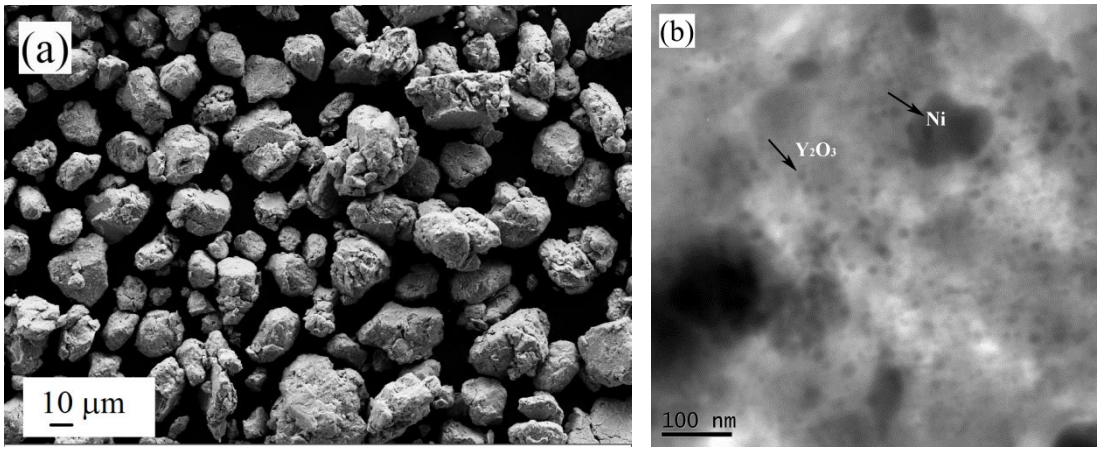

Figure 8.2. (a) A SEM micrograph of the ball milled (2 h) Ni–20Cr–1.2Y_2O_3 powder, and (b) a TEM bright field micrograph of the ball milled (2 h) Ni–20Cr–1.2Y_2O_3

8.3.2. Density and microhardness of the SPSed alloys

The physical density, relative density and microhardness of the SPSed Ni–20Cr and Ni–20Cr–1.2Y_2O_3 alloys are summarized in Table 8.2. Since the SPS was performed at high temperature, the specimens obtained were near fully dense (≈99%). The effect of Y_2O_3 addition becomes apparent in that the Vickers microhardness of Ni–20Cr–1.2Y_2O_3 alloy increased by about 53% over the Ni–20Cr alloy SPSed under similar conditions. Interestingly, Nanko *et al.* [3] used SPS to consolidate two Ni–20Cr powder batches at 650–720 ^{o}C temperature for 0–1200 s and a pressure of 13 MPa under vacuum, resulting in relative densities of 60–70% only.

Table 8.2. Density and microhardness values of SPSed Ni–20Cr and Ni–20Cr–1.2Y_2O_3 alloys (1100 °C/30 min)

Alloy	Physical Density (g/cm^3)	Relative Density (%)	Vickers Hardness ($kg_f.mm^{-2}$)
Ni–20Cr	8.19	98.95 ± 0.03	307.6 ± 2.7
Ni–20Cr–1.2Y_2O_3	8.17	99.55 ± 0.04	471.6 ± 7.5

8.3.3. Microstructural characteristics of the SPSed alloys

The SPSed Ni–20Cr and Ni–20Cr–1.2Y_2O_3 alloys were further characterized for microstructure. The microstructural characteristics were examined using XRD, SEM and TEM. However, SEM performed on the specimens could not provide detailed description of the microstructure due to the strong etchant (Aqua Regia). The XRD results of the SPSed Ni–20Cr and Ni–20Cr–1.2Y_2O_3 alloys revealed the presence of Cr_2O_3 and Cr_2O_5 as well as Cr_3C_2 and Cr_7C_3. Some blocky particles were also observed in the SEM micrographs that were highly enriched in Cr. These particles were not observed in TEM due to the electropolishing artifact. Park *et al.* [7] found similar elongated particles and identified them as Cr_2O_3 and Cr_3O_8 based on the XRD and electron probe microanalysis (EPMA) results.

Figure 8.3(a) shows a bright field TEM image of the SPSed Ni–20Cr alloy while Fig. 8.3(b) shows that of the Ni–20Cr–1.2Y_2O_3 alloy. Both the images were taken under the same magnification to better compare between the two microstructures. The grain size of the Ni–20Cr–1.2Y_2O_3 alloy is considerably larger than that of Ni–20Cr alloy. The smallest grain size of the Ni–20Cr–1.2Y_2O_3 alloy was measured to be 130 nm while that of the Ni–20Cr alloy was about 630 nm. The effect of Y_2O_3 addition on the grain size is clearly evident. The presence of homogenously distributed nano dispersoids in a large volume fraction led to a higher microhardness values and grain refinement in the Ni–20Cr–1.2Y_2O_3 alloy.

Twin bands were observed in the SPSed Ni–20Cr alloy frequently as shown in Fig. 8.4(a) On the other hand; Fig. 8.4(b) shows the twin bands that were occasionally observed in somewhat larger grains in the microstructure of the Ni–20Cr–1.2Y_2O_3 alloy. The boundaries twin bands were straight-edged typically shown by annealing twins. While

the origin of the twin bands in the SPSed alloys is not clear at this point, it is likely that twin bands are '*annealing twins'* created during the recrystallization of the ball milled powder during some stage of SPS.

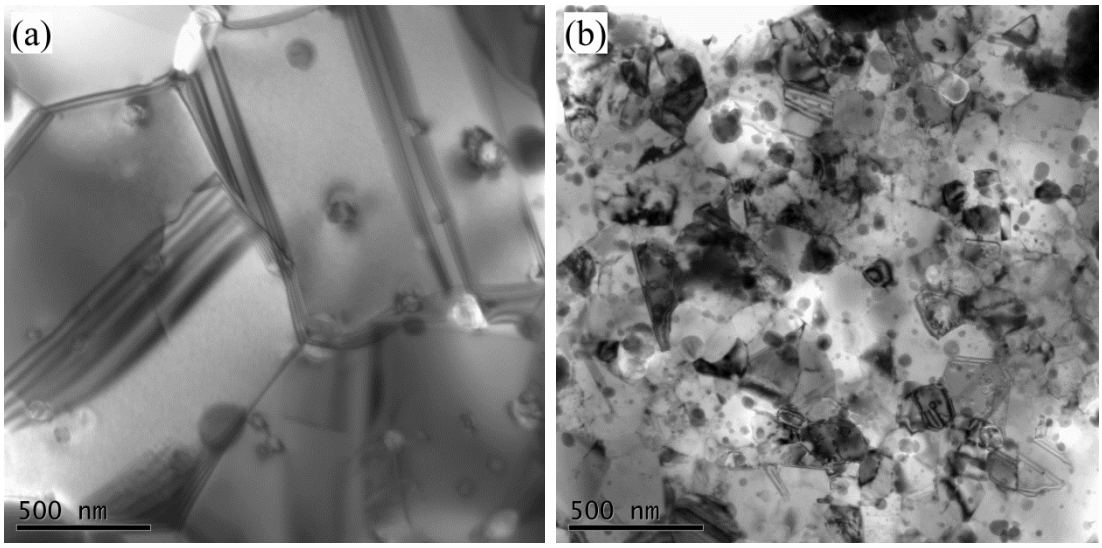

Figure 8.3. TEM bright field images of SPSed (a) Ni–20Cr and (b) Ni–20Cr–1.2Y_2O_3 alloys

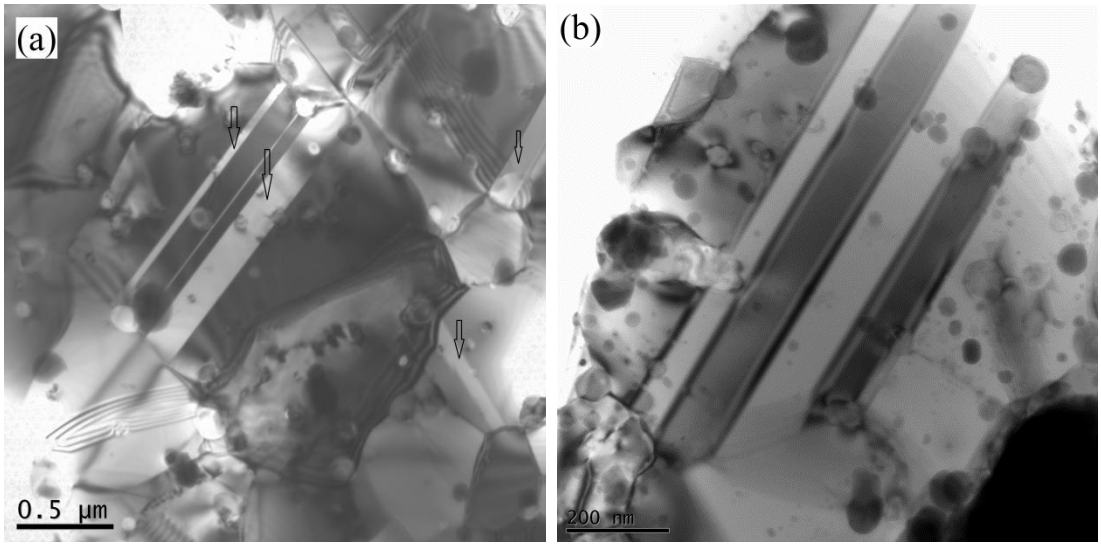

Figure 8.4. Twin bands observed in SPSed (a) Ni–20Cr and (b) Ni–20Cr–1.2Y_2O_3 alloys

Figures 8.5(a–b) illustrate the second phase particles in the SPSed Ni–20Cr and Ni–20Cr-1.2 Y_2O_3 alloys, respectively. The majority of the particles in the SPSed Ni–20Cr alloy were in a wide range of 22–180 nm in diameter (as shown in Fig. 8.5(a)). On the other hand, the microstructure of Ni–20Cr–1.2Y_2O_3 alloy contained a larger fraction of the smaller particles (the particles diameter was in the range of 3–50 nm as shown in Fig. 8.5(b). It is likely that at the elevated temperatures during SPS, Cr started precipitating out of the Ni–Cr solid solution in the form of Cr based oxides and carbides [4,7]. Yttrium-containing particles as small as 3–5 nm in diameter were also found in the microstructure of Ni–20Cr–1.2Y_2O_3 alloy, as shown in Fig. 8.5(b). The fine and stable particles were crucial for retaining a much finer grain size in the Ni–20Cr–1.2Y_2O_3 alloy. The microhardness of the Ni–20Cr–1.2Y_2O_3 alloy was higher than that of Ni–20Cr alloy mainly due to the greater contributions of the particle strengthening and Hall – Petch strengthening effects. More analyses are in progress to evaluate the chemical composition and crystal structure of the particles.

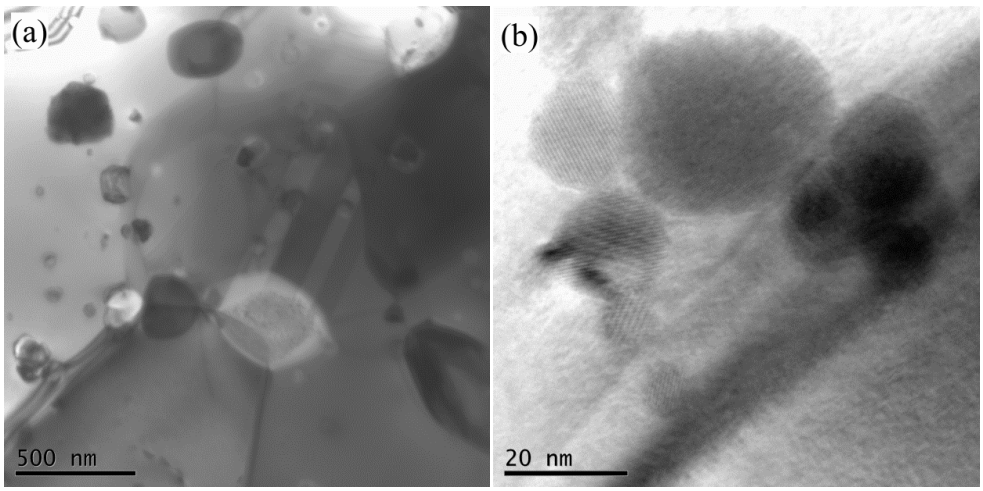

Figure 8.5. Particles in the (a) SPSed Ni–20Cr alloy and (b) Ni–20Cr–1.2Y_2O_3 alloy

Conclusions

The study demonstrated the feasibility of a processing route for two Ni-based alloys (Ni–20Cr and Ni–20Cr–1.2Y_2O_3) using high energy ball milling and SPS. A number of characterization techniques (XRD, SEM and TEM) were used to characterize the ball milled powder. Ball milling for 2 h with a BPR of 10 and ball diameter of 5 mm was found to be optimal and led to the homogeneous distribution of yttria particles in the matrix of the Ni–20Cr–1.2Y_2O_3 alloy. The ball milled powder was consolidated by SPS at 1100 ^oC for a dwell time of 30 min. Both alloys achieved close to full density. Because of the finer grain size and fine, stable yttrium-containing particles, the SPSed Ni–20Cr–1.2Y_2O_3 alloy exhibited the higher hardness over the Ni–20Cr alloy SPSed under similar conditions. Further microstructural studies will be performed in our future work.

Acknowledgements

The support of the University Coal Research Program of the US Department of Energy (DOE) via a grant (DE–FE0008648) managed by the National Energy Technology Laboratory (NETL) is gratefully acknowledged. Also, Somayeh Pasebani and Indrajit Charit thank the Center for Advanced Energy Studies (CAES) and Boise State University staff for facilitating access to the SPS facility.

References

[1] R. Viswanathan, US program on materials technology for ultra supercritical coal fired boilers, in: R. Viswanathan, D. Gandy, K. Coleman (Eds.), Advances in materials technology for fossil power plants, ASM International, Materials Park, Ohio, USA, 2008, pp. 1−15.

[2] Z.A. Munir, U. Anselmi-Tamburini, M. Ohyanagi, The effect of electric field and pressure on the synthesis and consolidation of materials: A review of the spark plasma sintering method, J. Mater. Sci. 41 (2006) 763−777.

[3] M. Nanko, M. Sato, K. Matsumaru, K. Ishizaki, Densification mechanism of fine Ni-20Cr powder during pulsed electric current sintering, Mater. Sci. Forum, 510−511 (2006) 818−821.

[4] M.K. Lee, J.J. Park, C.K. Rhee, Synthesis and structural properties of Ni–20Cr–2Y_2O_3 nanocomposite alloy by a very high energy mechanical milling, Mater. Chem. Phys. 137 (2012) 129−134.

[5] I. Lopez-Baez, E. Martinez-Franco, H. Zoz, and L.G. Trapaga-Martinez, Structural evolution of Ni−20Cr alloy during ball milling of elemental powders, Revista Mexicana De Fisica 57 (2011) 176−183.

[6] J.J. Park, H.J. Choe, S.M. Hong, M.K. Lee, C.K. Rhee, Synthesis of Ni–Y_2O_3 nanocomposite powders by a very high speed planetary milling process: Microstructural development and refinement behavior, Powder Technol. 230 (2012) 139−144.

[7] J. Park, J. Jang, T.K. Kim, S.J. Kim, J.H. Ahn, Formation of nanostructures in Ni–22Cr–11Fe–1X (X=Y_2O_3, TiO_2) alloys by high energy ball milling, J. Nanosci. Nanotechnol. 11 (2011) 6213−6218.

[8] J.B. Nelson, D.P. Riley, An experimental investigation of extrapolation methods in the derivation of accurate unit cell dimensions of crystals, Proc. Phys. Soc. 57 (1945) 160−177.

[9] G.K. Williamson, W.H. Hall, X-ray line broadening from filed aluminum and wolfram, Acta Metall. 1 (1953) 22−31.

CHAPTER 9: Nickel-Based Oxide Dispersion Strengthened Alloys via Spark Plasma Sintering

Somayeh Pasebani[1], Aniket K. Dutt[2], Jatu Burns[3] Indrajit Charit[1] and Rajiv S. Mishra[2]

[1] University of Idaho, Moscow, ID 83844-3024, USA

[2] University of North Texas, Denton, TX 76203, USA

[3] Boise State University, Center for Advanced Energy Studies, Idaho Falls, ID 83401, USA

(To be submitted to the Journal of Acta Materialia)

Abstract

Nickel-based oxide dispersion strengthened (ODS) alloys were developed by adding 1.2 wt.% Y_2O_3 to Ni–20Cr matrix via mechanical milling and spark plasma sintering (SPS). Additionally, 5 wt.% Al_2O_3 was added to Ni–20Cr–1.2Y_2O_3 to provide composite strengthening. The effects of milling times, sintering temperature, and time were investigated on mechanical properties and microstructural evolutions. A high fraction of annealing twins was observed in the sintered microstructure regardless of milling time. However, longer milling time contributed to higher hardness, higher volume fraction of twins and narrower twin boundary thickness in the consolidated alloys. Higher sintering temperature led to higher fraction of recrystallized grains, higher hardness, density, and higher volume fraction of twins. Adding 1.2 wt.% Y_2O_3 to Ni–20Cr matrix significantly reduced the grain size but the grains were slightly larger in Ni–20Cr–1.2Y_2O_3–5Al_2O_3 due to dispersion of nanoparticles and coarser particles. The strengthening mechanisms at room temperature were quantified based on both experimental and analytical calculations with a

good agreement. Higher compression yield stress at 800 °C for Ni–20Cr–1.2Y_2O_3–5Al_2O_3 alloy was attributed to a combined effect of dispersion and composite strengthening.

Keywords: Nickel-based alloys; ODS alloys; Composite strengthening; High energy ball milling; Spark plasma sintering

9.1. Introduction

Increasing the operating temperatures in coal-fired power plants, gas turbine inlets, and other high temperature structural components in order to improve their efficiency and economy will require new materials with high mechanical and creep strength, oxidation and corrosion resistance. Nickel-based alloys are promising candidates for such applications due to their excellent corrosion resistance at elevated temperatures [1-3]. While conventional nickel-based alloys may not be absolutely reliable and efficient at high temperatures due to coarsening or dissolution of the second phase particles, nickel-based ODS alloys, reinforced by homogeneous dispersed nanoparticles (usually Y_2O_3), are potentially stable during high temperature applications in excess of 1000 °C [4]. Homogeneous dispersion of nanometer and stable oxide particles in the matrix of nickel-based ODS alloys can act as effective barriers against the dislocation motion [2, 5-7] and improve the high temperature mechanical properties and creep strength [8]. The pinning effects of oxide nanoparticles depend on the mean particle separation, (the mean distance between the particles) which is a direct result of the particles' number density [1]. According to theoretical calculations and experiments, a combination of a mean particle separation of 100–250 nm for 10–20 nm yttria particles and

grain aspect ratio of minimum 10 could be promising for high temperature applications [3, 6].

In nickel-based ODS powder containing both Al and Y_2O_3, different Y–Al–O particles such as $Y_3Al_5O_{12}$, $YAlO_3$ (perovskite), $Y_4Al_2O_9$ and $YAlO_3$ (hexagonal) can be formed during consolidation [1]. Recently, it has been noted that adding some minor elements such as Ti and Hf can replace the Y–Al–O particles with Y–Ti–Hf–O particles. The effects of adding minor elements such as Ti, Mg, Zr, Ca and Hf to Ni–0.5Al–1Y_2O_3 (wt.%) was studied by Tang *et al.* [1], and Hf was found to be the most effective oxide at refining the formed oxide particles, especially at a concentration of 0.8 wt.%. Formation of $Y_2Hf_2O_7$ was found to be responsible for oxide particle refinement and consequent improvement in mechanical properties through operation of the Orowan mechanism [9].

Another strengthening mechanism to consider for developing nickel-based ODS alloys would be composite strengthening mechanism or load transfer mechanism [10]. For example, studies have also shown that submicron Al_2O_3 of (0.5–1 μm diameter) could be efficient for composite strengthening due to lower density and higher modulus of elasticity [11, 12]. Hornbogen *et al.* [13] and Roseler *et al*. [14] predicted that a combination of nanoparticles and coarser particles dispersed in the microstructure would offer both dispersion strengthening and composite strengthening. In this approach, dislocations would effectively shear the nanoparticles that were smaller than a “critical size” and bypass the coarser particles that were larger than a “critical size”. Through dispersion strengthening and composite strengthening as dominant mechanisms at high temperatures, reliable mechanical properties would be achieved. Furthermore, adding Al_2O_3 to Ni-20Cr-1.2Y_2O_3 alloy could

increase the corrosion resistance due to aluminum oxide film formation and ductility due to high volume fraction of annealing twins.

Nickel-based ODS alloys are conventionally produced by mechanical alloying (MA) or ball milling of elemental or pre-alloyed powders in combination with nano-sized Y_2O_3 (yttria) powder followed by canning, degassing and consolidation either via hot extrusion (for rods and wires) or hot isostatic pressing (HIP) and rolling (for sheets) [3]. One of the critical steps in producing nickel-based ODS alloys is the milling process in which powder blend of yttria and pure nickel or pre-alloyed nickel (for example, Ni–20Cr) are milled, and a fine homogeneous distribution of yttria particles in the metal matrix can be attained. If powder blends of yttria and two or more metal powders are milled in addition to homogeneous yttria dispersion, formation of solid solution may be also achieved [3]. During milling, the metal powder particles become trapped between the colliding balls (milling media) and cold welded together while the oxide particles become finer until trapped between layers of metal powders sandwich forming a composite. After cold welding and particle agglomeration, a fracture stage occurs and large composite powders break down until a steady state situation is reached between cold welding and fracturing. Consequently, a uniform distribution of oxide nanoparticles within metallic components would be achieved [15, 16].

In conventional consolidation methods such as extrusion or HIP, a final annealing at high temperature is usually required to develop a stable coarse grain structure alloy [16]. The numbers of numerous thermal processing steps could be eliminated if a pulsed direct current (DC) is simultaneously used with a uniaxial pressure to primarily sinter the powders [17, 18]. This could reduce the time, cost and possibly deformation texture in the

consolidated materials [19]. Field activated assisted sintering technique (FAST), also known as SPS or pulsed electric current sintering (PECS), applies a pulsed DC to enhance sintering rate of the powders to near full density at a relatively lower temperatures. Pulsed DC flows through the die and powder compact producing heat via Joule heating mechanism, providing a much higher heating rate and shorter sintering time. Thus, grain growth during sintering can be essentially minimized, leading to improvement in mechanical properties [18, 20-22].

There are limited reported applications of SPS in the processing of nickel-based ODS alloys containing Y_2O_3 as dispersoids [1, 2, 4, 23, 24]. Park *et al.* [2] developed Ni–22Cr–11Fe–1TiO_2, Ni–22Cr–11Fe–1Y_2O_3 and Ni–22Cr–11Fe–0.5TiO_2–0.5Y_2O_3 (wt.%) by milling for 40 h in a planetary ball mill and SPSed the ball milled powder at 1100 °C for 5 minutes under a pressure of 40 MPa. They suggested nano-sized TiO_2 and Y_2O_3 were dissolved during MA, and then precipitated out during SPS, forming Y–Ti–O particles. However, Ni–22Cr–11Fe–1Y_2O_3 exhibited the best mechanical properties among all of the developed alloys.

In the present study, Ni–20Cr–1.2Y_2O_3 (wt.%) alloy was processed by ball milling and SPS, and the effects of milling times and sintering parameters on the properties of sintered nickel-based ODS alloy were investigated. There have been very limited studies on the effects of milling parameters and microstructural evolution during milling of nickel-based ODS powder [25]. Furthermore, Ni–20Cr, and Ni–20Cr–1.2Y_2O_3–5Al_2O_3 (wt.%) alloys were processed by milling and SPS, and their mechanical properties and microstructural evolutions were studied. Here, 1.2Y_2O_3 wt.% (or 2 vol.%) and 5Al_2O_3 wt.% (or 10 vol.%) were added to Ni–20Cr matrix for dispersion strengthening effect and composite strengthening effect, respectively.

9.2. Experimental procedure

9.2.1. Powder processing and characterization

Gas atomized Ni–20Cr powder with nominal composition of Ni–19.6Cr–0.2Fe–0.8Mn–0.9Si (wt.%) and mean particle size of 23.6±1.1 μm, yttrium oxide (yttria / Y_2O_3) powder with high purity (99.99%) and mean particle size of 30–40 nm and aluminum oxide (alumina / Al_2O_3) powder with 99.99% purity and mean particle size of 300–400 nm were procured from the American Elements Inc.

Powder batches were prepared in a glove box under high purity argon atmosphere and poured into hardened steel grinding vial (SPEX 8001). In order to minimize powder agglomeration and cold welding during milling, 1 wt.% stearic acid was added to the powder mixture prior to the ball milling process as a process control agent (PCA). The ball milling was carried out in a SPEX 8000M shaker mixer / mill using steel balls with 5 mm in diameter and a ball to powder ratio (BPR) of 10:1 (the powder mass and the ball mass of each batch was 10 g and 100 g, respectively). A variety of Ni-based alloys altering in milling time (0 h, 2 h and 4 h) and nominal composition (Ni–20Cr, Ni–20Cr–1.2Y_2O_3, Ni–20Cr–1.2Y_2O_3–5Al_2O_3, wt.%) were milled.

For preparing the Ni–20Cr–1.2Y_2O_3–5Al_2O_3 powder, Ni–20Cr–1.2Y_2O_3 was first milled for 2 h, and then 5 wt.% Al_2O_3 powder was added to the milled Ni–20Cr–1.2Y_2O_3 alloy to and subsequently ball milled distribute all the Al_2O_3 particles homogeneously. In our former experiments, Al_2O_3 powder was only blended (i.e. milled without the steel balls) with the milled Ni–20Cr–1.2Y_2O_3 powder, and the results were unsatisfactory because all the Al_2O_3 powder particles were found to be mostly located on the prior particle boundaries after consolidation.

X-ray diffraction (XRD) experiments of the as-milled powders were performed using a Siemens 5000D diffractometer with Cu-$K\alpha$ radiation. Modifications such as $k\alpha_2$ Rachinger and background correction by Sonnerveld were applied to XRD patterns using the Powder–X software [26]. Lattice parameters, crystallite size and lattice strain were calculated based on the Nelson – Riley extrapolation [27] and Williamson – Hall (W – H) formula, respectively [28].

The morphology and size distribution of the as-received powder batches and as-milled powder were analyzed using a Zeiss Supra 35 field emission gun scanning electron microscope (FEG–SEM). The milled powders were hot mounted in phenolic powder and polished to 0.05 μm. The cross section of the hot mounted and polished milled powders were observed in backscatter electron (BSE) mode in SEM. The SEM micrograph obtained from the as received Al_2O_3 powder and high angle annular dark field (HAADF) scanning transmission electron microscopy (STEM) and the micrograph obtained from Y_2O_3 powder are shown in Figs. 9.1(a–b), respectively.

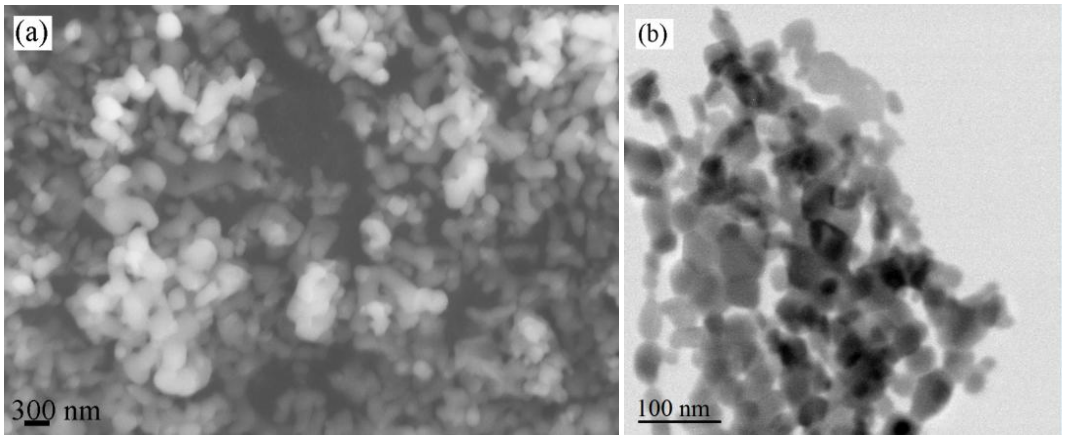

Figure 9.1. (a) A SEM micrograph of the as received Al_2O_3 powder, and (b) HAADF STEM micrograph of the Y_2O_3 powder

9.2.2. Spark plasma sintering

The ball milled powder was consolidated via SPS using a Dr. Sinter Lab SPS-515S machine (SPS Syntex Inc., Kanagawa, Japan) with maximum capacity of 30 kN and 1500 A. A Tri-Gemini cylindrical graphite die with an inner diameter of 12.7 mm and an outer diameter of 38 mm were used. The inner surface of the die and radial surfaces of punches were covered with a graphite foil (0.25 mm in thickness) to facilitate the removal of the sintered specimens. In order to inhibit the diffusion of carbon from the punches and graphite foil to the powder mixture, a thin niobium foil (0.06 mm in thickness) was placed between the powder and the graphite foils. The die was wrapped in graphite felt (4 mm in thickness) to minimize heat loss by thermal radiation.

All the SPS experiments were performed under vacuum (7×10^{-3} Torr or ~ 0.9 Pa), using a heating rate of 100 ^{o}C/min and force of 10 kN (equals to about 80 MPa considering punch configuration used in this study). An intermediate 15 min dwell time at 450 ^{o}C (with 4.5 kN applied force) was given for all the SPS runs to allow the stearic acid to volatilize. Following that, the temperature was ramped up to different levels (600 ^{o}C, 900 ^{o}C, 1000 ^{o}C and 1100 ^{o}C), kept at those temperatures for different times (5 and 30 min), and cooled down with at the rate of about 50 ^{o}C/min. The temperature was monitored by a K-type thermocouple that was inserted into a hole in the die such that the tip was located 6 mm away from the sintering powder. The final product was in the form of a disk with dimensions of 12.5 mm in diameter and 8 mm in thickness. All the Ni-based alloys processed in this study varying in milling times, compositions, sintering temperatures and times are listed in Table 9.1.

Table 9.1. Different milling time, SPS temperatures, SPS dwell times and alloy compositions altered in processing Ni-based ODS alloys considered for current study

	Alloy (wt.%)	Milling Time (h)	SPS Parameters	Alloy Code
Effect of Milling Time	Ni–20Cr–1.2Y_2O_3	0	1100 ^oC/ 30 min	A
	Ni–20Cr–1.2Y_2O_3	2	1100 ^oC/ 30 min	B
	Ni–20Cr–1.2Y_2O_3	4	1100 ^oC/ 30 min	C
Effect of SPS Parameters	Ni–20Cr–1.2Y_2O_3	2	600 ^oC/ 5 min	D
	Ni–20Cr–1.2Y_2O_3	2	900 ^oC/ 5 min	E
	Ni–20Cr–1.2Y_2O_3	2	1000 ^oC/ 5 min	F
	Ni–20Cr–1.2Y_2O_3	2	1100 ^oC/ 5 min	G
	Ni–20Cr–1.2Y_2O_3	2	1100 ^oC/ 30 min	B
Effect of Alloy Composition	Ni–20Cr	2	1100 ^oC/ 30 min	H
	Ni–20Cr–1.2Y_2O_3	2	1100 ^oC/ 30 min	B
	Ni–20Cr–1.2Y_2O_3–5Al_2O_3	2.5	1100 ^oC/ 30 min	I

9.2.3. Density measurement and microstructural studies

Upon SPS, physical density of the bulk specimens was measured using Archimedes' principle with at least six measurements for each specimen. The final relative density was calculated as the ratio between the measured density and the theoretical density of each composition. Electron backscattered diffraction (EBSD) study was performed using a JEOL JSM–6610LV scanning electron microscope (SEM) equipped with an EDAX / TSL Hikari EBSD system.

The transmission electron microscopy (TEM) specimens were mechanically thinned and electropolished at a temperature of about –35 ^oC using a solution of nitric acid and methanol (10:90, vol.%) and a Fischione twin-jet polisher operating at 30 V. Microstructural studies were conducted using a JEOL–2010 TEM operating at 200 kV. A focused ion beam (FIB) was used to prepare a TEM foil from the specimen with a composition of Ni–20Cr–1.2Y_2O_3–5Al_2O_3 due to the unsatisfactory results after electropolishing (likely caused by low conductivity of this alloy). FIB experiment was done by using an FEI Quanta 3D FEG instrument with a Ga-ion source.

9.2.4. Mechanical properties studies

The sample surface for microhardness testing was mechanically polished using standard metallographic procedures involving grinding and polishing down to 0.5 μm finish. The Vickers microhardness tests were performed with a Leco LM100 microhardness tester at 0.5 kg_f (5 N) load applied for 15 s on the sintered samples. The microhardness tests were repeated on random spots in the center of each specimen up to 10 times.

Compression testing was performed on an Instron 5982 machine at both 25 °C and 800 ^oC applying a strain rate of 10^{-3} s^{-1}. The disk shaped SPSed specimens were electro-discharge machined to a square based rectangular prism shape with dimensions of 4×4×6 mm^3. After compression testing, the deformed sample was cooled in water to maintain the microstructure for further studies planned for our future work.

9.3. Results

9.3.1. Effect of milling time

The powder morphology of the Ni–20Cr–1.2Y_2O_3 powder milled for 0 h (alloy A), 2 h (alloy B) and 4 h (alloy C) are displayed in the secondary electron (SE) SEM micrographs shown in Figs. 9.2(a, c and e), respectively. The BSE micrographs from the cross sectional view of powders milled for 0 h, 2 h and 4 h, mounted and polished are presented in Figs. 9.2(b, d and f), respectively.

The morphology of the as-received Ni–20Cr–1.2Y_2O_3 powder was a mixture of round and irregular particles with a mean diameter of 23.6±2.1 μm uniformly covered with stearic acid and Y_2O_3 nanopowder as shown in Fig. 9.2(a).

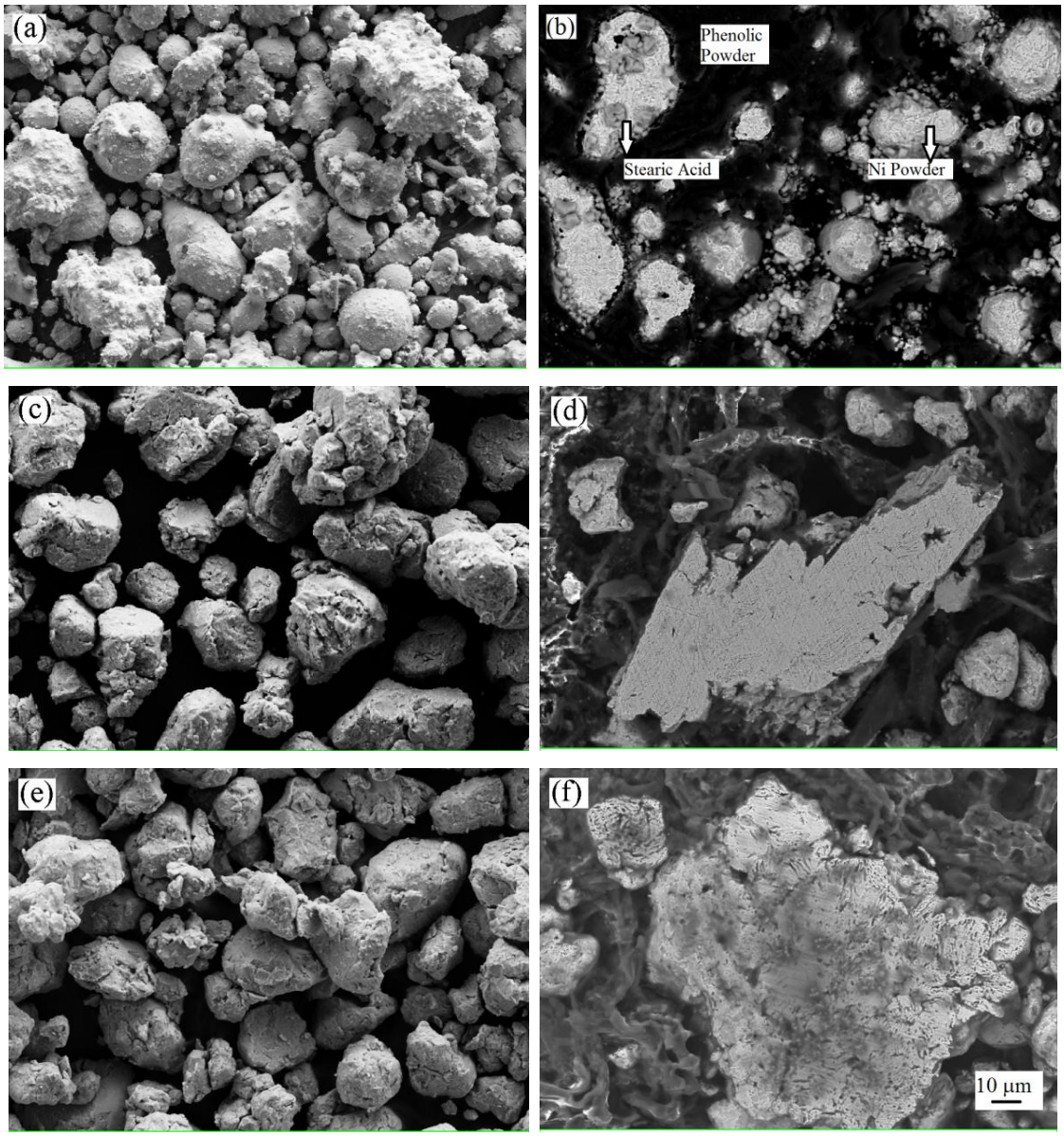

Figure 9.2. SEM micrographs of Ni–20Cr–1.2Y_2O_3 (1 wt.% stearic acid): (a) powder morphology after 0 h milling, (b) cross sectional observation after 0 h milling, (c) powder morphology after 2 h milling, (d) cross sectional observation after 2 h milling, (e) powder morphology after 4 h milling, and (f) cross sectional observation after 4 h milling

The areas with darker contrast in Fig. 9.2(b) were due to stearic acid. The morphology of Ni–20Cr–1.2Y_2O_3 powder after 2 h milling is shown in Fig. 9.2(c) and exhibited major agglomeration due to great ductility of powder particles and high tendency of cold welding at an early stage of milling. At an early stage of milling (2 h), the ductile Ni–20Cr powder

particles became flat and cold welded, and trapping of Y_2O_3 powder particles between Ni–20Cr lamellae likely occurred. The morphology of powder particles was round and the mean particle size after 2 h milling was estimated to be 33.6±1.5 μm. The plastic flow and deformed layers in a powder lamella after 2 h of milling can be clearly discerned in Fig. 9.2(d). Powder agglomeration continued to occur up to 4 h as shown in Fig. 9.2(e); however, numerous cracks on the powder particles were detected, too. Accumulation of work hardening led to fatigue and fragmentation within the powder flakes that could refine powder particle upon further milling. The powder shape was round with a mean particle size of 39.4±3.1 μm. Figure 9.2. (f) revealed significant work hardening, cracks and signs of fragmentation after 4 h of milling.

The XRD patterns for Ni–20Cr–1.2Y_2O_3 powder after 0 h, 2 h and 4 h milling (alloys A, B and C, respectively) are plotted in Fig. 9.3. In the XRD pattern of alloy A, the peaks of (111), (200) and (222) confirmed an *fcc* crystal structure in Ni–20Cr and the remaining peaks presented a *cubic* crystal structure in Y_2O_3. The peaks in the XRD of Y_2O_3 were indexed as (222), (400), (411), (422) and (622) in the order of appearance. The Ni–20Cr peaks exhibited significant broadening after 2 h of milling due to refinement in crystallite size. After 4 h of milling in alloy C, the distinct Y_2O_3 peaks were no longer observed, and the Ni–20Cr peaks shifted to lower diffraction angles as a result of partial dissolution of Y_2O_3 in the Ni–20Cr matrix and increasing lattice parameter.

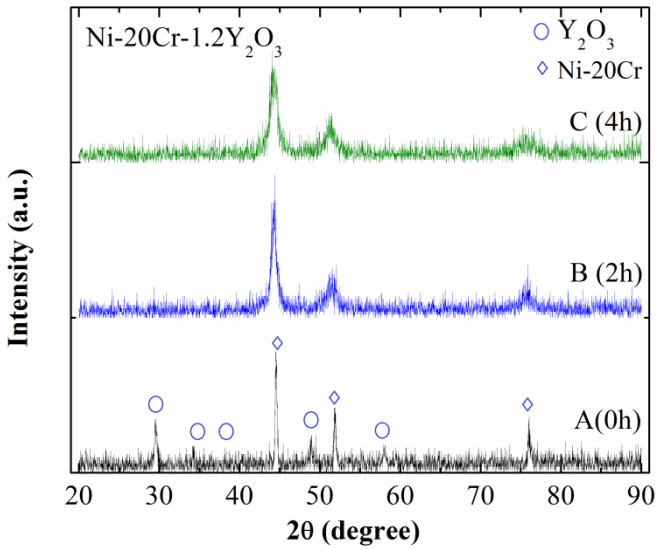

Figure 9.3. XRD patterns of Ni–20Cr–1.2Y_2O_3 alloys milled for 0 h (alloy A), 2 h (alloy B), and 4 h (alloy C)

The structural quantification results are summarized in Table 9.2. The lattice parameters of the *fcc* Ni–20Cr matrix increased after 4 h of milling indicating dissolution of Y_2O_3. As the milling time increased, the average crystallite size constantly decreased from 44 nm in the blended powder to 14 nm after 2 h of milling, and thereafter decreased to 4 nm with further milling up to 4 h.

Table 9.2. Microstructural parameters of Ni–20Cr–1.2Y_2O_3 powder milled for 0 h, 2 h and 4 h as determined by XRD

Milling Time (h)	Crystallite Size (nm)	Lattice Strain (%)	Lattice Constant (nm)
0	44±12	0.03±0.001	0.3530±0.0002
2	14±7	0.03±0.001	0.3536±0.0003
4	4±2	0.15±0.003	0.3560±0.0004

The microstructure of the as-milled Ni–20Cr–1.2Y_2O_3 powder after 2 h milling is shown in Fig. 9.4 and exhibited a homogeneous distribution of Y_2O_3 particles with reduced diameter of 3 nm in Ni–20Cr nanocrystalline matrix with reduced average size of 25 nm. The selected area diffraction (SAD) pattern shown in Fig. 9.4 revealed the presence of a

cubic crystal structure of Y_2O_3 particles distributed in Ni–20Cr matrix with *fcc* crystal structure. The density and microhardness of the Ni–20Cr–1.2Y_2O_3 milled for 0 h, 2 h and 4 h and then sintered at 1100 °C for 30 min were measured and presented in Table 9.3. Full density (100%) was achieved after sintering of Ni–20Cr–1.2Y_2O_3 powder milled for 0 h and 4 h; however the relative density of 2 h milled and sintered Ni–20Cr–1.2Y_2O_3 powder (alloy B) showed a slight reduction in density (99.55%). The microhardness values of sintered Ni–20Cr–1.2Y_2O_3 alloys increased with increasing milling time up to 4 h. This hardness increase due to longer milling time are likely due to the refined crystallite size, accumulation of work hardening and formation of complex Y–Cr–O particles specifically after 4 h of milling as will be shown later.

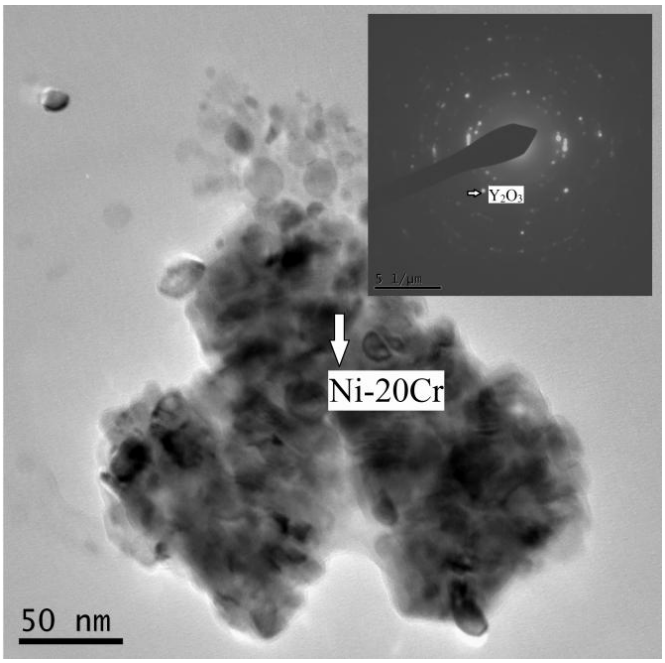

Figure 9.4. Microstructure of Ni–20Cr–1.2Y_2O_3 powder milled for 2 h (alloy B) and the corresponding diffraction pattern

Table 9.3. Physical density, relative density and microhardness values using different milling times; for alloys A, B and C

Alloy	Physical Density (g/cm^3)	Relative Density (%)	Microhardness (HV)
A (0 h)	8.228	100	202±6
B (2 h)	8.170	99.55	472±7
C (4 h)	8.226	100	527±21

The microstructure of sintered Ni–20Cr–1.2Y_2O_3 alloys milled for 0 h, 2 h and 4 h (alloy A, B and C, respectively) are shown in Figs. 9.5(a–d), respectively. The microstructure of alloy A was observed using EBSD because of coarser grains as shown in Fig. 5(a). The grains were equiaxed and fully recrystallized with average size of 8 μm. A high volume fraction of annealing twins and $\Sigma 3$ boundaries were observed in Fig. 9.5(a). Figure 9.5(b) shows a bright field TEM image from the 2 h milled Ni–20Cr–1.2Y_2O_3 (alloy B) with randomly oriented nanograins smaller than 300 nm. The presence of homogeneously distributed nanoparticles in a large volume fraction led to a significant grain refinement in microstructure of Ni–20Cr–1.2Y_2O_3 alloy.

The microstructure of Ni–20Cr–1.2Y_2O_3 alloy after milling for 4 h (alloy C) revealed a bimodal grain size distribution containing nanograins with an average size of 120 nm as shown in Fig. 9.5(c) and coarse grains with an average size of 400 nm as shown in Fig. 9.5(d). The corresponding SAD patterns obtained from Fig. 9.5(c) and Fig. 9.5(d) also confirmed this bimodal grain size distribution.

High fraction of straight and coherent annealing twin boundaries were found in all of the sintered Ni–20Cr–1.2Y_2O_3 alloys regardless of milling time (alloys A, B and C) as shown in Fig. 9.5(a) and Figs. 9.6(a–b), respectively.

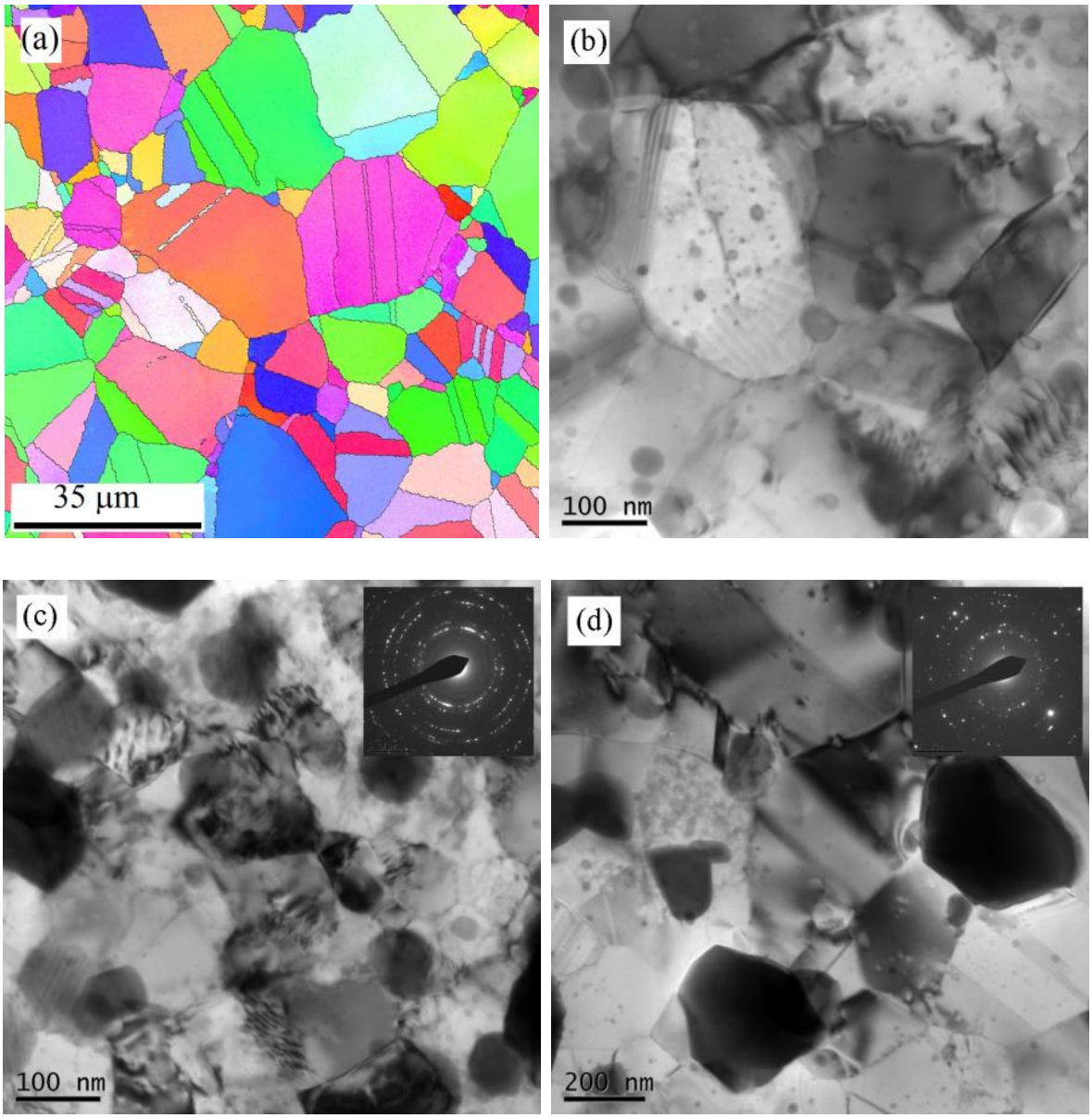

Figure 9.5. The micrographs of Ni–20Cr–1.2Y_2O_3 alloy milled for (a) 0 h (alloy A), (b) 2 h (alloy B), (c) 4 h (alloy C) showing nanograins, and (d) 4 h (alloy C) showing coarser grains

According to studies, formation of these twin boundaries would significantly reduce the grain boundary energy Ni–20Cr–1.2Y_2O_3 powder during sintering stage [29-31]. These twin boundaries were observed in Ni–20Cr–1.2Y_2O_3 alloy milled for different times (0 h, 2 h and 4 h) implying that formation of these twin boundaries was due to sintering and is not dependent on milling stage. However, the twin width in the sintered Ni–20Cr–1.2Y_2O_3

alloys was strongly dependent on milling time because narrower twin boundaries were observed for alloy milled for longer hours (4 h or alloy C) as shown in Fig. 9.6(c). The average twin boundary width reduced with increasing milling time and was measured to be 2.6 μm in alloy A, 127 nm in alloy B and 32 nm in alloy C.

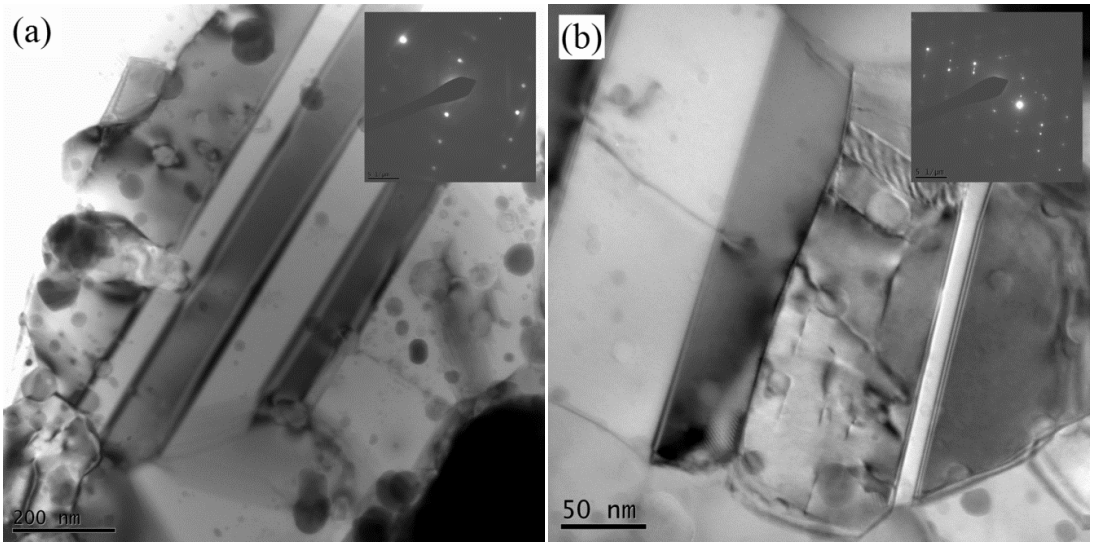

Figure 9.6. Twins in the microstructure of Ni–20Cr–1.2Y_2O_3 alloy milled for (a) 2 h (alloy B), and (b) 4 h (alloy C)

Figures 9.7(a–b) show the second phase particles in the sintered Ni–20Cr–1.2Y_2O_3 alloys after milling for 2 and 4h, respectively. For alloy B, the smallest and the average particle diameter were determined to be 3 nm and 14 nm, respectively as shown in Fig. 9.7(a). In alloy B, three main categories of oxide particles were found based on energy dispersive spectroscopy (EDS): (1) Ni-based oxides in the range of 80–100 nm; (2) Cr-based oxides in the range of 20–60 nm; and (3) Y-based oxides smaller than < 15 nm. Similarly, the smallest and the average particle diameter were determined to be 2 nm and 7 nm,

respectively for alloy C, as shown in Fig. 9.7(b). The average particle size decreased at a longer milling time.

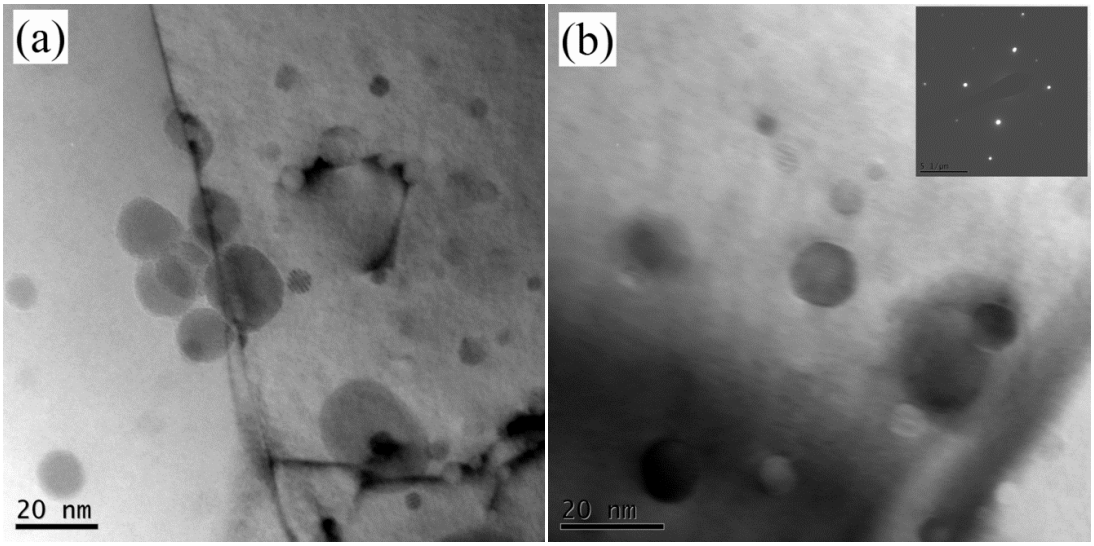

Figure 9.7. The oxide dispersiods in the microstructure of the SPSed Ni–20Cr–1.2Y_2O_3 alloys milled for (a) 2 h (alloy B), and (b) 4 h (alloy C)

The particles in Fig. 9.7(a) were mainly Cr-based oxides or Y_2O_3 whereas the majority of particles shown in Fig. 9.7(b) had chemical composition close to $YCrO_3$. This could be attributed to possible dissolution and decomposition of Y_2O_3 and formation of $YCrO_3$ as new compounds.

9.3.2. Effect of SPS parameters

The Ni–20Cr–1.2Y_2O_3 alloy, milled for 2 h was sintered at 600 °C for 5 min (alloy D), at 900 °C for 5 min (alloy E), at 1000 °C for 5 min (alloy F), at 1100 °C for 5 min (alloy G) and at 1100 °C for 30 min (alloy B). The physical density, relative density and microhardness values of these alloys were measured and presented in Table 9.4. The density

values significantly increased from 72.2% after sintering at 600 °C to 99.3% after sintering at 1000 °C and only slightly increased to 99.5% and 99.6% after sintering at 1100 °C for 5 and 30 min, respectively. The main densification occurred at 1000 °C and density values did not significantly improve with further increase of sintering temperature or time.

Table 9.4. Physical density, relative density and microhardness values of Ni–20Cr–1.2Y_2O_3 alloys sintered at different temperatures and times; for alloys D, E, F, G and B

Alloy	Physical Density (g/cm^3)	Relative Density (%)	Microhardness (HV)
D (600 °C for 5 min)	5.924	72.18	131±31
E (900 °C for 5 min)	7.708	93.93	395±11
F (1000 °C for 5 min)	8.15	99.26	556±4
G (1100 °C for 5 min)	8.163	99.48	470±7
B (1100 °C for 30 min)	8.170	99.55	472±7

The microhardness values constantly increased from 130.8±31.5 HV after sintering at 600 °C to 556±5 HV after sintering at 1000 °C at a constant dwell time (5 min). However, the microhardness decreased to 470±8 HV after sintering at 1100 °C for 5 min and did not change significantly after a dwell time of 30 min.

The overview of microstructure of Ni–20Cr–1.2Y_2O_3 alloy sintered at 900 °C (alloy E), 1100 °C for 5 min (alloy G) and 1100 °C for 30 min (alloy B) are shown in Figs. 9.8(a–c), respectively. Subgrains with an average size of 200 nm were distinguished from each other with arrays of dislocations as shown in Fig. 9.8(a). The grains shown in Fig. 9.8(b) were larger with an average size of 350 nm and separated from each other with well-defined sharp boundaries. After sintering of alloy B at 1100 °C for 30 min, the average grain size was reduced even further and an extensive dislocation activity was observed, as shown in Fig. 9.8(c). This could be explained considering that dynamic recrystallization phenomenon

likely occurred in the alloy after 30 min at 1100 °C. During dynamic recrystallization, dislocation activity became significant and led to more grain refinement. Meanwhile, the interaction of nanoparticles with dislocations and mobile boundaries effectively inhibited the grain growth process.

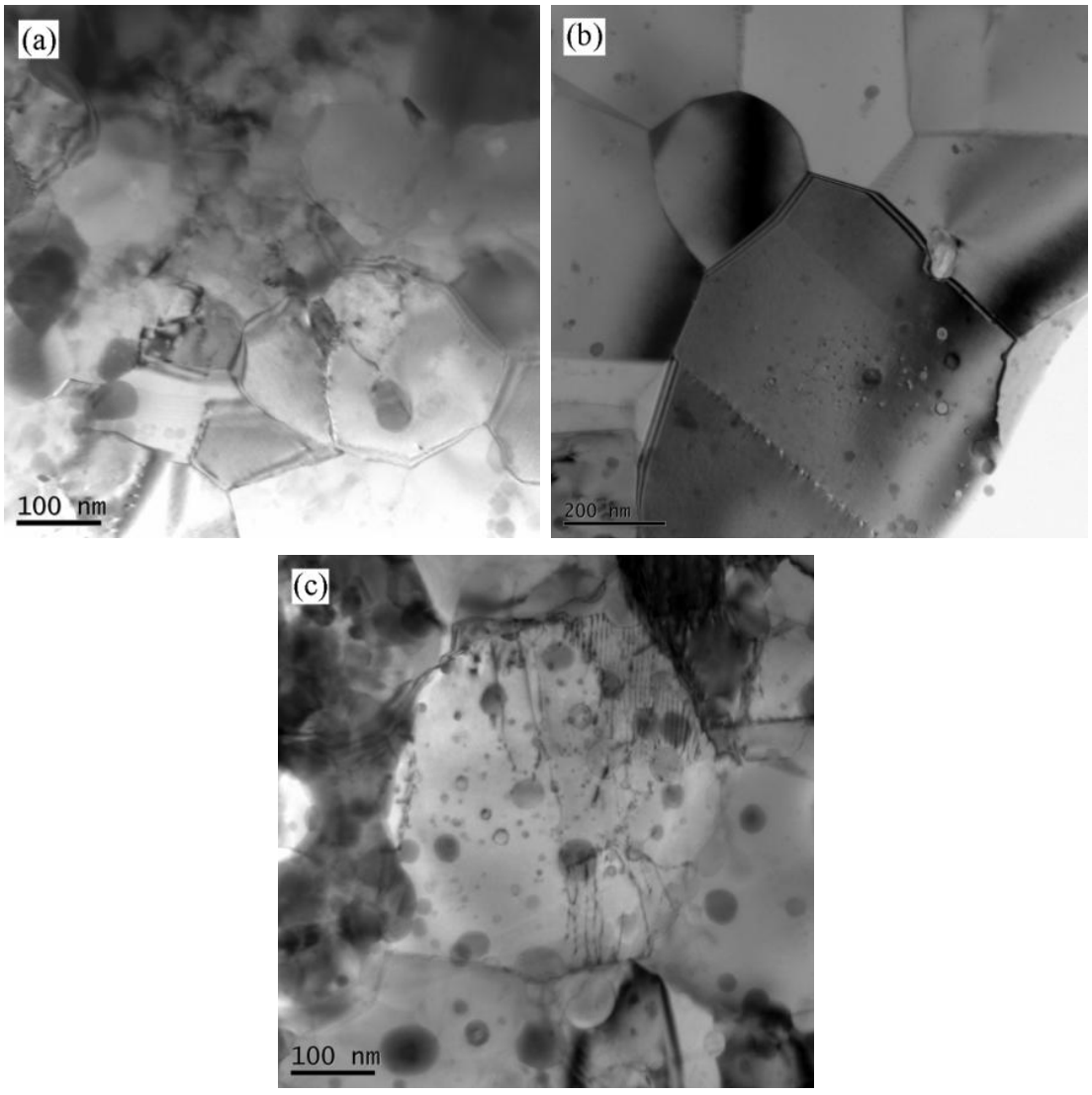

Figure 9.8. The microstructure of Ni–20Cr–1.2Y_2O_3 alloy sintered at (a) 900 °C for 5 min (alloy E), (b) 1100 °C for 5 min (alloy G), and (c) 1100 °C for 30 min (alloy B)

The twinning activity as a function of sintering temperature and time can be observed in Figs. 9.9(a–c). The microstructure of Ni–20Cr–1.2Y_2O_3 alloy sintered at 900 °C for 5 minutes (alloy E) shown in Fig. 9.9(a), contained very limited and localized twin activities with average thickness of 10 nm and volume fraction of 2.8%. The average twin boundary width and volume fraction significantly increased to 150 nm and 10%, respectively, after sintering at 1100 °C for 5 minutes (alloy G) as shown in Fig. 9.9(b).

Twins in Ni–20Cr–1.2Y_2O_3 alloy sintered at 1100 °C for 30 minutes (alloy B) are shown in Figure 9.9(c), and the average twin boundary thickness and volume fraction were estimated to be 127 nm and 11.6%, respectively. With increasing sintering time from 5 to 30 minutes, the twin boundary width was reduced slightly, but twin boundary volume fraction increased slightly. This could be attributed to the smaller grain size with a higher density of grain boundary areas in alloy B.

The oxide particles in alloy E and G are shown in Figs. 9.10(a–b), respectively. The oxide particles in alloy B were formerly shown in Fig. 9.7(a), and thus not repeated here. The average particle size in alloy E was measured to be 4.1 nm, and the smallest particle size was found to be 2 nm. Similarly, for alloy G, the average particle size was 12 nm, and the smallest particle size was 4 nm. The oxide particle size increased with increasing sintering temperature and time, plausibly due to faster kinetics of diffusion and particle coarsening at higher sintering temperature and longer sintering time.

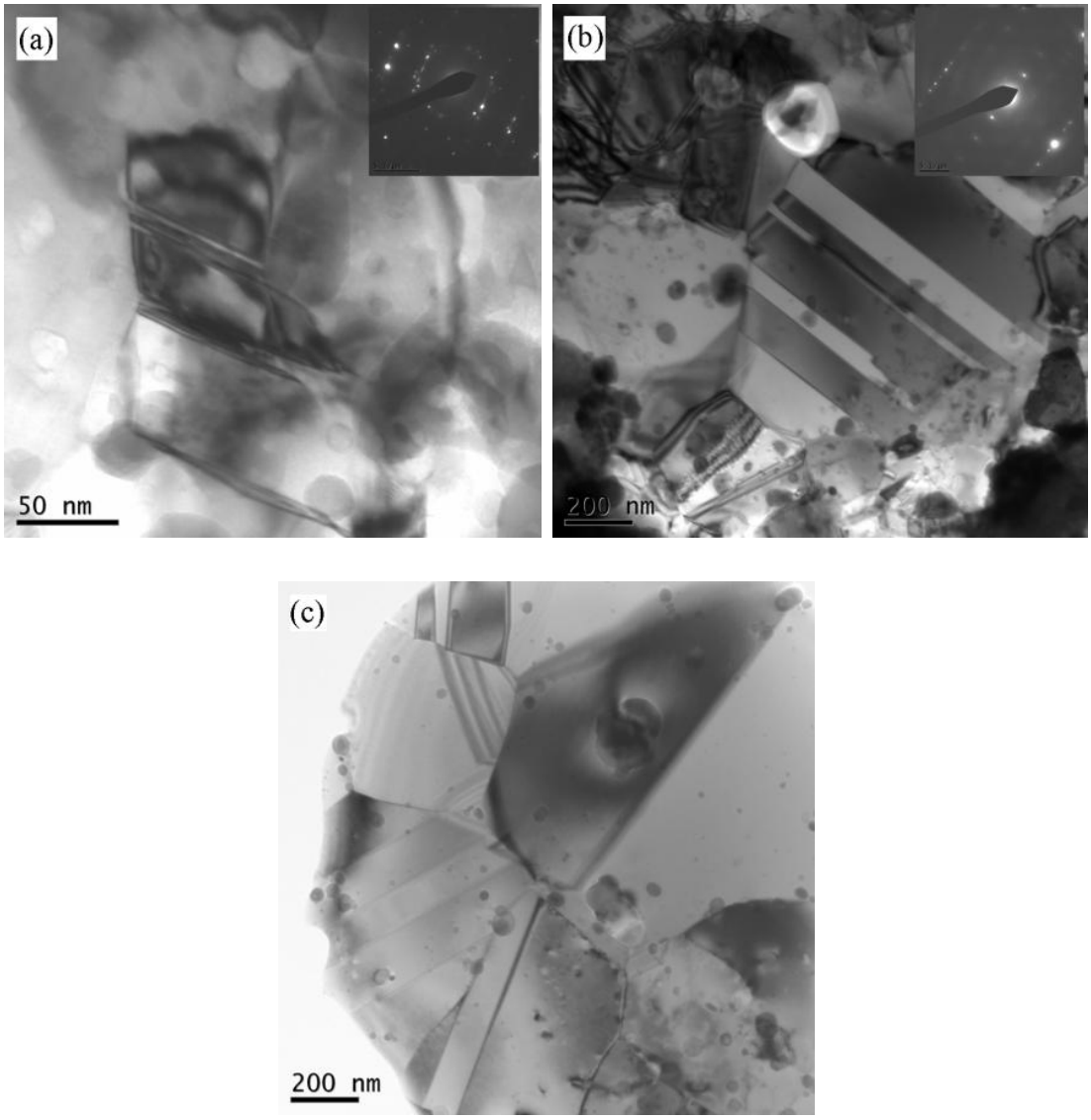

Figure 9.9. Twins in the microstructure of Ni–20Cr–1.2Y_2O_3 alloys sintered at (a) 900 °C for 5 min (alloy E), (b) 1100 °C for 5 min (alloy G), and (c) 1100 °C for 30 min (alloy B)

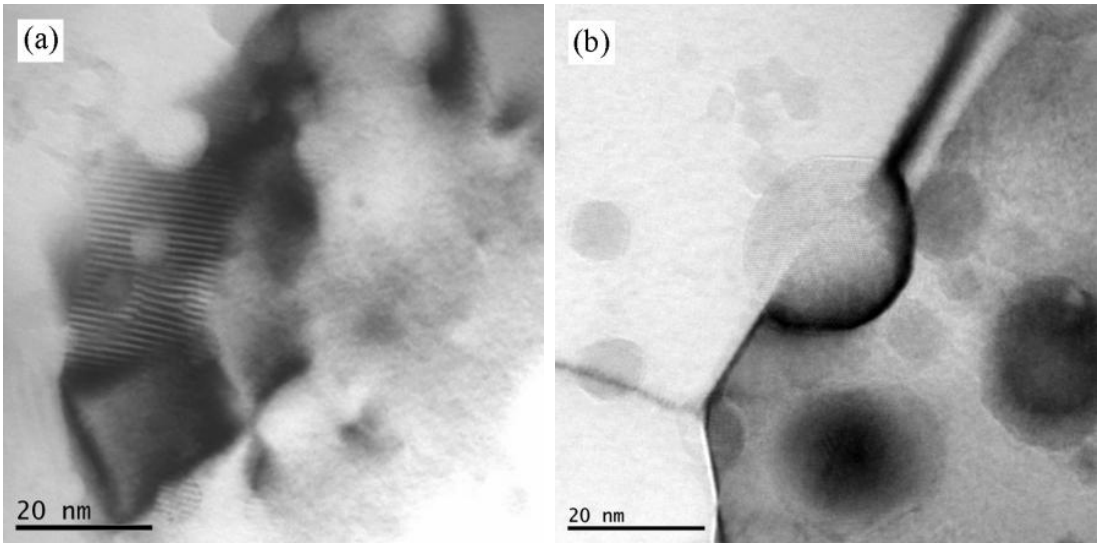

Figure 9.10. The oxide dispersiods in the microstructure of Ni–20Cr–1.2Y_2O_3 alloy sintered at (a) 900°C for 5 min (alloy E), and (b) 1100 °C for 5 min (alloy G)

9.3.3. Effect of alloy composition

The physical density, relative density and microhardness values of different alloy compositions; Ni–20Cr (alloy H), Ni–20Cr–1.2Y_2O_3 (alloy B) and Ni–20Cr–1.2Y_2O_3–5Al_2O_3 (alloy I) were evaluated and presented in Table 9.5. Adding 1.2 wt.% Y_2O_3 to Ni–20Cr alloy increased the relative density from 98.95±0.03% to 99.55±0.04%; however, addition of 5 wt.% Al_2O_3 to Ni–20Cr–1.2Y_2O_3 slightly decreased the relative density to 99.18±0.02%. The microhardness values showed significant increase from 307±3 HV in Ni–20Cr alloy to 472±8 HV in Ni–20Cr–1.2Y_2O_3 and 505±10 HV in Ni–20Cr–1.2Y_2O_3–5Al_2O_3 alloy.

Table 9.5. Physical density, relative density and microhardness values using different alloying composition; for alloys H, B and I

Alloy	Physical Density (g/cm^3)	Relative Density (%)	Microhardness (HV)
H (Ni–20Cr)	8.19±0.01	98.95±0.03	307±3
B (Ni–20Cr–1.2Y_2O_3)	8.170±0.01	99.55±0.04	472±7
I (Ni–20Cr–1.2Y_2O_3–5Al_2O_3)	7.70±0.01	99.18±0.02	505±10

The microstructures of Ni–20Cr (alloy H), Ni–20Cr–1.2Y_2O_3 (alloy B) and Ni–20Cr–1.2Y_2O_3–5Al_2O_3 (alloy I) are displayed in Figs. 9.11(a–c), respectively. The microstructure of the Ni−20Cr alloy contained fully recrystallized grains with well-defined sharp boundaries and fewer dislocations as shown in Fig. 9.11(a).

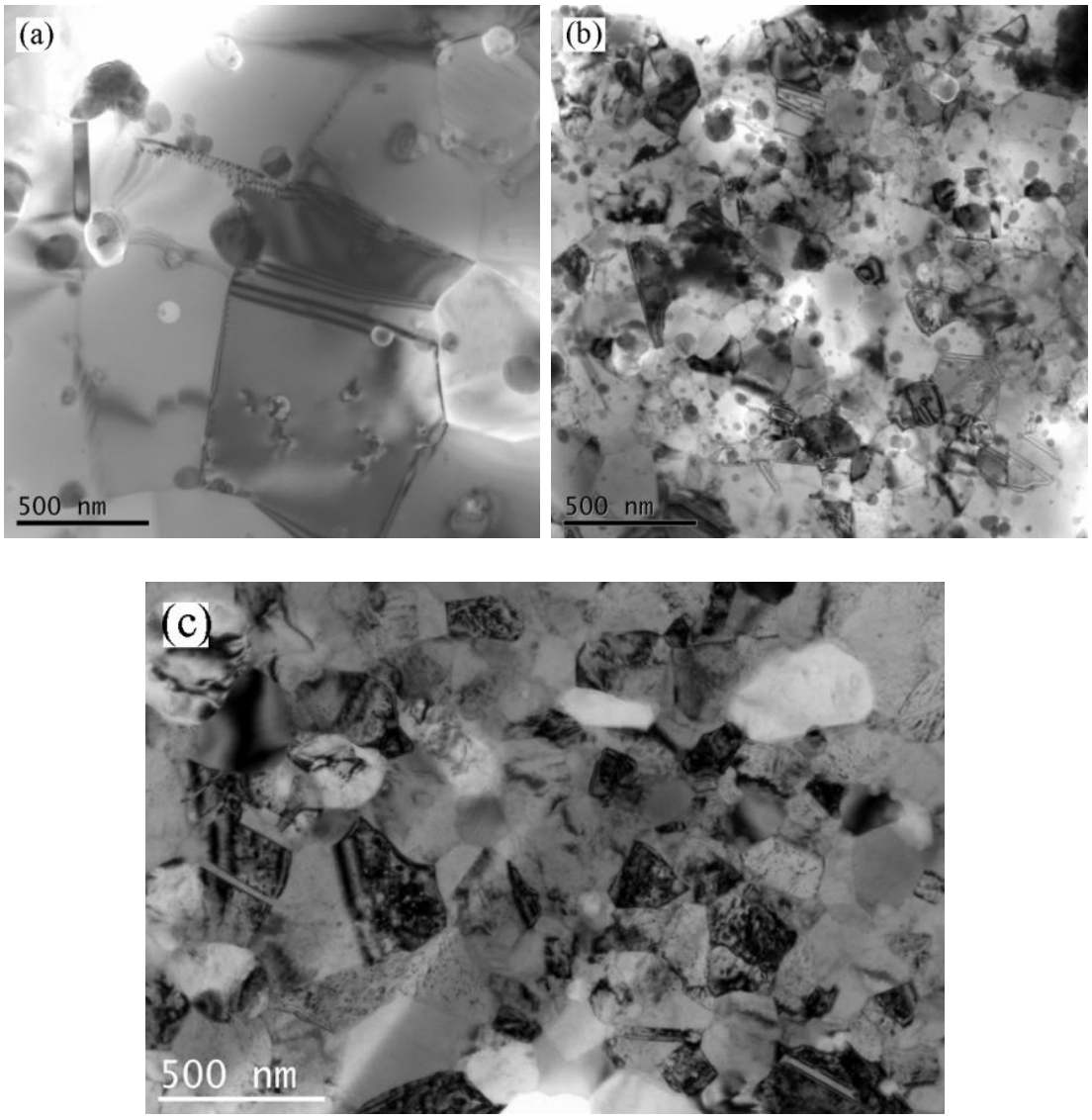

Figure 9.11. The TEM micrographs of alloys with different compositions; (a) Ni–20Cr (alloy H), (b) Ni–20Cr–1.2Y_2O_3 (alloy B), and (c) Ni–20Cr–1.2Y_2O_3–5Al_2O_3 (alloy I)

The average grain size of the Ni–20Cr alloy was measured to be 630 nm, and the number density of oxide particles was less than that of Ni–20Cr–1.2Y_2O_3 formerly shown in Fig. 9.7(a). The effect of Y_2O_3 addition on the grain refinement was clearly evident in Fig. 9.11(b). The presence of homogeneously distributed nanodispersoids in a large volume fraction led to a higher microhardness and grain refinement in the Ni–20Cr–1.2Y_2O_3 alloy. The microstructure of Ni–20Cr–1.2Y_2O_3–5Al_2O_3 (alloy I) is shown in Fig. 9.11(c), and revealed randomly oriented grains with extensive dislocation activity and an average grain size of 385 nm.

The microstructure of Ni–20Cr alloy sintered at 1100 °C for 30 minutes (alloy H), contained twins with average width of 161 nm and volume fraction of 9% as shown in Fig. 9.12(a). The average twin width and volume fraction in Ni–20Cr–1.2Y_2O_3 (alloy B) were determined to be 127 nm and 11.6%, respectively as previously shown in Fig. 9.6(a). The average twin width and volume fraction were found to be 60 nm and 16.1% in the microstructure of Ni–20Cr–1.2Y_2O_3–5Al_2O_3 (alloy I) shown in Fig. 9.12(b). Thus, addition of 5 wt.% Al_2O_3 to Ni–20Cr–1.2Y_2O_3 alloy led to a higher volume fraction of twins with narrower width.

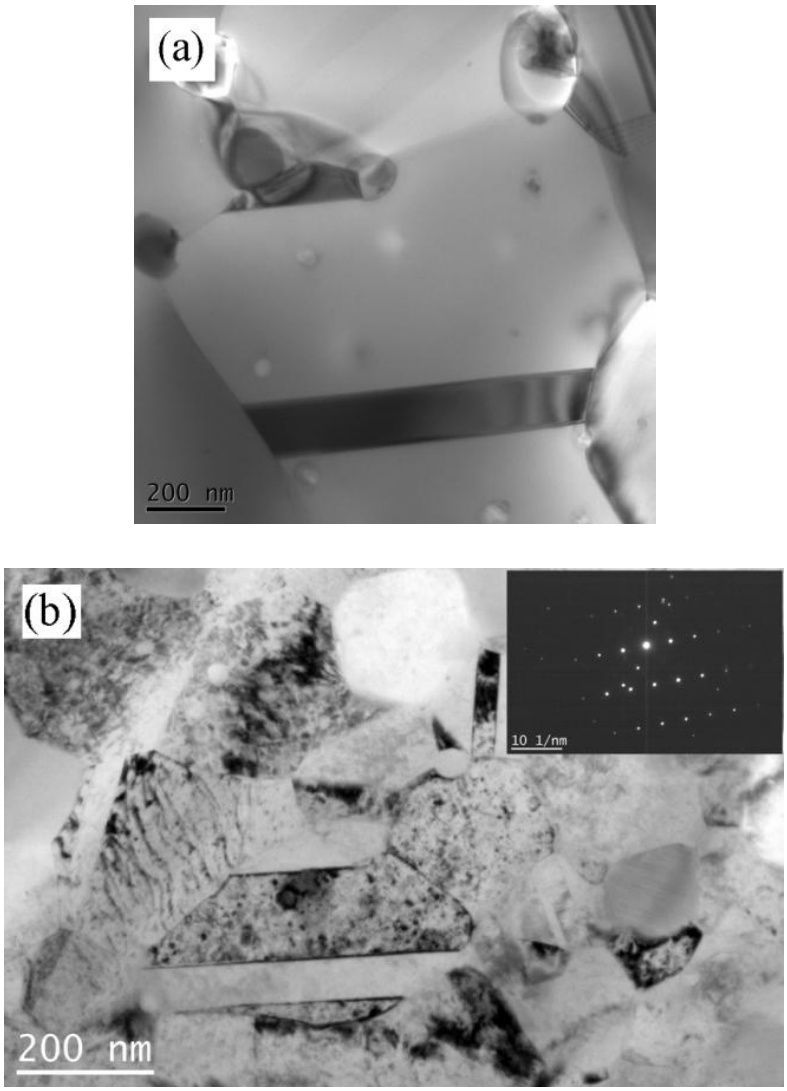

Figure 9.12. Twins in the microstructure of alloys with different compositions; (a) Ni–20Cr (alloy H), and (b) Ni–20Cr–1.2Y_2O_3–5Al_2O_3 (alloy I) (twinning in alloy B is previously shown in Fig. 9.6(a))

The size distribution of second phase particles in Ni–20Cr (alloy H) is shown in Fig. 9.13(a). Coarser particles were found to be mostly located on the grain boundaries. The oxide particles in Ni–20Cr–1.2Y_2O_3 (alloy B) were previously shown in Fig. 9.7(a). A HAADF STEM micrograph obtained from Ni–20Cr–1.2Y_2O_3–5Al_2O_3 (alloy I) is shown in Fig. 9.13(b). The ultra fine particles with darker contrast and smaller than 400 nm were

more enriched in Al. Figure 9.13(c) revealed oxide particles with diameter varying from 2–3 nm to 50 nm in alloy I.

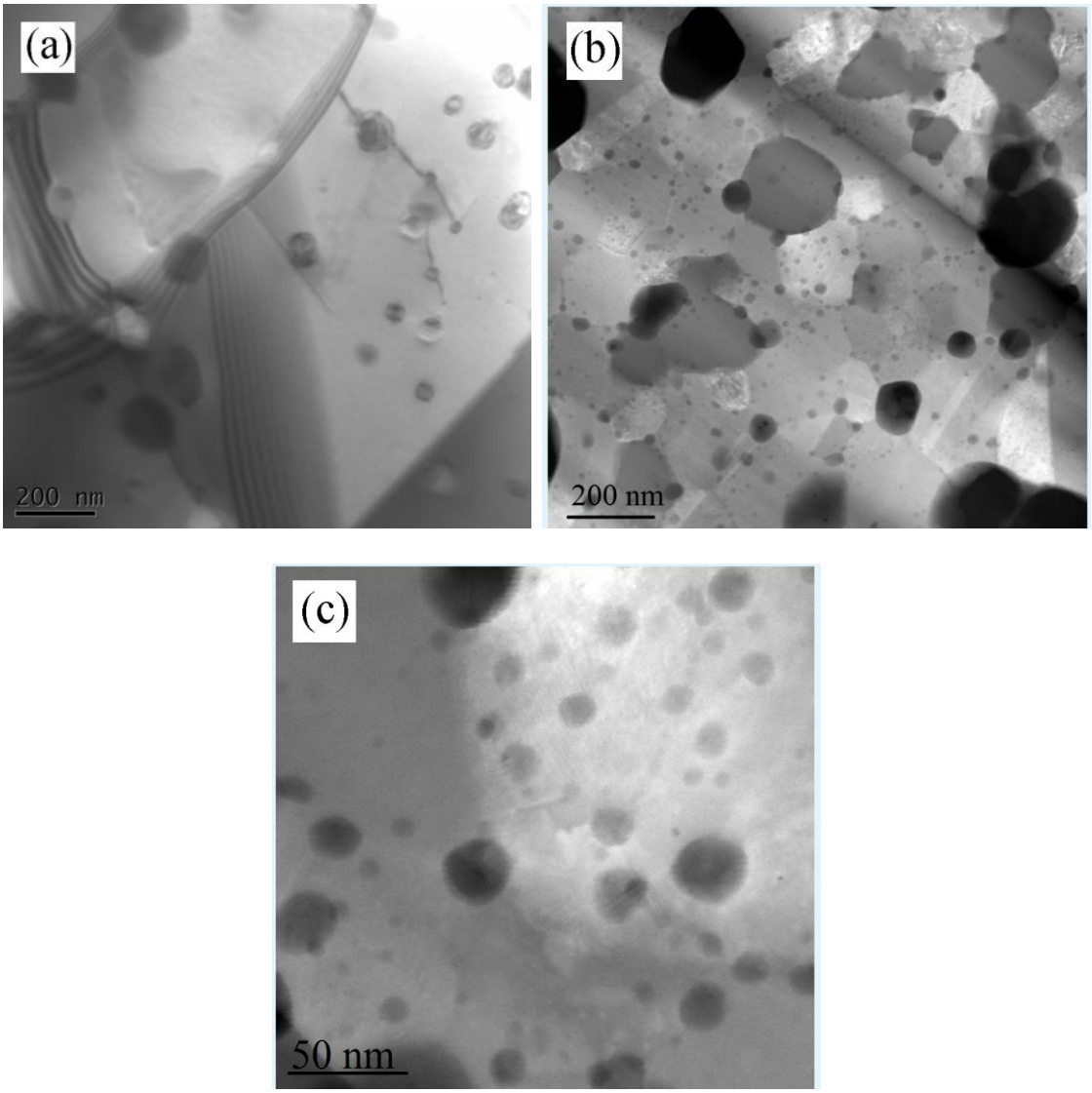

Figure 9.13. The oxide dispersoids with different compositions: (a) a BF TEM micrograph of alloy H, (b) HAADF STEM micrograph obtained from alloy I, and (c) higher magnification micrograph of alloy H

The combined results of XRD, SEM / EDS and TEM / EDS revealed the presence of Cr_2O_3, Cr_2O_5, Y_2O_3, Y_2CrO_4, and $YCrO_3$ as well as Cr_3C_2 and Cr_7C_3 in SPSed Ni–20Cr and

Ni–20Cr–1.2Y_2O_3 alloys. Some of these particles were not observed in TEM due to the electropolishing artifact. The types of particles in Ni–20Cr–1.2Y_2O_3–5Al_2O_3 (alloy I) varied between Al_2O_3, $YAlO_3$ and negligible percentage of $CrAlO_3$. The particle size distributions were calculated from TEM micrographs using following equation [1];

$$\lambda = [(\frac{3\pi}{4f})^{1/2} - 1.64] \times r \qquad (9.1)$$

where λ is the mean particle separation (nm), r is the mean particle radius and f is the volume fraction of dispersion particles based on several TEM micrographs. Approximately 500 particles were considered for these calculations for better statistical data. For Ni–20Cr, the average particle diameter, average particle radius and mean particle separation were determined to be 88 nm, 44 nm and 187 nm, respectively. From the TEM micrographs of Ni–20Cr–1.2Y_2O_3 alloy, the average particle diameter, average particle radius and mean particle separation were determined to be 14 nm, 7 nm and 58 nm, respectively. For Ni–20Cr–1.2Y_2O_3–5Al_2O_3, the average dispersion oxide particle diameter, average particle radius and mean particle separation were determined to be 22 nm, 11 nm and 72 nm, respectively. In this calculation, the coarser particles enriched in Al were not included.

The particle size distribution histograms for different alloy compositions are shown in Figs. 9.14(a–c). A broad range of oxide particles were observed in Ni–20Cr alloy as shown Fig. 9.14(a). With addition of Y_2O_3 to Ni–20Cr, both average particle diameter and mean particle separation decreased significantly. In Ni–20Cr–1.2Y_2O_3–5Al_2O_3 alloy, there was a range of nanoparticles smaller than 15 nm and coarser particles larger than 250 nm.

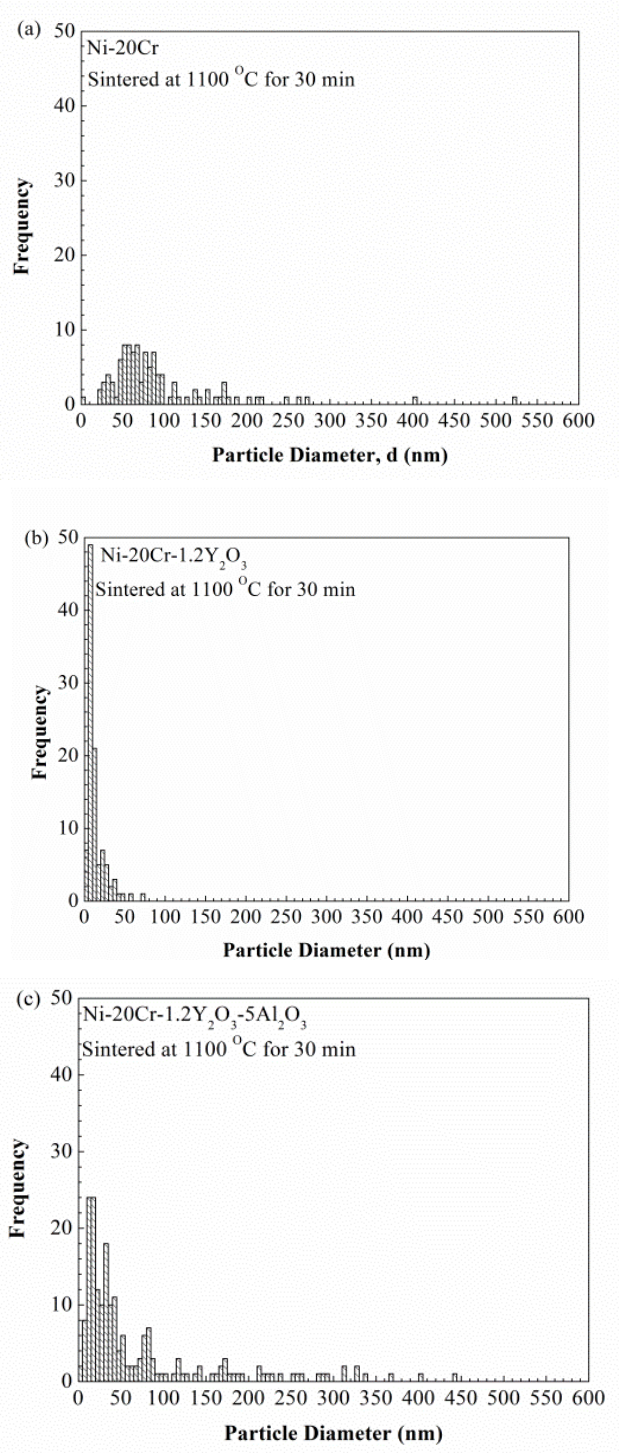

Figure 9.14. Particle size distribution of alloys with different compositions; (a) alloy H, (b) alloy B, and (c) alloy I (approximately 500 particles were counted for each plot)

The compression tests were performed on Ni–20Cr, Ni–20Cr–1.2Y_2O_3 and Ni–20Cr–1.2Y_2O_3–5Al_2O_3 alloys at 25 °C and 800 °C by applying a strain rate of 10^{-3} s^{-1}. The results are summarized in Table 9.6. The true compression stress–plastic strain plots (at 800 °C) for different compositions are illustrated in Fig. 9.15.

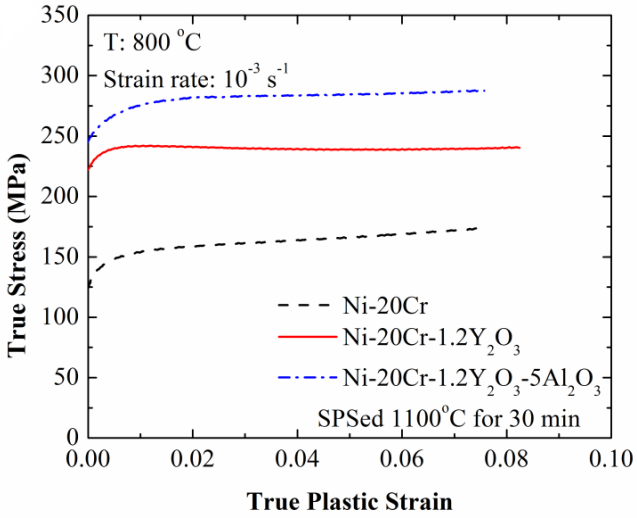

Figure 9.15. True stress – true plastic strain curves obtained at 800 °C for Ni–20Cr, Ni–20Cr–1.2Y_2O_3, and Ni–20Cr–1.2Y_2O_3–5Al_2O_3 alloys sintered at 1100 °C for 30 min

Table 9.6. The compression yield stress values of Ni–20Cr, Ni20–Cr–1.2Y_2O_3 and Ni–20Cr–1.2Y_2O_3–5Al_2O_3 alloys sintered at 1100 °C for 30 min

Alloy	Compression Yield Stress at 25 °C (MPa)	Compression Yield Stress at 800 °C (MPa)
H (Ni–20Cr)	790	125
B (Ni–20Cr–1.2Y_2O_3)	1286	225
I (Ni20–Cr–1.2Y_2O_3–5Al_2O_3)	1470	250

9.4. Discussion

9.4.1. Microstructural evolutions

During high energy ball milling several phenomena could occur; initially Ni–20Cr powder particles agglomerate and then continue to form fine lamellar sandwich structure until they break up due to high energy colliding balls at later stages [25]. After milling of Ni–20Cr–1.2Y_2O_3 alloy for 2 h, Ni–20Cr powder became cold-welded and Y_2O_3 particles became finer and increased the interfacial energy (Figs. 9.2(c–d)). As milling proceeded for 4 h, accumulative plastic strain became significant and caused crack initiation in the milled particles as shown in Fig. 9.2(f). After 4 h of milling, Y_2O_3 particles had a sufficient driving force for decomposition. The peak broadening effect shown in Fig. 9.3 can be attributed to the progressive reduction in crystallite size (i.e. grain refinement) and increase in lattice strain arising from crystal imperfections (vacancies and dislocations) and severe plastic deformation induced by high energy ball milling. No peak of Y_2O_3 was observed in the XRD pattern corresponding to 4 h milling and shown in Fig. 9.3. Dissolution of Y_2O_3 in Ni–20Cr matrix was not the goal of the milling experiments, rather the intention of this study was to homogeneously distribute Y_2O_3 fine particles in the Ni–20Cr matrix as shown in Figs. 9.4(a–b). So other milling experiments will be continued for 2 h of milling.

Park *et al.* [8] investigated phase transformation in high energy ball milling of Y_2O_3 (50 μm in size) in pure Ni matrix (40 μm size) after short time in a custom made high speed planetary milling machine. After milling for 20 min, Y_2O_3 particles became fine (10 nm size) and transformed from *cubic* crystal structure to *monoclinic* structure. Upon further milling for 60 min, nanocrystalline *monoclinic* Y_2O_3 and nanograins of Ni were surrounded by an amorphous phase layer due to decomposition of Y_2O_3 particles. In the

current study, such phase transformation and amorphous layer formation were not observed in after 2 and 4 h of milling.

In alloy A, there was no milling and plastid deformation involved prior to sintering, so large particles and crystallites of Ni–20Cr were recrystallized by hot deformation caused during SPS. Non-uniformly distributed Y_2O_3 particles were located at prior particle boundaries upon consolidation. The recrystallized grains were dislocation free, equiaxed and without any preferred texture.

In alloy B, recrystallization and grain growth were efficiently controlled by a high volume fraction of oxide nanoparticles with mean particle separation of 58 nm and average radius of 7 nm (smallest particle size of 3 nm).

With further milling for 4 h, there was a tendency for developing a bimodal grain structure in the sintered alloy as shown in Figs. 9.5(c–d). The reason for the bimodal grain size distribution was likely due to heterogeneous plastic deformation and dissolution of Y_2O_3 in Ni–20Cr matrix after milling for 4 h. Because the heterogeneity in Ni–20Cr powder particles incorporated by longer milling hours from one hand and alteration in chemical compositions from one particle to another particle or from inside to outside of a particle in another hand could initiate the bimodal grain structure [25]. More distinct bimodal grain size distribution has already been reported for the iron-based ODS alloys and was attributed to heterogeneity developed in the microstructure due to long hours of milling and subsequent sintering process [17, 32, 33].

Microstructures of the sintered Ni–20Cr–1.2Y_2O_3 alloy milled for 0 h, 2 h and 4 h comprised multiple twin boundaries as shown in Fig. 9.5(a) and Figs. 9.6(a–c). With

increasing milling time from 0 h to 4 h, twin boundaries width reduced and twin boundaries volume fraction increased.

Presence of twin boundaries in 0 h milled sintered Ni–20Cr–1.2Y_2O_3 (alloy A) implied that twin boundary formation may not depend on milling process, rather depending on thermal and sintering process. Annealing twins have been frequently observed during grain growth of nickel at temperatures of $0.68T_m$ and above (i.e. ≥ 950 °C) [30], and were associated with annealing temperature. Formation of twin boundaries in nickel alloys is because of their low stacking fault energy. For example, adding only 0.04 mole fraction of Cr as an alloying element to pure Ni decreases the stacking fault energy of the alloy to –40 ($mJ.m^{-2}$) [34].

The longer milling time would produce the smaller crystallize size and consequently the narrower twin boundaries. It is because smaller crystallite size would significantly limit the space in grain interior for twins in order to nucleate and grow [35]. Besides, crystallographic orientation would alter more frequently in nanograins and lead to narrower twins.

Twin volume fraction was approximately determined to be 8.5%, 11.6% and 16.8% for alloys A, B and C, respectively. The twin volume fraction increased at longer milling time. The accurate measurement of twin volume fraction is usually challenging because some twins may not visible in TEM if the grains are not oriented to certain orientation or angles. Longer milling time produced higher amount of plastic deformation and stored energy. Higher amount of stored energy in the crystallites and crystallite boundaries of Ni–20Cr–1.2Y_2O_3 alloy could effectively lower the activation energy and favor the twin boundary formation. Twin boundaries are mobile during sintering and could minimize the

grain boundary energy and total interfacial energy independently of grain growth and grain boundary migration [30]. Therefore, higher amount of stored energy in the milled powder can be lowered during sintering through the formation of higher volume of twin boundaries.

The size and chemical composition of oxide particles found in the sintered Ni–20Cr–1.2Y_2O_3 alloys Figs. 9.7(a–c) could be different from each other as a function of milling time. It is likely that during SPS at the elevated temperatures, Cr started precipitating out of the Ni–Cr solid solution in the form of Cr based oxides and carbides [23]. The oxide particles of alloy B as shown in Fig. 9.7(b) were mostly Cr-based and Y-based oxides. However, the oxide particles of alloy C shown in Fig. 9.7(c) had composition close to Y–Cr–O. This could be due to decomposition of Y_2O_3 after 4 h milling as confirmed by XRD results (shown in Fig. 9.3, and re-precipitation along with Cr to form smaller and more stable particles [8]. Similar behavior was also reported in former studies where the original Y_2O_3 particles were changed into other complex more stable oxides (for example Y–Ti–O, Y–Cr–O and Y–Al–O) [4, 36-38].

The enthalpy of formation of $YCrO_3$ and Y_2O_3 are –1493 and –1907 kJ/mol, respectively [39]. Despite the high enthalpy of formation for Y–O, the formation of Y–Cr–oxides could be promoted due to higher concentration and diffusivity of Cr compared to Y [33, 40]. This was provided via accumulated lattice imperfections (vacancies and dislocations) introduced by longer milling times.

The SPS parameters such as temperature, time, heating rate and applied pressure could significantly influence the mechanical properties and microstructural evolutions. In current study, only the effect of SPS temperature and time were investigated on alloys D, E, F, G

and B. Densification constantly improved with increasing SPS temperature; however, microhardness decreased at temperatures above 1000 °C likely due to potential coarsening of oxide particles. The subgrains formed at 900 °C were distinguished by arrays of dislocations and revealed a recovered microstructure as shown in Fig. 9.8(a). However, after SPS at 1000 °C, most of the grains were larger, recrystallized and separated from one another with sharp boundaries as shown in Fig. 9.8(b). The grain size and microhardness at 1100 °C did not change with increasing time for 5 min to 30 min, suggesting that for SPS, temperature was more dominant than time.

Dislocations observed in Fig. 9.8(c) could not be due to work hardening since the hardness values did not show significant change between alloy G (1100 °C for 5 min) and B (1100 °C for 30 min). They could be due to dynamic recrystallization continuously occurring during SPS with increasing time for 5 min to 30 min.

Lower hardness of alloy E compared to alloy G and B could be due to less volume fraction of twin boundaries as shown in Figs. 9.9(a–c). Because annealing twins have high strength and load transfer capability and could contribute to hardness by blocking dislocations and mobile grain boundaries [41]. Increasing SPS temperature increased volume fraction of twin boundaries and their thickness. Increasing sintering time did not significantly change twin boundary properties. Recrystallization process is controlled by oxide dispersion and one way to facilitate the recrystallization stage is through twin formation. In other word, higher sintering temperature may lower the activation energy of twin formation because twinned grains can facilitate the recrystallization stage [42].

Similar twin activities have recently been reported in powder processing and SPS of bulk multimodal nickel [41]. Fang *et al.* [43] suggested that during the SPS process and applying a high uniaxial pressure (here 80 MPa), certain parallel crystal faces might move toward opposite of each other along a direction with a certain value of distance. This approach could activate a certain twin boundary system by a critical resolved shear stress that could be achieved at higher sintering temperatures. Randle *et al.* [30] suggested that twin formation kinetics in nickel may actually be independent of grain growth and the relationship between grain growth and twin formation may be only coincidentally related with temperature. Nonetheless, the origin of annealing twins in Ni alloys is still a matter of conjecture.

Oxide particle size significantly increased with increasing SPS temperature as shown in Figs. 9.10(a–b) with smallest oxide particle size found in alloy E (900 °C for 5 min). In current study, sintering time did not cause any significant oxide particle coarsening. Sequential adding of Y_2O_3 and Al_2O_3 to Ni–20Cr significantly improved the hardness due to grain refinement and high density of oxide nanoparticles as shown in Figs. 9.11(a–c).

Fully recrystallized microstructure with less density of particles was observed in the microstructure of Ni–20Cr alloy. The microstructure of Ni–20Cr–1.2Y_2O_3 and Ni–20Cr–1.2Y_2O_3–5Al_2O_3 alloys revealed nanograins with higher density of dislocations and oxide nanoparticles.

Higher volume fraction of second phase particles or oxide particles increased the volume fraction of twin boundaries and reduced width of twin – matrix lamellae (Figs. 9.12(a–b)). The presence of high volume fraction of precipitates and solutes at the boundaries of Ni–20Cr–1.2Y_2O_3 and Ni–20Cr–1.2Y_2O_3–5Al_2O_3 alloys might impede the grain rotations

and increase the activation energy of grain rotations [44]. This could facilitate and ease formation of more annealing twins with narrower width and higher volume fraction.

9.4.2. Mechanical properties

Higher hardness values with increasing milling time could be attributed to smaller crystallite size, more plastic strain and narrower twin width. Because annealing twins are considered as strong obstacles to dislocation motion especially when the thickness of twin / matrix lamellae decreases [41, 43]. Microhardness value was 307±3 HV for Ni–20Cr alloy, 471.6±7.5 HV in Ni–20Cr–1.2Y_2O_3 and 505±10 HV in Ni–20Cr–1.2Y_2O_3–5Al_2O_3. Park *et al.* [2] reported hardness values of 526.3 HV for Ni–22Cr–11Fe–1TiO_2, 645.3 HV for Ni–22Cr–11Fe–1Y_2O_3 and 593.3 HV for Ni–22Cr–11Fe–0.5TiO_2–0.5Y_2O_3 (wt.%) alloys SPSed at 1100 °C. Tang *et al.*[1] found adding 0.8 wt.% Hf to Ni–0.5Al–1Y_2O_3 increased the hardness from 360 HV to 460 HV.

Higher hardness value in Ni–20Cr–1.2Y_2O_3 alloy compared to that of Ni–20Cr alloy could be attributed to grain refinement and high volume fraction of homogeneously distributed oxide nanoparticles. The strengthening in Ni–20Cr–1.2Y_2O_3–5Al_2O_3 alloy could be attributed to combination of solid solution, Hall – Petch (due to grain refinement), precipitation (due to Y_2O_3) and composite strengthening (due to Al_2O_3 particles) mechanisms. The total strengthening was estimated by simple linear addition of all the contributing mechanisms, assuming that strengthening mechanisms operate independently of one another [45] Hence, σ_Y can be estimated by following equation;

$$\sigma_Y = \sigma_o + \Delta\sigma_{SS} + \Delta\sigma_D + \Delta\sigma_{GB} + \Delta\sigma_{Oro} + \Delta\sigma_C \quad (9.2)$$

where, σ_Y is the estimated yield strength, σ_o is the Peierls – Nabarro stress or lattice-friction stress and negligible, $\Delta\sigma_{SS}$ the solid solution strengthening contribution, $\Delta\sigma_D$ the dislocation strengthening contribution, $\Delta\sigma_{GB}$ the grain boundary strengthening contribution, $\Delta\sigma_{Oro}$ is the Orowan or dispersion mechanism contribution and $\Delta\sigma_C$ is the composite strengthening contribution factor. The Peierls – Nabarro or lattice friction-stress for an isotropic pure *fcc* crystal structure at room temperature is generally a negligible quantity (here, a value of σ_o = 6–8 MPa was assumed) [46].

9.4.2.1. Solid solution strengthening

The solid solution strengthening due to multiple alloying elements in Ni alloys has been investigated [47] and the strengthening can be expressed by the following relation

$$\Delta\sigma_{SS} = \left(\sum_i k_i^{1/n} c_i \right)^n \tag{9.3}$$

where, σ_s is the solid solution contribution, k_i is the strengthening constant for solute *i*, c_i is the concentration of solute *i*, and *n* is taken as 0.5 here. For Ni–Cr alloy, the value of *k* is 337 $MPa^{-1/2}$ [48]. Considering the nominal composition of Ni–20Cr alloy, the strengthening due to solutes is 158 MPa assuming that the Y_2O_3 and Al_2O_3 particles did not get dissolved in the matrix.

9.4.2.2. Dislocation strengthening

The contribution of dislocation strengthening can be evaluated by using Bailey – Hirsch equation [49];

$$\Delta\sigma_D = \alpha G b \rho^{1/2} \tag{9.4}$$

Here, a value of 0.5 was used for the dislocation strengthening coefficient [50] and *G* (shear modulus) and *b* (Burgers vector) were taken as 82 GPa and 0.25 nm, respectively [1, 51]. Using several TEM micrographs, the dislocation density was calculated for the three alloys and estimated to be 3.4×10^{13} m^{-2} for Ni–20Cr, 9.6×10^{13} m^{-2} for Ni–20Cr–1.2Y_2O_3 and 1.2×10^{14} m^{-2} for Ni–20Cr–1.2Y_2O_3–5Al_2O_3 alloys. Therefore, the contributions of dislocation strengthening were 68 MPa for Ni–20Cr, 96 MPa for Ni–20Cr–1.2Y_2O_3 and 111 MPa for Ni–20Cr–1.2Y_2O_3–5Al_2O_3.

9.4.2.3. Grain boundary (Hall – Petch) strengthening

The classic Hall – Petch relationship is used for estimating the grain boundary strengthening contribution. The average grain size for different alloys was measured and presented in the results section. By substituting the given average grain size values in the equation suggested by Bui *et al.* [52]:

$$\Delta\sigma_{GB} = 5538\, d^{-1/2} \qquad (9.5)$$

The grain boundary strengthening values were determined to be 257 MPa for Ni–20Cr, 360 MPa for for Ni–20Cr–1.2Y_2O_3 and 319 MPa for Ni–20Cr–1.2Y_2O_3–5Al_2O_3 alloy.

9.4.2.4. Orowan (dispersion) strengthening

The additional yield strength caused by Orowan strengthening mechanism can be determined by the following equation [53]:

$$\Delta\sigma_{Oro} = M\,\frac{0.4Gb}{\pi\sqrt{1-\upsilon}}\,\frac{\ln(\frac{2r}{b})}{\lambda} \qquad (9.6)$$

where r is the average particle radius, λ the mean particle separation, f the volume fraction of particles, υ the Poisson ratio, and M the Taylor factor. The values of λ and f were calculated to be 187 nm and 0.055 for Ni–20Cr, 58 nm and 0.235 for Ni–20Cr–1.2Y_2O_3, and 72 nm and 0.19 for Ni–20Cr–1.2Y_2O_3–5Al_2O_3 alloys, respectively. In this calculation, M was taken as 3 for *fcc* materials [54]. Based on these calculations, the contribution of Orowan strengthening mechanism at room temperature was calculated to be 295 MPa for Ni–20Cr, 650 MPa for Ni–20Cr–1.2Y_2O_3 and 587 MPa for Ni–20Cr–1.2Y_2O_3–5Al_2O_3 alloys. The pinning effects imply that the strength of oxide particles depends on particle size and mean particle separation. Therefore, reduction in the mean particle separation and homogeneously distributed Y_2O_3 nanoparticles could essentially improve the strength properties in Ni–20Cr–1.2Y_2O_3 compared to Ni–20Cr alloy [1].

9.4.2.5. Composite strengthening

Composite strengthening differs from the dispersion strengthening in terms of particle size, which is much larger. In the particle-reinforced composite, the reinforcement phase is significantly stronger than the matrix and during loading a large fraction of load is transferred to the reinforcement phase. Strength of the discontinuously-reinforced composite depends on the particle size and volume fraction. For uniformly distributed reinforcement in the matrix, the rule of mixture can be used to calculate the net properties of the composite given by the following relation: [55]

$$\sigma_c = V_p\sigma_p + V_m\sigma_m \tag{9.7}$$

where σ_c is the estimated strength of the composite, V_p and V_m are the volume fraction of the particle and matrix respectively, σ_p and σ_m are the yield strength of the particle and the

matrix. Here Al_2O_3 particles were added as composite reinforcement phase and its contribution was calculated to be 295 MPa assuming the yield strength value of 2945 MPa and the volume fraction of 0.1 for the Al_2O_3 particles.

Table 9.7 summarizes the contribution of different strengthening mechanisms in Ni–20Cr, Ni–20Cr–1.2Y_2O_3 and Ni–20Cr–1.2Y_2O_3–5Al_2O_3 alloys sintered at 1100 °C for 30 min and compares the estimated yield strength values with the experimentally determined ones. The estimated yield strength at room temperatures was found to be very close to the experimental values. For estimating the yield strength values at 800 °C and investigating deformation mechanisms, microstructural studies of as-compressed specimens are required that will be considered in our future work. The compression yield strength for the Ni–20Cr alloy was reported to be 790 MPa at 25 °C and 125 MPa at 800 °C. It appears that the only strengthening mechanism for the Ni–20Cr alloy at 800 °C was solid solution strengthening and other mechanisms were not actively working at high temperatures. The compression yield values for Ni–20Cr–1.2Y_2O_3 alloy were reported to be 1286 MPa at 25 °C and 225 MPa at 800 °C. The yield value for Inconel 754 (with nominal composition of Ni–20Cr–0.3Al–0.5Ti–0.6Y_2O_3) was reported to be 586 MPa at 25 °C and 214 MPa at 871 °C [56].

Table 9.7. Contribution of different strengthening mechanisms in Ni–20Cr, Ni20–Cr–1.2Y_2O_3 and Ni–20Cr–1.2Y_2O_3–5Al_2O_3 alloys sintered at 1100 °C for 30 min

Alloy	σ_o (MPa)	$\Delta\sigma_{SS}$ (MPa)	$\Delta\sigma_D$ (MPa)	$\Delta\sigma_{GB}$ (MPa)	$\Delta\sigma_{Oro}$ (MPa)	$\Delta\sigma_C$ (MPa)	σ_Y Cal. (MPa)	σ_Y Exp. (MPa)
H (Ni–20Cr)	8	158	68	257	295	0	786	790
B (Ni–20Cr–1.2Y_2O_3)	8	158	96	359	650	0	1271	1286
I (Ni20–Cr–1.2Y_2O_3–5Al_2O_3)	8	158	111	319	587	295	1478	1470

Figure 9.16. shows the variation of microhardness and true compression yield stress obtained at room temperature (25 °C) as a function of mean particle separation (λ) for different alloy compositions. For Ni–20Cr–1.2Y_2O_3 alloy, high hardness and yield stress values were obtained through the smallest mean particle separation, and for Ni–20Cr, the lower hardness and yield stress values were obtained due to large mean particle separation. This implies that efficiency of dispersion strengthening mechanism increased with lower mean particle separation, resulting in the improved hardness and compression yield values. In case of Ni–20Cr–1.2Y_2O_3–5Al_2O_3 alloy, high hardness and yield stress values were obtained even though the mean particle separation was slightly larger than that of Ni–20Cr–1.2Y_2O_3 alloy. This could demonstrate the efficiency of Al_2O_3 particles as the composite reinforcement particles improving the overall hardness.

Although the yield strength of Inconel 754 at 800 °C was slightly lower than the yield value of Ni–20Cr–1.2Y_2O_3 (alloy B) at 800 °C. However, the yield strength of Ni–20Cr–1.2Y_2O_3 alloy at 25 °C was almost twice larger than that of Inconel at 25 °C. This could suggest that strengthening mechanism at high temperatures could be due to dispersion of stable oxide particles in both alloys. Because the stable Y_2O_3 particles in Ni–20Cr–1.2Y_2O_3 alloy not only inhibited the dislocation motion and increased the resistance of the matrix to deformation but also controlled the recovery and recrystallization process and inhibited grain growth. However, at 25 °C, other strengthening mechanisms such as grain boundary strengthening mechanism could be actively working along with the Orowan mechanism in the case of Ni–20Cr–1.2Y_2O_3 alloy due to presence of fine grains consolidated via SPS. This could be mentioned as an advantage of using SPS to consolidate Ni–20Cr–1.2Y_2O_3 alloy with finer grains. It is worth mentioning that the contribution of fine

grains and dislocation density to strength is higher at room temperature, and those contributions would diminish significantly or disappear altogether at high temperatures due to propensity for grain boundary sliding and reduction in dislocation density.

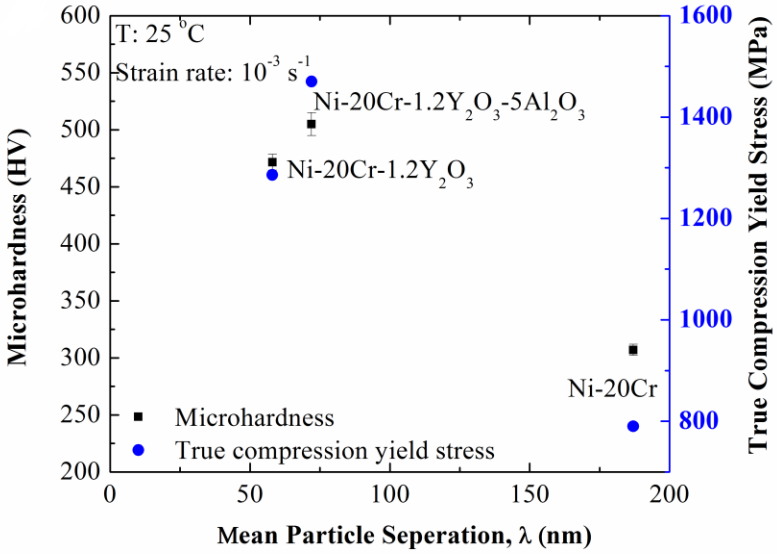

Figure 9.16. The variations of microhardness and true compression yield strength values (at room temperature) as a function of mean particle separation (λ)

9.5. Conclusions

In current study, Ni–20Cr, Ni–20Cr–1.2Y_2O_3 and Ni–20Cr–1.2Y_2O_3–5Al_2O_3 were developed via milling and SPS. The effects of milling time, sintering time, sintering temperature and alloying composition on overall microstructure, annealing twins, particles size distribution, microhardness values and compression yield stress of the nickel-based ODS alloys were investigated. The following conclusions were made:

1. Milling time: The grains in unmilled sintered alloys were in micron size range. The grain size was significantly reduced after 2 and 4 h of milling. The presence or absence of

milling has no influence on manifestation of the annealing twins. However, for longer milling times, higher amount of stored energy decreased the activation energy of twin formation and led to a higher volume fraction of twin. The twin width also decreased at longer milling times due to finer crystallites. Longer milling time (> 4 h) led to dissolution of Y_2O_3 in Ni–20Cr and produced complex Y–Cr–O-enirched particles.

2. Sintering time and temperature: Higher sintering temperature provided higher hardness and density and higher volume fraction of twins. The oxide particles were stable up to 1100 °C and could efficiently control the recrystallization process and inhibit any grain growth. The oxide particle size increased with increasing sintering temperature and time, plausibly due to faster kinetics of diffusion and particle coarsening at higher sintering temperature and longer sintering time.

3. Alloy composition: Adding Y_2O_3 to Ni–20Cr contributed to significant dispersion hardening and additional Al_2O_3 could provide further composite strengthening in Ni–20Cr matrix alloy. A high compression yield stress of 250 MPa at 800 °C was obtained for Ni–20Cr–1.2Y_2O_3–5Al_2O_3 alloy. The microstructure of this alloy contained a high density of nanograins and dislocations that were effectively controlled by high number density of the nanoparticles.

Acknowledgments

The support of the University Coal Research Program of the US Department of Energy (DOE) via a grant (DE–FE0008648) managed by the National Energy Technology Laboratory (NETL) is gratefully acknowledged. Also, we would like to thank the Center for Advanced Energy Studies (CAES) staff for facilitating access to the SPS facility.

References

[1] Tang Q, Hoshino T, Ukai S, Leng B, Hayashi S, Wang W. Maters Trans 2010;51:2019.

[2] Park J, Jang J, Kim TK, Kim SJ, Ahn JH. J Nanosci Nanotechnol 2011;11:6213.

[3] Zibral J. Metall Mater Trans A 1996;27A:1371.

[4] Lee MK, Park JJ, Rhee C. Mater Chem Phys 2012;137:129.

[5] Srolovitz DJ, Luton MJ, Petkovic RA, Narnett DM, DJ N. Acta Metall 1984;32:1079.

[6] Artz E, Rosler J. Acta Metall 1988;36:1053.

[7] Reppich B. Acta Mater 1998;46:61.

[8] Park JJ, Choe HJ, Hong SM, Lee MK, Rhee CK. Powder Technol 2012;230:139.

[9] Orowan E. Symposium on internal stresses in metals and alloys. London: Institute of Metals, 1948. p.451.

[10] Arsenault RJ. Strengthening Mechanisms in Discontinuous SiC/Al Composites. In: Marshall IH, editor. Composite Structures 4. Springer Netherlands, 1987. p.70.

[11] Wang H, Shi P, Yu H, Xu B. Phys Procedia 2013;50:225.

[12] Kuruvilla AK, Bhanuprasad VV, Prasad KS, Mahajan YR. Bull Mater Sci 1989;12:495.

[13] Hornbogen E, Starke EA. Acta Metall Mater 1993;41:1.

[14] Rosler J, Baker M. Acta Mater 2000;48:3553.

[15] Suryanarayana C, Al-Aqeeli N. Prog Mater Sci 2013;58:383.

[16] Hong SH, Kim YG, Kim HY, Poole JM, Debarbadillo JJ. Proceeding of the 2nd International Confrence on Structural Applications of Mechanical Alloying. Vancouver, British Columbia, 1993. p.69.

[17] Allahar KN, Burns J, Jaques B, Wu Y, Charit I, Cole JI, Butt DP. J Nucl Mater 2013;443:256.

[18] Munir Az, Anselmi-Tamburini U, Ohyanagi M. J Mater Sci 2006;41:763.

[19] Alinger MJ, Odette RG, Lucas GE. J Nucl Mater 2002;307:484.

[20] Kandukuri S. Met Powder Rep 2008;63:22.

[21] Ke H, Qiang LX, Chao Y, Yuan LY. Trans Nonferrous Met Soc China 2011;21:493.

[22] Groza JR. Met Powder Rep 2000;55:16.

[23] Pasebani S, Dutt AK, Charit I, Mishra RS. Mater Sci Forum 2014;783–786:1099.

[24] Nanko M, Sato M, Matsumaru K, K I. Mater Sci Forum 2006;510–511:818.

[25] Lopez BI, Fracnco EM, Zoz H, T M. Revista Mexican De Fisica 2011;57:176.

[26] Dong C. J Appl Cryss 1999;32:838.

[27] Nelson JB, Riley DP. Proc Phys Soc 1945;57:160.

[28] Williamson GK, Hall WH. Acta Metall 1953;1:22.

[29] Horton D, Thomson CB, Randle V. Mater Sci Eng A 1995;203:408.

[30] Randle V, Rios PR, Hu Y. Scripta Mater 2008;58:130.

[31]Randle V. The Role of the Coincident Site Lattice in Grain Boundary Engineering. London: The Institute of Materials, 1996.

[32] Srinivasarao B, Ohishi K, Ohkubo T, Hono K. Acta Mater 2009;57:3277.

[33] Pasebani S, Charit I. J Alloys Compd 2014;599:206.

[34] Shang SL, Zacherl CL, Fang Y, Du Y, Liu ZK. J Phys: Condens Matter 2012;24:505403.

[35] Wen H, Lavernia EJ. Scripta Mater 2012;67:245.

[36] Nganbe M, Heilmaier M. Mater Sci Eng A 2004;387–389:609.

[37] Hsiung L, Fluss M, Tumey S, Kuntz J, El-Dasher B, Wall M, Choi B, Kimura A, Willaime F, Y S. J Nucl Mater 2011;409:72.

[38] Miller MK, Hoelzer DT, Kenik EA, Russell KF. J Nucl Mater 2004;329–333:338.

[39] Gale W, Totemeier T. Smithells metals reference book. Amsterdam: Elsevier, 2004.

[40] Pasebani S, Charit I, Wu YQ, Butt DP, Cole JI. Acta Mater 2013;61:5605.

[41] Farbaniec L, Dirras G, Krawczynska A, Mompiou F, Couque H, Naimi F, Bernard F, Tingaud D. Mater Charact 2014;doi.org/10.1016/j.matchar.2014.05.008.

[42] Bair JL, Hatch SL, Field DP. Scripta Mater 2014;81:52.

[43] Fang S, Chen W, Fu Z. Mater Design 2014;54:973.

[44] Thomson CB, V R. Scripta Mater 1996;35:385.

[45] Hornbogen E, Haasen P, Gerold V, Kostorz G, Gupt S. proceedings of ICAPP ’06 of the 5th International Conference. Aachen, Germany: Pergamon press, 1979. p.137.

[46] Norfleet DM, Dimiduk DM, Polasik SJ, Uchic MD, Mills MJ. Acta Mater 2008;56:2988.

[47] Gypen LA, Deruyttere A. J Mater Sci 1977;12:1034.

[48] Roth A, Davis CL, Thomson RC. Metall Mater Trans A 1997;28:1329.

[49] Bailey JE, Hirsch PB. Philos Mag 1960;5:485.

[50] Nakashima K, Suzuki M, Futamura Y, Tsuchiyama T, Takaki S. Mater Sci Forum 2006;503–504:627.

[51] Pollock TM, Sammy T. J Propul Power 2006;22:361.

[52] Bui QH, Dirras S, Ramtani G, Gubicza R. Mater Sci Eng A;527:3227.

[53] Brown LM, Ham RK, Kelly A. Elsevier, Amsterdam, 1971:9.

[54] Parthasarathy TA, Rao SI, Dimiduk DM. Superalloys TMS 2004.

[55] Chawla N, Chen Y. Adv Eng Mater 2001;3:357.

[56] Suryanarayana C. Prog Mater Sci 2001;46:1.

Appendix A: Mechanical Properties

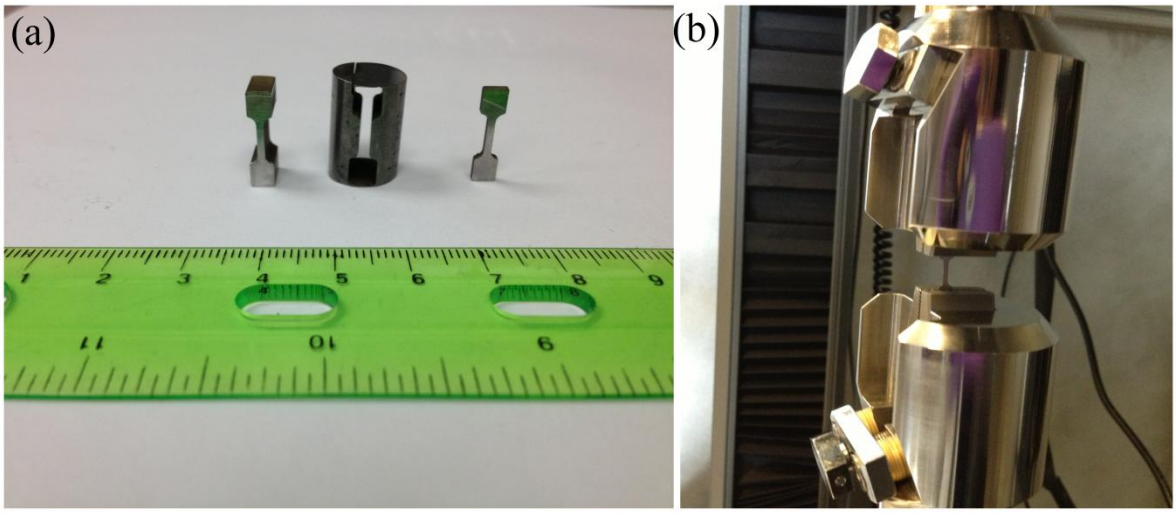

Figure 1. (a) The machined mini-tensile specimens, and (b) minit-tensile test set-up

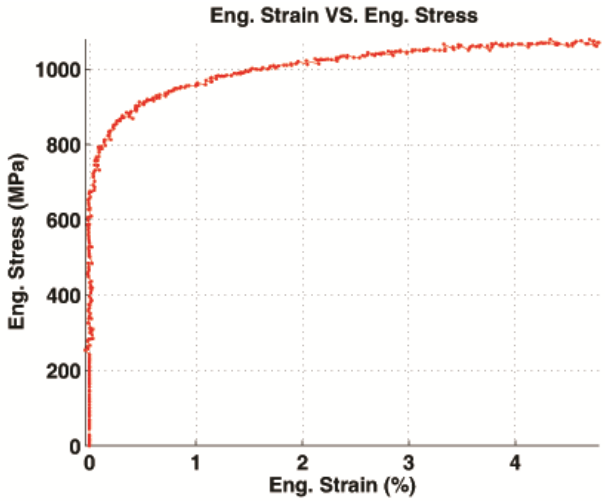

Figure 2. Engineering stress – strain curve for 14LMT alloy obtained after tensile test at room temperature applying strain rate of 10^{-3} s^{-1}

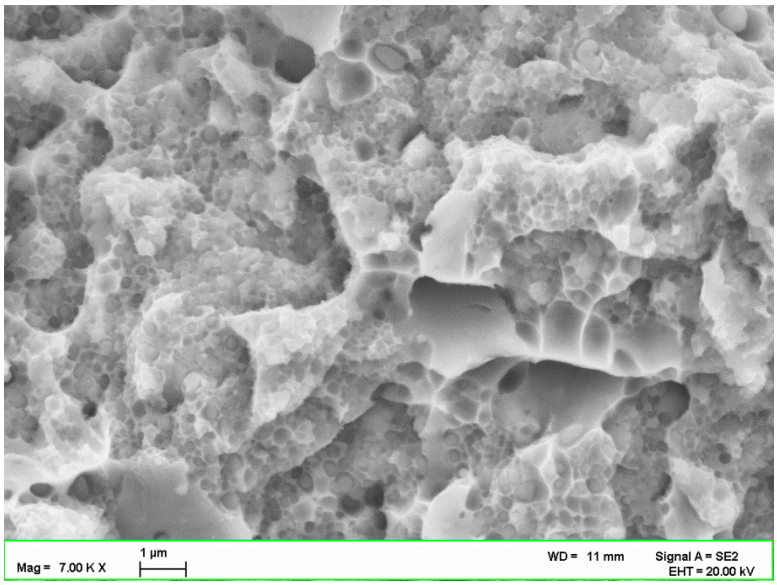

Figure 3. SEM micrograph showing the fractured surface of the 14LMT alloy

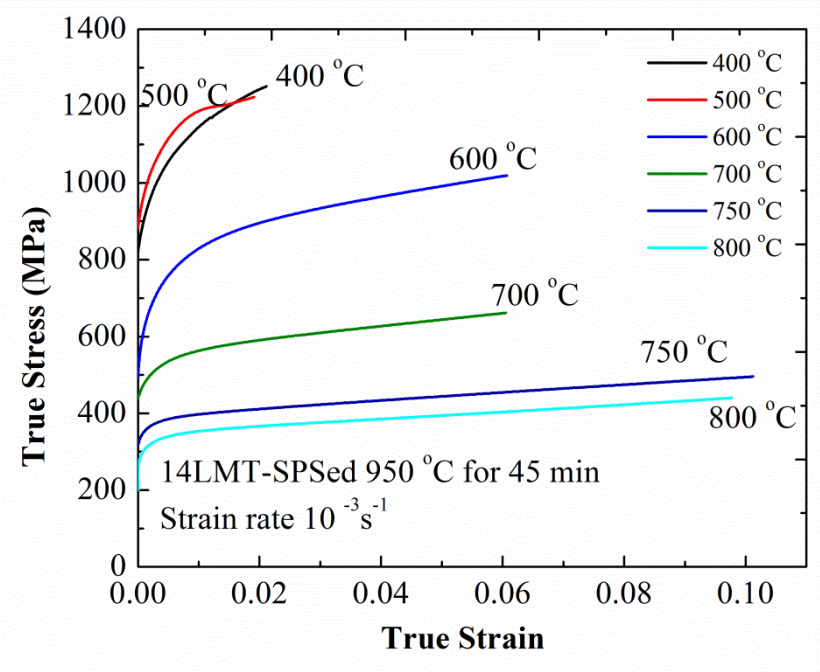

Figure 4. True compression – true plastic strain for 14LMT alloy obtained after compression tests at different temperature applying strain rate of 10^{-3} s^{-1}